Methodological Developments for an Improved Evaluation of Climate Change Impact on Flow Hydrodynamics in Estuaries

Hamidreza Shirkhani

Thesis submitted to the
Faculty of Graduate and Postdoctoral Studies

in partial fulfillment of the requirements
for the Doctorate in Philosophy degree in civil engineering

Department of Civil Engineering
Faculty of Engineering
University of Ottawa

Université d'Ottawa | University of Ottawa

Abstract

The knowledge of flow hydrodynamics within the next decades is of particular importance in many practical applications. In this study, a methodological improvement has been made to the evaluation of the flow hydrodynamics under climate change. This research, indeed, proposes an approach which includes the methods that can consider the climate change impact on the flow in estuaries, gulfs, etc. It includes downscaling methods to project the required climate variables through the next decades. Here, two statistical downscaling methods, namely, Nearest Neighbouring and Quantile-Quantile techniques, are developed and implemented in order to predict the wind speed over the study area. Wind speed has an essential role in flow field and wave climatology in estuaries and gulfs.

In order to make the proposed methodology computationally efficient, the flow in the estuary is simulated by a large-scale model. The finite volume triangular C-grid is analysed and shown to have advantages over the rectangular (finite difference) one. The dispersion relation analysis is performed for both gravity and Rossby waves that have crucial effects in oceanic models. In order to study the unstructured characteristic of the triangular grids, various isosceles triangles with different vertex angles are considered. Moreover, diverse well-known second-order time stepping techniques such as Leap-Frog, Adams-Bashforth and improved Euler are studied in combination with the C-grid semi discrete method. The fully discrete method is examined through several numerical experiments for both linear and non-linear cases. The results of the large-scale model provide the boundary conditions to the local coastal model.

In order to model the flow over a local coastal area, a well-balanced positivity preserving central-upwind method is developed for the unstructured quadrilateral grids. The quadrilateral grid can effectively simulate complex domains and is shown to have advantages over the triangular grids. The proposed central-upwind

scheme is well-balanced and preserve the positivity. Therefore, it is capable of modelling the wetting and drying processes that may be the case in many local coastal areas. It is also confirmed that the proposed method can well resolve complex flow features. The local model incorporates the outputs of the downscaling and large-scale flow models and evaluates the flow hydrodynamics under changing climate.

Acknowledgements

I would like to express my deepest gratitude to my supervisors, Dr. Ousmane Seidou and Dr. Majid Mohammadian, for their invaluable guidance, advice, and continued supports. I appreciate all their contributions of time and inspiration to make my PhD experience productive and stimulating. None of this would have been possible without their dedication.

I would like to acknowledge my committee members, Drs. Colin Rennie, Ioan Nistor, Tew-Fik Mahdi, and Abhijit Sarkar, for providing precious suggestions and comments on my thesis. I would like to express my sincere appreciation to Dr. Alexander Kurganov for his valuable collaboration and advice.

I would like to thank my family for their everlasting encouragement and specially my parents for their unconditional love and support in all my pursuits. Most of all, I would like to give my huge thanks to my beloved wife Parna who has always been by my side with patience, endless love, and faithful support.

To Parna

and

My parents

List of figures

List of Tables

List of Symbols

X_{GCM}: Value extracted from raw GCM

X_{CORR}: Corrected (downscaled) climate variable

U_A: Wind stress factor

F: Fetch length

g: Gravity acceleration

H: Constant Average depth

η: Surface elevation

(u, v): Velocity components

ω: frequency

(k, l): Wave numbers

U: Normal velocity

C_r: Phase speed ratio

G: Group velocity

t: Time

Δt: Time step

J: Bessel function of first kind

τ_{bx}, τ_{by}: Bottom friction components

τ_x, τ_y: Wind stress components

C: Chezy friction

f: Coriolis parameter

β: Linear Coriolis coefficient

E: Lamb parameter

λ: Rossby radius

$h(x, y, t)$: Water depth

B: Bottom topography

Contents

Chapter 1

Introduction

The knowledge of flow characteristics in the next decades is an essential requirement for sustainable development of coastal areas and should be considered in the planning, design, construction, and operation of harbours as well as the protection of offshore and coastal structures. The environmental impacts of the potential modifications of water level, velocity and wave regimes should be considered as well, because they may impact ecosystems and marine activities such as fishing. In order to do so, we need to know how important climatic variables such as wind speed will evolve in the future, and how they will impact water level, velocity and wave regimes. In this study, we develop and/or improve a suite of models to simulate the flow under the changing climate. These models, indeed, include downscaling models for projecting the required climate variables as well as large and local scale hydrodynamic models.

1.1. Research Objectives, Significance and background

Flow hydrodynamics play an essential role in various practical aspects of civil and environmental engineering, ranging from environmental and hydrodynamic studies of lakes, estuaries and coastal regions to designing the coastal and harbour structures.

Given that flow hydrodynamics are likely to change in the future because of global warming, it is essential to determine how much this will impact (positively or negatively) human activities and ecosystem health. Therefore, evaluation of the environmental impacts is an important issue. For instance, there are firm regulations on the level of required dilution of the concentrated outfall of desalination plants in order to protect aquatic life and the ecosystem. There is a growing number of plants all around the world that discharge their industrial outfalls in lakes, estuaries, gulfs, etc. A good projection of flow hydrodynamics in the threatened environments is a fundamental requirement for studying the environmental impact assessment and taking the appropriate adaptation measures. The main objective of this research is to contribute to the improvement of a suite of models that

are used for evaluation of future impacts of climate change on flow hydrodynamics in estuaries in support of environmental impact studies.

As an example of environmental impact assessment study, the environmental impacts of desalination plants have been investigated through a number of research studies. Didier (2003) developed the COHERENS model for simulating tidal-modulated dispersion of brine and used it in a coastal desalination plant in Singapore. Jenkins and Wasyl (2005) studied oceanographic considerations for desalination plants in southern California coastal waters using SEDXPORT model. Al-Mutaz et al. (2006) studied brine dispersion at Al-Jubail and Al-Khobar plants using several simplifying assumptions. Okely et al. (2006) studied the impact of the Perth Seawater DesalinationPlant (Australia) using ELCOM-CAEDYM. Alameddine and El-Fadel (2007) simulated the heated effluent from a desalination-power plant in the Gulf region using CORMIX model. Vaselali et al. (2009) investigated the effect of a tidally oscillating flow on the dispersion of brine waste discharge into the Gulf using the Mike-21 model for far field. Malcangio and Petrillo (2009) used the MIKE 3-D model to simulate brine discharge in a coastal region in the south of Italy.

In the current study, in order to evaluate future impacts of climate change, various climate change scenarios will be considered and the projected results of general circulation models (GCMs) will be downscaled and employed in numerical simulations. In addition, improved numerical schemes for flow simulation in both large and local scale will be developed.

1.1.1. Wind Speed Downscaling

Wind characteristics in the future will be obtained by downscaling the outputs of three different GCMs, namely, a coupled physical model (CM3) and earth system models (ESM2M and ESM2G).The ensemble average of these models will also be considered. The models were generated in the CMIP5 experiment (http://pcmdi-cmip.llnl.gov/cmip5/), which is an integrated set of experiments that offer a multimodel perspective of simulated climate change and climate variability. Within the core set of CMIP5 runs, there are four future projection simulations forced with specified concentrations, which are referred to as Representative Concentration Pathways (RCPs) (Taylor et al. 2012; Hemer et al. 2013).

The RCPs are used to initiate climate model simulations for developing climate scenarios for use in a broad range of climate-change-related research and assessment. There are four RCPs for various radiative forcing, referred to as RCP85, RCP60, RCP45, and RCP26 (IPCC Expert Meeting Report 2007).

Near-surface wind speeds have a particular importance for a wide variety of practical applications such as coastal engineering and wind energy resource estimation (Pryor et al. 2005a; Viles and Goudie 2003). Wind plays an essential role in wave climatology as it impacts several flow characteristics. It is well known that a mismatch exists between the spatial resolution of climate variables simulated by general circulation models (GCMs) and the resolution required by most practical applications (Carter et al. 1994; Chong-yu 1999). Downscaling is used as a mean for converting coarse-scale output of GCMs to finer scales for specific applications (Jolley and Wheater 1996; Horvath et al. 2011; Legates 2002). Downscaling can be performed either dynamically or statistically. In dynamical downscaling, a regional climate model (RCM) with a higher spatial resolution is executed on a limited domain, using boundary conditions provided by the GCM (Raisanen et al. 2004). The statistical downscaling approach develops an empirical relationship that relates large-scale climate variables to the observed climate variable (Pryor et al. 2005b; Wilby and Wigley 1997; Wilby et al. 2004).

The vast majority of downscaling studies deal with temperature and precipitation (Wilby et al. 2003; Rowell 2005; Argüeso et al. 2013; Vasiliades et al. 2009; Hashmi et al. 2011), and focus on the estimation of the mean value of the predictands. The knowledge of mean wind speed value is insufficient in most applications (wind energy, wave height estimation, forces on structures) because of inherent wind variability in small time-scales. Indeed, wind speed exhibits variability at much smaller spatial and temporal scales than the outputs of general circulation models (de Rooy and Kok 2004). Proper projection of wind variations as well as peak values is required since they have essential impacts in various practical applications. In Shirkhani et al. (2013), a regression-based downscaling technique was used to downscale wind speed at the Agadez city located in Niger, West Africa. Results indicated that both linear and nonlinear regression techniques are incapable of predicting wind speeds variations even when bias correction is applied. Pryor et al. (2005b)

proposed a probabilistic approach for wind speed projection in Northern Europe. Instead of directly using GSM-simulated wind speed and observed wind speed as predictors and predictands, they used the mean and standard deviation of large-scale and local-scale data. Monahan (2012) assessed the statistical predictability of wintertime wind speed and direction in the subarctic northeast Pacific off the west coast of Canada. He demonstrated that daily wind fluctuations are generally more predictable than monthly-mean variability, and that monthly averages of the predicted daily winds generally represent the monthly-mean surface winds better than the predictions directly from monthly mean predictors. Devis et al. (2013) implemented a statistical regression approach to downscale large-scale wind speed data to wind speed distribution at the hub-height of tall wind turbines in Northern Europe. The regression analysis is based on the parameters of the PDF of both large-scale and local-scale wind speed.

This study uses the Quantile-Quantile and the nearest neighbor techniques to downscale wind speed. The employed downscaling techniques in this research allow the estimation of the monthly PDF of daily mean wind speed. They have the advantage of being nonparametric as no distribution is assumed for the predictand and predictors. For each of the mentioned techniques, observations will be split into a calibration and validation sets. In addition, results will be assessed by comparing the monthly PDFs of the downscaled wind field to that of the observation on both the calibration and validation period using both visual observation and the Kolmogorov-Smirnoff test.

The results of the wind speed downscaling, can be used for many practical purposes. Here, we use them as an input to the numerical flow model in order to consider the climate change impact on the flow hydrodynamics.

1.1.2. Large-Scale Flow Model: Finite Volume Triangular C-Grid Scheme

The focus of this part ofthe study is to develop an appropriate large-scale numerical model based on shallow water (SW) equations in order to simulate the flow over the estuaries and gulfs. The SW equations, which resulted from the Navier–Stokes equations, play a vital role in environmental and hydrodynamic studies of lakes, estuaries and coastal regions. In particular, various oceanic waves such as gravity, inertia and inertia-gravity waves have an

important role in the ocean flows. Indeed, an ideal ocean model needs to be capable of simulating a wide range of oceanic waves.

In numerical modeling of SW system, due to the coupling between the momentum and continuity equations, there are many possibilities of variable placement for certain choice of grids. This may lead to spurious oscillation in the numerical solutions (Le Roux et al. 2007). The effect of variable placement on a variety of grids has been studied for solving shallow water equations (SrdjanDobricic 2006; Despotisand Tsangaris 1996; Popinet and Rickard 2009; Langtangen et al. 2002; Walters and Carey 1984).Mesinger and Arakawa (1976) proposed various staggered grids. These grids were analyzed, and among them, the C-grid was found to be promising (Akawara and Lamb 1977; Walters and Carey 1984). In the C-grid approach, the water surface elevation (pressure) is stored at the circumcenter of the cells while the normal velocity components are retained at the finite volume cell edges. There has been an increased trend in using the C-grid approach with different numerical schemes such as finite difference, finite element and finite volume (Casulli and Walters 2000; Walters et al. 2009; Walters and Casulli 2001; Popinet and Rickard 2009). The C-grid approach has been widely used in different oceanic models such as Princeton Ocean Model (Blumberg and Mellor 1987), MICOM (Bleck and Smith 1990), MIKE3HS (Pietrzak et al. 2002), MITgcm (Marshall et al. 1997; Adcroft et al. 2004), ROMS (Shchepetkin and McWilliams 2003; 2005) and UnTRIM (Jankowski, 2007; 2009).

The dispersion relation and Fourier analyses are useful tools to study the effect of spatial and temporal discretization schemes on the quantities which analytical ones should be preserved by an ideal numerical model. The dispersion relation and Fourier analyses, in addition to indicating the limitations and advantages of the discretization schemes, are useful for choosing parameters such as the Courant–Friedrich–Lewy (CFL) number. The Fourier and dispersion relation analyses have been used for shallow water equations using finite difference (Adcroft et al. 1999) ; (Sankaranarayanan and Spaulding 2003), finite elements (Kinnmark and Gray 1985; Jaber and Mohtar 200; Le Roux and Pouliot 2008; Le Roux 2005) and finite volume methods (Gossard and Kolar 2000; Mohammadian 2010).

Dispersion relation analysis of finite difference C-grid on structured rectangular grids for SW with Coriolis force term was well investigated and documented. Dukowicz (1995) obtained the dispersion relation of various grids, including the C-grid, for inertia-gravity waves in terms of accuracy. Adcroft et al. (1999) performed dispersion relation analysis for a finite difference C-grid and reported spurious modes due to the Coriolis term. They suggested a new treatment by augmenting the C-grid variables using D-grid ones, and they proposed the CD-grid. Le Roux (2005) used dispersion relation analysis for the finite element method and compared the results to a finite difference C-grid and CD-grid. He reported poor behaviour of finite difference structured C-grid in modelling inertia-gravity waves due to the Coriolis mode, particularly for low-resolution grids. Using dispersion relation analysis, Thuburn (2007) also reported artificial slowing of inertial waves in the numerical results for the finite difference structured C-grid. He showed that numerical Rossby wave dispersion is sensitive to the details of the discretization of the Coriolis terms. However, to the best knowledge of the authors, the behaviour of the finite volume triangular C-grid either for the gravity or the inertia-gravity waves has not been analyzed.

Since the temporal discretization can also affect the behaviour of the triangular C-grid scheme, its performance in combination with different time-stepping methods is also of essential importance. Mohammadian and Le Roux (2008) studied the behaviour of a class of upwind schemes in shallow water systems. In the current study, different time-stepping techniques are assessed in combination with the finite volume C-grid scheme: forward Euler, Improved Euler, Leap-Frog and second-order Adams–Bashforth temporal schemes. Indeed, the Euler scheme is employed as a very basic method. Improved Euler is a second order method which tries to improve the forward Euler method by combining it using implicit time stepping. Gray and Lynch (1997) analyzed Leap-Frog and Adams–Bashforth techniques for solving the long-wave surface water equations using the finite element method in terms of stability and accuracy. The Leap-Frog scheme is a second-order scheme which has been implemented in many practical models, e.g., POM (Mellor 2004), and has a wide range of applications in oceanic and atmospheric contexts (Aiki and Greatbatch 2014; Iwasaki et al. 2014). The Adams–Bashforth second-order method is also a well known temporal scheme which has been used in the MITgcm Model.

First, the dispersion relation is obtained and analyzed for the semi-discrete C-grid scheme. In this regard, the wave amplitude, phase speed and group velocity of the C-grid spatial discretization scheme are compared to those of analytical analysis. In presence of Coriolis term, which has an essential role in large scale ocean modelling, in order to generalize the study, we consider isosceles triangular cells with various vertex angles that may represent a general sketch of arbitrary triangular grids. We then analyze the behaviour of the semi-discrete scheme in combination of various well-known second-order time stepping techniques. Different linear and non-linear numerical tests are simulated in order to verify the analytical dispersion analysis and investigate the performance of the proposed fully discrete methods.

1.1.3. Local Coastal Flow Model: Quadrilateral Central-upwind scheme

For modelling the coastal flow, a well-balanced positivity preserving central-upwind scheme for unstructured quadrilateral grids is developed. An appropriate local flow model should be capable of correctly simulating the sharp waves. Moreover, it should be positivity preserving and well-balanced. 2D SWEs are commonly used to simulate a wide range of problems in water resources engineering, modelling oceans, rivers and coastal areas, etc. SWEs, generally, admit several steady-state solutions. One of the practically most important steady states is a so-called "lake at rest" state. A good numerical method for the SWEs should be well-balanced, that is, it should be capable to exactly preserve the "lake at rest" steady states. It should also preserve positivity of the water depth h.

Many numerical methods for SWEs were developed in past decades. We refer the reader, for example, to finite difference (Casulli 1990; Xing and Shu 2005; Casulli and Walters 2000), finite element (Hanert et al. 2005; White et al. 2008; Triki 2014) and finite volume (Casulli and Walters 2000; Bonaventura et al. 2006; Mohamed 2014) methods. There are also high order schemes developed for hyperbolic systems (Liu et al. 1994; Bassi andRebay 1997; Giraldo et al. 2002; Xing et al. 2010) but they are comparatively computationally expensive. In this paper we focus on the finite volume methods which are based on the integral form of SWEs and thus are naturally designed to conserve the mass.

Central-upwind schemes are finite volume methods that are both well-balanced and positivity preserving. Central-upwind schemes are Riemann-problem-solver- free Godunov-type methods that were originally introduced in Kurganov and Tadmor (2000) for general multidimensional systems of hyperbolic conservation law and further developed in (Kurganov et al. 2001; Kurganov and Tadmor 2002; Kurganov and Lin 2007; Kurganov and Petrova 2005). In (Kurganov and Levy 2002; Kurganov and Petrova 2007), the central- upwind schemes for SWEs were developed in the 1D and 2D cases using Cartesian grids. In (Bryson et al. 2011), the central-upwind schemes were extended to unstructured triangular meshes, and in (Beljadid et al. 2014), they were also generalized for polygon cell-vertex meshes.

The main goal of this part of the study is to develop a second-order well-balanced positivity preserving central-upwind scheme for SWEs on unstructured quadrilateral grids. Such grids have been widely used in finite volume methods for various applications such as solving incompressible Navier–Stokes, diffusion equations, semilinear elliptic and elliptic systems, see, e.g., (Chou et al. 2003; Sheng and Yuan 2008; Feng et al. 2012; Xie and Xiao 2014) and references therein. In particular, quadrilateral grids have been used to develop finite volume methods for the 2D SWEs, see, e.g., (Kuiryaet al. 2012; Wu et al. 2011; Chou et al. 1999; Suli1992; Kernkampet al. 2011; Begnudelli and Sanders 2007). Unstructured quadrilateral grids are popular since they allow one to relatively easily implement local and adaptive mesh refinement techniques (Liang et al. 2008; Greaves 2004), increase the formal order of spatial accuracy of the scheme, as well as discretize second- and higher-order terms (Wu et al. 2011; Alcrudo and Garcia-Navarro 1993). Comparing to the triangular grids, one of the main advantages of the quadrilateral ones is that quadrilateral cells have more neighbouring cells and thus the quadrilateral time evolution procedure is typically more accurate.

The proposed quadrilateral central-upwind scheme is an extension of the triangular central -upwind scheme from (Bryson et al. 2011). However, some of the ingredients of the triangular scheme cannot be directly carried to the quadrilateral case. For example, one cannot obtain a continuous piecewise linear approximation of the bottom topography. Instead, we introduce a new bottom topography approximation: In each quadrilateral cell

the bottom topography function B is replaced with four continuous linear pieces, each of which connects the values of B at two of the neighbouring cell vertices with the approximate value of B at the geometric center of the cell. Another novelty of our quadrilateral scheme is a new water surface reconstruction correction technique, required to guarantee the positivity of the water depth at the reconstruction step of the central-upwind scheme. To this end, we first perform a piecewise linear reconstruction of the water surface and then, in the cells where some values of the reconstructions fall below the corresponding values of the bottom topography, we replace the linear piece with four continuously matched linear pieces whose shape is similar to the bottom topography approximant in this cell. As we prove in Theorem 1, this will guarantee positivity of water depth h. To ensure the well-balanced property of the proposed scheme, we design a special quadrature for the cell average of the geometric source term, which leads to a perfect balance of the source and fluxes for the "lake at rest " state. To the best of our knowledge, the designed central-upwind scheme is among the first well-balanced positivity preserving schemes on unstructured quadrilateral grids.

1.2. Thesis Outline

The first step in the current study was to develop a multi-model multi-scenario approach in order to project the wind speed over the coastal area. Indeed, the wind speed as an important climate variable which can affect the flow hydrodynamics, was required to be projected under the changing climate. In order to decrease the uncertainties associated with the GCM outputs, we used the outputs of three different GCMs as well as the ensemble average under various emission scenarios. We also used the Quantile-Quantile and nearest neighbour methods. With respect to the validation results, the performance of the Quantile-Quantile was shown to be better and capable of projecting the extreme events. Developing this approach and its application to estimate the significant wave height through the Qatar coastal areas led to the publication in the *Natural Hazards Review* of *ASCE* which will be presented in Section 2.

In the next step, we implemented a dispersion relation analysis in order to analyze the performance of the triangular finite volume C-grid scheme. We also proposed different

fully-discrete models by combining the C-grid semi-discrete method with different time-stepping techniques and investigated the behaviour of the fully-discrete models. The dispersion relation analysis has been divided into two major parts. In the first part, the finite volume C-grid scheme for gravity waves, i.e. without considering the Coriolis force term were investigated. The focus was on the short fast gravity waves and results showed that the scheme is capable of modeling those kind of waves in both linear and non-linear cases. The results also showed that the Adams-Bashforth scheme is more accurate while the Leap-Frog is more stable to be used in combination with the unstructured C-grid semi-discrete method. The outcomes of this part of the study was published as a research paper in *Advances in Water Resources* that can be found in Section 3.

As the next step, the finite volume triangular C-grid in presence of Coriolis term was considered. It should be noted that the Coriolis term is of particular importance in large scale flow simulation. The dispersion relation analysis showed a great improvement in Coriolis modes compared to the structured rectangular C-grid, especially for the low resolution case. Both linear and non-linear SW equations were then considered with different source terms such as surface wind stress, bottom friction and topography changes. The proposed scheme was examined through various numerical tests and results demonstrated that it is capable of modelling various kind of waves such as gravity and inertia-gravity waves. This led to our next publication in *Advances in Water Resources* which is presented in Section 4.

As for the local flow model, a well-balanced positivity preserving central-upwind scheme for quadrilateral grids was developed. A quadrilateral grid was employed and its potential advantage over the triangular one was shown. A new method for bottom topography reconstruction was proposed, which along with the new method for water surface modification ensures positivity preserving. In addition, a new quadrature was designed in order to make the model well-balanced. This was the focus of our fourth publication in *Computer and Fluids* which is presented in Section 5.

In Section 6, in fact, as a proof of the concept for the methodology proposed in this thesis, the flow hydrodynamics through the Persian Gulf is simulated using the improved models

developed in this study. The objective is to show the ability of the developed models to consider the effect of climate change in simulation of flow hydrodynamics. This work is in preparation to be submitted and published as a peer-reviewed journal paper.

Finally, in Section 7, we summarize the concluding remarks of this study.

Chapter 2

Projection of Significant Wave Height in a Coastal Area under RCPs Climate Change Scenarios[1]

Abstract

This article provides multimodel and multiscenario projections of significant wave height for the Qatar coast. Significant wave height is used for practical purposes such as offshore and coastal structure design as well as transport of marine and lake pollutants. It is mainly driven by near-surface wind speed. In this paper, the outputs of the different general circulation models (GCMs), under RCP (representative concentration pathways) emission scenarios RCP26, RCP45, RCP60, and RCP85, were used to project the monthly probability distribution of wind speed over the coastal areas. The simulations are part of the Coupled Model Intercomparison Project-Phase5 (CMIP5) experiment. Two statistical downscaling techniques are used: the Quantile-Quantile transformation and nearest neighbor search. Observed wind speed at the Doha Airport station was used as a proxy for wind speed over Qatar coast. The GCM-simulated wind speeds as well as minimum and maximum temperatures were used as predictors while the observed wind speed is used as predictand in the nearest neighbor method. In the Quantile-Quantile approach, the GCM-simulated wind speed is the sole predictor. These two techniques were assessed by comparing the probability distribution of the observed and corrected (downscaled) wind-fields. Finally, the projected wind speed was used to estimate the expected changes in significant wave height under climate change. Results show that: (1) both methods can reasonably reproduce the shape of the daily wind-speed probability distribution function at the study location but the nearest neighbor method is inappropriate for extreme wind speed estimation in the future; and (2) the Quantile-Quantile method suggests that significant wave height can increase up to 40% on the Qatar coast.

[1]This part of the study has been published as: **H. Shirkhani**, O. Seidou, A. Mohammadian, H. Qiblawey, "Projection of Significant Wave Height in a Coastal Area under RCPs Climate Change Scenarios", *Natural Hazards Review, ASCE*, 2015, DOI: 10.1061/(ASCE)NH.1527-6996.0000192.

.

keywords: *Statistical downscaling, Wind speed downscaling, Wave height projection, Quantile-Quantile transformation, Nearest neighbor search, Representative concentration pathway*

2.1. Introduction

Near-surface wind speeds have a particular importance for a wide variety of practical applications such as coastal engineering and wind energy resource estimation (Pryor et al. 2005a; Viles and Goudie 2003). Wind plays an essential role in wave climatology as it impacts several wave characteristics. Knowledge of wave characteristics is an essential requirement for marine activities such as planning, design, construction and operation of harbors as well as protection of offshore and coastal structures. Wave height is affected by wind speed, direction, fetch length, and water depth (Andreas and Wang 2007) but wind speed is the characteristic that has the greatest effect on wave height. Indeed, a higher wind speed directly results in a higher wave height. Therefore, the accuracy of any wave height estimation will be affected by accuracy of the wind speed estimation.

The main objective of this study is the estimation of the impact of global warming on the monthly probability distribution function (PDF) of daily wind speeds for the Qatar gulf. Projected changes in wind speed will be used to estimate changes in significant wave heights in the study area. Wind characteristics in the future will be obtained by downscaling the outputs of three different models, namely, a coupled physical model (CM3) and earth system models (ESM2M and ESM2G), as well as the ensemble average. The models were generated in the CMIP5 experiment (http://pcmdi-cmip.llnl.gov/cmip5/), which is an integrated set of experiments that offer a multimodel perspective of simulated climate change and climate variability. Within the core set of CMIP5 runs, there are four future projection simulations forced with specified concentrations, which are referred to as Representative Concentration Pathways (RCPs) (Taylor et al. 2012; Hemer et al. 2013). The RCPs are used to initiate climate model simulations for developing climate scenarios for use in a broad range of climate-change-related research and assessment. There are four RCPs for various radiative forcing, referred to as RCP85, RCP60, RCP45, and RCP26 (IPCC Expert Meeting Report 2007). All RCP scenarios are considered in this paper.

It is well known that a mismatch exists between the spatial resolution of climate variables simulated by general circulation models (GCMs) and the resolution required by most practical applications (Carter et al. 1994; Chong-yu 1999). Downscaling is used as a mean for converting coarse-scale output of GCMs to finer scales for specific applications (Jolley and Wheater 1996; Legates 2002; Horvath et al. 2011). Downscaling can be performed either dynamically or statistically. In dynamical downscaling, a regional climate model (RCM) with a higher spatial resolution is executed on a limited domain, using boundary conditions provided by the GCM (Raisanen et al. 2004). The statistical downscaling approach develops an empirical relationship that relates large-scale climate variables to the observed climate variable (Pryor et al. 2005b; Wilby and Wigley 1997; Wilby et al. 2004).

The vast majority of downscaling studies deal with temperature and precipitation (Wilby et al. 2003; Rowell 2005; Argüeso et al. 2013; Vasiliades et al. 2009; Hashmi et al. 2011), and focus on the estimation of the mean value of the predictands. The knowledge of mean wind speed value is insufficient in most applications (wind energy, wave height estimation, forces on structures) because of inherent wind variability in small time-scales. Indeed, wind speed exhibits variability at much smaller spatial and temporal scales than the outputs of general circulation models (de Rooy and Kok 2004). Proper projection of wind variations as well as peak values is required since they have essential impacts in various practical applications. In Shirkhani et al. (2013), a regression-based downscaling technique was used to downscale wind speed at the Agadez city located in Niger, West Africa. Results indicated that both linear and nonlinear regression techniques are incapable of predicting wind speeds variations even when bias correction is applied. Pryor et al. (2005b) proposed a probabilistic approach for wind speed projection in Northern Europe. Instead of directly using GSM-simulated wind speed and observed wind speed as predictors and predictands, they used the mean and standard deviation of large-scale and local-scale data. Monahan (2012) assessed the statistical predictability of wintertime wind speed and direction in the subarctic northeast Pacific off the west coast of Canada. He demonstrated that daily wind fluctuations are generally more predictable than monthly-mean variability, and that monthly averages of the predicted daily winds generally represent the monthly-mean surface winds better than the predictions directly from monthly mean predictors.

Devis et al. (2013) implemented a statistical regression approach to downscale large-scale wind speed data to wind speed distribution at the hub-height of tall wind turbines in Northern Europe. The regression analysis is based on the parameters of the PDF of both large-scale and local-scale wind speed.

This paper uses the Quantile-Quantile and the nearest neighbor techniques to downscale wind speed at the International Doha Airport station located near to the shore of Qatar within the short-term (years 2026–2050), medium-term (years 2051–2076), and long-term (years 2076–2100) climate-change periods. The employed downscaling techniques in this paper allow the estimation of the monthly PDF of daily mean wind speed. They have the advantage of being nonparametric as no distribution is assumed for the predictand and predictors. For each of the mentioned techniques, observations will be split into a calibration and validation sets. In addition, results will be assessed by comparing the monthly PDFs of the downscaled wind field to that of the observation on both the calibration and validation period using both visual observation and the Kolmogorov-Smirnoff test. After the downscaling exercise, the 100-year wind speed is estimated and the downscaled wind speed resulting from Quantile-Quantile technique is used to estimate wave height under the RCPs climate change scenarios.

2.2. Material and Methods

2.2.1. Data and Area of Study

The main objective of this paper is to downscale the GCM output of wind speed to the specific location in Qatar coast where observation data of wind speed are available. The observation data were downloaded from the National Climatic Data Center of the National Oceanic and Atmospheric Administration (NCDC 2015). Observation data include 43 years (1973–2012) of mean daily measurements of wind speed as well as maximum and minimum temperatures at the Doha International Airport located in Qatar. The airport is situated at 25°15′39″ N; 51°33′54″ E, respectively.

The CM3, ESM2M, and ESM2G were developed by the Geophysical Fluid Dynamics Laboratory (GFDL) of the NOAA. The outputs were generated as a contribution to the CMIP5 experiment. They include simulations of the historical period (1860–2005) and

future periods (2006–2100) under the four future RCP scenarios that are described briefly in Table 2.1.

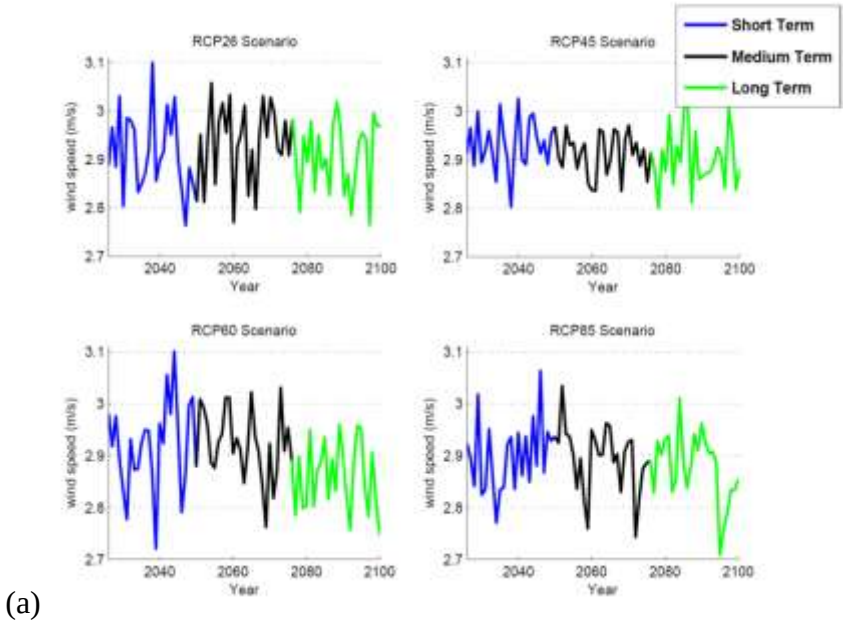

(a)

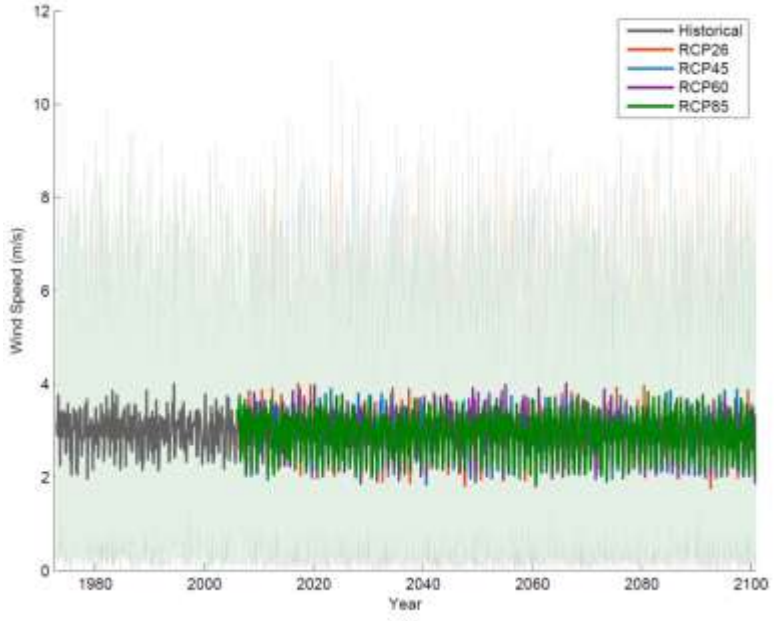

(b)

Fig. 2.1 - Ensemble average of raw GCMs data for different RCPs: (a) annual mean wind speed within short-term, medium-term, and long-term futures; (b) monthly mean wind speed, where shaded area represents the range of changes projected by different models; the model ensemble averages for each RCP are shown with thick lines

Table 2.1 - Overview of Representative Concentration Pathways (RCPs)

Scenario name	Scenario description
RCP85	Rising radiative forcing pathway leading to $8.5\ W/m^2$ in 2100
RCP60	Stabilization without overshoot pathway to $6\ W/m^2$at stabilization after 2100
RCP45	Stabilization without overshoot pathway to $4.5\ W/m^2$at stabilization after 2100
RCP26	A so-called “peak” scenario: its radiative forcing level first reaches a value around 3.1 W/m2midcentury, returning to $2.6\ W/m^2$by 2100

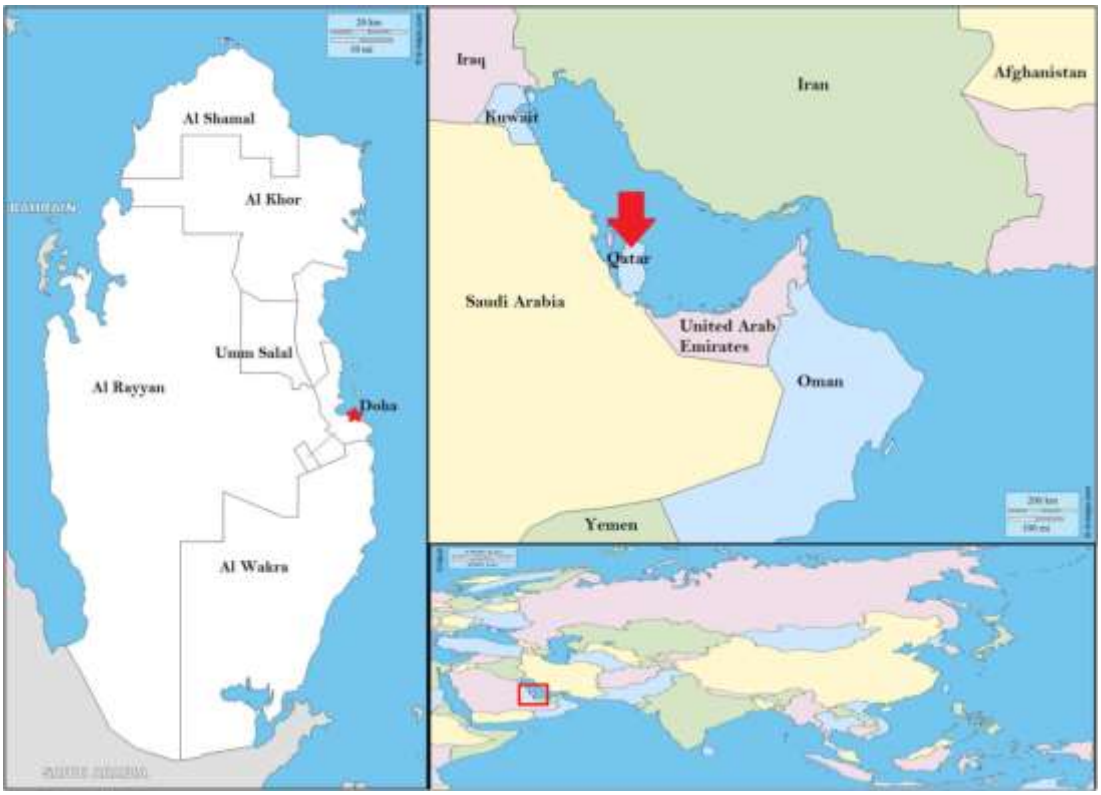

Fig. 2.2 - Study area through the Qatar coast (Doha), with weather station indicated in the figure (adapted from http://d-maps.com/carte.php?num_car=56002&lang=en; http://d-maps.com/carte.php?num_car=66536&lang=en; http://d-maps.com/carte.php?num_car=3494&lang=en)

In this paper, daily mean wind speed as well as maximum and minimum temperatures were extracted. The annual mean of wind speed of the ensemble average for all RCP scenarios are plotted in Fig. 2.1(a) for short-term, medium-term, and long-term future periods. Significant fluctuations in mean daily wind speed can be observed in that figure. Fig. 2.1(b) also illustrates the historical and future monthly mean wind speed of the ensemble average.

The study area location is also presented in Fig. 2.2. The ultimate objective of this paper is to provide estimates of wind speed and significant wave height changes over the Qatar gulf, but no off-shore wind speed observations are available. The closest weather station to the study area is the Doha International Airport and therefore the observed daily mean wind speed at that station is used as a proxy for wind speeds on the Qatar coast.

2.3. Downscaling Methods

Statistical downscaling methods share some key assumptions that are inherent within them. For instance, the relationship that is found by the downscaling method is assumed to be stationary in time, i.e., remain the same for future periods (Fowler et al. 2007). The validity of this assumption can best tested by model validation. Hewitson and Crane (2006) assess the impact of this assumption on projected climate change and find that it is small. The objective of the procedures described in this section is to apply a transformation to GCM outputs so that the magnitude and distribution of the downscaled variable become closer to those of observations at a given point. The 1973–2012 wind speeds as well as maximum and minimum temperature simulated data sets under RCPs scenarios were downloaded. The time-series of each variable were extracted for the place in which the observation data is available. Both Quantile-Quantile and nearest-neighbor methods, which will be discussed in the next section, are employed to project the monthly probability distribution of wind speed in the future.

2.3.1. Quantile-Quantile Transformation

The Quantile-Quantile transformation (JakobThemeßl et al. 2011; Maraun et al. 2010), also referred to as quantile-mapping or quantile-matching, aims to make the statistical

distribution of a given climate variable as close as possible to the statistical distribution of the observed variable within the historical period. The transformation for a given month and a given climate variable is performed as follows:

1. First, the historical data are split into calibration and validation periods. The daily time series of each month are extracted for both periods from both observations and GCM simulations.

2. An empirical cumulative distribution function, FOBS, is developed using the observations from the calibration period. The estimate of the distribution is nonparametric and uses a normal kernel function, and is evaluated at equally spaced points that cover the range of the data set. The number of points is set to one-tenth of the size of the data set. Another cumulative distribution function, FGCM, is also developed by applying the same technique to the GCM outputs on the calibration period.

3. Once FOBS and FGCM are obtained for the calibration period, corrected (downscaled) GCM simulations are generated for the validation period and future periods using the following transformation:

$$X_{CORR} = (FOBS)^{-1}\,(FGCM(X_{GCM})) \quad (2.1)$$

where X_{GCM} = variable extracted from the raw GCM simulation; and X_{CORR} = corrected climate variable.

4. In order to evaluate the performance of Eq. (5.1), obtained in the previous step, it is applied to the validation period. It should be assessed if the developed relationship can also improve the match between GCM outputs and observations within the validation period. To this end, monthly distributions of the modeled climate variable are visually compared with those of historical validation period (which have not been used for developing the relationship in Step 3). In addition, the validation results are quantitatively examined by using a kolmogorov-smirnov (KS) test.

5. If the results of the validation step is satisfactory, the developed relationship is employed to project the climate variable within the future period.

2.3.2. Nearest Neighbor Search

In addition to the Quantile-Quantile method, future value of wind speed is generated using the nearest neighbor approach. Given that precipitation is rare in Qatar, the authors used temperature as a similarity index for daily climate in the future. The underlying assumption is that two days from the same month and similar temperatures will have similar wind speeds. In this approach for each day d_f in the future period, a day d_h is selected in the historical period so that (1) it is from the same month as d_f; and (2) the absolute difference between the average temperature of df and the average temperature of d_h is minimal. Then, for projecting future wind speed, the measured wind speed of dh is assigned to df. The average of maximum and minimum temperature resulting from the Quantile-Quantile method is used in this approach as future values for temperature. Finally, at the end of the process, a PDF of downscaled wind speed is generated for each month.

2.3.3. Wave Height Calculation

As this paper's study area of interest is the Qatar coastal areas, the wave-height calculation procedure for shallow water is considered. There are several equations that can be used for estimation of the significant wave height. For instance, one may use the formula from Coastal Engineering Manual (CEM). The equation employed here for estimating the significant wave height for shallow waters is as follows (U.S. Department of Army Corps of Engineers 1984):

$$H = 0.283\tanh\left(0.53\left(\frac{gd}{U_A^2}\right)^{\frac{3}{4}}\right)\tanh\left(\frac{0.00565\sqrt{\frac{gF}{U_A^2}}}{\tanh\left(0.53\left(\frac{gd}{U_A^2}\right)^{\frac{3}{4}}\right)}\right)\frac{U_A^2}{g} \quad (2.2)$$

where$H$ = shallow water significant wave height (ft); g=32.2 ft/s^2; d = effective depth (ft); U_A = wind stress factor (ft/s); and F = fetch length (ft). The wind speed may be converted to a wind stress factor by the following equation:

$$U_A = 0.589U^{1.23} \quad (2.3)$$

where$U$ = wind speed (mph). As Eq. (2.2) states, the significant wave height, in addition to the wind speed, depends on water depth (d) and fetch length (F). Since the main objective of this study is investigation of the impact of wind speed changes on the significant wave height, the other two parameters are considered in a range of d = [10.00 to 50.00]m and F = [5.00 to 50.00]km. Finally, the significant wave height is calculated using Eq. (2.2), given the 100-year wind speed of each month for both historical (1973–2010) and future (2026–2100) periods.

2.4. Results

2.4.1. Downscaling Results

Using the previously described downscaling methods, the monthly distribution of wind speed was projected for short-term, medium-term, and long-term futures. In downscaling the wind speed, the multimodel analysis is used for the Quantile-Quantile method while only ESM2M model output is downscaled by nearest neighbor method. As will be shown later in this section, nearest neighbor technique is not promising for projection of extreme events and therefore, only the Quantile-Quantile method is used in multimodel and multiscenario approaches for projection of extreme events.

The calibration and validation results for both Quantile-Quantile and nearest neighbor methods are presented on Figs. 2.3 and 2.4. In Fig. 2.3, the empirical PDF of wind speed is plotted for each month within both calibration and validation periods for models ensemble as well as CM3 model under various RCP scenarios. Fig. 2.4 also shows the same results for nearest neighbor method but for the ESM2M model. It can be visually assessed that the distribution of the projected data is almost identical to the distribution of the observations. Therefore, the model performance is acceptable within the validation period (also for other GCM models not shown here), and the model can be used for future period. In order to assess the downscaling methods, the monthly distribution of raw (uncorrected) and downscaled (corrected) ESM2M output are compared with the observation data in Fig. 2.5 (calibration period not shown). It can be seen that the corrected probability distribution of wind speed is much closer to the observations than the distribution of the uncorrected GCM outputs.

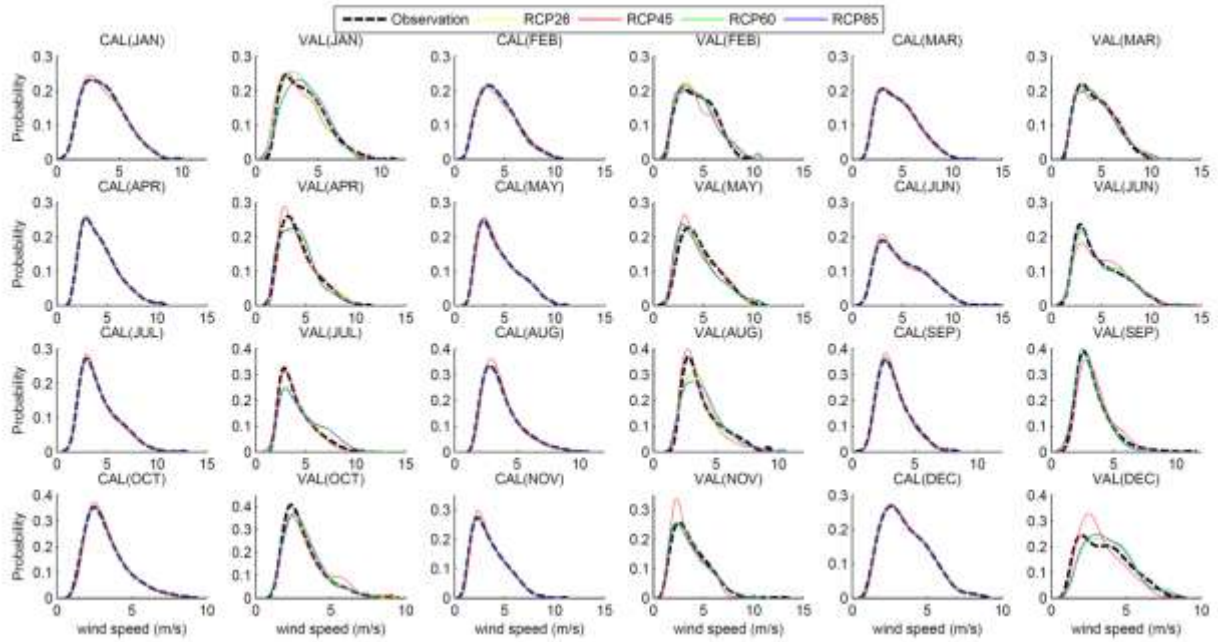

(a)

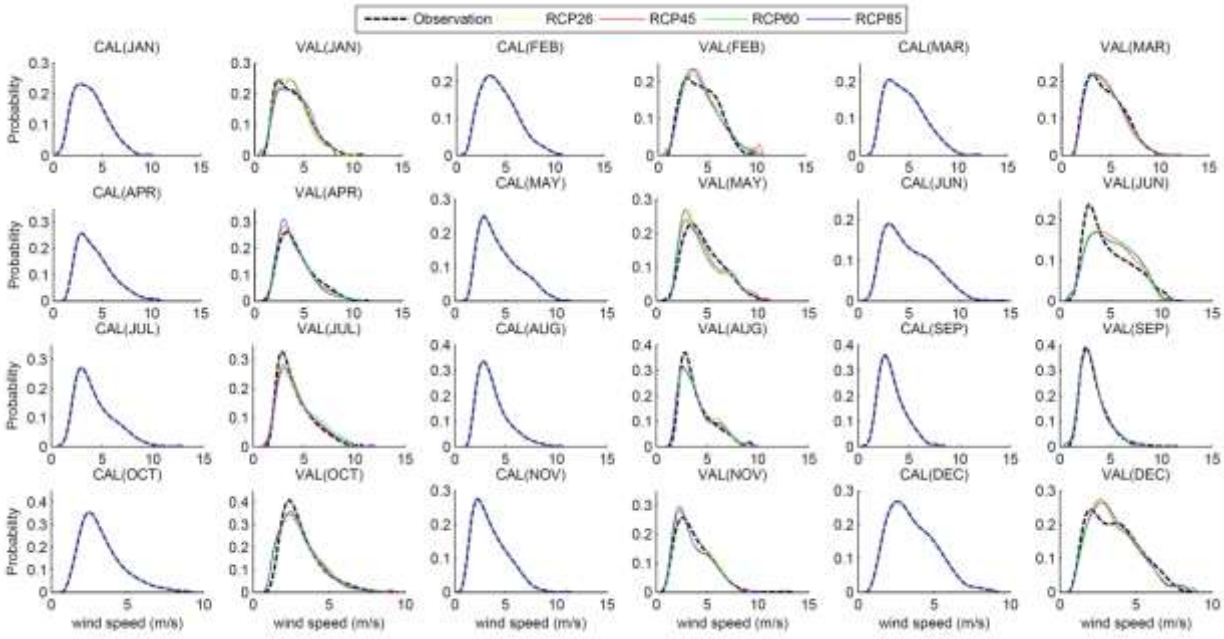

(b)

Fig. 2.3 - Monthly distribution of observed and projected daily mean wind speed using Quantile-Quantile transformation for calibration and validation period: (a) ensemble average; (b) CM3

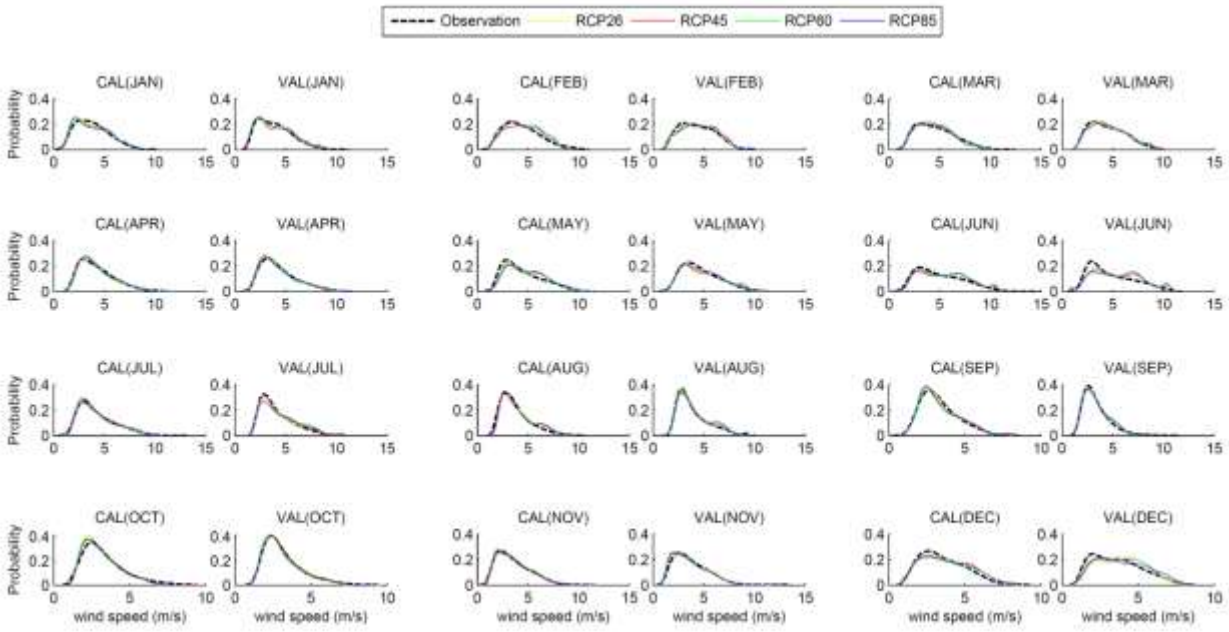

Fig. 2.4 - Monthly distribution of observed and projected daily mean wind speed using nearest neighbor method for calibration and validation period (ESM2M)

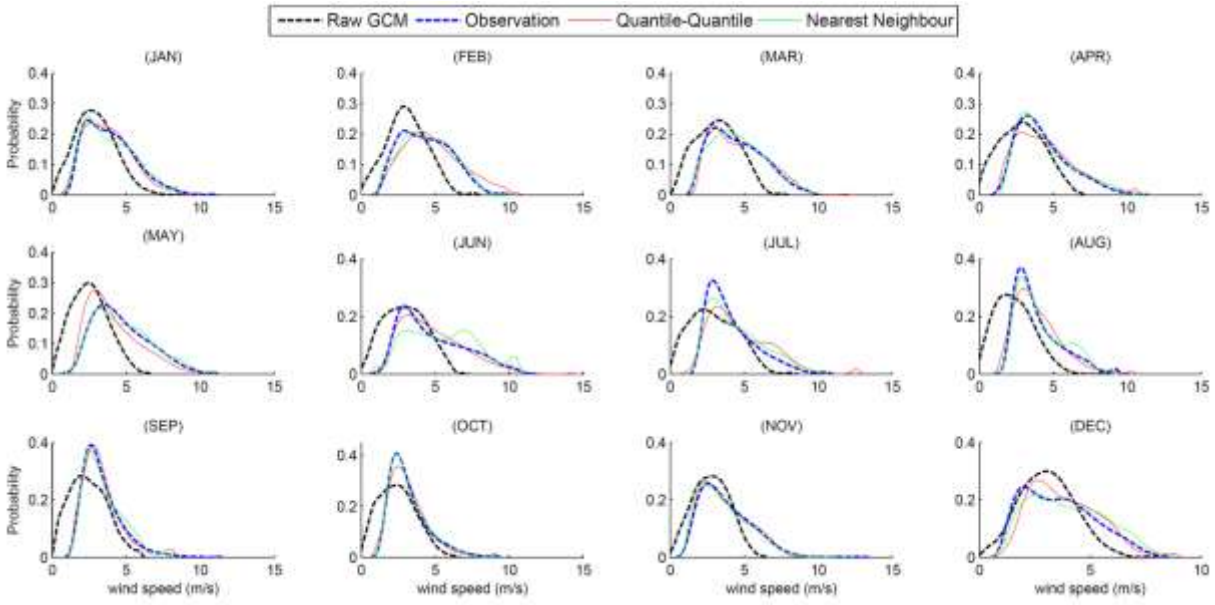

Fig. 2.5 - Comparison of raw and corrected (downscaled) wind speeds for ESM2M with observation within validation period

The performance of the downscaling method is further studied for the Quantile-Quantile method using Taylor diagrams. Taylor diagrams are a suitable way to compare different models using three related parameters: standard deviation, correlation with observed data, and root mean square (RMS). Fig. 2.6(a) shows the monthly mean wind speed for observed data, as a reference, along with the raw and corrected (downscaled) GCM models within the historical period. It shows that Quantile-Quantile method improves the raw GCM data and the performance is good for all the models. Fig. 2.6(b) illustrates the box plot of daily mean wind speed for the observations as well as raw and corrected GCM models. It also confirms the ability of the employed technique.

Moreover, for quantitative assessment of presented downscaling methods, two-sample KS tests were performed to compare the distribution of observed and downscaled (ESM2M) climate variables (wind speed, minimum temperature, and maximum temperature) on both the calibration and validation periods. The null hypothesis of the KS-test is

Table 2.2 - KS Test Results for ESM2M under RCP85 Scenario

Month	Quantile-Quantile transformation												Nearest neighbor			
	Wind speed				Maximum temperature				Minimum temperature				Wind speed			
	Calibration		Validation		Calibration		Validation		Calibration		Validation		Calibration		Validation	
	Before	After	Before	After	Before	After	Before	After	Before	After	Before	After	Before	After	Before	After
January	0.12	1.00	0.03	0.43	0.72	1.00	0.08	0.30	0.41	1.00	0.02	0.05	0.12	0.97	0.03	0.97
February	0.56	1.00	0.03	0.30	0.56	1.00	0.13	0.43	0.41	1.00	0.03	0.30	0.56	0.72	0.02	1.00
March	0.28	1.00	0.02	0.43	0.87	1.00	0.08	0.43	0.41	1.00	0.03	0.13	0.28	0.72	0.02	1.00
April	0.12	1.00	0.03	0.13	0.72	1.00	0.20	0.43	0.41	1.00	0.03	0.30	0.12	0.87	0.02	0.97
May	0.03	1.00	0.01	0.61	0.15	1.00	0.47	0.23	0.45	1.00	0.06	0.33	0.03	0.44	0.01	0.98
June	0.03	1.00	0.00	0.61	0.15	1.00	0.62	0.15	0.45	1.00	0.15	0.33	0.03	0.89	0.00	0.32
July	0.03	1.00	0.01	0.77	0.32	1.00	0.15	0.23	0.45	1.00	0.06	0.62	0.03	0.98	0.01	0.90
August	0.03	1.00	0.01	0.61	0.32	1.00	0.15	0.15	0.45	1.00	0.23	0.33	0.03	0.76	0.01	0.98
September	0.00	0.89	0.00	0.13	0.13	1.00	0.08	0.43	0.08	1.00	0.89	0.08	0.00	0.45	0.00	0.20
October	0.00	0.89	0.01	0.13	0.08	1.00	0.08	0.43	0.30	1.00	0.58	0.20	0.00	0.65	0.01	0.20
November	0.00	0.89	0.01	0.13	0.13	1.00	0.20	0.43	0.20	1.00	0.75	0.13	0.00	0.54	0.01	0.13
December	0.00	0.89	0.01	0.13	0.13	1.00	0.08	0.30	0.30	1.00	0.43	0.13	0.00	0.13	0.00	0.08

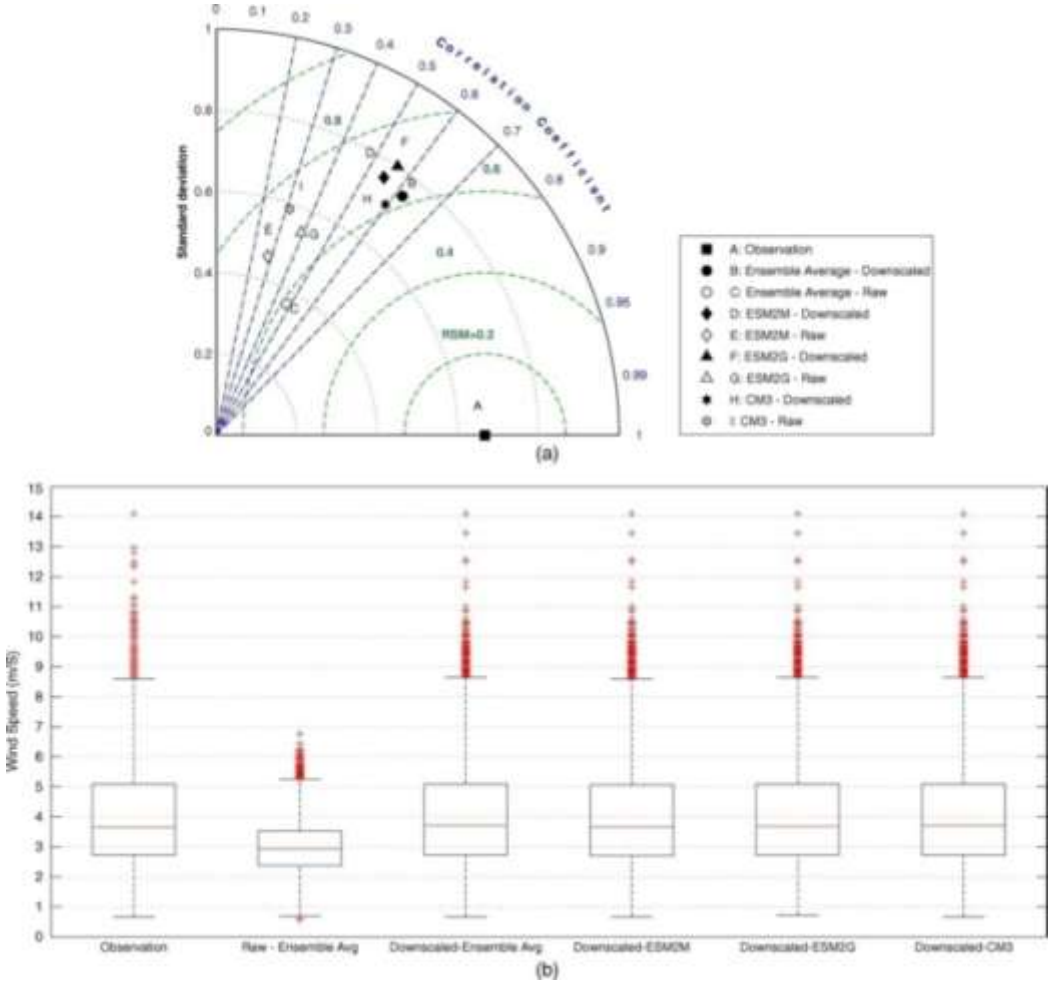

Fig. 2.6 - (a) Taylor diagrams for raw and corrected (downscaled) monthly mean wind speeds, comparing observations with the various models and model ensemble simulations for the historical period; (b) box plot for raw and corrected (downscaled) daily mean wind speed versus observations.

that the two distributions are identical. The null hypothesis is rejected when the p-value of theKS-test is below 0.05. Results of this test are presented for all four RCPs in Table 2.2. There is no rejected hypothesis between observed and projected values for either Quantile-Quantile or nearest neighbor methods. There is a dramatic increase of the p-value when the downscaling is applied, especially for wind speed. Therefore, it can be concluded that both the Quantile-Quantile and the nearest neighbor methods significantly improve the shape of the PDF of GCM-simulated climate variables. They were therefore used to downscale wind speeds at the Doha International Airport station from 2026 to 2100. The monthly corrected

PDFs for the Quantile-Quantile method for a variety of future time spans, various models, and different RCP scenarios for are illustrated in Figs. 2.7–2.9, respectively. In addition, downscaled monthly and daily mean wind speeds are compared with the observation data in Figs. 2.10(a–d) for both Quantile-Quantile transformations and the nearest neighbor method (ESM2M).

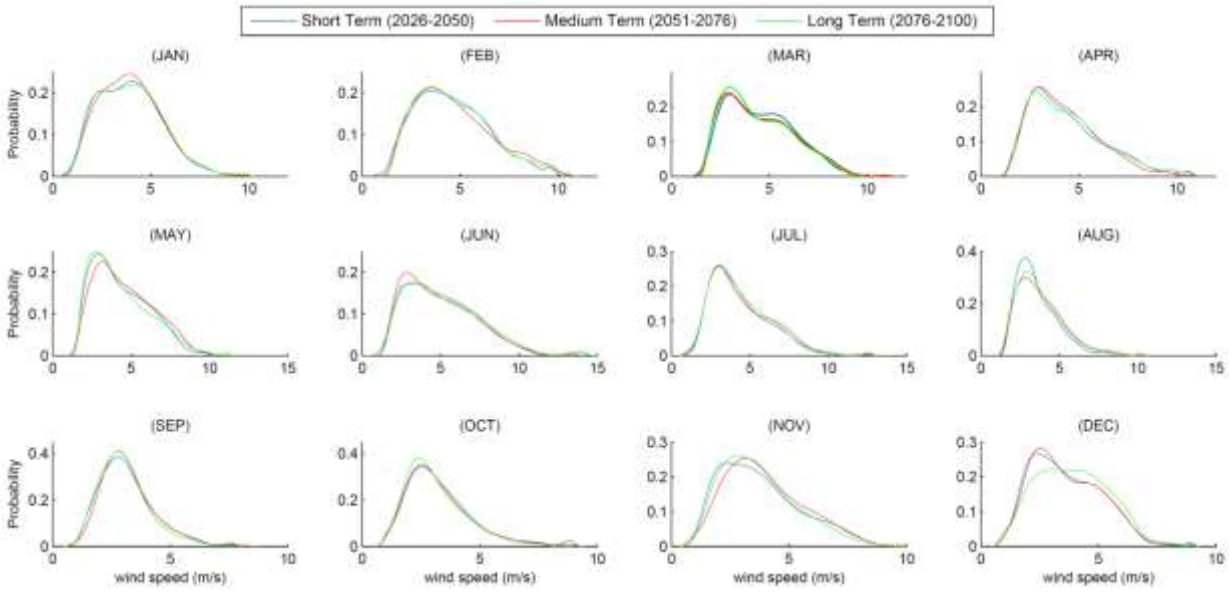

Fig. 2.7 - Time spread of monthly distribution for projected mean daily wind speed (Quantile-Quantile) for ESM2M under the RCP26 scenario

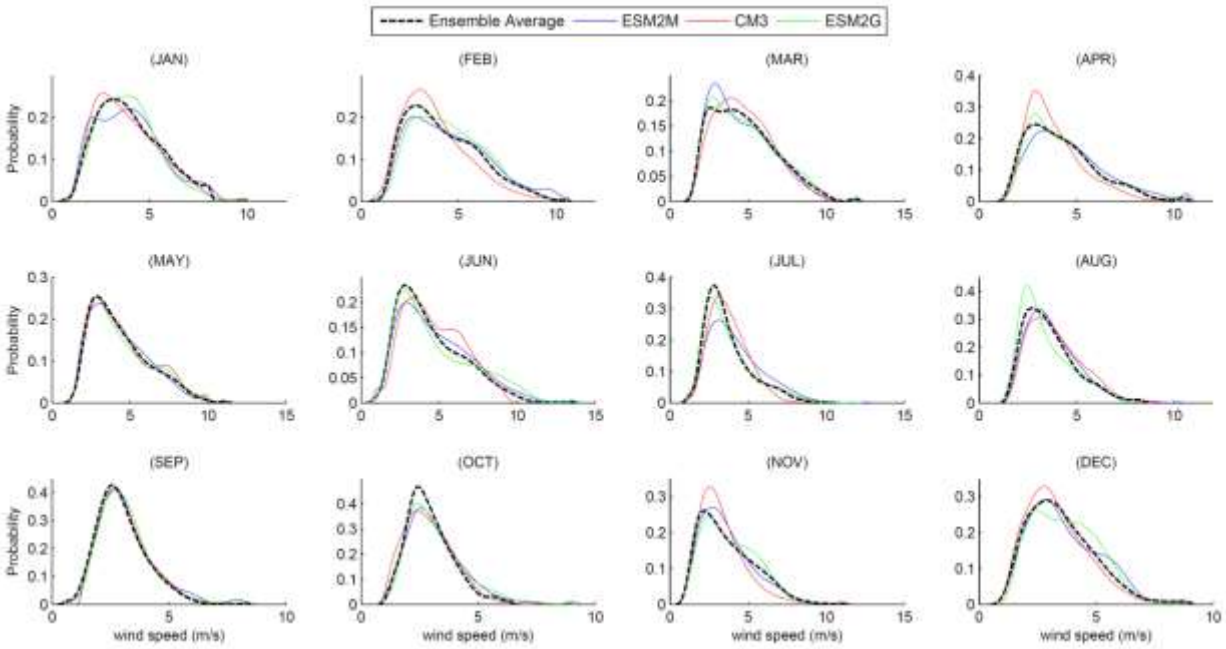

Fig. 2.8 - GCM spread of monthly distribution for long-term projection of mean daily wind speed (Quantile-Quantile) under the RCP85 scenario

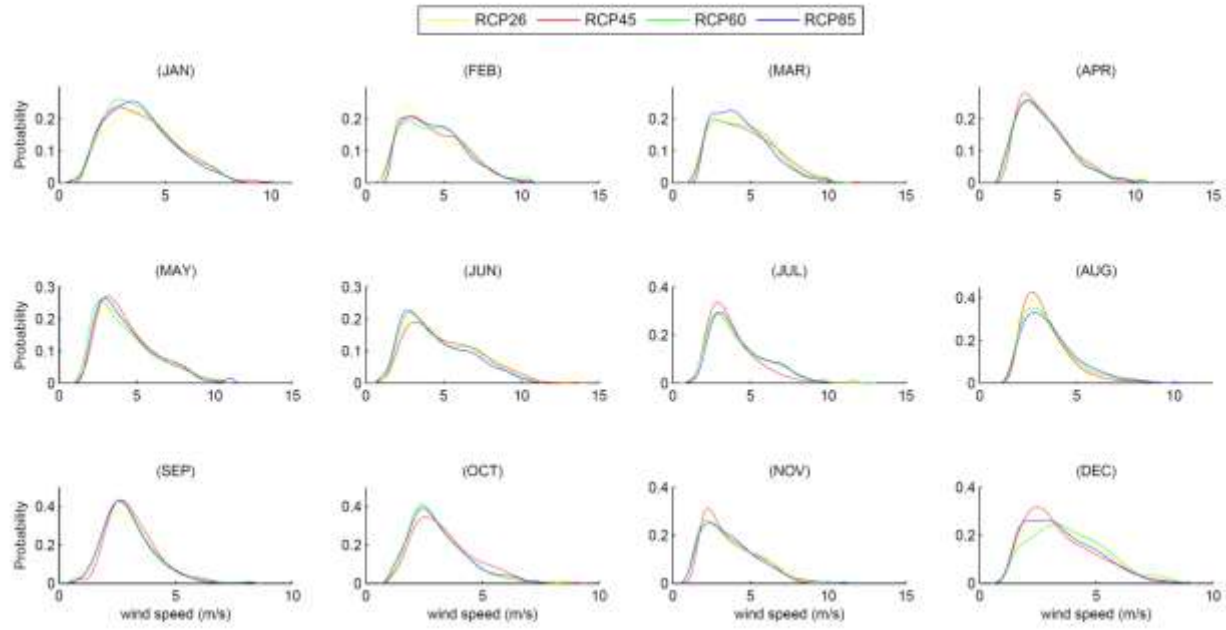

Fig. 2.9 - Scenario spread of ensemble average for monthly distribution of short-term projection of mean daily wind speed (Quantile-Quantile)

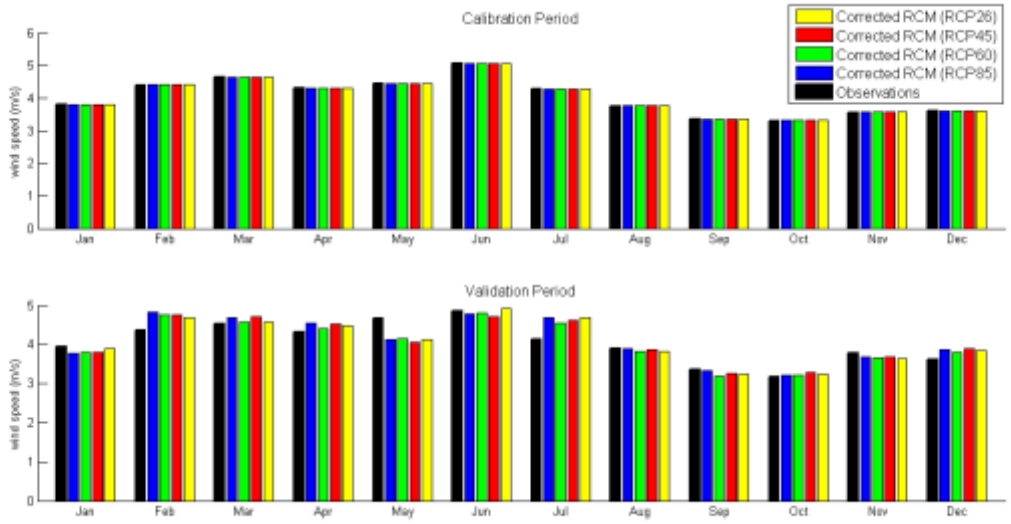

(a)

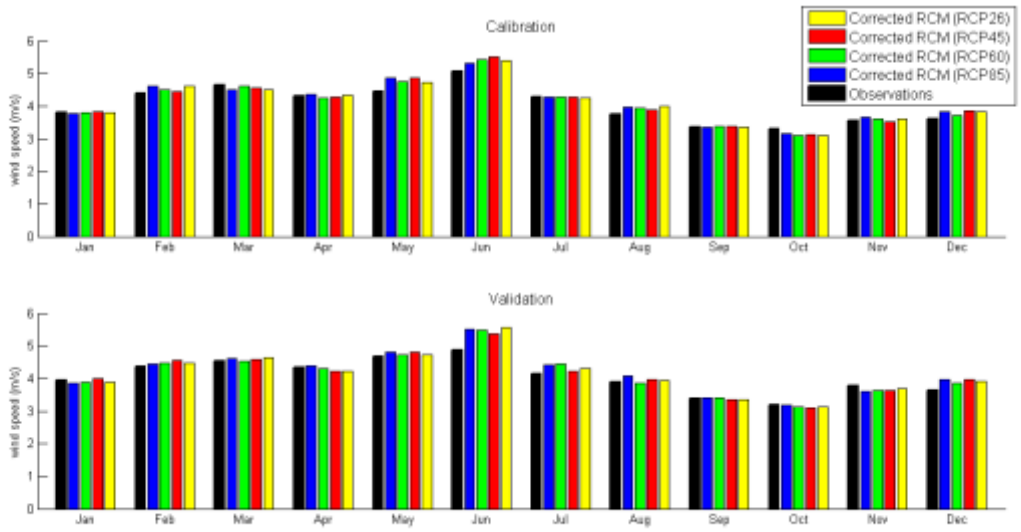

(b)

Fig. 2.10 - Observed and downscaled (ESM2M) wind speed for the 1981–2010 period: (a) monthly mean, Quantile-Quantile; (b) monthly mean, nearest neighbor; (c) daily mean time series, Quantile-Quantile; (d) daily mean time series, nearest neighbor

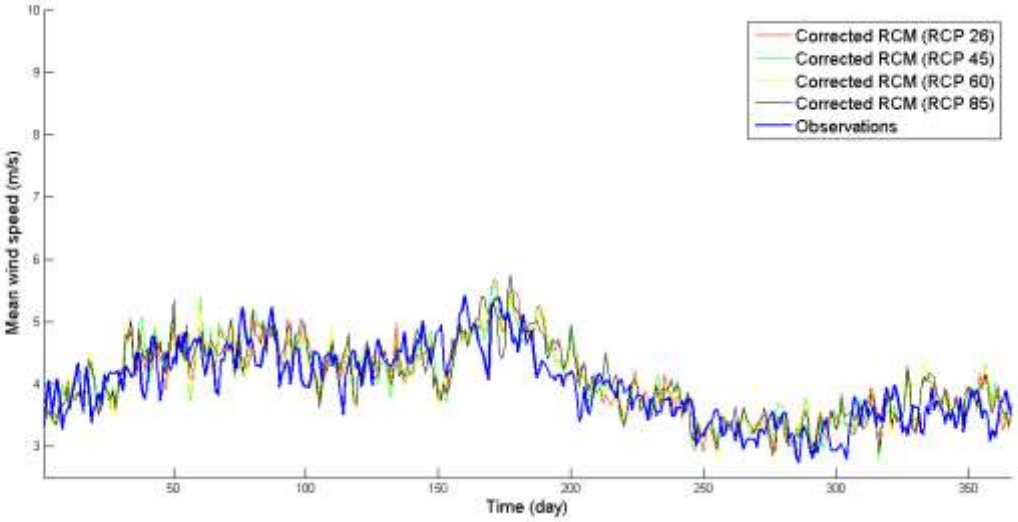

(c)

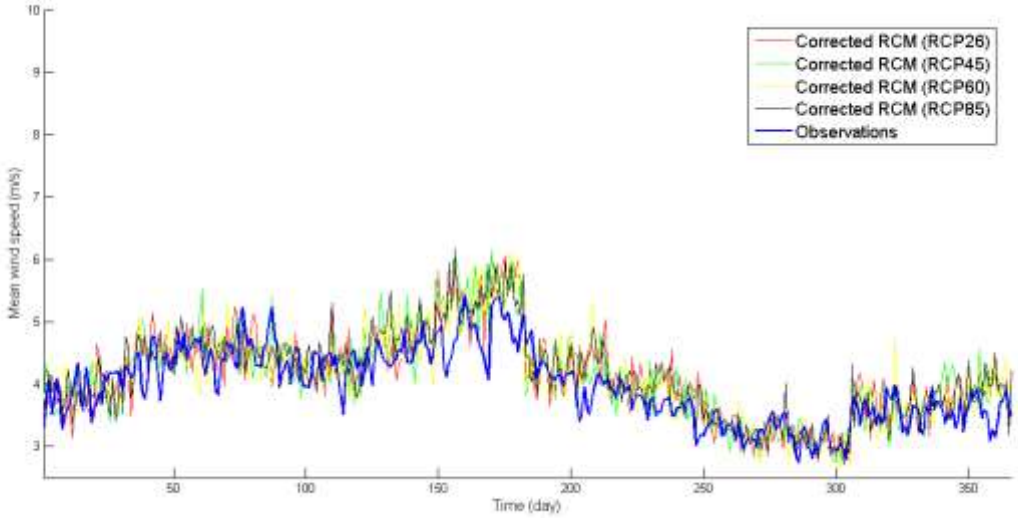

(d)

Fig. 2.10 - Continued

The next step in the analysis is to extract the 100-year maximum wind speed for each month from the corrected PDF, then use these values to calculate significant wave heights. It was found that the extreme winds calculated by the nearest neighbor method were not

sensitive to the GCM scenario. That problem originates from the fact that, by construction, the nearest neighbor approach is unable for simulating values outside the historical range. It is therefore not recommended for the downscaling of extremes. As a result, only the Quantile-Quantile method was used for multimodel and multiscenario projections of extreme wind speed events. The observed and projected 100-year wind speed of the ensemble average for each month using the Quantile-Quantile method is illustrated in Fig. 2.11. Good agreement can be seen between observed and projected 100-year wind speeds in the historical period.

To have a better view of Quantile-Quantile method's performance, the projected mean and 100-year wind speed for all models are compared to the observations over the historical period in Table 2.3. It shows that the CM3 model's errors are less than 5% for all months except for February, when it is 8%. The errors of ESM2M are acceptable for all months, except for June and October, when they are almost 10%. The results of ESM2G show errors either close to or more than 10% in June, July, and October. The relative errors of the downscaled ensemble average are acceptable and lower than 5.5%, except in June. The changes in significant wave heights, which are due to the wind speed changes within future time spans, will be discussed in the next section.

2.4.2. Wave Height under Climate Change

The downscaled wind speeds were used to estimate climate change's impact on significant wave height along the Qatar coast. A multimodel, multiscenario estimation of significant wave height changes will be analyzed during various future spans in this section. Equipped with the projected 100-year wind speed values from the Quantile-Quantile method and employing Eqs. (2) and (3), one can estimate the changes of significant wave height for a range of depths and fetch lengths. For instance, for the ensemble average under the RCP85 scenario within the short-term future, the contour plot of significant wave changes with respect to the historical period [Fig. 2.12(a)] is presented in Fig. 2.12(b) for each month. The water depth varies between 5 and 50 m while the fetch length has a range of 5–50 km. It shows that up to a 10% increase is expected in April, November, and December, while either it does not change significantly or decreases for other months. As Fig. 2.12(b)

shows, for various values of water depths and fetch lengths, the variety of changes in 100-year wave height is not high (up to 5%). Therefore, for thorough multimodel and multiscenario analyses, the average changes of 100-year significant wave height over the range water depth and fetch length is considered for each month.

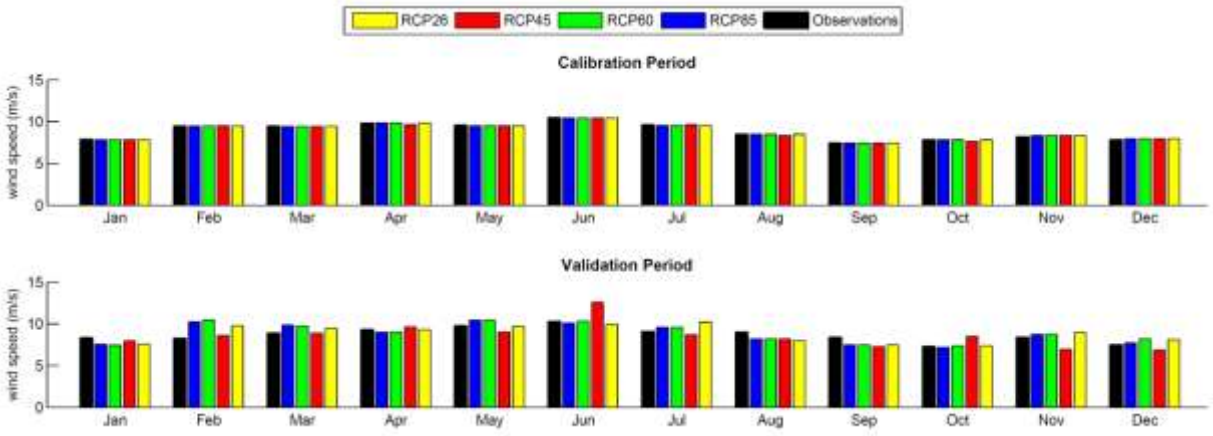

Fig. 2.11 - Monthly 100-year wind speed (Quantile-Quantile) within calibration and validation periods for ensemble average

Figs. 2.13(a–d) show the changes in 100-year significant wave heights during short-term, medium-term, and long-term futures for various models under RCP scenarios. As for the RCP26 scenario, the ensemble average and CM3 show more than 40 and 25% increases in wave height in the medium-term future in November. Ensemble average also confirms around a 10% increase in December for all future time spans. Moreover, under all RCP scenarios, almost all models and ensemble averages confirm an increase between 5 and 15% in February.

The ESM2M shows high jumps in June and October over almost all the future periods and under various RCPs; however, neither the other models nor ensemble averages confirm those changes. However, ESM2M has a relative large error in October within the historical period. The high changes of ESM2G in June and July are not also reliable since ESM2G

has a high error rate within the historical period. CM3 under the RCP 45 scenario also shows an increase between 10 and 25% in November.

Table 2.3 - Comparison of Observed and Downscaled Mean (100-year) Wind Speed, and Future Change in Wind Speed (m/s) for RCP85 Scenario Using Quantile-Quantile

Month	Mean (100-year) wind speed over historical period (1973–2010)					Relative error (%)			
	Observation	Ensemble average	ESM2M	ESM2G	CM3	Ensemble average	ESM2M	ESM2G	CM3
January	3.9 (8.1)	4 (7.7)	3.9 (8.2)	3.9 (7.9)	3.9 (7.8)	1.7 (4.1)	0.4 (1)	0.7 (2.5)	0.2 (2.9)
February	4.4 (9.1)	4.4 (9.5)	4.6 (9.5)	4.3 (9.4)	4.4 (9.8)	0.4 (5.4)	4.1 (4.6)	2.6 (4)	0.6 (8)
March	4.6 (9.1)	4.6 (9.5)	4.6 (8.8)	4.6 (9.4)	4.6 (9.5)	1.8 (4.8)	1.5 (2.3)	1.7 (4.3)	1.7 (4.8)
April	4.3 (9.5)	4.3 (9.6)	4.4 (10.1)	4.2 (10.3)	4.2 (9.3)	1.6 (1.4)	2.2 (5.9)	3.5 (8.1)	2.5 (1.9)
May	4.6 (9.6)	4.5 (9.6)	4.3 (9.2)	4.6 (9.6)	4.5 (9.6)	2.5 (0.5)	6.4 (4.5)	0.6 (0.5)	2.5 (0.5)
June	5 (10.3)	4.9 (10.2)	5 (10.4)	5 (11.8)	5 (10.4)	1.1 (1.2)	0.1 (1)	0.4 (14.4)	1.1 (0.7)
July	4.2 (9.3)	4.5 (10.2)	4.5 (10.2)	4.5 (10.2)	4.3 (9.4)	7.8 (10)	6.6 (9.9)	6 (9.9)	3 (1.4)
August	3.8 (8.8)	3.9 (8.9)	3.8 (8.5)	3.9 (8.3)	3.9 (8.5)	0.8 (0.9)	2.3 (4.1)	0.2 (5.8)	0.9 (4.1)
September	3.3 (7.5)	3.3 (7.5)	3.3 (7.5)	3.3 (7.5)	3.3 (7.5)	1.5 (0)	0.1 (0)	1.7 (0.7)	0.6 (0.7)
October	3.2 (7.5)	3.3 (7.4)	3.3 (8.2)	3.5 (8.5)	3.2 (7.6)	1.5 (0.3)	0.5 (9.7)	7.1 (14.1)	1.8 (2.1)
November	3.7 (8.3)	3.6 (8.7)	3.6 (7.9)	3.6 (8.3)	3.6 (7.9)	0.8 (4.9)	2.7 (4.6)	2.5 (0)	1.7 (4.6)
December	3.6 (7.7)	3.7 (7.9)	3.7 (8.1)	3.7 (8.2)	3.6 (8.1)	3.2 (3.7)	3.3 (6)	2 (6.7)	0.3 (6)

These results suggest that damaging waves could occur due to strong winds on the Qatar coast and that Qatar's coastal areas would be subject to an increased coastal flooding hazard in the future. The 100-year significant wave height is projected to increase by more than 0.8 m (up to 40% in November, where Fig. 2.12(a) corresponds to a 2-m wave height). The risk of damages from storm waves to coastal structures will therefore increase, and these structures will need to be retrofitted to maintain the level of safety for which they were designed. The new level of risk should also be considered for both new offshore and onshore facilities. Strong winds and waves can also generate other types of hazards in coastal areas. They can disturb the sea floor and increase the amount of suspended

sediments near the surface. This would increase the amount of sunlight reflected by the water and enhance the green signal from chlorophyll-rich plankton. The economic and environmental impacts of changed wind characteristics may be estimated with more detailed impact models of the areas that would be forced with modified climate variables.

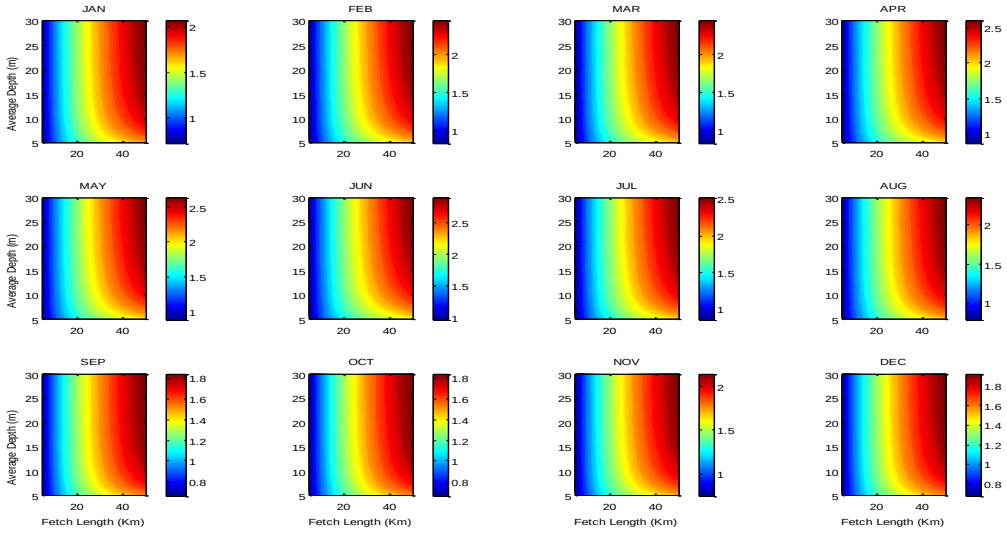

(a)

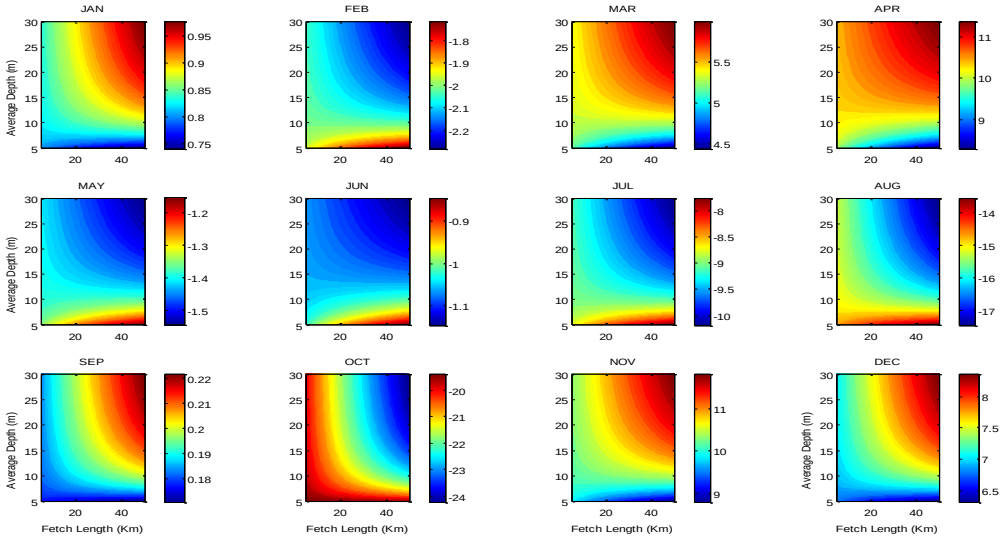

(b)

Fig. 2.12 - Contour plots of (a) 100-year significant wave heights (m) from historical wind observations; (b) short-term 100-year significant wave height changes (%) for ensemble average under RCP26

The ESM2M shows high jumps in June and October over almost all the future periods and under various RCPs; however, neither the other models nor ensemble averages confirm those changes. However, ESM2M has a relative large error in October within the historical period. The high changes of ESM2G in June and July are not also reliable since ESM2G has a high error rate within the historical period. CM3 under the RCP 45 scenario also shows an increase between 10 and 25% in November.

These results suggest that t damaging waves could occur due to strong winds on the Qatar coast and that Qatar's coastal areas would be subject to an increased coastal flooding hazard in the future. The 100-year significant wave height is projected to increase by more than 0.8 m (up to 40% in November, where Fig. 2.12(a) corresponds to a 2-m wave height). The risk of damages from storm waves to coastal structures will therefore increase, and these structures will need to be retrofitted to maintain the level of safety for which they were designed. The new level of risk should also be considered for new both offshore and onshore facilities. Strong winds and waves can also generate other types of hazards in coastal areas. They can disturb the sea floor and increase the amount of suspended sediments near the surface. This would increase the amount of sunlight reflected by the water and enhance the green signal from chlorophyll-rich plankton. The economic and environmental impacts of changed wind characteristics may be estimated with more detailed impact models of the areas that would be forced with modified climate variables.

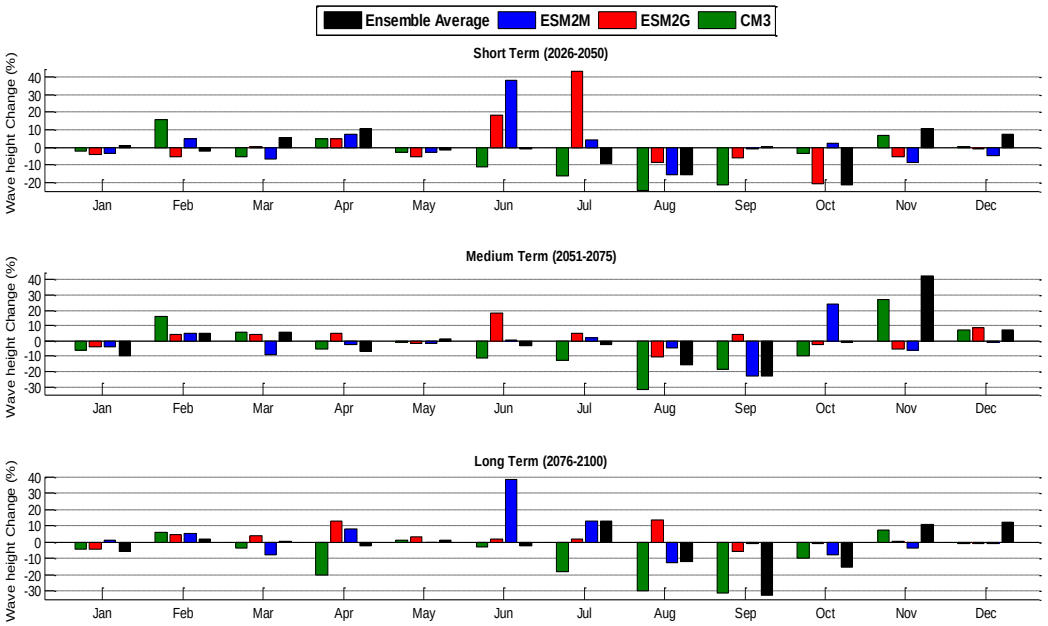
Ensemble Average
ESM2M
ESM2G
CM3
Short Term (2026-2050)
Medium Term (2051-2075)
Long Term (2076-2100)
Wave height Change (%)
Jan
Feb
Mar
Apr
May
Jun
Jul
Aug
Sep
Oct
Nov
Dec

(a)

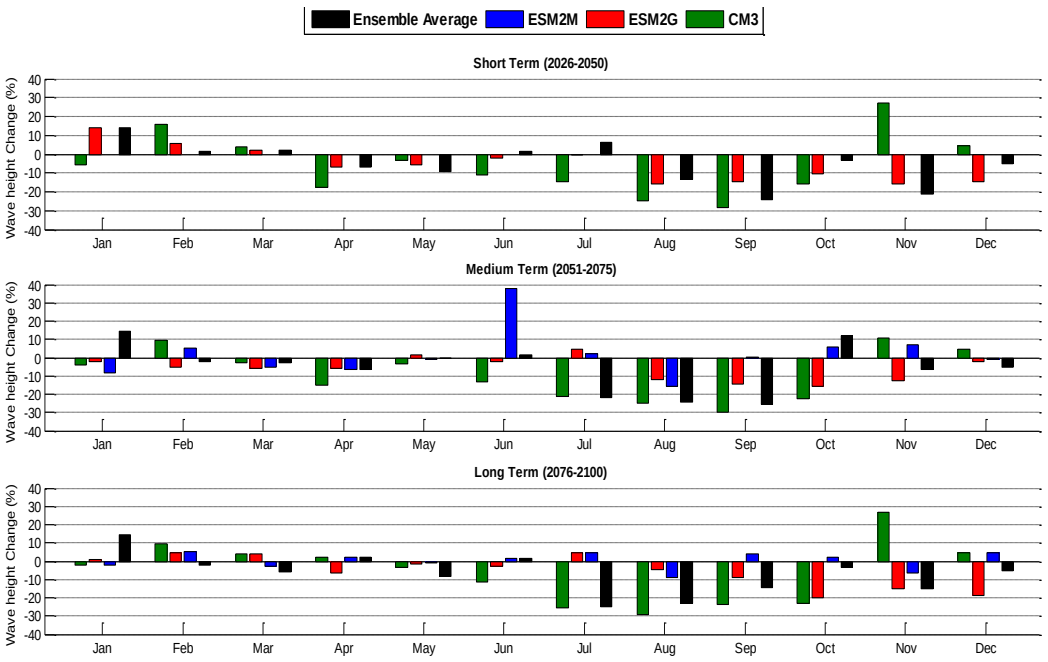
Ensemble Average
ESM2M
ESM2G
CM3
Short Term (2026-2050)
Medium Term (2051-2075)
Long Term (2076-2100)
Wave height Change (%)
Jan
Feb
Mar
Apr
May
Jun
Jul
Aug
Sep
Oct
Nov
Dec

(b)

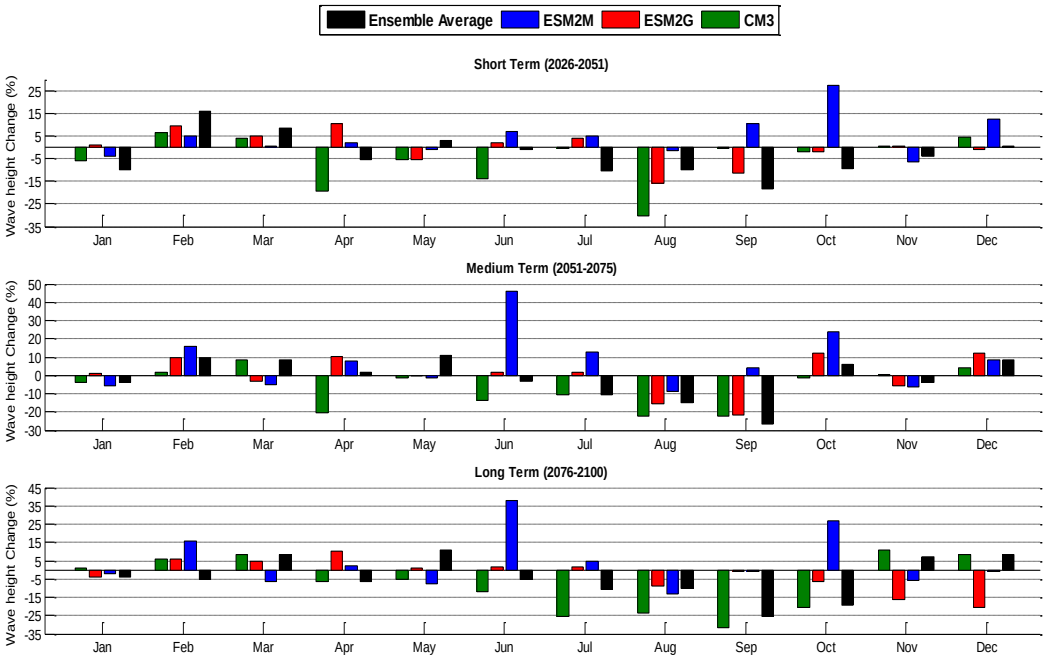

(c)

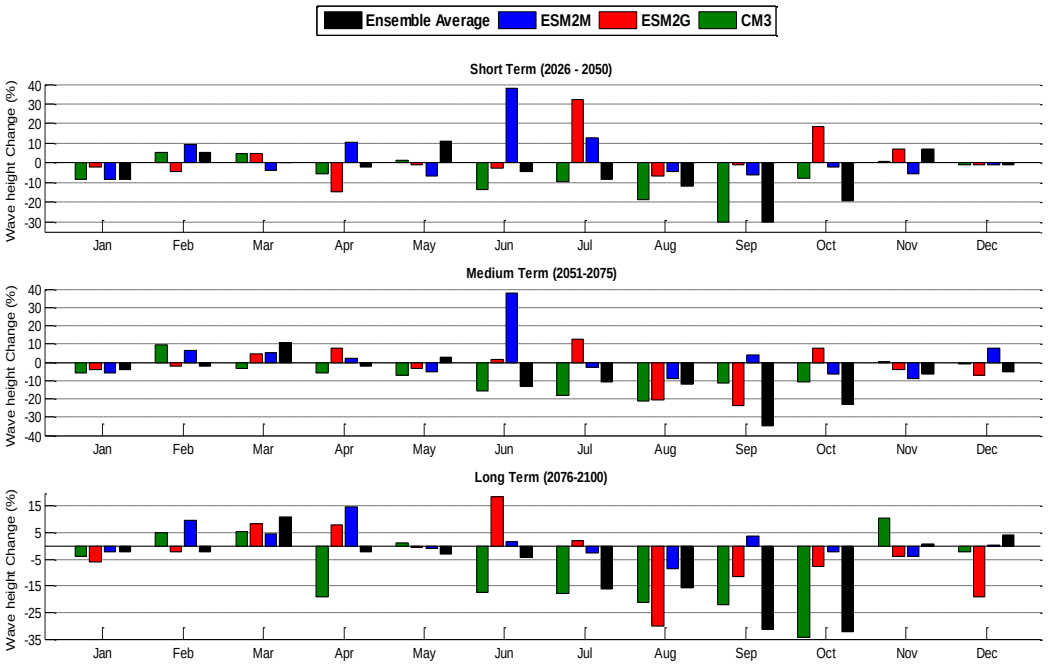

(d)

Fig. 2.13 -Multimodel average changes of 100-year significant wave height for a range of depths and fetch lengths under (a) RCP26; (b) RCP45; (c) RCP60; (d) RCP85 emission scenarios

2.5. Conclusions

In the current study, the monthly distribution of wind speed was statistically downscaled to station-level scale using Quantile-Quantile transformation and nearest neighbor search methods. Observed daily wind speed data at International Doha Airport station were used as predictand while climate variables including wind speed and maximum and minimum temperature from CMIP5 models under RCP emission scenarios were used as predictors. The empirical probability density functions derived from observations and downscaled GCM outputs were favorably compared using visual analysis and a two-sample Kolmogorov-Smirnoff test. In addition, the probability distribution of raw and downscaled GCM data were compared to the observations, which revealed that both models are capable of constructing the probability distribution of wind speed. It was, however, found that the nearest neighbor approach was not suitable for the estimation of future extreme wind speeds. Downscaling results indicated that under RCP26/RCP45 scenarios, changes between 20 and 40% in the 100-year significant wave height might take place. The increase of wind speed in future will result in higher waves with greater significant wave heights. These waves will affect the Qatar coast both economically and environmentally, and vulnerable areas must be assessed to adjust them to the new level of risk.

Chapter 3

Analysis of triangular C-grid finite volume scheme for shallow water flows[2]

Abstract

In this paper, a dispersion relation analysis is employed to investigate the finite volume triangular C-grid formulation for two-dimensional shallow-water equations. In addition, two proposed combinations of time-stepping methods with the C-grid spatial discretization are investigated. In the first part of this study, the C-grid spatial discretization scheme is assessed, and in the second part, fully discrete schemes are analyzed. Analysis of the semi-discretized scheme (i.e. only spatial discretization) shows that there is no damping associated with the spatial C-grid scheme, and its phase speed behavior is also acceptable for long and intermediate waves. The analytical dispersion analysis after considering the effect of time discretization shows that the Leap-Frog time stepping technique can improve the phase speed behavior of the numerical method; however it could not damp the shorter decelerated waves. The Adams–Bashforth technique leads to slower propagation of short and intermediate waves and it damps those waves with a slower propagating speed. The numerical solutions of various test problems also conform and are in good agreement with the analytical dispersion analysis. They also indicate that the Adams–Bashforth scheme exhibits faster convergence and more accurate results, respectively, when the spatial and temporal step size decreases. However, the Leap-Frog scheme is more stable with higher CFL numbers.

Keywords: *Dispersion relation analysis; Fourier analysis; C-grid scheme; Shallow water; Ocean modeling*

[2]This part of the study has been published as: **H. Shirkhani**, A. Mohammadian, O. Seidou, H. Qiblawey, "Analysis of triangular C-grid finite volume scheme for shallow water flows", *Advances in Water Resource*, 2015, 10.1016/j.advwatres.2015.04.011.

3.1. Introduction

The shallow water (SW) equations, which resulted from the Navier–Stokes equations, play a vital role in environmental and hydrodynamic studies of lakes, estuaries and coastal regions. In numerical modeling of SW systems, due to the coupling between the momentum and continuity equations, there are many possibilities of variable placement for certain choice of grids. This may lead to spurious oscillation in the numerical solutions (Le Roux et al. 2007). The effect of variable placement on a variety of grids has been studied for solving shallow water equations (SrdjanDobricic 2006; Despotisand Tsangaris1996; Popinet and Rickard 2009; Langtangen et al. 2002; Walters and Carey 1984).

Among various finite-volume semi-discrete schemes, the triangular C-grid exhibited a good performance in the solution of shallow water equations. However, its capability to simulate geostrophic waves is sometimes problematic (Ringler et al. 2010). In this approach, the water surface elevation (pressure) is stored at the circumcenter of the cells while the normal velocity components are retained at the finite volume cell edges. This method also can be introduced as the RT0 lumped finite element scheme (Waltersa et al. 2009). There has been an upward trend in the use of an unstructured C-grid mesh for modeling atmospheric and oceanic problems (SrdjanDobricic 2006; Stuhne and Peltier 2009; Thuburn et al. 2009; Wolfram and Fringer 2009;Lazure and Dumas 2008; Schwab and Beletsky 1998). The C-grid approach has been employed in some well-known models such as MITgcm(Marshall et al. 1997; Adcroft et al. 2004), ROMS (Shchepetkinand McWilliams 2003, 2005) and UnTRIM(Jankowski 2007, 2009), which are broadly used for a wide range of applications. Considering the growing interest in the unstructured triangular C-grid scheme, assessing the semi-discrete technique as well as its performance in combination with time-stepping methods is of essential importance. It should be noted that the performance of a spatial discretization scheme in combination with time-stepping techniques in fully discrete systems is also crucial. Mohammadian and Le Roux (2008) studied the behaviour of a class of upwind schemes in shallow water systems. In the current study, three different time-stepping techniques are assessed in combination with the

finite volume C-grid scheme: Euler forward, Leap-Frog and Adams–Bashforth second-order temporal schemes. Indeed, the Euler scheme is employed as a very basic method. Gray and Lynch (1997) analyzed Leap-Frog and Adams–Bashforth techniques for solving the long-wave surface water equations using the finite element method in terms of stability and accuracy. The Leap-Frog scheme is a second-order scheme which has been implemented in many practical models, e.g., POM (Mellor 2004), and has a wide range of applications in oceanic and atmospheric contexts (Aiki and Greatbatch 2014; Iwasaki et al. 2014). The Adams–Bashforth second-order method is also a well known temporal scheme which has been used in the MITgcm Model.

The dispersion relation and Fourier analyses are useful tools to study the effect of spatial and temporal discretization schemes on the quantities which analytical ones should be preserved by an ideal numerical model. The dispersion relation and Fourier analyses, in addition to indicating the limitations and advantages of the discretization schemes, are useful for choosing parameters such as the Courant–Friedrich–Lewy (CFL) number. The Fourier and dispersion relation analyses have been used for shallow water equations using finite difference (Adcroft et al. 1999) and (Sankaranarayananand Spaulding 2003), finite elements (Kinnmark and Gray1985; Jaber andMohtar 200;Le Roux and Pouliot 2008; Le Roux 2005) and finite volume methods (Gossard and Kolar 2000;Mohammadian 2010). However, the discretization of shallow water equations using the triangular C-grid scheme has not been studied, and the current paper is dedicated to the two-dimensional dispersion and Fourier analyses of the finite volume C-grid scheme for gravity waves. Szpilka and Kolar (2003) used the Fourier and dispersion analysis to propose a numerical analogs to these analysis for classic finite difference and finite element discretizations of the shallow water equations.

The main objectives of this paper are: (i) dispersion analysis for the finite-volume triangular C-grid solutions of two-dimensional linearized shallow water equations and, (ii) examination of fully discrete schemes based on the combination of the C-grid spatial discretization method with different time-stepping techniques. First, the dispersion relation is obtained and analyzed for the semi-discrete C-grid scheme. In this regard, the wave amplitude, phase speed and group velocity of the C-grid spatial discretization scheme are

compared to those of analytical analysis. Then, various temporal schemes, namely, the Forward Euler, Leap-Frog and Adams–Bashforth techniques, are examined in combination with C-grid spatial discretization method. Different linear and non-linear numerical tests are simulated in order to verify the analytical dispersion analysis and investigate the performance of the proposed fully discrete methods.

3.2. Governing Equations

The two-dimensional inviscid linear form of shallow water equations in Cartesian coordinates can be expressed in the following form:

$$\frac{\partial \eta}{\partial t} + H\left(\frac{\partial u}{\partial x} + \frac{\partial v}{\partial y}\right) = 0 \tag{3.1}$$

$$\frac{\partial u}{\partial t} + g\frac{\partial \eta}{\partial x} = 0 \tag{3.2}$$

$$\frac{\partial v}{\partial t} + g\frac{\partial \eta}{\partial y} = 0 \tag{3.3}$$

Where η stands for the surface elevation with respect to the reference level of $z = 0$, u and v are the velocity variables, g is the gravitational acceleration and H is the constant average depth. Because the governing equations are linear, by considering the behavior of one Fourier mode, the solution can be examined. Then, the solutions of equations (3.1) to (3.3) in the form of $u = \tilde{u}e^{i(kx+ly+\omega t)}$, $v = \tilde{v}e^{i(kx+ly+\omega t)}$ and $\eta = \tilde{\eta}e^{i(kx+ly+\omega t)}$ are sought, where k and l are wave numbers in the x and y directions respectively. Replacing the wave form of u, v and η in governing equations (3.1) to (3.3) results in a square matrix for the amplitudes $\tilde{u}, \tilde{v}$and $\tilde{\eta}$. For a nontrivial solution, the determinant of the matrix should be equal to zero, which leads to a relationship between the wave numbers k and l and the frequency ω. The relationship is called the dispersion relation and is obtained as follows:

$$\omega\left(\omega^2 - gH(k^2 + l^2)\right) = 0 \tag{3.4}$$

The first solution is $\omega = 0$, which corresponds to the geostrophic mode, and the other two solutions are as follows:

$$\omega_{AN} = \pm\sqrt{gH(k^2 + l^2)} = 0 \tag{3.5}$$

In which ω_{AN} stands for the analytical solution and corresponds to the free surface gravitational mode. As equation (3.5) shows, ω is purely real, and therefore all modes are naturally stable and neither amplify nor decay.

3.3. Spatial Discretization and Analysis

In the C-grid approach, surface elevation is located at the cell's circumcenter, while the normal velocities are considered at the cell mid-edges; see Fig. 3.1 (left). To obtain the equations for the normal component of momentum at each edge, the dot product of the edge normal vector$\overrightarrow{n}$ will be taken with the momentum equations (3.2) and (3.3), which leads to:

$$\frac{\partial U}{\partial t} + g\frac{\partial \eta}{\partial n} = 0 \qquad (3.6)$$

Where $\frac{\partial}{\partial n}$ is the edge normal gradient and $U = \vec{n}.(u, v)$. The edge normal vector n is defined at the middle of the three different edge types of each cell, as shown in Fig. 3.3. The edge normal gradient of free surface at each cell mid-edge is defined as follows:

$$\left(\frac{\partial \eta}{\partial n}\right)_j = \frac{\eta_f - \eta_b}{D_j} \qquad (3.7)$$

Where D_j is the distance between the circumcenters of two neighbor cells, $j = 1,2,3$ is the edge type index and f provides the index of the cell in the direction of n_j, while b provides the index for the cell in the opposite direction ; see Fig. 3.1 (right).

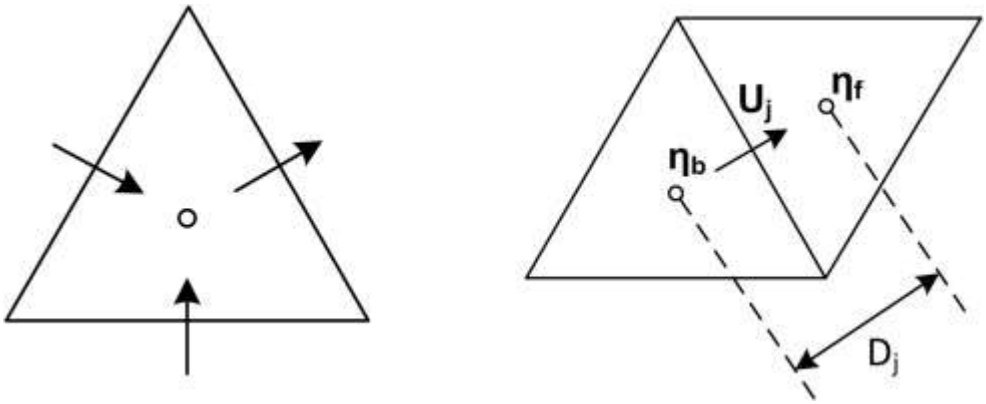

Fig. 3.1 - Normal velocity and water surface elevation locations are presented by the symbols ○ and →, respectively (left); estimation of normal gradient of water surface elevation at face j (right).

The continuity equation (3.1) also can be written in the following form:

$$\frac{\partial \eta}{\partial t} + H\frac{\partial U}{\partial n} = 0 \qquad (3.8)$$

Considering the triangular cell shown in Fig. 3.1 (left) as the control volume for the water surface elevation, the discretized form of continuity equation (3.1) is given as follows:

$$\frac{\partial \eta}{\partial t} + \frac{H}{A}\sum_{j=1}^{3} U_j d_j = 0 \qquad (3.9)$$

Where A is the area of the cell, d_j is the length of the jth edge of the cell and U_j is the normal component of velocity at the jth edge of each cell. It must be noted that the C-grid semi-discrete scheme is formally second-order accurate.

For the Fourier analysis, a uniform mesh made up of equilateral triangles, as shown in Fig. 3.2a, is sufficient. As is shown in Fig. 3.2b (left), the normal velocity Umay be located on three possible edge types; i.e., either on the horizontal one or the other two biased ones. Similarly, Fig. 3.2b (right) shows that the water surface elevation can be placed at two different locations i.e. either the up-ward or down-ward triangles.

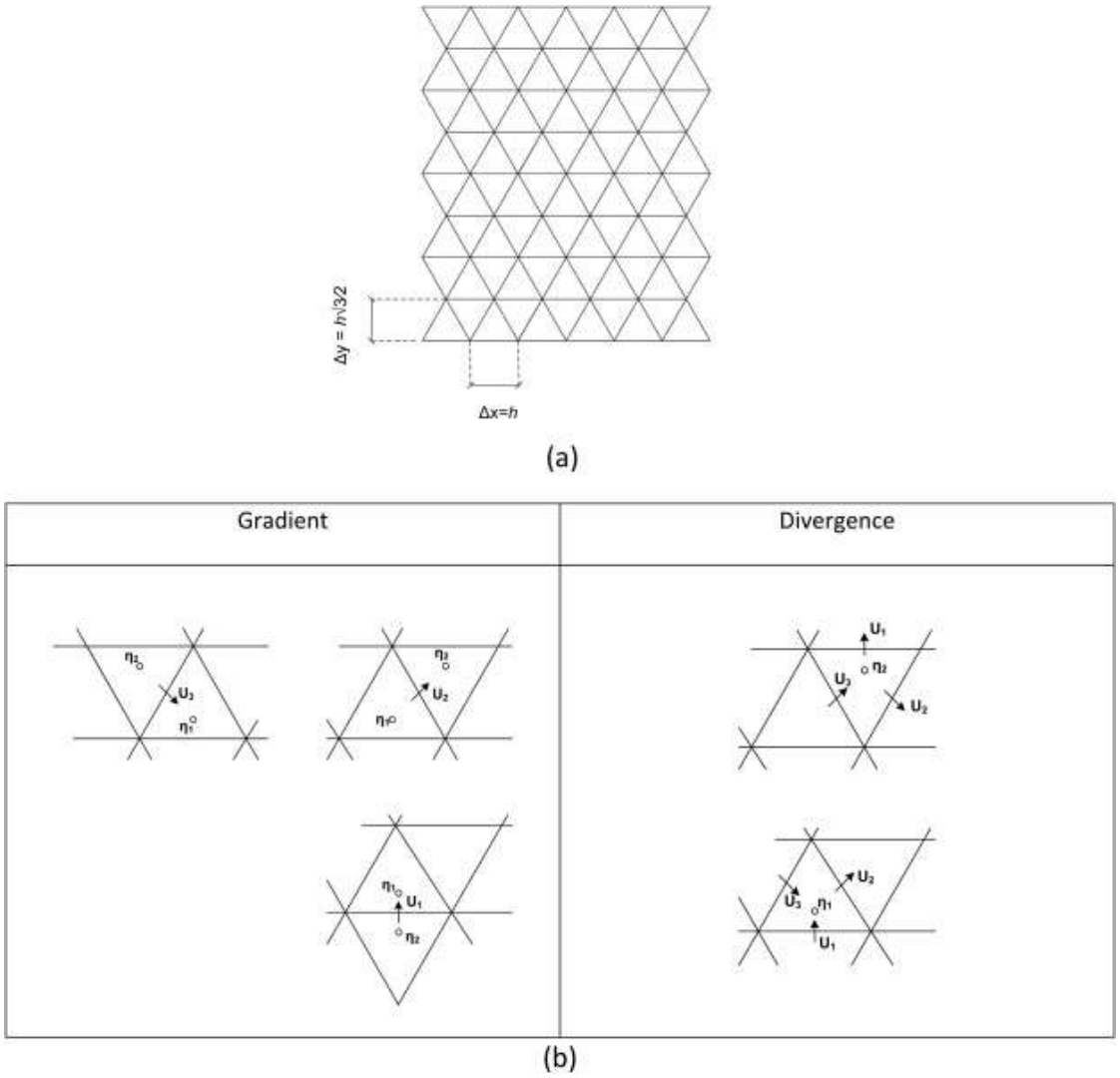

Fig. 3.2 - (a) Triangular mesh grid made up of equilateral triangles of length h. (b) Gradient (left) and divergence (right) stencils of the C-grid spatial discretization.

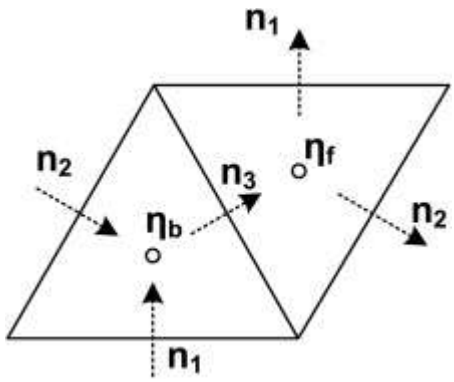

Fig. 3.3 - Discretization of spatial term in momentum equation.

Having Equations (3.7) and (3.9) as discrete forms of governing Equations (3.6) and (3.8), similar to the continuum case the dispersion relationship for the discrete form is found using the Fourier analysis. The discrete solutions corresponding to $U = \tilde{U}e^{i(kx_j+ly_j+\omega t)}$ and $\eta = \tilde{\eta}e^{i(kx_j+ly_j+\omega t)}$ are sought, where $\tilde{u}, \tilde{v}$ and$\tilde{\eta}$ are amplitudes, (x_j, y_j) coordinates are expressed in terms of distance to a reference circumcenter and the periodic solution form of the normal components can be stated as follows:

$$\tilde{U}e^{i(kx_j+ly_j+\omega t)} = \tilde{u}e^{i(kx_j+ly_j+\omega t)}\cos\left(\frac{\pi}{3}\right) + \tilde{v}e^{i(kx_j+ly_j+\omega t)}\sin\left(\frac{\pi}{3}\right)$$

For the C-grid, the discretized equations include two momentum equations at two possible types of circumcenters $(\tilde{\eta}_1, \tilde{\eta}_2)$ and three continuity equations at three possible types of edges $(\tilde{U}_1, \tilde{U}_2, \tilde{U}_3)$. Substituting the periodic solution of U and η in the discrete equations leads to a square matrix system of amplitudes as:

$$\begin{pmatrix} i\omega I_2 & \frac{H}{h}A \\ \frac{g}{h}B & D \end{pmatrix}\begin{pmatrix} \vec{\tilde{U}} \\ \vec{\tilde{\eta}} \end{pmatrix} = \begin{pmatrix} 0 \\ 0 \end{pmatrix} \tag{3.10}$$

Where $\vec{\tilde{U}} = \left(\tilde{U}_1, \tilde{U}_2, \tilde{U}_3\right)$, $\vec{\tilde{\eta}} = (\tilde{\eta}_1, \tilde{\eta}_2)$, I_2 is square identity matrix and we also have:

$$A = \frac{4}{\sqrt{3}}\begin{pmatrix} -a & b & c \\ \frac{1}{a} & -\frac{1}{b} & -\frac{1}{c} \end{pmatrix}, B = \sqrt{3}\begin{pmatrix} \frac{1}{a} & -a \\ -\frac{1}{b} & b \\ -\frac{1}{c} & c \end{pmatrix}, D = \sqrt{3}\begin{pmatrix} i\omega & 0 & 0 \\ 0 & i\omega & 0 \\ 0 & 0 & i\omega \end{pmatrix}$$

$$a = e^{-ilh\frac{\sqrt{3}}{6}}, b = e^{ih\left(\frac{k}{4}+l\frac{\sqrt{3}}{12}\right)}, c = e^{ih\left(-\frac{k}{4}+l\frac{\sqrt{3}}{12}\right)}$$

The dispersion relationship is then obtained by setting the determinant of the 5×5 matrix system to zero, which leads to:

$$\omega_1 = 0, \qquad \omega_{2,3} = \omega_{AN} + o(h^2), \qquad \omega_{4,5} = \pm\frac{\sqrt{24\,Hg}}{h} + o(h)$$

It should be noted that in limit as mesh spacing $h \to 0$, only $\omega_{2,3}$ correspond to a continuous solution, while $\omega_{4,5}$ correspond to spurious modes.

Considering $\omega_{2,3}$that correspond to the continuous solution, the dispersion relation for the semi-discretized equations is obtained by vanishing the 5×5 matrix in equation (3.10) :

$$\omega_{cp} = \pm 2 \frac{\sqrt{Hg\left(3-\sqrt{2\cos\left(lh_y-\frac{kh_x}{2}\right)+2\cos\left(lh_y+\frac{kh_x}{2}\right)+2\cos(kh_x)+3}\right)}}{h} \quad (3.11)$$

Where $h_x = h$ and $h_y = \frac{h\sqrt{3}}{2}$. We can examine the obtained dispersion relation (3.11) as a function of kh_x and lh_y.

As equation (3.11) shows, the two roots of ω have no imaginary parts and have the same real parts with different signs, i.e., the two waves move in different directions as in the continuous system. The imaginary part of ω, which deals with damping, equals zero here. In other words, all waves, including both short and long waves, are transferred without damping. However, this is not always desirable, since most discretization schemes have a phase speed error for high frequencies, which may lead to oscillatory results unless they are effectively damped. Of essential importance is the observation that we have zero frequency, i.e., $\omega = 0$ at the following values of $(kh_x, lh_y), (0, \pm 2\pi), (\pm 2\pi, \pm \pi)$, which implies zero phase speed for all waves. Therefore, all waves do not propagate, which may lead to numerical oscillation. However, it can be shown that all of these waves are shorter than the shortest resolvable wave of the C-grid mesh for which we have $(kh_x, lh_y) = (\pi, \pi)$.

For a 2-dimensional wave, phase speed is generally defined as $C = \omega/\sqrt{k^2 + l^2}$. Therefore, the phase speed for both analytical and discrete cases can be written based on the dispersion relations (3.5) and (3.11)as follows:

$$C_{AN} = \frac{\omega_{AN}}{\sqrt{k^2+l^2}} \quad (3.12)$$

$$C_{CP} = \frac{\omega_{CP}}{\sqrt{k^2+l^2}} \quad (3.13)$$

Where C_{AN} and C_{CP} are the analytical and computed phase speed, respectively. Then, the phase speed ratio is defined as a ratio of the computed phase speed to the analytical one:

$$C_r = \frac{C_{CP}}{C_{AN}} = \frac{\omega_{CP}}{\sqrt{gH(k^2+l^2)}} \tag{3.14}$$

For an ideal discretization scheme, the phase speed ratio is $C_r = 1$, which would be the case in the absence of numerical dispersion. Fig. 3.4 shows the surface function of C_r depending on kh_x and lh_y . As previously mentioned, since $(kh_x, lh_y) = (\pi, \pi)$ corresponds to the shortest resolvable wave, kh_x and lh_y vary over $[0, \pi]$.It can be seen that the phase speed ratio is $0.9 < C_r < 1$ for both long and intermediate waves with kh_x and lh_y roughly lower than 0.8π, and suddenly decreases for shorter waves. Therefore, the long and intermediate waves, which transfer most of the energy, travel at almost the same speed as continuous waves. On the other hand, the shorter waves are travelling slower than expected. As mentioned above, since theses waves are not damped, they may lead to numerical oscillation in the results.

The group velocity is the velocity at which the energy is carried by the waves. It is defined as $G = (\frac{\partial \omega}{\partial k}\ ,\ \frac{\partial \omega}{\partial l})$ and can be estimated for both continuous and discrete cases as follows:

$$G_{AN} = (\frac{\partial \omega_{AN}}{\partial k}\ ,\ \frac{\partial \omega_{AN}}{\partial l}) \tag{3.15}$$

$$G_{CP} = (\frac{\partial \omega_{CP}}{\partial k}\ ,\ \frac{\partial \omega_{CP}}{\partial l}) \tag{3.16}$$

Where ω_{AN} and $\omega_{CP}$are given by (3.5) and (3.11), respectively. The group velocity for continuous and semi-discrete forms is illustrated in Fig. 3.5. As is shown, the group velocity for the semi-discrete form is mostly consistent with the analytical solutions except for higher values of $lh$and kh.

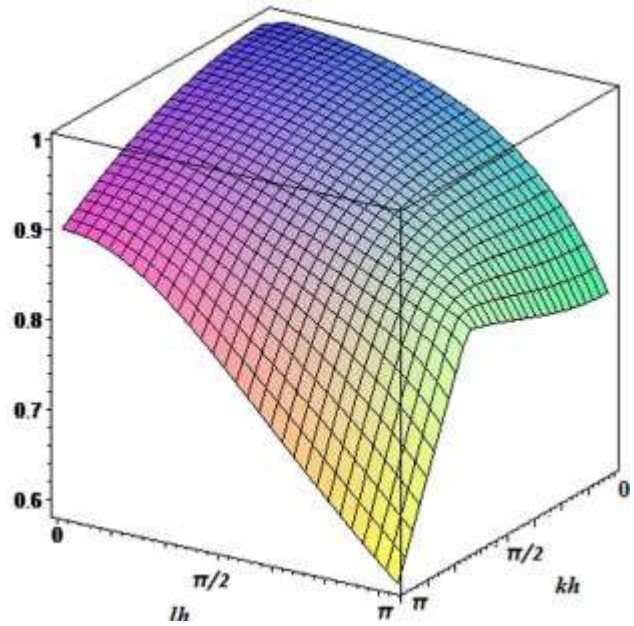

Fig. 3.4 - Phase speed ratio for C-grid spatial discretization.

In addition to the group velocity, the directional derivatives $G_{AN}.\boldsymbol{d}$ and $G_{CP}.\boldsymbol{d}$ are calculated, where $\boldsymbol{d}$is a unit vector in the OX, OY and OD directions as shown in Fig. 3.6. They correspond to the waves travelling in the $-$, $y-$ and diagonal axes for $lh_y = 0, kh_x = 0$ and $kh_x = lh_y$, respectively.

As Fig. 3.7 shows, for small and intermediate $kh_x$and lh_y , the group velocity is consistent with the analytical solution. However, at the values of $(kh_x, lh_y) = (0, \pi)$ (wave of length $2h$) they equal zero, which means although the waves are propagating, the associated energy is not. It can be also seen that in the OD direction we have a wrong (negative) sign for wave length greater than $2h$ and smaller than $3h$.

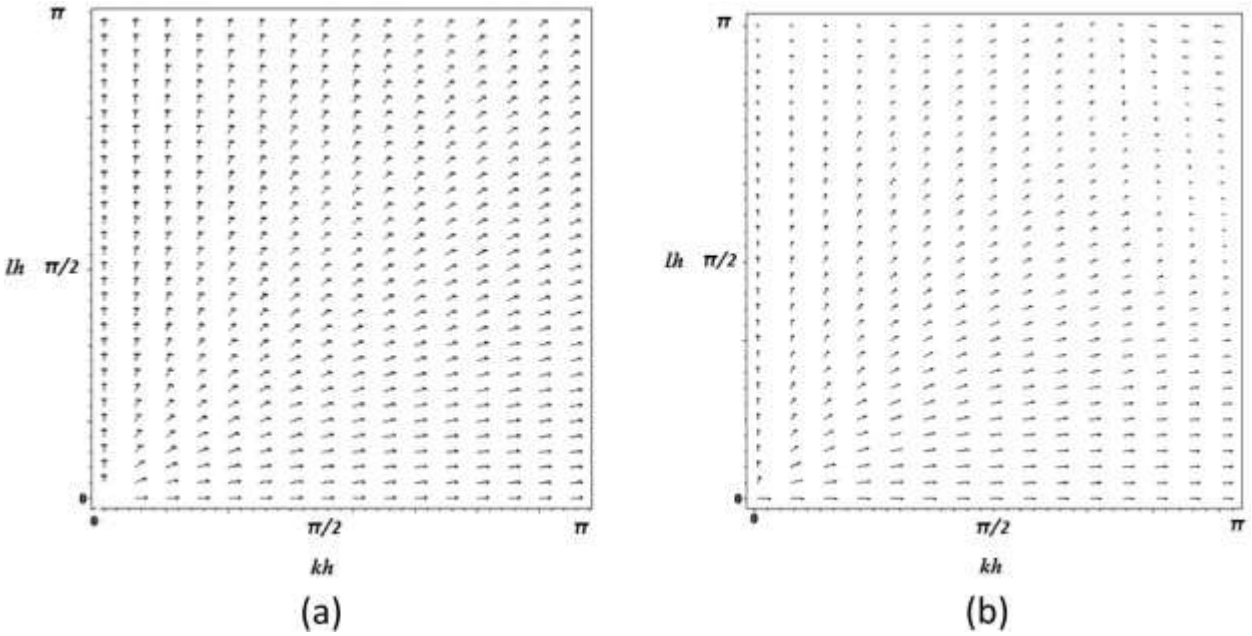

Fig. 3.5 - The group velocity vectors of (a) the continuous case and (b) C-grid spatial discretization.

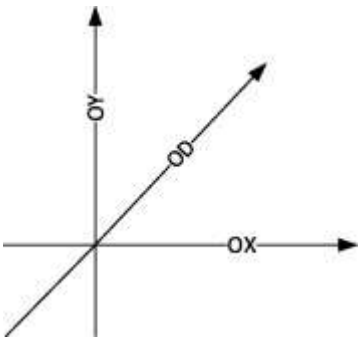

Fig. 3.6 - Definition of the directions OX, OY and OD on a Cartesian coordinate.

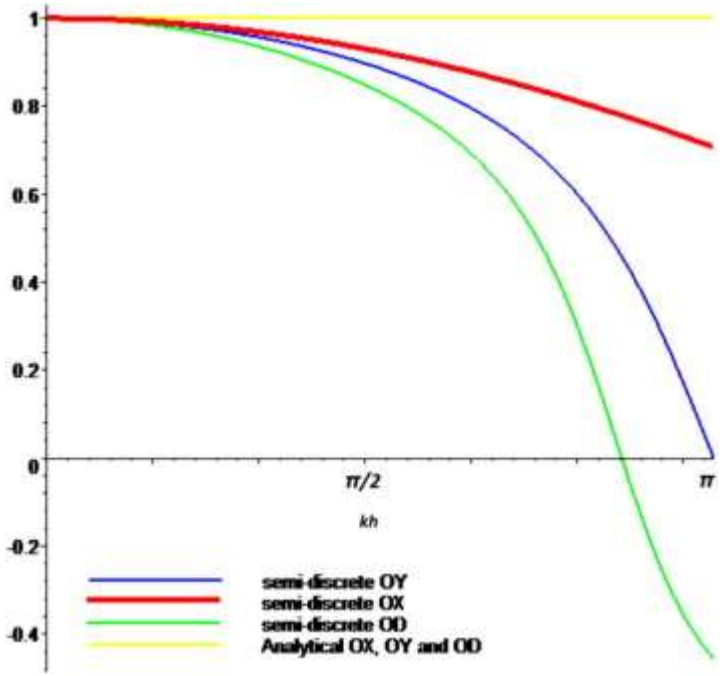

Fig. 3.7 - Computational and analytical directional derivative (Gcp.d and Gan.d) in OY, OX and OD directions.

3.4. Temporal Discretization and Analysis

A Fourier analysis is now conducted for both the spatial and temporal schemes. In this section, first, by using various temporal schemes in combination with the C-grid spatial scheme, the governing equations (3.6) and (3.8) are discretized. Then, by submitting the periodic solution of the form $U = \widetilde{U}e^{i(kx_j+ly_j+\omega t)}$ and $\eta = \tilde{\eta}e^{i(kx_j+ly_j+\omega t)}$ into the discretized form and vanishing the matrix, we can obtain the corresponding dispersion relation. In this study, forward Euler, Leap-Frog and Adams-Bashforth temporal schemes are examined in combination with the C-grid spatial scheme.

3.4.1. Forward Euler Scheme

Using the forward Euler method and at a given time-step $\Delta t = t^{n+1} - t^{n}$, the temporal terms of Equations (3.6) and (3.8) can be written as follows:

$$\frac{\partial U}{\partial t} = \frac{U^{n+1} - U^{n}}{\Delta t} \tag{3.17}$$

$$\frac{\partial \eta}{\partial t} = \frac{\eta^{n+1} - \eta^{n}}{\Delta t} \tag{3.18}$$

and the spatial discretized terms are evaluated at time step n. We can obtain the following matrix form:

$$\begin{pmatrix} (E-1)I_2 & \beta HA \\ \beta gB & (E-1)I_3 \end{pmatrix} \begin{pmatrix} \vec{U} \\ \vec{\eta} \end{pmatrix} = \begin{pmatrix} 0 \\ 0 \end{pmatrix} \tag{3.19}$$

Where $E = e^{i\omega\Delta t}$ is the propagation factor, $\beta = \frac{\Delta t}{\Delta x}$ and $\alpha = \frac{\sqrt{gH}\Delta t}{d}$ is the CFL number where $d = \frac{\sqrt{3}}{6}h$ is the shortest distance among the grid points. The dispersion relation is then obtained for the propagation factor by setting the detriment of the matrix in the left-hand side of equation (3.19) equal to zero for a non-trivial solution. The dispersion relation for the fully discretized scheme using the forward Euler method is as follows:

$$E = 1 + \frac{\sqrt{3}}{3}\alpha\sqrt{3 - \sqrt{2\cos\left(lh_y - \frac{kh_x}{2}\right) + 2\cos\left(lh_y + \frac{kh_x}{2}\right) + 2\cos(kh_x) + 3}} \tag{3.20}$$

3.4.2. Leap-Frog Scheme

The temporal terms can be discretized as follows using the Leap-Frog temporal scheme:

$$\frac{\eta^{n+2} - \eta^{n}}{\Delta t} + \frac{H}{A}\sum_{j=1}^{3} {U_j}^{n+1} d_j = 0 \tag{3.20}$$

$$\frac{U^{n+2} - U^{n}}{\Delta t} + g\left(\frac{\partial \eta}{\partial n}\right)_j^{n+1} = 0 \tag{3.21}$$

Note that in the Leap-Frog method, the spatial terms are estimated at the time step $n + 1$.

$$\begin{pmatrix} (E^2-1)I_2 & \beta HAE \\ \beta gBE & (E^2-1)I_3 \end{pmatrix} \begin{pmatrix} \vec{U} \\ \vec{\eta} \end{pmatrix} = \begin{pmatrix} 0 \\ 0 \end{pmatrix} \tag{3.22}$$

The dispersion relationship is obtained by vanishing the left-hand side matrix of (3.22). However, the explicit form of the dispersion relation is too long to be written, and will be shown graphically and discussed in the following section.

3.4.3. Adams-Bashforth second order Scheme

Employing the Adams-Bashforth temporal scheme leads to the following fully discretized form of the governing equation:

$$\frac{\eta^{n+2}-\eta^{n+1}}{\Delta t}+\frac{3}{2}\left(\frac{H}{A}\sum_{j=1}^{3}U_j{}^{n+1}d_j\right)-\frac{1}{2}\left(\frac{H}{A}\sum_{j=1}^{3}U_j{}^{n}d_j\right)=0 \tag{3.23}$$

$$\frac{U^{n+2}-U^{n+1}}{\Delta t}+\frac{3}{2}g\left(\frac{\partial\eta}{\partial n}\right)_j^{n+1}-\frac{1}{2}g\left(\frac{\partial\eta}{\partial n}\right)_j^{n}=0 \tag{3.24}$$

This fully discrete scheme can be written in the following matrix for:

$$\begin{pmatrix}(E^2-E)I_2 & \beta HA\left(\frac{3E}{2}-\frac{1}{2}\right)\\ \beta gB\left(\frac{3E}{2}-\frac{1}{2}\right) & (E^2-E)I_3\end{pmatrix}\begin{pmatrix}\vec{\tilde{U}}\\ \vec{\tilde{\eta}}\end{pmatrix}=\begin{pmatrix}0\\0\end{pmatrix} \tag{3.25}$$

Similarly, the dispersion relation for this scheme is obtained by canceling the determinant of the left-hand side of the matrix, but it is too long to be written, and will be shown graphically and discussed in the following section.

3.4.4. Dispersion Relation Analysis

In order to analyze the fully discrete schemes, the dispersion relation of each method is investigated. The phase speed ratio and amplification factor $|E|$ for each fully discrete scheme is presented in Figs. 8 to 10.

Since the Euler forward time stepping technique is a basic method, the results are only shown for the Leap-Frog and Adams-Bashforth schemes. As the figures show, for a small CFL number ($CFL = 0.1$), the results of fully discrete systems are close to those of the semi-discrete form. Since the semi-discrete form can be considered as the fully discrete method when $t \to 0$.

Based on the dispersion relationship analysis, it can be concluded that the performance of the different schemes depends on the CFL number. As the dispersion relation (3.20) of the forward Euler scheme shows, for all wave numbers and CFL numbers the amplification factor is $|E| > 1$. Therefore, even with a small CFL number ($CFL = 0.1$), the Euler scheme may lead to unstable results.

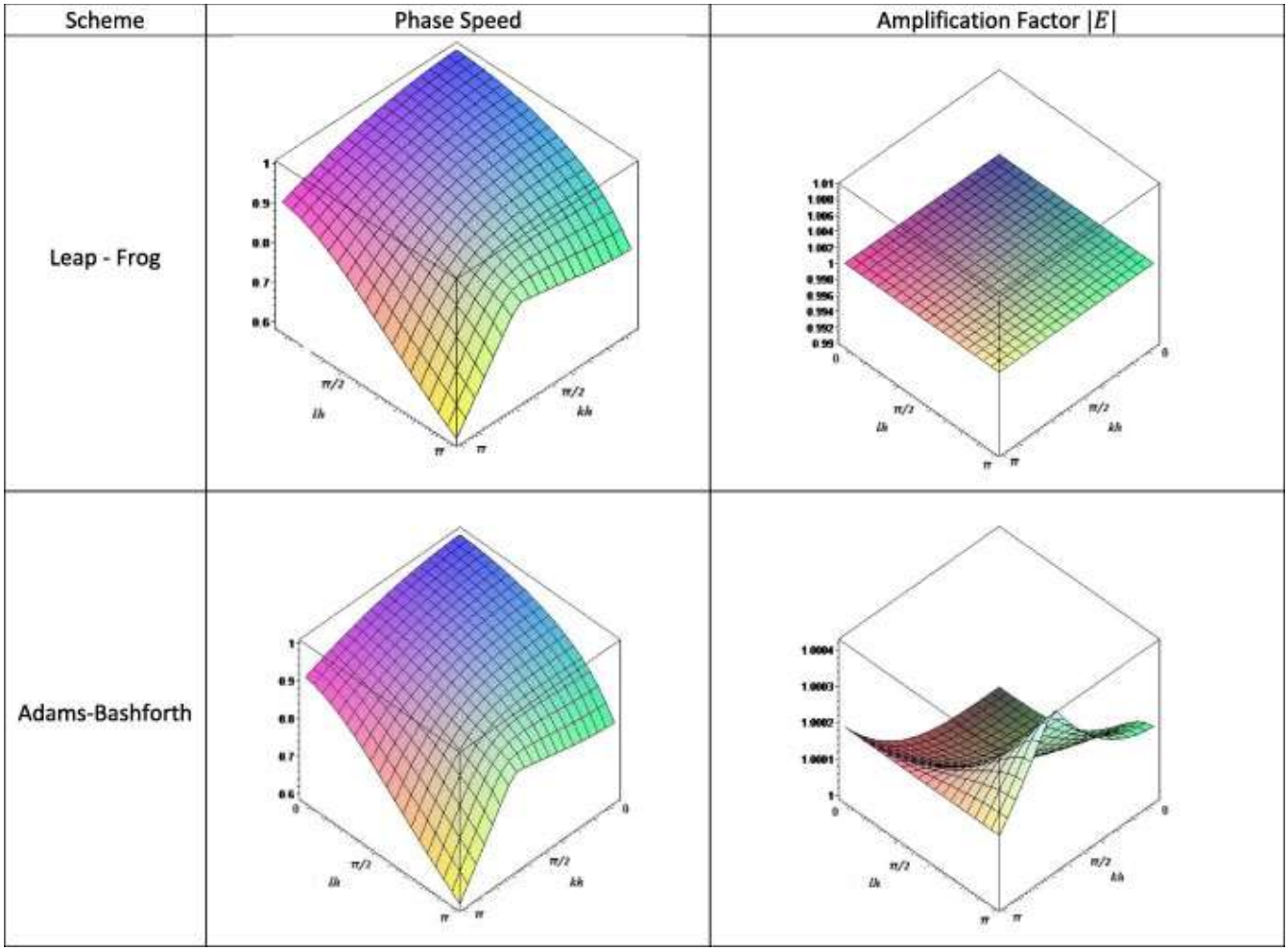

Fig. 3.8 - The phase speed ration as a surface function for *CFL* = 0.1.

In the Leap-Frog scheme, the amplification factor is very close to one for small and medium CFL numbers ($CFL = 0.1 \text{and } 0.5$), while it suddenly decreases for high wave numbers at the high CFL condition. The Adams-Bashforth scheme exhibits more sensitive performance with regard to the CFL number. The amplification factor is close to one for a

small CFL number of 0.1, but in the high CFL numbers it significantly decreases for all wave numbers.

The phase speed ratio is also presented for different fully discrete systems. As previously mentioned, the performance of all schemes is very close to that of the semi-discrete form when the phase speed ratio is close to one for the long waves (small wave numbers), while it departs from one when the wave number increases. However, increasing the CFL number results in a different performance of the fully discrete schemes.

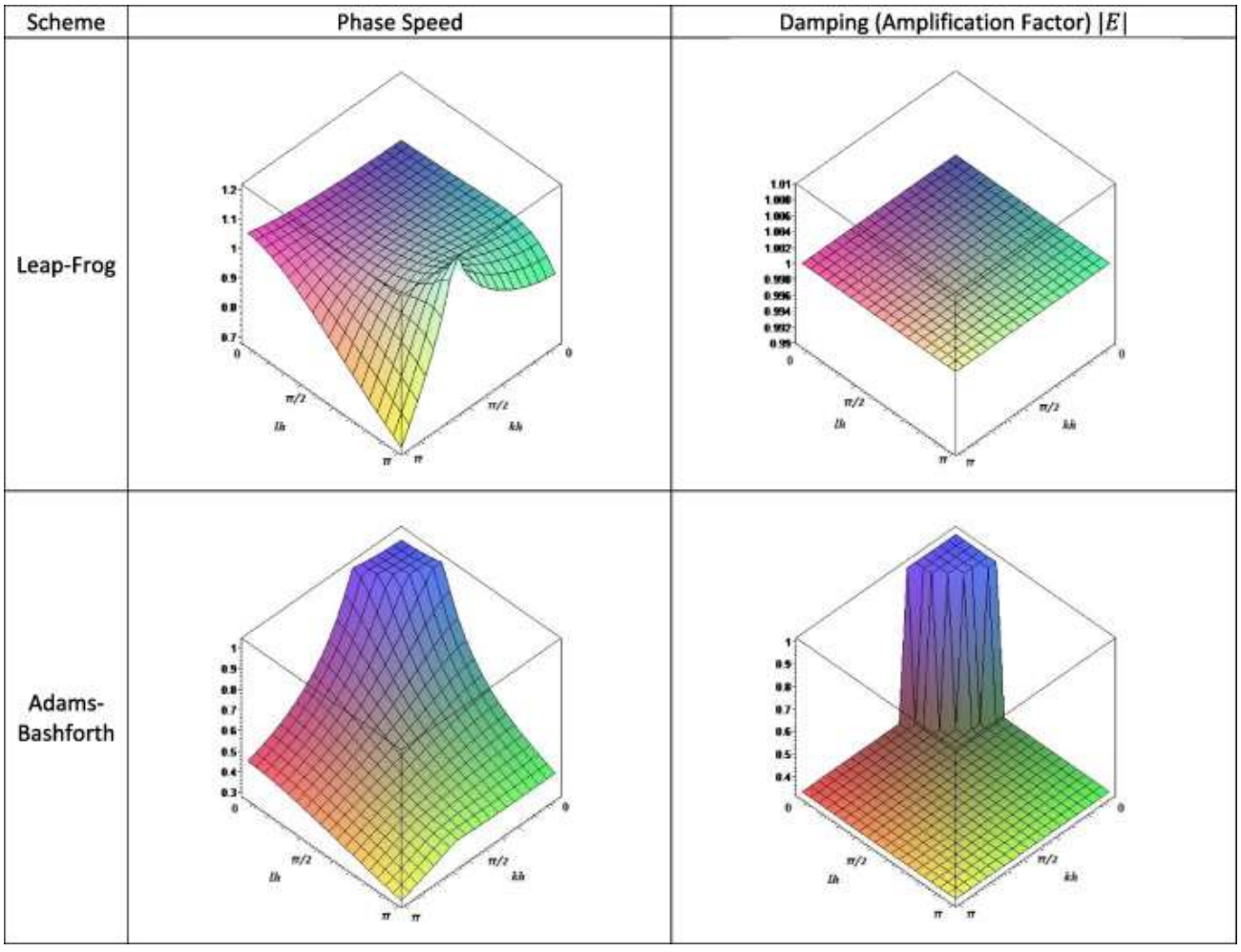

Fig. 3.9 - As for Fig. 3.8 but for CFL = 0.5.

In fact, the phase speed ratio decreases in the Euler (not shown) and Adams-Bashforth methods. Indeed, for the higher CFL numbers, the waves are traveling much slower than expected, especiallyforthe higher wave numbers. This may result in oscillatory results for these two methods with high CFL numbers ($CFL > 0.1$). On the other hand, in the Leap-Frog scheme, for $CFL = 0.5$ the phase speed ratio is increased. In fact, this leads to the phase speed ratio being close to one for a wide range of wave numbers and it improves the phase speed ratio of the high wave numbers. However, one should note that the phase speed ratio is a little higher than one for some medium wave numbers. For $CFL = 0.9$, the phase speed ratio is still increasing, and it reaches 1.4. In this case, for the low wave numbers (long waves) the phase speed ratio is higher

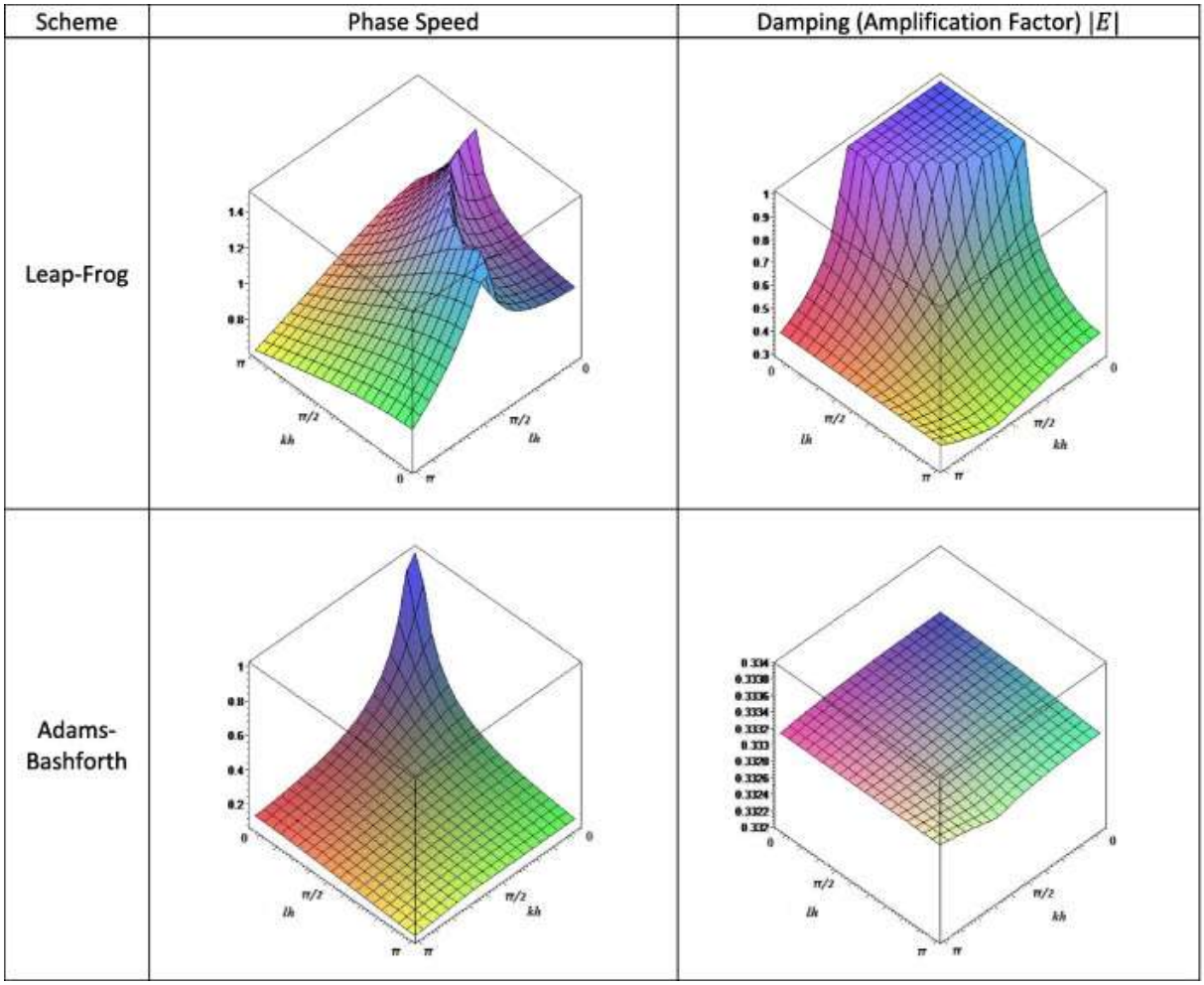

Fig. 3.10 -As for Fig. 3.8 but for CFL = 0.9.

than one, while it is less than one for the higher wave numbers (shorter waves). It should be noted that when the phase speed ratio is higher than one, the waves are travelling in higher speed than expected.

As dispersion relation analysis shows, the combination of the Leap-Frog temporal scheme with the C-grid spatial scheme improves the phase speed ratio performance of the semi-discrete form. In addition, it shows that the amplification factor is almost equal to one, not only for a small CFL number ($\mathrm{CFL} = 0.1$) but also for a higher CFL number ($\mathrm{CFL} = 0.5$).

In the dispersion relation analysis, it should be considered that most of the energy is transferred via long waves. Therefore, the waves with a high number do not transfer much energy. In addition, the results show that both numerical schemes have a phase speed error for higher wave numbers, as most of the numerical schemes have. However, these waves do not transfer a significant amount of energy in the domain, and there may be oscillatory results unless the numerical scheme damps them efficiently.

3.5. Numerical Tests

The results of the various numerical tests where the governing equations are (3.6) and (3.8) will be presented in this section. It should be noted that the numerical results of some tests, which are not presented here, confirm that the Euler method is unstable even for small CFL numbers. Therefore, the results of the Euler method are not presented in this section.

3.5.1. Validation of Analysis

The first test aims to validate the analytical dispersion analysis obtained in the previous section for various temporal schemes. The grid used for the numerical tests is made up of equilateral triangles, as shown in Fig. 3.1. The domain extent is $500\mathrm{km} \times 200\mathrm{km}$, and the length of the triangles selected is $h = 10\mathrm{km}$. The fluid is initially at rest and, except for the left boundary, a zero normal velocity is specified at the other lateral boundaries. The condition $\eta = 1\,m$ is prescribed at each time step at the left lateral boundary, with $H = 1000\,m$ and $g = 9.81\,\frac{m}{s^2}$. The results of the numerical tests for different CFL numbers are presented in Figs. 11 and 12 for the Leap-Frog and Adams-Bashforth schemes,

respectively. In these figures, the vertical sections of the wave propagation are shown after $2000\ s$and $4000\ s$. The time step is set to $dt = 1.85s\ , 9.22s\ and\ 16.6s$ for gravitational CFL numbers of $CFL = 0.1, 0.5$ and 0.9, respectively.

Based on the dispersion analysis, the phase speed ratio for the Adams-Bashforth and Leap-Frog scheme, as shown in Figs. 8 to 10, is close to 1 for small values of wave numbers. Therefore, the wave front propagates at the analytical speed of $\sqrt{gH} \cong 99\ ms^{-1}$. The computed wave front speeds observed in Figs. 11 and 12 are in good agreement with the analytical one.

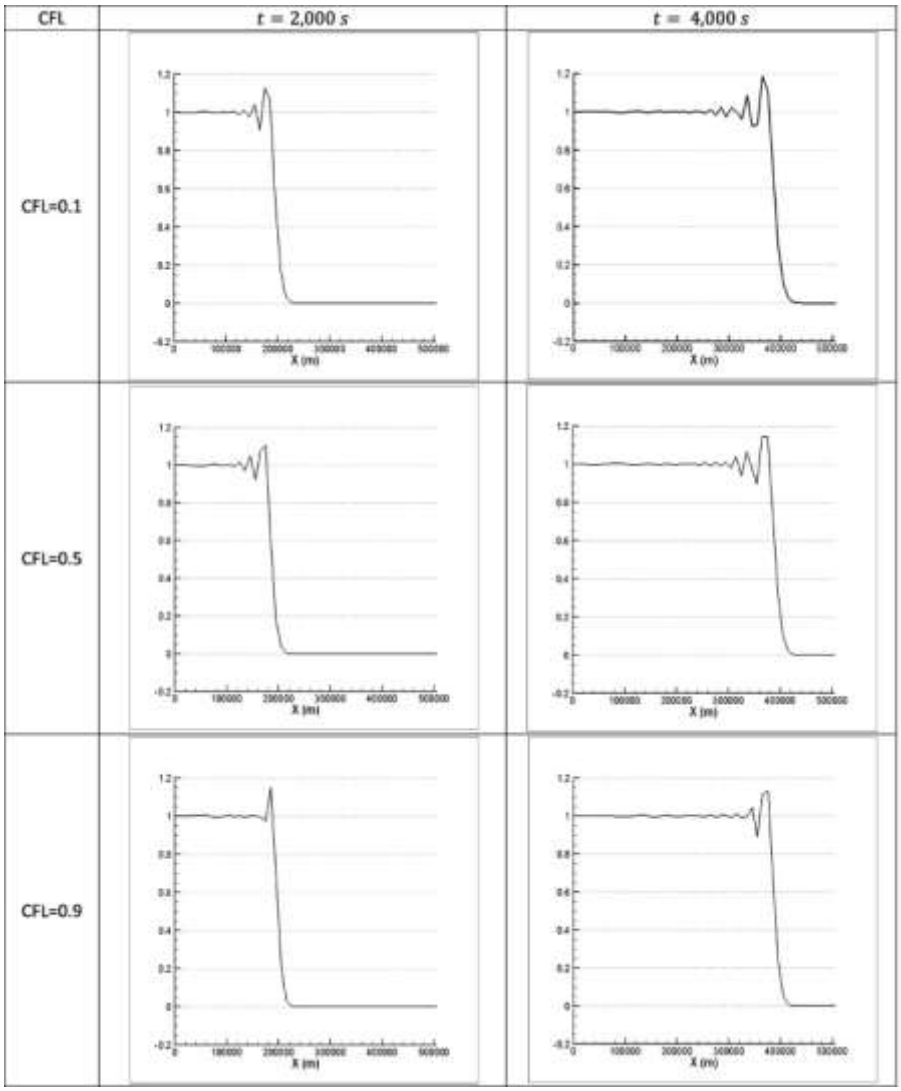

Fig. 3.11 - Cross sections of the water surface elevation at times 2000 s and 4000 s for the Leap-Frog method

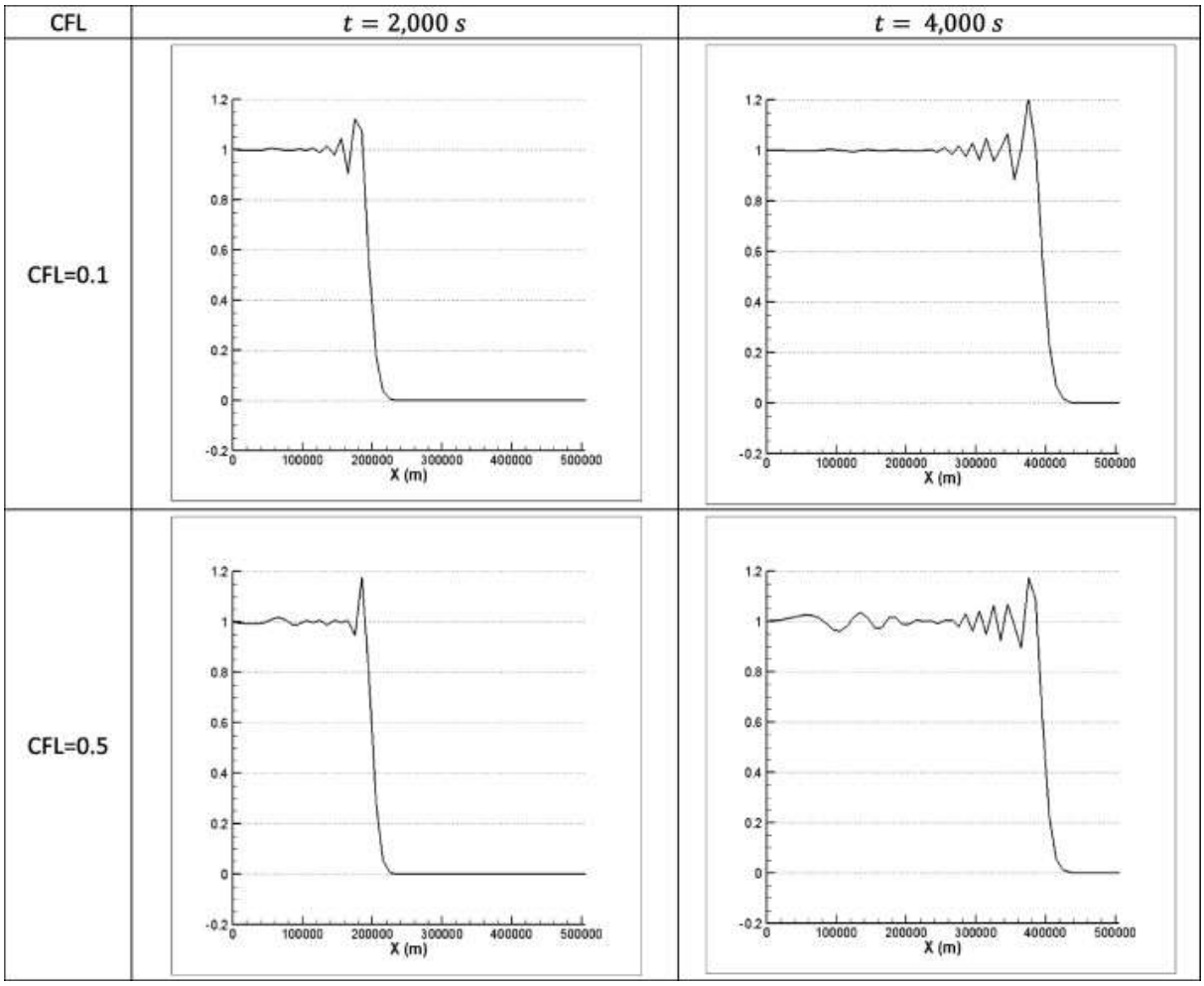

Fig. 3.12 - Cross sections of the water surface elevation at times 2000 s and 4000 s for the Adams–Bashforth method.

There is also good agreement between the numerical dispersion shown in Figs. 3.8 to 3.10 and the numerical test results presented in Figs. 3.11 and 3.12. For both the Leap-Frog and Adams-Bashforth schemes, we have a phase speed ratio of $C_r < 1$ for most of the wave numbers, specifically for the small values of $kh$and lh. This implies that $C_{CP} < C_{AN}$, which means the waves are traveling slower than expected, and leads to dispersion effects as oscillation prior to the front wave, as can be seen in Figs. 3.11 and 3.12. For the Leap-Frog scheme, since by increasing the CFL number the phase speed ratio gets closer to 1, the dispersion effects lessen. Hence, as shown in Fig. 3.11, for $CFL = 0.9$ the oscillation

appearing downstream of the wave front is less compared to that of $CFL = 0.1$. On the other hand, as previously shown in Figs. 8 to 10, for the Adams-Bashforth scheme the phase speed ratio significantly departs from 1 by increasing the CFL number. Therefore, as shown in Fig. 3.12, there are more oscillations observed for $CFL = 0.5$ in comparison with $CFL = 0.1$. For the higher CFL numbers (e.g., $CFL = 0.9$) the oscillation leads to unstable results, which are not presented here. The isolines of the wave propagation at $5000\ s$ are presented in Fig. 3.13 for $CFL = 0.1$. This confirms that both numerical schemes are able to preserve the symmetry characteristic of the solution.

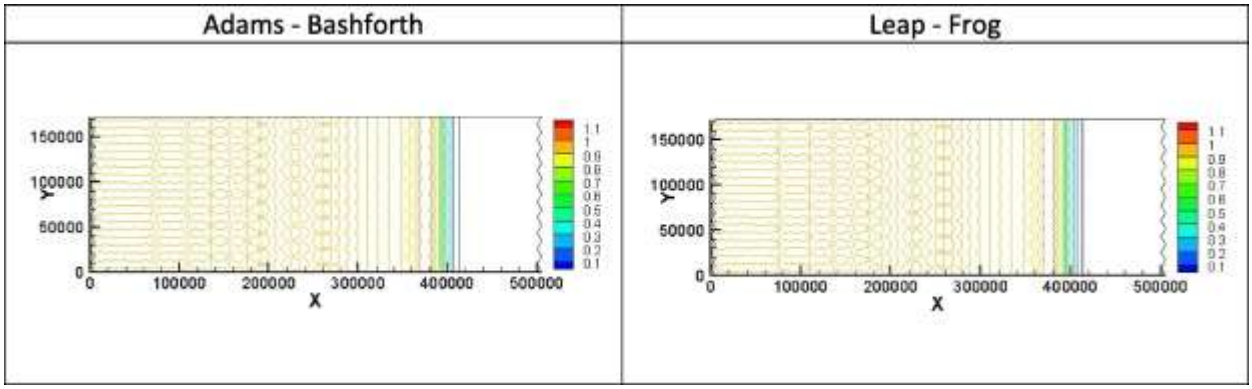

Fig. 3.13 -Isolines of water surface elevation of wave propagation at time 5000 s and CFL = 0.1.

3.5.2. Seiche Wave (Standing Wave)

In the second numerical test, a seiche is simulated as an example of shallow-water waves. In fact, a seiche is standing wave formed by the superposition of two waves of equal wavelength and propagating in opposite directions. Such a situation happens in confined water bodies such as a lake by reflection from lateral boundaries. The water surface elevation of the seiche in a closed, long and non-rotating rectangular basin of length L and uniform depth H has a simple trigonometric exact solution:

$$\eta(x,t) = A\cos(kx)\cos(\omega t) \tag{3.26}$$

Where A is the wave amplitude, x is the along-basin coordinate, t is time, $k = 2\pi/\lambda$ is the wave number, λ is the wavelength, $\omega = 2\pi/T$ is the angular wave frequency, and T is the wave period. The angular frequencyand wave number can be calculated based on the wave propagation speed $c = \sqrt{gH}$,

$$\omega = kc \tag{3.27}$$

In this numerical test, the fourth oscillation mode of the seiche is considered, where $k = \frac{4\pi}{L}$and $\lambda = \frac{2L}{4}$. Indeed, in the fourth mode of the seiche the wave length is equal to half of the basin length. Different values for the closed basin length L results in a seiche with a specific wave number and length. The length of the triangles selected is $h = 2.5\ km$ and the initial water surface$\eta(x, 0) = 0.01cos\ (kx)\cos\ (\omega t)$ is prescribed, with $H = 10\ m$ and $g = 9.81\ \frac{m}{s^2}$.

For various wave numbers, the results of the numerical test are presented in Figs. 3.14 and 3.15 for both numerical schemes with $CFL = 0.1$ .In the results, the entire seiche is presented at $t = 5T$, as well as the oscillation of the midpoint of the domain at $5T < t < 6T$.

Fig. 3.15 shows the results of the Leap-Frog method with $CFL = 0.9$ and wave number $k = \frac{\pi}{2}$. Comparing to Fig. 3.14 for $CFL = 0.1$ with the same wave number, the phase speed error is improved by increasing the CFL number. This confirms the results of the dispersion relation analysis in Fig. 3.10.

In Fig. 3.16, the results for a wave number of $k = \frac{\pi}{8}$ is presented for different CFL numbers, and it shows that as expected for the long waves, the phase speed error increases by increasing the CFL number.

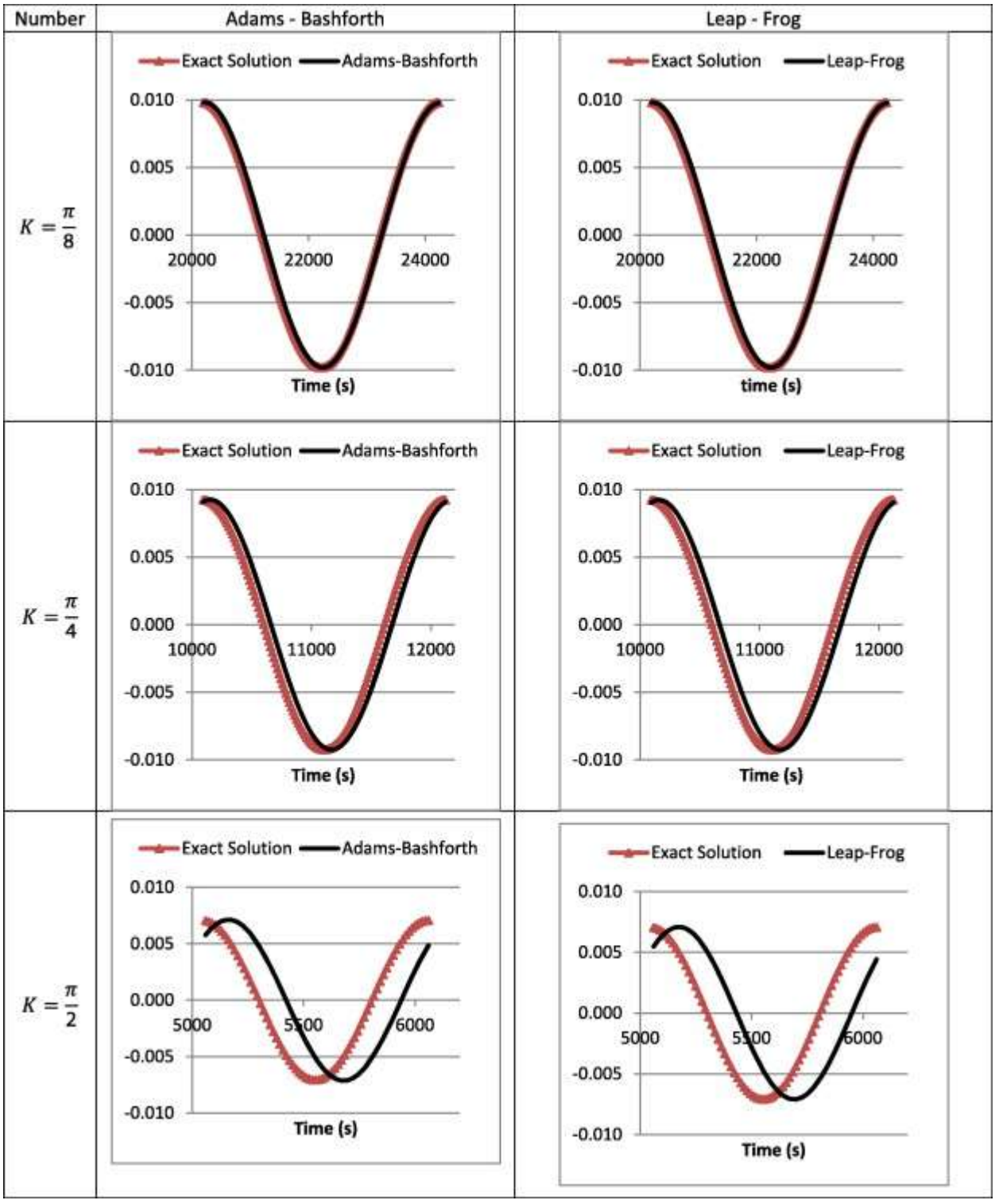

Fig. 3.14 - Water surface elevation of the seiche wave for the domain midpoint at time 5T < t < 6T for $CFL = 0.1$.

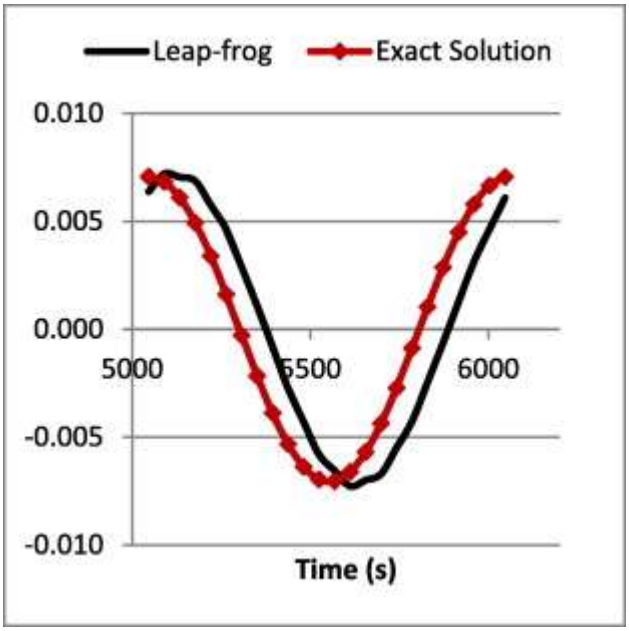

Fig. 3.15 - As Fig. 3.14 but with CFL = 0.9 and k = π/2 for the Leap-Frog scheme.

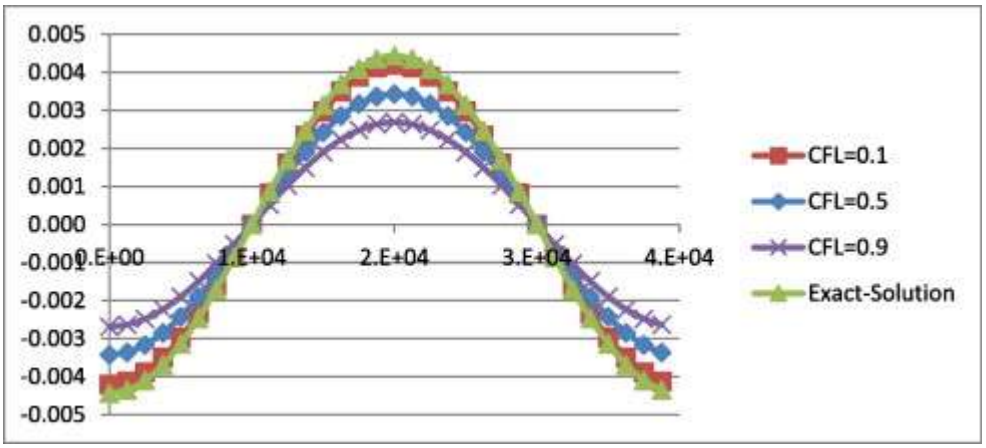

Fig. 3.16 - Water surface elevation of the seiche (standing wave) versus time for k = π/8 with different CFL numbers.

3.5.3. Gravity Wave

In the third numerical test, the pure gravity wave with Gaussian initial distribution is investigated. In a closed basin, for a water surface initial condition in the form of $\eta(r,t) = ae^{-\frac{x^2+y^2}{b}}$ and zero initial velocity in the domain, the exact solution of this problem can be found in the polar coordinates system as follows (Le Roux 2001):

$$\eta(r,t) = \sum_1^\infty \mu_n J_0\left(r\sqrt{\lambda_n}\right)\cos\left(c\sqrt{\lambda_n}t\right), \tag{3.28}$$

Where $\mu_n = \frac{\int_0^R \eta(r,0) J_0\left(r\sqrt{\lambda_n}\right) rdr}{\int_0^R {J_0}^2\left(r\sqrt{\lambda_n}\right) rdr}$, R is the radius of the domain, $r = \sqrt{x^2+y^2}$, J is the Bessel function of first kind and λ_n are estimated from the roots of $J_1\left(r\sqrt{\lambda_n}\right) = 0$.

In this numerical test, a domain with $R = 400\ km$ and the length of the triangles $h = 4\ km$ is considered, with $H = 1$, $a = 1$ and $b = 1000$. In Fig. 3.17, the results of the water surface elevation for the Adams - Bashforth and Leap-Frog schemes are compared with the exact solution ($CFL = 0.1$). As can be seen, they are in good agreement for both schemes.

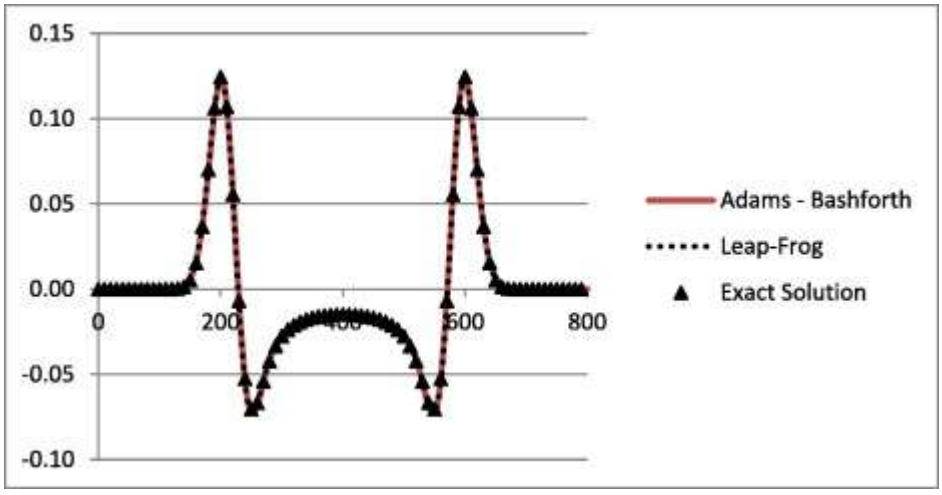

Fig. 3.17 - Comparison of numerical and exact solution of pure gravity wave at time 60 s with *CFL* = 0.1.

In Fig. 3.18, the contour and results of the water surface presented after reflecting off the basin walls for both numerical schemes confirm that they are capable of preserving the symmetry of the solution.

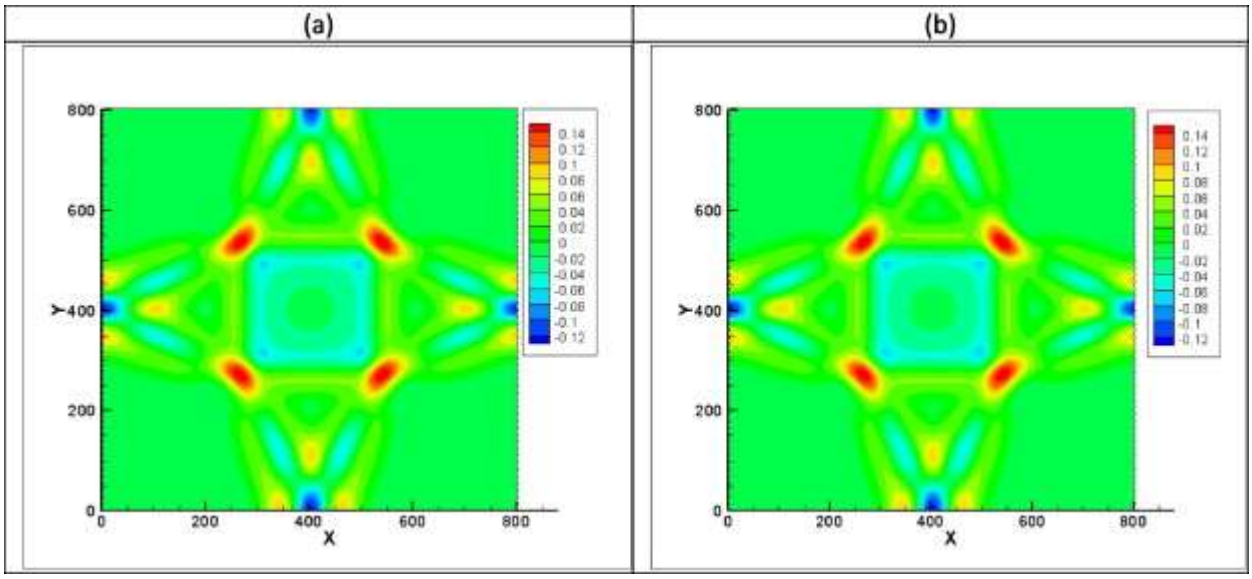

Fig. 3.18 - Water surface elevation after water reflects off the side walls of the basin at time 400 s with CFL = 0.1 using (a) Adams–Bashforth and (b) Leap-Frog schemes.

In order to investigate the effect of the spatial C-grid scheme in the proposed combination of temporal schemes, the numerical test for a pure gravity wave is done with the same time step while the length of the triangle of the mesh decreases. The L^2 error of the water surface is calculated for each case and presented in Table 3.1. The results show that when the spatial grid size decreases, despite the fact that the CFL number increases, both numerical schemes converge. Table 3.1 shows that the numerical method with the Adams-Bashforth temporal scheme converges faster than that of the Leap-Frog scheme.

Table 3.1 - Spatial evolution of L2 error.

***h* (m)**	**Δ *t* (s)**	**CFL**	**L^2 error**	
			Leap-Frog	Adams-Bashforth
20	0.15	0.04	0.0000638	0.0000614
10	0.15	0.08	0.0000192	0.0000107
5	0.15	0.16	0.0000187	0.0000087

In addition, the evolution of L^2 error in log-log scale for gravity test is illustrated in Fig. 3.19. In fact, the L^2 error is calculated for various values of triangle length while CFL is kept constant and small in order to exclude the error due to time discretization. As can be seen, the results of the Leap-Frog and Adams - Bashforth are almost the same. This, indeed, implies that the error of temporal scheme is almost eliminated in this test. Therefore, the order of spatial accuracy associated with the C-grid scheme is obtained approximately equal to 3.18, which is very promising.

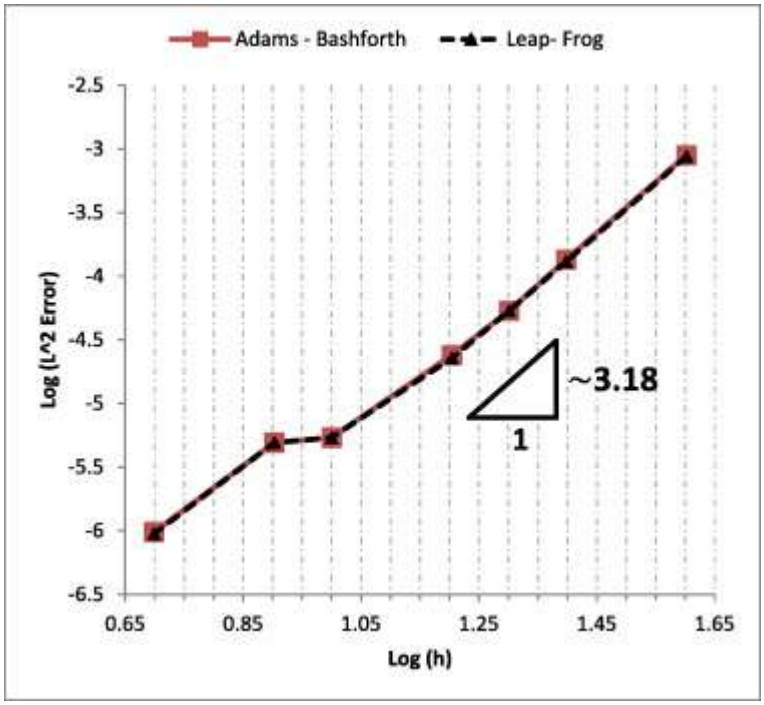

Fig. 3.19 - Evolution of L2 error in Log–Log scale for pure gravity wave at t = 60 s.

Similarly, the numerical tests are performed with the same triangle length of $h = 8\,m$ and various time step sizes, and the L^2 error of the water surface is estimated for each case at $t = 60\,s$. Since for lower time steps more iterations are required and the error due to the temporal scheme accumulates, the L^2 error per time step for each case is presented in Table 3.2. As can be seen, both numerical schemes converge to the analytical solution, while the

Table 3.2 - Temporal evolution of L2 error.

***h* (m)**	**Δ*t* (s)**	**CFL**	**L^2 error per time step**	
			Leap-Frog	Adams–Bashforth
8	0.51	0.35	83.7E−08	Unstable
8	0.45	0.30	9.7E−08	Unstable
8	0.3	0.20	6.4E−08	Unstable
8	0.15	0.10	2.9E−08	2.7E−09
8	0.075	0.05	1.5E−08	1.7E−09
8	0.0375	0.03	0.8E−08	0.9E−9

time step decreases. The results indicate that the error has a lower order of magnitude for the Adams-Bashforth method, and therefore the rate of convergence is faster. However, it should be noted that the Leap-Frog scheme is stable for larger time steps and CFL numbers, while the Adams-Bashforth method exhibits instability for higher time steps and CFL numbers.

3.5.4. Grid structure effect

The mesh structure can directly affect the numerical solutions and therefore, the impact of mesh shape and structure on the quality of the solutions is also analyzed in this study. For this aim, the organized-unstructured triangular as well as fully-unstructured triangular meshes are employed as are shown in Fig. 3.20. In order to specify the shape of the organized-unstructured grid, the following skewness parameter is used as an indicator of mesh quality (Roldán et al. 2013):

$$Skewness = \frac{Optimal\ Cell\ Size - Cell\ size}{Cell\ Size} \tag{3.29}$$

where the optimal cell size is defined as the area of an equilateral triangle with the same circumscribed circle. For an acceptable, good and excellent mesh, the skewness parameter must be in range of $0 - 0.25$, $0.25 - 0.5$ and $0.5 - 0.75$, respectively. The pure gravity tests are performed and water levels at $t = 60s$ are then compared to the exact solution. Table. 3.3 presents L^2 errors for three organized-unstructured meshes. As results show, the errors for all three cases are lower than 5.00×10^{-5} and the c-grid spatial discretization method in the proposed combination with both time-stepping techniques performs well.

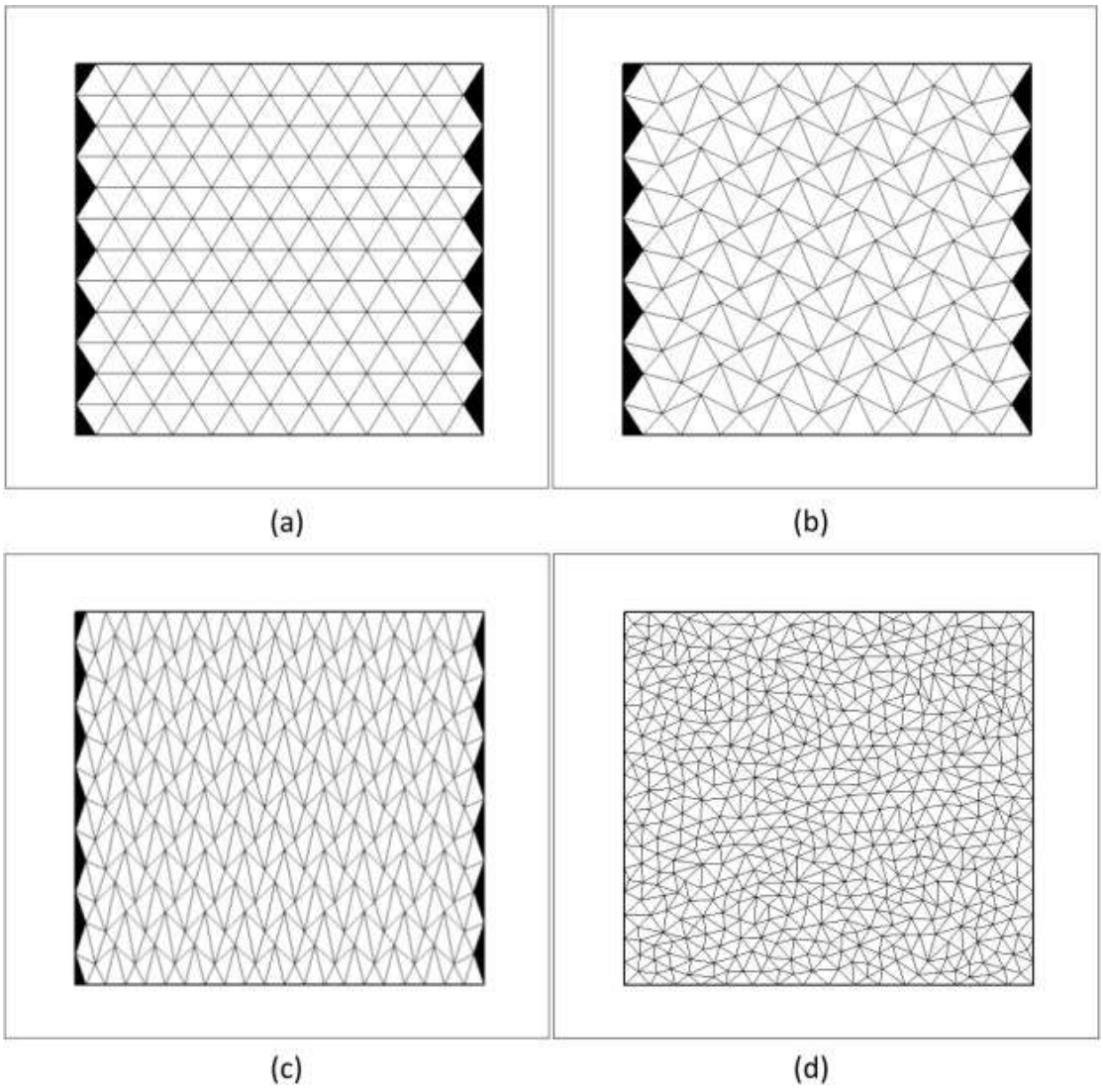

Fig. 3.20 - Organized-unstructured triangular meshes with (a) excellent, (b) good, (c) acceptable shape and (d) fully-unstructured triangular mesh.

The evolution of L^2 error in log-log scale for a organized-structured with good shape and fully-unstructured meshes are illustrated in Fig. 3.21. As is shown, the order of spatial accuracy associated with the C-grid scheme is obtained approximately equal to 2.5and 1.9, respectively.

Table 3.3 -L^2 error for different mesh types.

	L^2 error		
	Mesh (a)	Mesh (b)	Mesh (3)
Adams–Bashforth	1.08E−06	2.00E−05	2.54E−05
Leap-Frog	9.08E−06	2.80E−05	3.32E−05

This implies that the mesh structure and quality can effectively influence the solutions and the rate of convergence. Three dimensional view of the water elevation at $t = 60\ s$ is illustrated in Fig. 3.22 for both organized and fully unstructured triangular meshes. It shows that the scheme preserves the symmetry of the solution over the entire domain.

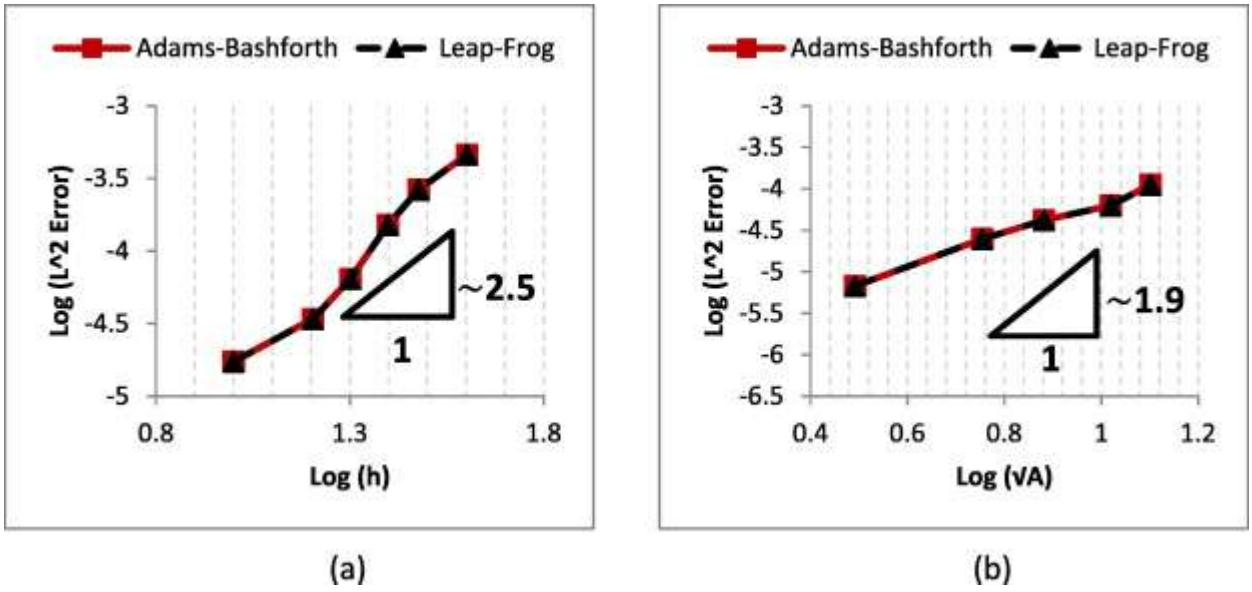

Fig. 3.21- Evolution of L2 error in log–log scale for pure gravity wave at t = 60 s (a) for organized-unstructured mesh with good shape (b) fully-unstructured triangular mesh.

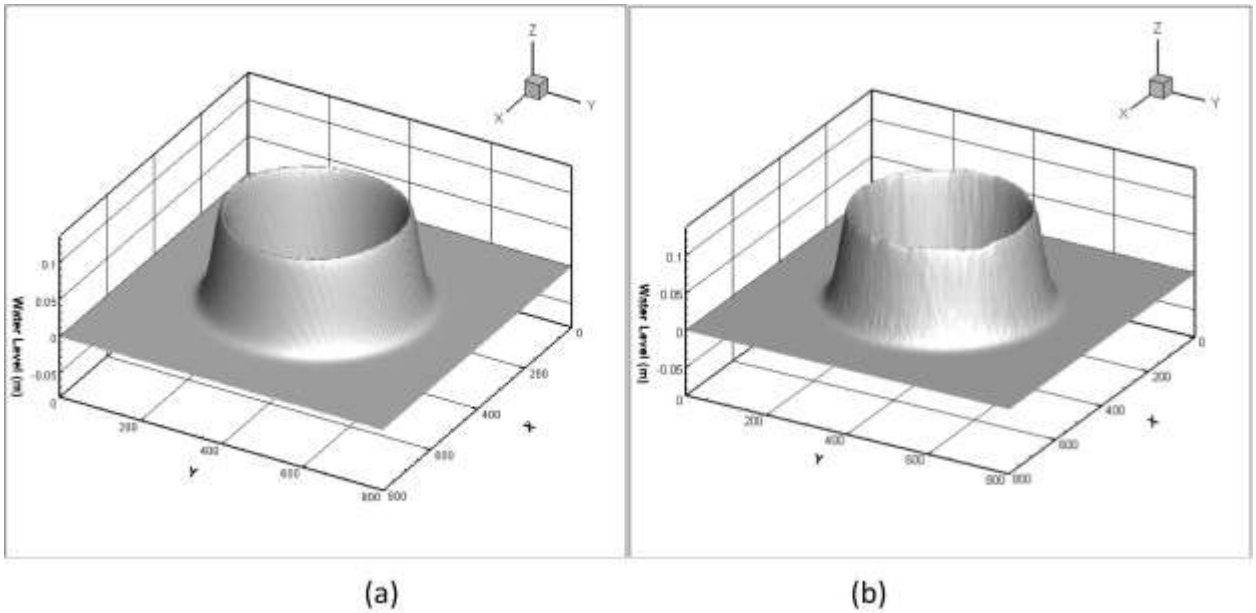

Fig. 3.22- Three dimensional view of water surface at t = 60 s using (a) good organized-unstructured triangular mesh (b) fully-unstructured triangular mesh.

3.5.5. Non-linear parabolic flood waves

In order to find out the behavior of the proposed combination of the Adams-Bashforth time stepping technique with the C-grid approach, in this test, the non-linear shallow water system is employed for modeling parabolic flood wave. The analytical solution of this example is given by Thacker (1981):

$$u = \frac{xt}{t^2+T^2} \tag{3.30}$$

$$v = \frac{yt}{t^2+T^2} \tag{3.31}$$

$$h = h_0\left[\frac{T^2}{t^2+T^2} - \frac{x^2+y^2}{R_0^2}\left(\frac{T^2}{t^2+T^2}\right)^2\right] \tag{3.32}$$

where the h_0 is the peak of the initial water surface elevation and T is calculated as a function of parameter R_0 as follows:

$$T = R_0(2gh_0)^{-1/2} \tag{3.33}$$

Here, a $24m \times 24m$ rectangular domain is considered with $h_0 = 1$ and $R_0 = 40$. The initial velocity is considered zero over the entire domain and $h = h_0(1 - \frac{x^2+y^2}{R_0^2})$ is the initial water level. It should be noted that following the work of Perot (2000), Casulli (1999) and Casulli and Zanolli (2002) the non-linear shallow water equations are spatially discretized using the C-grid approach (Appendix) and Adams-Bashforth time stepping scheme is employed for temporal discretization. Fig. 3.23a shows the analytical and numerical solutions of water surface elevation the wave at the $t = 7s$. The results show good agreement and the 3D view of the wave in Fig. 3.23b also confirms that the symmetric forms of the solution is preserved by the method.

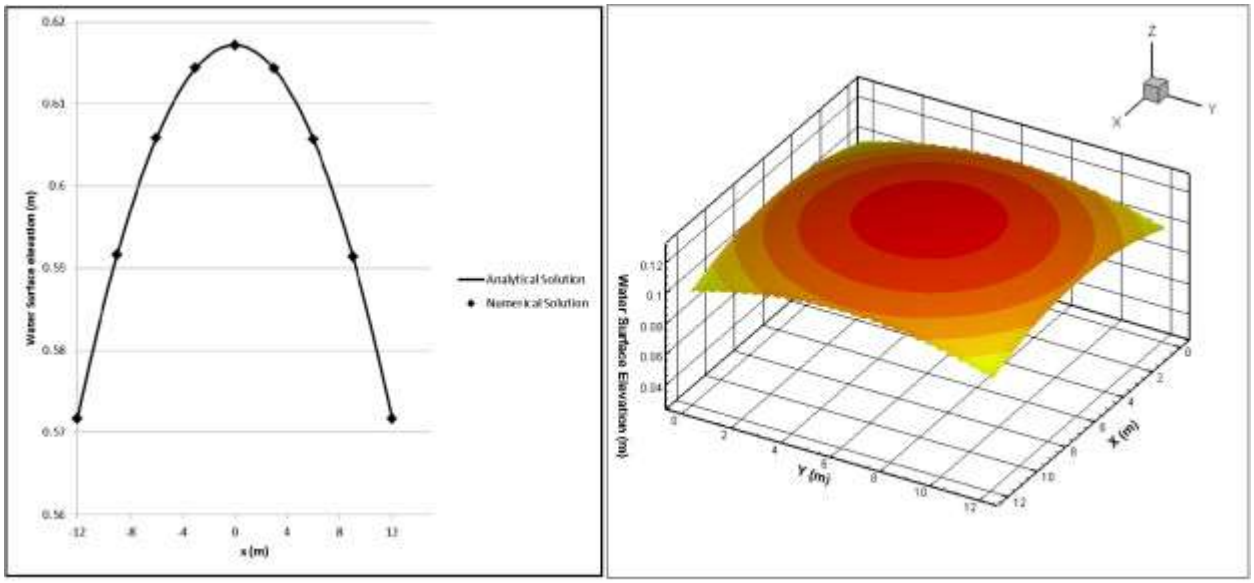

Fig. 3.23 - (a) Comparison of analytical and numerical solutions of a parabolic flood wave at t = 7 s (b) three dimensional view of the parabolic flood at t = 25 s.

In order to obtain the order of spatial accuracy of the proposed scheme for the non-linear shallow water equations, we consider the same example with a rectangular domain of $[-6\,,6] \times [-6\,,6]$. The evolution of the L^2 error in the log-log scale is illustrated in Fig. 3.24. As can be seen, the obtained order of accuracy is 2.36, which is promising.

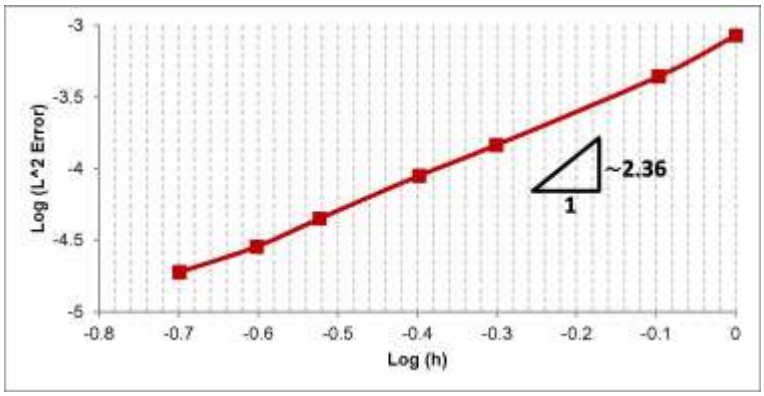

Fig. 3.24 - Evolution of the L2-error for parabolic flood wave in log–log scale.

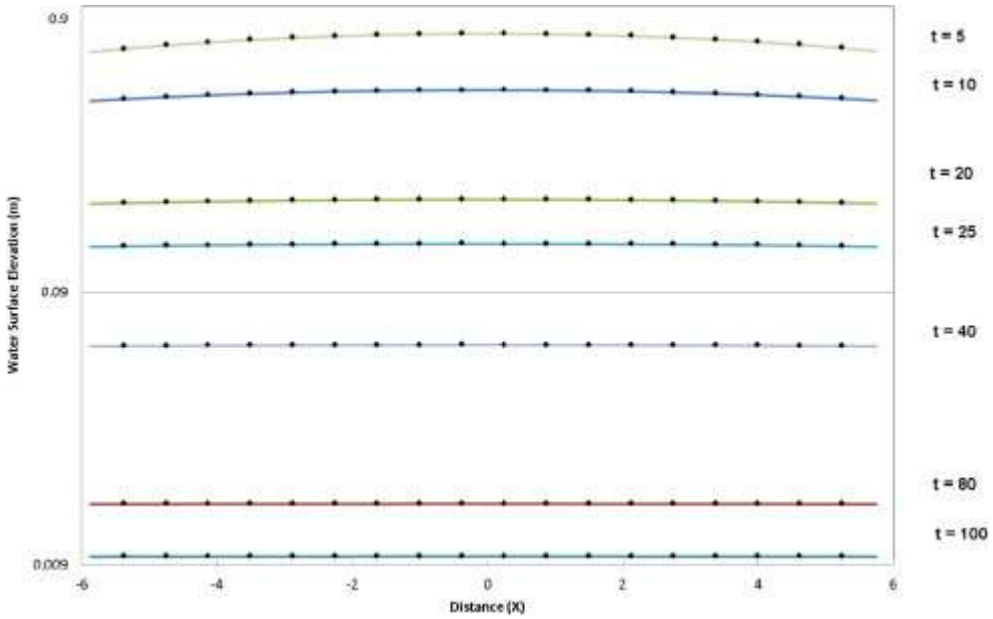

Fig. 3.25 - Comparison of the computed (dots) and analytical (lines) water surface elevation for parabolic flood wave at different time stage.

We also examine the proposed model in terms of conservation properties. To this end, we consider the long time simulation of the flood wave up to $t = 100$. The evolution of the computed water surface elevation is compared to the analytical solution in Fig. 3.25. It must be noted that for an appropriate visualization, the water surface elevation is shown in logarithmic scale. One can see that the obtained results are in good agreement with the analytical ones. In addition, it can be seen that the proposed scheme preserves the maximum water surface elevation through the simulation time and that there is no significant damping associated with the results. Moreover, the numerical scheme preserves the symmetric shape of the solution. It also can be seen that even at $t = 100$, where the water depth becomes very close to zero, the scheme performs well and there is no noise in the solution.

Table 3.4 - Comparison of computed and analytical maximum water surface elevation at different time stages.

t	**5**	**10**	**20**	**25**	**40**	**80**	**100**
Proposed scheme	0.79653	0.49487	0.19679	0.13558	0.05787	0.01511	0.00972
Analytical	0.79673	0.49494	0.19679	0.13555	0.05771	0.01508	0.00970
True relative error %	0.02	0.02	0.00	0.03	0.28	0.16	0.15

For a quantitative comparison, the computed and analytical maximum water surface elevations at various times along with the corresponding true relative errors are presented in Table 3.4. The results show that the errors are negligible and confirm the capability of the model.

3.5.6. Non-linear wind-induced currents in a rectangular basin

This numerical example, which has various practical applications in mixing, stratification and chaotic advection, has been widely used in the literature (Pattantyus-Abraham et al., 2008; Wang et al., 2001; Liang et al., 2006). In this example we examines the proposed C-grid scheme with a consideration of various source terms in momentum equations which are of essential importance in practical applications. This particular example is useful for checking the ability of the proposed scheme to account correctly for non-uniform bed topography, wind surface stress bed friction.

In this test we consider a square lake with a domain extension of $[-1000,1000]m \times [-1000,1000]m$, which can represent a shallow lake. Except for the near-shore field, one can assume a mild linear bottom slope from the shore line toward the center of the lake. This form of bottom topography will result in topographic gyres in the flow circulation pattern. In this example we set the still water depth at $h_s = 2.5\ m$ at the center point of the lake while we consider $h_s = 2.5\ m$ through the shore lines. Fig. 3.26 shows the still water depth that represents the bottom topography of the lake.

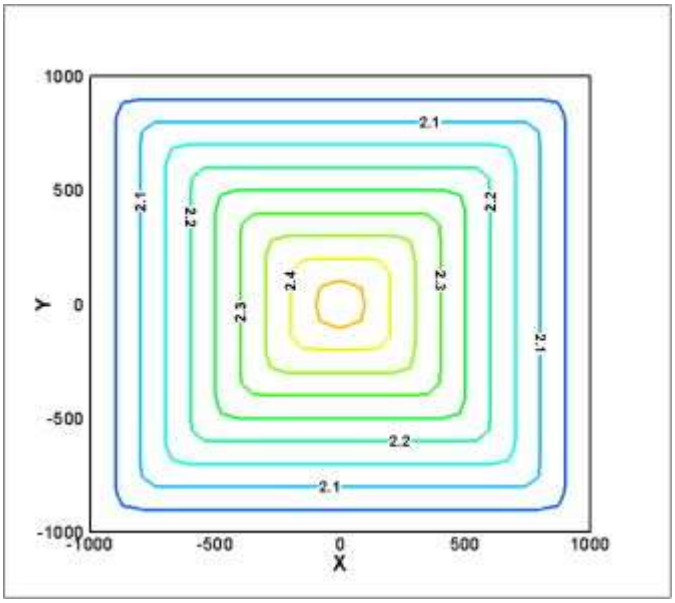

Fig. 3.26 - Contour lines of still water depth over the model-lake.

The bed friction terms are given by $\tau_{bx} = \rho C_f u\sqrt{u^2 + v^2}$and $\tau_{by} = \rho C_f v\sqrt{u^2 + v^2}$, where C_f is an empirical coefficient based on bed roughness. We use the following equation based on the Chezy friction law:

$$C_f = \frac{g}{C^2}$$

where$C$ is the Chezy friction coefficient. Triangular grids with an approximate cell area of $2771\ m^2$ are used and CFL is set to $CFL = 0.2$. A no-flow boundary with a free-slip condition is applied at the basin wall. The north and east wind components of $2\ N/m^2$ is assumed that is $\tau_x = \tau_y = 2\ N/m^2$, and the wind direction changes from north-east to north-west every $2\ hr$ s. The Chezy parameter of the bed friction is taken as $C = 33.11\ m^{\frac{1}{2}}/s$.

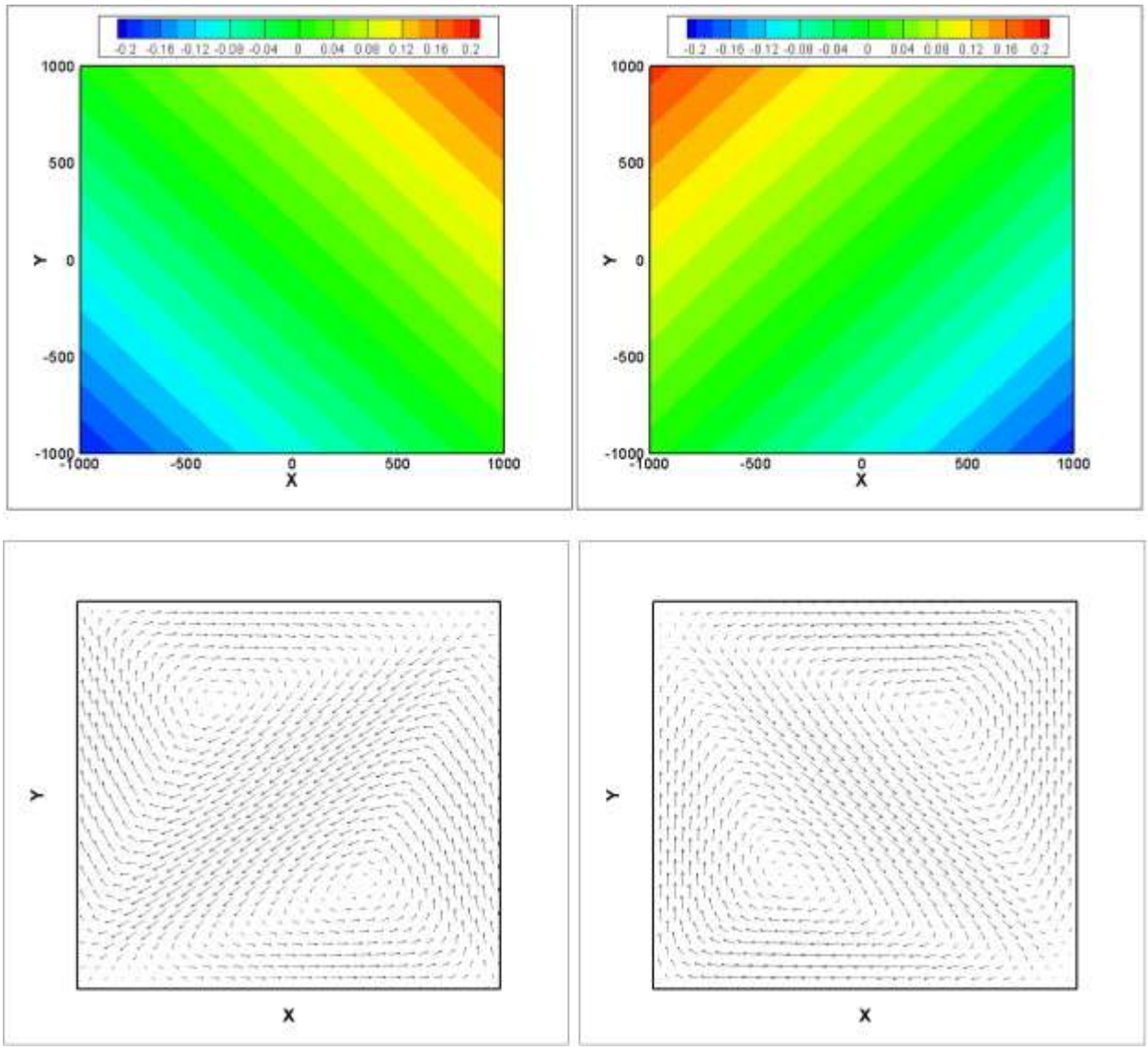

Fig. 3.27 - Steady-state water surface elevation and horizontal velocity field for (left) North-East wind direction at$t$ = 2 h and (right) North-West wind direction at t = 4 h.

The results obtained from the C-grid scheme while the Adams-Bashforth method is used for time marching. Fig. 3.27 shows the steady-state water surface elevation η and horizontal velocity field corresponding to the north-east and north-west wind directions at $t = 2$ hr and $t = 4$ hr, respectively. One can see the flow pattern is as expected where a pair of primary topographic gyres is observed perpendicular to the wind direction.

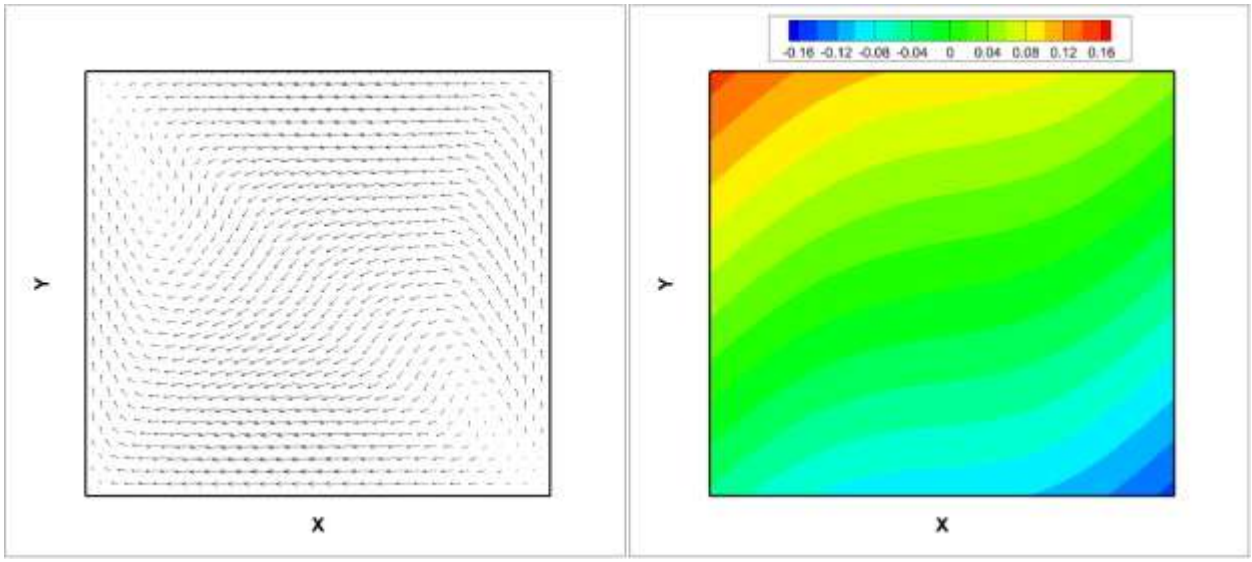

Fig. 3.28 - Horizontal velocity field (left) and water surface elevation (right) after wind direction changes at t = 3 h.

Fig. 3.28 displays the water surface elevation η and the horizontal velocity filed at the transient time when the wind direction changes from north-east to north-west. As can be seen, the results are free of spurious modes and demonstrate the ability of the proposed scheme in simulations of wind-induced circulation with an uneven bathymetry.

3.6. Discussion and Conclusion

While the finite volume triangular classic C-grid scheme is employed in many numerical models and is very common, the current study seems to be the first one of the dispersion relation analysis of this spatial scheme. In this paper, the numerical solution of two-dimensional linearized shallow water equations is assessed. First, the dispersion relation of a semi-discrete scheme was obtained for shallow water system and then analyzed. The results showed that the dispersion relation of the spatial scheme is purely real; i.e., there is no imaginary part. Therefore, all waves, including long and short waves, were not damped in the numerical solution. The phase speed ratio was also close to one for the long and intermediate waves. However, the spatial scheme decelerates the shorter waves. Despite

the fact that the short waves do not transfer much energy in the domain, since they are not effectively damped by the numerical scheme they may lead to oscillatory results.

In the second section, the fully discrete schemes are analyzed. They were developed based on the proposed combination of three different temporal schemes: namely, the forward Euler, Leap-Frog and Adams-Bashforth methods, with the C-grid spatial discretization scheme. In fact, the implementation of various time-stepping methods can change the semi-discrete performance. For all numerical schemes, with a small CFL number (CFL=0.1) the phase speed ratio is very close to the semi-discrete one.

In regard to the amplification factor, for the forward Euler scheme we have $|E| > 1$, which means that the scheme is not stable unless there is a small CFL number. The dispersion relation analysis for the Leap-Frog method showed that the time-stepping scheme improves the phase speed behavior of the spatial discretization and makes it much closer to one for a wide range of wavelengths, including the shorter waves. In addition, the amplification factor is almost equal to 1, which shows that the numerical scheme does not damp the results. For higher CFL numbers (CFL=0.9), the Leap-Frog scheme accelerates the intermediate waves, while it is very close to one for long waves. The Adams-Bashforth scheme exhibits higher phase speed errors with higher CFL numbers (CFL>0.1) for a wider range of wave lengths, including the intermediate waves. However, the results show that it could also damp the results for shorter waves.

Three numerical tests were performed in order to first confirm the analytical results and, second, assess the convergence rate and accuracy of the proposed fully discrete methods. The first experiment was intended to confirm the results of analytical dispersion results by propagating a pure gravity wave in a channel. The results of the test showed that the wave front propagated at the same speed as the analytical results indicated. In addition, it showed the dispersion effects prior to the front, which confirms that numerical schemes decelerate the waves ($C_r \leq 1$). It also showed that by increasing the CFL number, the oscillation decreases for the Leap-Frog scheme, while it increases for the Adams-Bashforth scheme. This clearly confirmed the analytical dispersion results. In the second test, a seiche in a rectangular closed basin was simulated as an example of shallow water waves. The results

of the numerical methods were compared with the exact solution. The results were examined with different wave numbers, and showed that the phase speed error increases for the shorter waves, as the analytical analysis indicated. However, the results showed that the phase speed error for the shorter waves with higher CFL numbers is decreased using the Leap-Frog time-stepping technique. In the third numerical test, numerical schemes were implemented for simulation of a pure gravity wave with Gaussian initial distribution. The results of both the Leap-Frog and Adams-Bashforth methods were compared to the analytical Bessel function solution and they were in good agreement. The spatial and temporal evolutions of the numerical solution were estimated based on the L^2error. The results showed that the proposed combination of spatial and temporal techniques converges, while the time step and spatial step decrease. In addition, the results showed that the error of the Adams-Bashforth scheme is lower and that the Leap-Frog scheme is stable for higher CFL numbers. The above analysis shows how the proposed method can help either in assessing the performance of the spatial discretization techniques or in the selection of the time-stepping technique in combination with it. In addition, the results of non linear tests confirm the ability of the C-grid approach, in the proposed combination with the Adams-Bashforth time stepping technique, to simulate the non-linear behavior of shallow water flows.

To summarize, the following points should be emphasized on to highlight the contributions of this study: (i) Finite volume unstructured C-grid scheme was analyzed based on dispersion relation for the semi-discrete case, (ii) The effects of Adams-Bashforth and Leap-Frog time-stepping methods on the behaviour of the C-grid scheme were investigated using the dispersion relation analysis, (iii) Results showed that the Leap-Frog improves the phase speed behaviour of the C-grid semi-discrete scheme, (iv) The Adams-Bashforth method was shown to be more accurate, while the Leap-Frog is more stable for higher CFL numbers, (v) The effect of the grid structure was investigated considering perturbed organized-unstructured grids as well as fully-unstructured grids, (vi) The asymptotic order of accuracy of the both linear and non-linear cases were estimated for various grid types and (vii) The behaviour of proposed scheme was found to be satisfactory for the various

numerical examples with consideration of various source terms which are of essential importance in practical applications.

Appendix

Considering the bottom topographical changes, the nonlinear shallow water equations in presence of surface wind stress and bed friction terms are as follows:

$$\frac{\partial \eta}{\partial t} + \frac{h_t}{A_i}\sum_{j=1}^{3} U_j d_j = 0 \quad \text{(A.1)}$$

$$\frac{\partial (h_t U)}{\partial t} + h_t(\boldsymbol{n}\cdot\boldsymbol{u}\nabla\boldsymbol{u}) + g h_t \frac{\partial(\eta)}{\partial n} = \frac{1}{\rho}(\boldsymbol{\tau} - \tau_{bx} n_x - \tau_{by} n_y) \quad \text{(A.2)}$$

with,

$$h_t = h_s + \eta \quad \text{(A.3)}$$

where h_t is the total depth, h_s is the still water depth at the basin, τ_{bx} and τ_{by} are bed friction stresses, $\boldsymbol{\tau} = (\tau_x, \tau_y)$ is the surface wind stress vector, and ρ is water density.

In order to take into account the bottom topographical changes, we estimate the gradient term in (A.2) as follows (Skoula 2006):

$$g h_t \frac{\partial(\eta)}{\partial n} = g\eta \frac{\partial(h_s\ )}{\partial n} + \frac{1}{2} g \frac{\partial(\eta^2 + 2\eta h_s)}{\partial n} \quad \text{(A.4)}$$

the nonlinear advection term of the momentum equation at cell face *j* can be discretized as follows:

$$(\boldsymbol{n}\cdot\boldsymbol{u}\nabla\boldsymbol{u})_j = \frac{1}{D_j}(d_{1j}^* C_1 + d_{2j}^* C_2) \quad \text{(A.5)}$$

Where d_{1j}^* and d_{2j}^* are thedistances between face *j* and the centers of cells 1 and 2 which share face j, respectively. Cis defined as the component of advection of momentum in the

direction of the normal vector $\boldsymbol{n}_j$ within cell i and is obtained by integrating the advection term over the cell area to yield:

$$C_i = \frac{1}{A_i}\sum_{m=1}^{3} \boldsymbol{n}_j \boldsymbol{u}_m U_m d_m \tag{A.6}$$

In equation (A.6), the u and v components of Cartesian velocity vector $\boldsymbol{u} = (u, v)$ are required at the cell faces. To this end, first the approximation of the velocity vector at the cell center $\boldsymbol{u}_i$ is required:

$$\boldsymbol{u}_i = \frac{1}{A_i}\sum_{j=1}^{3} \boldsymbol{n}_j U_j d_j d_{ij}^* \tag{A.7}$$

Then, $\boldsymbol{u}_j$ is given by a linear interpolation of the velocity vectors at the cell centers on either side of face j:

$$\boldsymbol{u}_j = \frac{1}{D_j}(d_{2j}^* \boldsymbol{u}_1 + d_{1j}^* \boldsymbol{u}_2) \tag{A.8}$$

It should be noted that wherever the total depth value is required at the cell face j, we use a linear interpolation of the total depths at the center of cells $i = 1,2$ which share the face j:

$$(h_t)_j = \frac{1}{D_j}(d_{1j}^* h_{t_1} + d_{2j}^* h_{t_2}) \tag{A.9}$$

Chapter 4

Dispersion Relation Analysis of Finite Volume Triangular C-grid Scheme for Shallow Water Equations with Coriolis Force[3]

Abstract

An ideal numerical model for ocean modelling should be able to simulate various types of waves and currents. The Coriolis term has an essential impact on the generation and derivation of many inertia-gravity waves as well as slow Rossby waves which propagate slowly and transfer considerable amount of energy through the oceans. Obtaining a balance between Coriolis force and other forces such as wind stress, bottom friction and gravity is very challenging and of essential importance. Generally, typical upwind finite volume methods are not capable of simulating these balances. From the dispersion analysis of the finite difference structured C-grid scheme it has been shown that the Coriolis mode leads to spurious numerical solutions. In this paper, dispersion analysis is employed in order to investigate the finite volume triangular C-grid scheme in shallow water equations for various types of triangles that may appear in an arbitrary triangular grid. In the presence of the Coriolis term, an improvement for triangular C-grid scheme is shown over the rectangular one for both low and high resolution cases. Moreover, we analyze the performance of triangular C-grid in combination of various time stepping techniques such as Adams-Bashforth, Leap-Frog and Improved Euler. Results show that the Leap-Frog scheme can improve the behaviour of the semi discrete method, specially for the higher CFL number. By considering various source terms in the shallow water equations, such as surface wind stress, bottom friction and uneven bottom topography, the proposed scheme is examined through different linear and non-linear numerical examples. The results confirm the theoretical analysis and demonstrate that the model can preserve the analytical solutions without considerable damping, even for long slow waves. The obtained results

[3]This part of the study has been published as: **H. Shirkhani**, A. Mohammadian, O. Seidou, H. Qiblawey, "Dispersion Relation Analysis of Finite Volume Triangular C-grid Scheme for Shallow Water Equations with Coriolis Force", 2015, (Submitted).

show the ability of the proposed finite volume C-grid scheme to obtain a balance between the Coriolis force and other forces to simulate various oceanic waves.

Keywords: *Shallow water equations, Dispersion relation analysis, Finite volume triangular C-grid, Coriolis Force, Ocean waves.*

4.1. Introduction

In recent years much attention has been paid to ocean modelling as an essential requirement in coastal and environmental engineering. In particular, various oceanic waves such as gravity, inertia and inertia-gravity waves play an important role in ocean models. Indeed, an ideal ocean model needs to be capable of simulating a wide range of oceanic waves. Shallow water equations are of essential interest and have considerable application for modelling oceanic waves. In numerical modelling of shallow water equations, one needs to couple the momentum and continuity equations. In order to do so, there are many possibilities of variable placement for certain choice of grids. Choosing the location of the variable is a delicate problem since may lead to spurious oscillation in the numerical solutions (Le Roux et al. 2007). Mesinger and Arakawa (1976) proposed various staggered grids. These grids were analyzed, and among them, the C-grid was found to be promising (Akawara and Lamb 1977; Walters and Carey 1984). There has been an increased trend in using the C-grid approach with different numerical schemes such as finite difference, finite element and finite volume (Casulli and Walters 2000; Walters et al. 2009; Walters and Casulli 2001; Popinet and Rickard 2009). The C-grid approach has been widely used in different oceanic models such as Princeton Ocean Model (Blumberg and Mellor 1987), MICOM (Bleck and Smith 1990), MIKE3HS (Pietrzak et al. 2002), MITgcm (Marshall et al. 1997; Adcroft et al. 2004), ROMS (Shchepetkin and McWilliams 2003; 2005) and UnTRIM (Jankowski, 2007; 2009).

Using the dispersion relation and Fourier analyses, one can investigate the effect of choosing variable location in the different discretization schemes. Indeed, an ideal numerical scheme should be able to preserve the analytical quantities of the dispersion relation. The Fourier and dispersion relation analyses have been used for shallow water equations for a wide range of numerical methods such as finite difference (Adcroft 1999;

Sankaranarayanan and Spaulding 2003), finite element (Le Roux and Pouliot 2006; Le Roux 2005) and finite volume methods (Gossard and Kolar 2000; Mohammadian 2010; Bernard et al. 2009).

Dispersion relation analysis of finite difference C-grid on structured rectangular were well investigated and documented. Dukowicz (1995) obtained the dispersion relation of various grids, including the C-grid, for inertia-gravity waves in term of accuracy. Adcroft et al. (1999) performed dispersion relation analysis for a finite difference C-grid and reported spurious modes due to the Coriolis term. They suggested a new treatment by augmenting the C-grid variables using D-grid ones, and they proposed the CD-grid. Le Roux (2005) used dispersion relation analysis for the finite element method and compared the results to a finite difference C-grid and CD-grid. He reported poor behaviour of finite difference structured C-grid in modelling inertia-gravity waves due to the Coriolis mode, particularly for low-resolution grids. Using dispersion relation analysis, Thuburn (2007) also reported that there are artificial slowing for inertial waves in the numerical results for the finite difference structured C-grid. He showed that numerical Rossby wave dispersion is sensitive to the details of the discretization of the Coriolis terms. Rostand and Le roux (2008) and Le roux et al. (2007) analyzed the RT0 finite element for shallow water equations and reported the difficulties associated with that method. Shirkhani et al. (2014) investigated the behaviour of the Finite volume triangular C-grid scheme for the shallow water equations. They investigated fast gravity waves and reported good performance of the numerical model for both linear and non-linear cases. However, to the best knowledge of the authors, the behaviour of the finite volume triangular C-grid in presence of Coriolis term has not been analyzed.

The main objective of this paper is to analyze the finite volume triangular C-grid scheme in presence of Coriolis term. In line with this goal, the linear shallow water equations with the Coriolis term, which has an essential role in large scale ocean modelling, are considered. In order to generalize the study, we consider isosceles triangular cells with various vertex angles that may represent a general sketch of an arbitrary triangular grids. The results of the semi discrete method analysis are compared first with the analytical one, which belongs to the continuous case, and second, with those of finite difference C-grid method. We then

analyze the behaviour of the semi-discrete scheme in combination of various well-known second-order time stepping techniques such as Adams-Bashforth, Leap-Frog and Improved Euler. Then, we examine the theoretical analysis and the performance of the proposed scheme through a number of numerical examples of both linear and non-linear shallow water equations. In addition to the Coriolis force, we consider wind stress, bottom friction and un-even topographical changes that are of essential importance in ocean modelling and practical applications.

Dispersion relation analysis confirms that the performance of the finite volume triangular C-grid scheme improves significantly compared to the finite difference C-grid. In addition, the results of the numerical experiments verify the theoretical analysis and show the capability of the proposed scheme in the simulation of both fast-short and slow-long oceanic waves. The results show that Leap-Frog time stepping technique is more stable and can also improve the behaviour of the semi-discrete method specially for higher CFL numbers. The results confirm that the proposed method is able to correctly take into account the effect of Coriolis force as well as other important terms in momentum equation. Moreover, it is shown that the proposed scheme also performs well for the non-linear shallow water equations.

The current paper is organized as follows. In Section 2 the linear and non-linear shallow water equations are introduced along with their dimensionless forms. Section 3 describes the finite volume triangular C-grid method used for spatial discretization. as well as the second-order Adams-Bashforth time-stepping technique. The dispersion relation analysis is shown in Section 4, and the proposed model is examined through the various numerical examples in Section 5. We finish the paper by remarking on the conclusions in Section 6.

4.2. Shallow water equations

In this section, we present the linear and non-linear versions of shallow water equations as well as their non-dimensional forms. The two-dimensional inviscid linear form of shallow water equations in Cartesian coordinates and in the presence of the Coriolis term can be written in the following form:

$$\frac{\partial \eta}{\partial t} + H\nabla \boldsymbol{u} = 0 \tag{4.1}$$

$$\frac{\partial \boldsymbol{u}}{\partial t} + f\boldsymbol{k} \times \boldsymbol{u} + g\nabla\eta = 0 \tag{4.2}$$

whereη stands for the surface elevation,u and v are the components of thedepth-averaged velocity vector $\boldsymbol{u} = (u, v)$ in the $x -$ and $y -$directions,f is the Coriolis parameter, $\boldsymbol{k}$ is a unit vector in thevertical direction,g is the gravitational acceleration, H is the reference depth of the water, and ∇ is the two-dimensional gradient operator. Since the main focus of this paper is on oceanic surface waves, we consider the Coriolis term, which plays an important role in the derivation of those waves. However, Equation (4.2) may include various source terms such as bed friction, wind stress and topographical changes. We will consider these terms in Section 5, where we examine the proposed method through various numerical examples.

In order to take the Coriolis term into account, the β-plane approximation is considered:

$$f = \beta y \tag{4.3}$$

where$y$is the meridional distance from the equator, and β, the linear coefficient of the variation of $f$with respect to y, is defined as follows:

$$\beta = \frac{2\Omega}{a} = 2.29 \times 10^{-11}\,\frac{1}{ms} \tag{4.4}$$

where Ωis the angular frequency of the Earth's rotation and $a$is the mean radius of the Earth.

In some numerical examples in this paper we employ the dimensionless form of the shallow water equations. Equations (4.1) and (4.2) on an equatorial β-plane can be stated in the dimensionless form using dimensionless variables $x' = x/L^*$, $y' = y/L^*$, $t' = t/T^*$, $\boldsymbol{u}' = \boldsymbol{u}/U^*$ and $\eta' = \eta/H$. Using the Lamb parameter $E = \frac{4\Omega^2 a^2}{gH}$, the characteristic length (L^*), time (T^*), and velocity (U^*) can be written as:

$$L^* = \frac{a}{E^{\frac{1}{4}}}$$

$$T^* = \frac{E^{\frac{1}{4}}}{2\Omega} \tag{4.5}$$

$$U^* = \sqrt{gH}$$

The non-linear shallow water equation read:

$$\frac{\partial \eta}{\partial t} + \nabla[(\mathrm{H} + \eta)\boldsymbol{u}] = 0 \tag{4.6}$$

$$\frac{\partial \boldsymbol{u}}{\partial t} + \boldsymbol{u}\nabla\boldsymbol{u} + f\boldsymbol{k} \times \boldsymbol{u} + g\nabla\eta = 0 \tag{4.7}$$

where$(\mathrm{H} + \eta)$ is the total fluid depth and $\boldsymbol{u}\nabla\boldsymbol{u}$is the non-linear advection term considered in the momentum equation. Similar to the linear shallow water equations, the non-linear model can also be converted into the dimensionless form on an equatorial β-plane by using dimensionless variables $x' = x/L^*$, $y' = y/L^*$, $t' = t/T^*$, $\boldsymbol{u}' = \boldsymbol{u}/U^*$, and $\eta' = \eta/H$, with characteristic parameters defined by Equation (4.5).

4.3. Finite Volume Triangular C-grid Method

In this section, the finite volume C-grid used for spatial discretization is introduced. We discretize the non-linear shallow water equations (4.6)-(4.7), which have a more general form and can be easily reduced to the linear model.

4.3.1. Momentum equation

In the C-grid approach, surface elevation is located at the cell's circumcenter, while the normal velocities are considered at the cell mid-edges; see Fig. 4.1a. To obtain the equations for the normal component of momentum at each edge, the dot product of the edge normal vector$\boldsymbol{n} = (n_x, n_y)$ will be taken with the momentum equation (4.7), which leads to:

$$\frac{\partial U}{\partial t} + \boldsymbol{n} \cdot \boldsymbol{u}\nabla\boldsymbol{u} + fvn_x - fun_y + g\frac{\partial \eta}{\partial n} = 0 \tag{4.8}$$

Where $\frac{\partial}{\partial n}$ is the edge normal gradient and $U = \boldsymbol{n}.(u, v)$ is the normal velocity defined at the cell edge. The edge normal vector $\boldsymbol{n}$ is defined at the middle of the three different edge

types of each cell. The edge normal gradient of the water surface elevation at each cell mid-edge is defined as follows:

$$(\frac{\partial \eta}{\partial n})_j = \frac{\eta_f - \eta_b}{D_j} \quad (4.9)$$

Where D_j is the distance between the circumcenter of two neighbour cells, $j = 1,2,3$ is the edge type index, and f provides the index of the cell in the direction of $\boldsymbol{n}_j$, while b provides the index for the cell in the opposite direction(Fig. 4.1b).

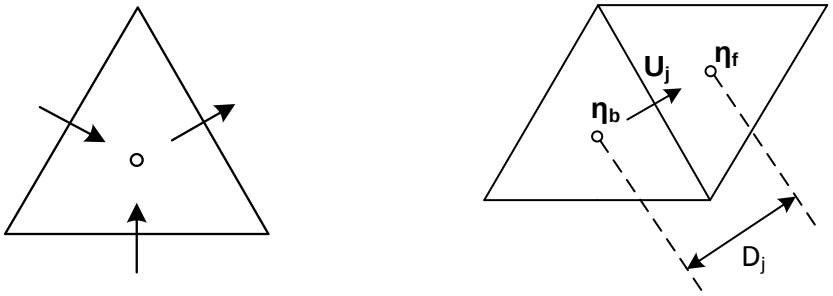

Fig. 4.1 – (a) Normal velocity and water surface elevation locations are presented by the symbols ∘ and →, respectively. (b) Estimation of normal gradient of water surface elevation at face j

Following the work of Fringer et al. (2006),Casulli and Zanolli (2002), Perot (2000), Casulli (1999), and, the nonlinear advection term of the momentum equation at cell face j can be discretized as follows:

$$(\boldsymbol{n} \cdot \boldsymbol{u} \nabla \boldsymbol{u})_j = \frac{1}{D_j}(d_{1j}^* C_1 + d_{2j}^* C_2) \quad (4.10)$$

Where d_{1j}^* and d_{2j}^* are thedistances between face j and the centers of cells 1 and 2 which share face j, respectively. Cisdefined as the component of advection of momentum in the direction of the normal vector $\boldsymbol{n}_j$ within cell i and is obtained by integrating the advection term over the cell area to yield:

$$C_i = \frac{1}{A_i} \sum_{m=1}^{3} \boldsymbol{n}_j \boldsymbol{u}_m U_m d_m \quad (4.11)$$

In equation (4.9), the u and v components of Cartesian velocity vector $\boldsymbol{u} = (u, v)$ are required at the cell faces. These are also needed for Coriolis terms in momentum equation (4.8). To this end, first the approximation of the velocity vector at the cell center $\boldsymbol{u}_i$ is required:

$$\boldsymbol{u}_i = \frac{1}{A_i}\sum_{j=1}^{3} \boldsymbol{n}_j U_j d_j d_{ij}^* \tag{4.12}$$

Then, $\boldsymbol{u}_j$ is given by a linear interpolation of the velocity vectors at the cell centers on either side of face j:

$$\boldsymbol{u}_j = \frac{1}{D_j}(d_{2j}^* \boldsymbol{u}_1 + d_{1j}^* \boldsymbol{u}_2) \tag{4.13}$$

4.3.2. Continuity Equation

If A_i is the area of the triangular cell, continuity equation (4.6) also can be discretized in the following form:

$$\frac{\partial \eta}{\partial t} + \frac{[H+\eta]}{A_i}\sum_{j=1}^{3} U_j d_j = 0 \tag{4.14}$$

where d_j is the length of the jth side of the cell and U_j is the normal component of velocity at the jth side. The discrete form of linear continuity equation (4.1) can also be written as:

$$\frac{\partial \eta}{\partial t} + \frac{H}{A_i}\sum_{j=1}^{3} U_j d_j = 0 \tag{4.15}$$

4.4. Dispersion relation of continuous case

For the purpose of dispersion relation analysis, it suffices that we consider the linear shallow water equations (4.1) and (4.2). Because the governing equations are linear, by considering the behaviour of one Fourier mode, the solution can be studied. Thus, the solutions in the form of $u = \tilde{u}e^{i(kx+ly+\omega t)}$, $v = \tilde{v}e^{i(kx+ly+\omega t)}$, and $\eta = \tilde{\eta}e^{i(kx+ly+\omega t)}$ are sought, where k and l are the wave numbers in the $x-$and $y-$ directions, respectively. Replacing the wave form of u, v, and η in governing equations (4.1) and (4.2) results in a square matrix for the amplitudes $\tilde{u}, \tilde{v}$, and $\tilde{\eta}$. For a nontrivial solution, the determinant of the matrix should be equal to zero, which leads to a relationship between the wave

numbers k and l and the frequency ω. The relationship is called the dispersion relation and is obtained as follows:

$$\omega\left(\omega^2 - f^2 - gH(k^2 + l^2)\right) = 0 \tag{4.16}$$

The first solution is $\omega = 0$, which corresponds to the geostrophic mode that matches to the slow Rossby mode on a β-plane, and the other two solutions are as follows:

$$\omega_{AN} = \pm\sqrt{f^2 + gH(k^2 + l^2)} \tag{4.17}$$

In which ω_{AN} stands for the analytical solution and corresponds to the inertia-gravity mode. As equation (4.18) shows, $\omega_{AN}$is purely real, and therefore all modes are naturally stable and neither amplify nor decay.

4.5. Dispersion relation of semi-discrete finite volume triangular C-grid

For dispersion analysis of the semi-discrete case, we consider various isosceles triangle cells with different vertex angles, as is shown in Fig. 4.2a. Note that, as Fig. 4.2b shows, the employed grid cells for dispersion relation analysis, which are isosceles triangles with different vertex angles, as proxies can adequately represent the behaviour of an arbitrary triangular grids.

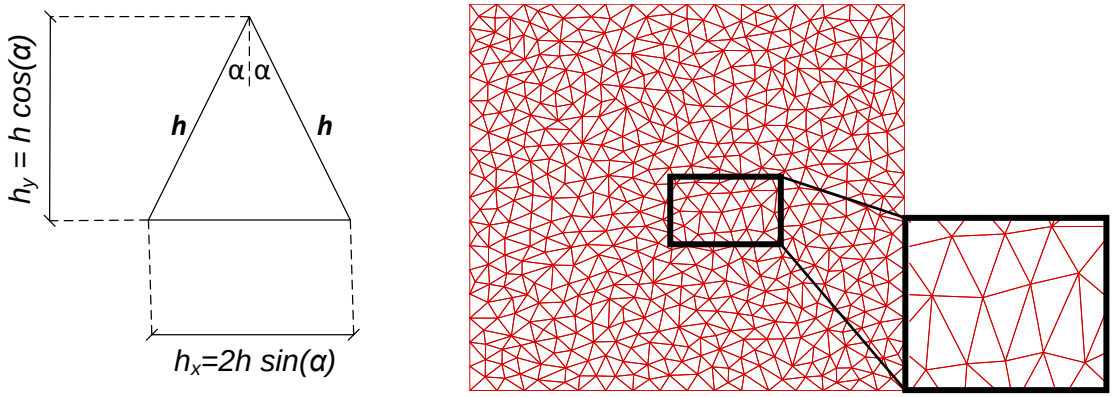

Fig. 4.2- Isosceles triangle cell grid with vertex angle α and side length of h (right) anda sample of fully unstructured mesh grid (right) which can be generally represented by grid cell shown in (a) with various values of α.

Considering the continuity equation (4.15) as well as momentum equation (4.8) without taking into account the non-linear advection term $\boldsymbol{n}\cdot\boldsymbol{u}\nabla\boldsymbol{u}$, we can use Fourier analysis similar to the continuous case in order to find the dispersion relation corresponds to the discrete form. The discrete solutions corresponding to $U=\widetilde{U}e^{i(kx_j+ly_j+\omega t)}$ and $\eta=\tilde{\eta}e^{i(kx_j+ly_j+\omega t)}$ are sought, where $\widetilde{U}$ and $\tilde{\eta}$ are amplitudes, and (x_j,y_j) coordinates are expressed in terms of distance to a reference circumcenter.

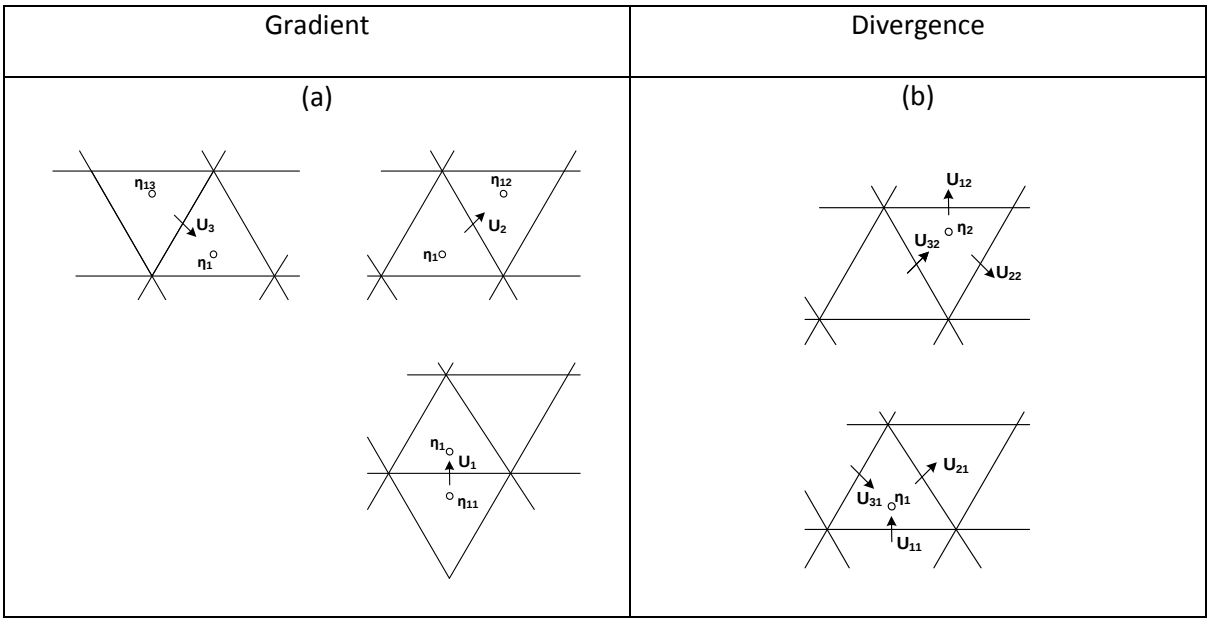

Fig. 4.3 - (a) Three possible location of normal velocity of gradient and (b) Two possible location for water surface elevation in the divergence stencils of the C-grid spatial discretization

As is shown in Fig. 4.3a,the normal velocity *U* may be located on three possible edge types; i.e., either on the horizontal one or the other two biased ones. Using the linear version of (4.8) along with (4.12) and (4.13), discrete forms of three possible normal velocities can be obtained as follows,

$$U_1^t+\left(fv_1^n fn_{x1}-fu_1^n n_{y1}\right)\quad+\frac{g}{hD_1}(\eta_1-\eta_{11})\quad=0$$

$$U_2^t + \left(fv_2^n fn_{x2} - fu_2^n n_{y2}\right) \quad + \frac{g}{hD_2}(\eta_{12} - \eta_1) \quad = 0 \tag{4.18}$$

$$U_3^t + \left(fv_3^n fn_{x3} - fu_3^n n_{y3}\right) \quad + \frac{g}{hD_3}(\eta_1 - \eta_{13}) \quad = 0$$

with$D_1 = \frac{2\cos\alpha^2 \ -1}{\cos\alpha}$ and $D_2 = D_3 = \frac{\sin\alpha}{\cos\alpha}$.

Similarly, as can be seen in Fig. 4.3b,the water surface elevation can be placed at two different locations. Using equation (4.15) we have:

$$\eta_1^t + \frac{H}{|T|}h(-U_{11}2\sin\alpha + U_{21} - U_{31}) \quad = 0$$

$$\eta_2^t + \frac{H}{|T|}h(U_{12}2\sin\alpha + U_{22} - U_{32}) \quad = 0 \tag{4.19}$$

where$|T| = h^2 \sin\alpha\cos\alpha$ is the cell area and we generally have $\varphi^t = \frac{\partial\varphi}{\partial t}$.

Using equations (4.12) and (4.13) and by substituting the periodic solution of $\widetilde{U}$ and $\tilde{\eta}$ into the discrete equations (4.18) and (4.19),one can obtain a square matrix system of amplitudes as:

$$\begin{pmatrix} i\omega I_2 & \frac{H}{h}A \\ \frac{g}{h}B & i\omega I_3 + fD \end{pmatrix}\begin{pmatrix} \vec{\widetilde{U}} \\ \vec{\tilde{\eta}} \end{pmatrix} = \begin{pmatrix} 0 \\ 0 \end{pmatrix} \tag{4.20}$$

where $\vec{\widetilde{U}} = \left(\widetilde{U}_1, \widetilde{U}_2, \widetilde{U}_3\right)$, $\vec{\tilde{\eta}} = (\tilde{\eta}_1, \tilde{\eta}_2)$, and I_n is the $n \times n$ identity matrix, and we also have:

$$A = \frac{1}{\sin\alpha\cos\alpha}\begin{pmatrix} -a & 2\sin\alpha & b & c \\ \frac{1}{a}2\sin\alpha & & -\frac{1}{b} & -\frac{1}{c} \end{pmatrix}, B = \begin{pmatrix} \frac{1}{D_1} & 0 & 0 \\ 0 & \frac{1}{D_2} & 0 \\ 0 & 0 & \frac{1}{D_3} \end{pmatrix}\begin{pmatrix} \frac{1}{a} & -a \\ -\frac{1}{b} & b \\ -\frac{1}{c} & c \end{pmatrix},$$

$$D = \frac{1}{2}\begin{pmatrix} 0 & \mu_1 \cos(\frac{kh_x + 2lh_y}{4}) & -\mu_2 \cos(\frac{kh_x - 2lh_y}{4}) \\ -\mu_1 \cos(\frac{kh_x + 2lh_y}{4}) & 0 & -2\mu_3 \cos(\frac{kh_x}{4}) \\ \mu_2 \cos(\frac{kh_x - 2lh_y}{4}) & 2\mu_3 \cos(\frac{kh_x}{4}) & 0 \end{pmatrix},$$

with:

$a = e^{-ilh_y \frac{D_1}{2\cos\alpha}}$, $b = e^{\frac{i}{2}(\frac{kh_x}{2} - lh_y D_1)}$, $c = e^{-\frac{i}{2}(\frac{kh_x}{2} + lh_y D_1)}$

$\mu_1 = \mu_2 = \frac{1}{\cos\alpha}$, $\mu_3 = \frac{\sin\alpha}{\cos\alpha}$

The dispersion relation then can be obtained by setting the determinant of the 5×5 matrix system (4.20) to zero. The dispersion relation will be a polynomial of degree 5 with the following form:

$$c_5\omega^5 + c_4\omega^4 + c_3\omega^3 + c_2\omega^2 + c_1\omega + c_0 = 0 \quad (4.21)$$

where coefficients $c_0, c_1, \dots, c_5$ are functions of kh_x and lh_y. In order to investigate the dispersion relation for various vertex angle, we consider three different cases, namely, $\alpha = \pi/6$, $\alpha = 5\pi/24$, $\alpha = \pi/8$.

4.5.1. Case1: $\alpha = \pi/6$

In this case, which leads to an equilateral triangle, c_4, c_2 and c_0 are zero in (4.22) that implies $\omega = 0$ is one the roots which corresponds to the slow Rossby wave and is identical to the continuous case (4.17). The other roots are obtained as follows:

$\omega_1 = 0,\ \omega_{2,3} = \pm O(1),\ \omega_{4,5} = \pm O(\frac{1}{h})$.

In the limit as mesh spacing $h \to 0$ we can obtain:

$$\omega_{2,3} = \omega_{AN} + O(h^2),\ \omega_{4,5} = \pm\frac{2\sqrt{6GH}}{h} + O(h) \quad (4.22)$$

As one can see, $\omega_{2,3}$ correspond to a continuous solution, while $\omega_{4,5}$ can be considered as spurious modes. The explicit form of the dispersion relation for the semi-discretized equations is, however, too long to be written, and will be shown and discussed graphically.

4.5.2. Cases 2 and 3: $\alpha = 5\pi/24$ and $\alpha = \pi/8$

In this part, we consider the isosceles triangles with different vertex angles. The five roots of the dispersion relation are obtained as follows:

$$\omega_1 = O(h),\ \omega_{2,3} = \pm O(1),\ \omega_{4,5} = \pm O(\tfrac{1}{h}). \tag{4.23}$$

In these cases, the coefficient $c_0 \neq 0$ in (4.22) and therefore the dispersion relation will not admit $\omega = 0$ as one of the solutions anymore. This implies that the slow mode of the discretized method is not identical to the continuous case(4.17) and it may lead to spurious mode. However, the mode is expected to be small and bounded. Moreover, despite to the equilateral triangle in the first case, the inertia-gravity modes $\omega_{2,3} = \pm O(1)$ do not coincide with the continuous case for infinitesimal mesh spacing i.e. $h \to 0$. The $\omega_{4,5}$also correspond to the spurious mode.

4.6. Analysis of semi-discrete method

In order to analyse the obtained dispersion relations of the semi-discrete triangular C-grid for various triangle cases, we compare the behaviour of their non-dimensional frequency (ω/f) with those corresponding to the continuous case. Moreover, we reproduce the results of the dispersion relation analysis for the finite-difference rectangular structured C-grid scheme in order to compare it with the behaviour of the triangular schemes. To this end, by defining the Rossby radius as $\lambda = \sqrt{gH}/f$, we can rewrite the continuous dispersion relation (4.16) as follows:

$$\left(\frac{w}{f}\right)^2 = 1 + \left(\frac{\lambda}{h}\right)^2 [(kh)^2 + (lh)^2] \tag{4.24}$$

The dispersion relation of an rectangular structured C-grid scheme with square grid cells of size h,corresponding to the inertia-gravity mode can be written as follows (Dukowicz 1994):

$$\left(\frac{w}{f}\right)^2 = \cos^2\frac{kh}{2}\cos^2\frac{lh}{2} + 4\left(\frac{\lambda}{h}\right)^2\left[\sin^2\frac{kh}{2} + \sin^2\frac{lh}{2}\right] \quad (4.25)$$

It must be mentioned that since the mesh spacing in the $x-$ and$y-$ directions are not equal for triangular grids, we define $h^* = \sqrt{2\sin\alpha\cos\alpha}\,h$ and use it to estimate the λ/h^* values. We plot the non-dimensional frequencies along the selected axes which are presented in Fig 4.4. The directions OX nad OY represent the waves ravelling in $x-$ and $y-$ directions where $kh_x = 0$and $lh_y = 0$, respectively. We select diagonal axes $OT1$ and $OT2$ for the triangle case as well as OD1 and OD2 for the rectangle cell for $kh_x = lh_y$, $kh_x = -lh_y$, $kh = lh$ and $kh = -lh$, respectively. We consider two cases, namely low-resolution mesh grids with $\lambda/h = 1/8$ and a high-resolution one with $\lambda/h = 2$. While the values of kh_x and lh_y vary over $[0,\pi]$, the non-dimensional frequency (ω/f) is plotted along the selected axes in Fig. 4.5.

For the high resolution ($left\ column$), one can see that the $O(1)$ which corresponds to the inertia-gravity waves in the continuous solution is monotonic in OX and OY directions for all the triangular cases. In the $OT1$ and $OT2$ directions, the mode in $O(1)$ is almost monotonic except for the kh and lh close to π. It should be noted that for the triangle with $\alpha = 5\pi/24$(or generally for $\alpha > \pi/6$) the maximum value of ω/f along the OX is higher than the other cases and closer to the continuous case while its lower along the OY direction. Similarly, for the triangle with $\alpha = \pi/8$ (or generally for $\alpha < \pi/6$) the maximum value of ω/f along the OY is higher than the other cases and closer to the continuous case while its lower along the OX direction. It is due to the fact that by deviation of vertex angle from $\pi/6$ the triangle lose its symmetry and yields better results only in one direction (which is resolved finer) compared to the equilateral triangle case. However, for all triangle cases in high resolution, since the $O(1)$behaves monotonically as for the continuous case, they are expected to yield accurate results. For the mode in $O(1/h)$, as can be seen, it approximately shows a reflected image of $O(1)$that can be considered as a spurious mode. Again, due to the loss of symmetry for triangles with $\alpha = 5pi/24$and $\alpha = \pi/8$, with respect to the equilateral case with $\alpha = \pi/6$, the mode in $O(1/h)$ is not a perfect image of $O(1)$ in OY and OX directions, respectively. One should

note that as mesh spacing $h \to 0$, only for equilateral triangle case with $\alpha = \pi/6$ the mode in $O(1)$ coincides with the continuous inertia- gravity mode.

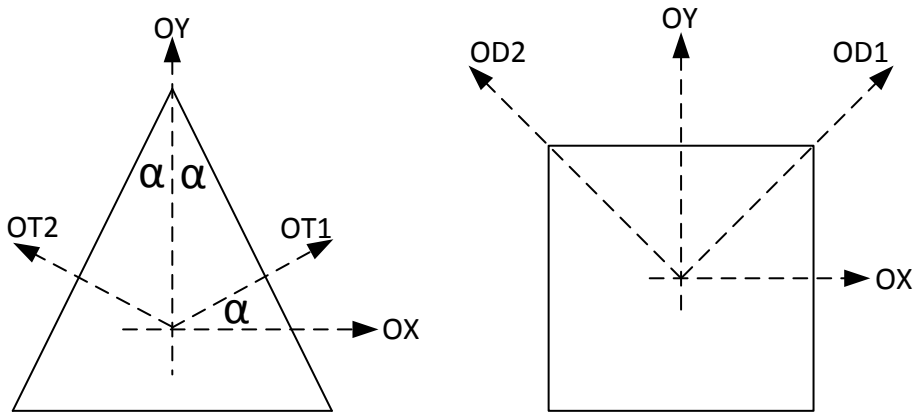

Fig. 4.4 - Selected directions for the triangular (left) and rectangular cell(right)

As it was found from the dispersion relation (4.24), for the triangles with $\alpha = 5\pi/24$ and $\alpha = \pi/8$ (or generally $\alpha \neq \pi/6$) there is no $\omega = 0$ mode which correspond to the slow Rossby (geostrophic) mode while there is a mode in $O(h)$. The mode in $O(h)$, as can be seen in Fig. 4.4, is very close to zero and bounded in all directions for both high and low resolution cases. It suggests that one can consider this $O(h)$mode as a spurious mode which tends to the geostrophic mode as $h \to 0$.

$\frac{\lambda}{h} = 2$	$\frac{\lambda}{h} = \frac{1}{8}$

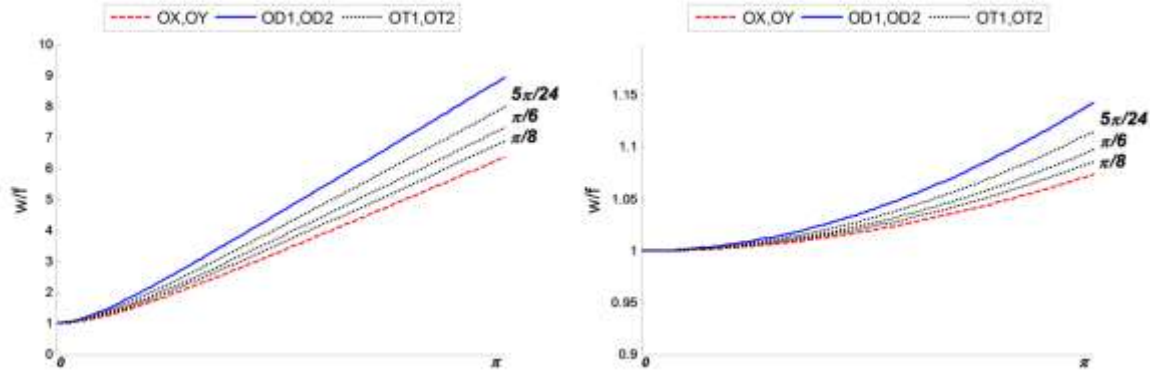

(a)

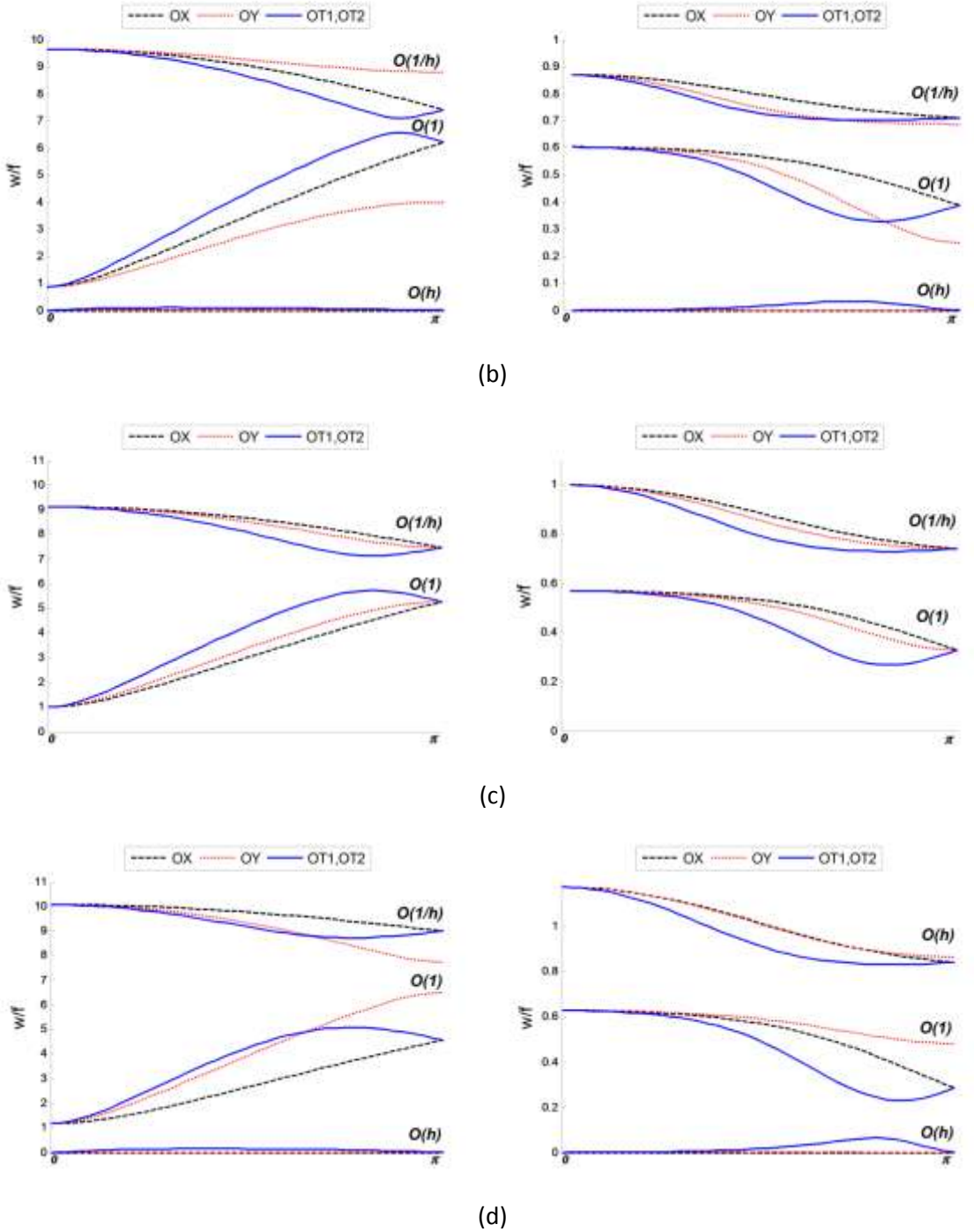

Fig. 4.5 - Dispersion relation results of non-dimensional frequency ω/f for (a) continuous, triangular C-grid with vertex angle of (b) $\alpha = 5\pi/24$, (c) $\alpha = \pi/6$, (d) $\alpha = \pi/8$. Left column ($\lambda/h = 2$) is high resolution and Right column ($\lambda/h = 1/8$) is low resolution.

For the low resolution case (right column), compared to the continuous case, the mode in $O(1)$ exhibits non-monotonic behaviour in kh and lh for all triangular cases in all directions OX, OY, $OT1$ and $OT2$. Indeed, the mode in $O(1/h)$ is closer to the continuous case than the one in $O(1)$. The $O(1)$, however, is likely to yield closer results to the continuous case as λ/h increases.

Numerically, we found that for $\lambda/h = 3/8$ the mode in $O(1)$ starts being monotonic in all directions as for the continuous case. The non dimensional frequency (ω/f) for all triangular cases as well as the structured rectangular (finite difference) case is illustrated in Fig. 4.6. As it can be seen, the mode in $O(1)$ is still not monotonic in all directions for the triangles with $\alpha \neq \pi/6$ as well as the finite difference C-grid. Moreover, the mode in $O(1)$ for triangles with $\alpha \neq 0$ is non-monotonic only in one direction while for structured rectangular case it is non-monomial in both OX and OY direction. In addition, triangular cases hold higher ω/f values compared to the rectangular one. We also found that the $O(1)$ will be monotonic in kh and lh in all directions for the rectangular cases for $\lambda/h \geq 0.50$. It shows that generally, one can expect triangular grids exhibit better performance than the structured rectangular case for the lower resolution.

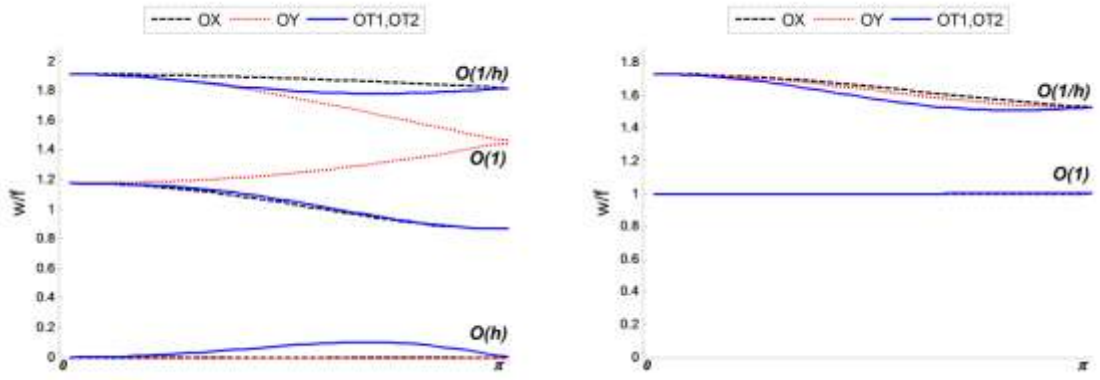

(a) (b)

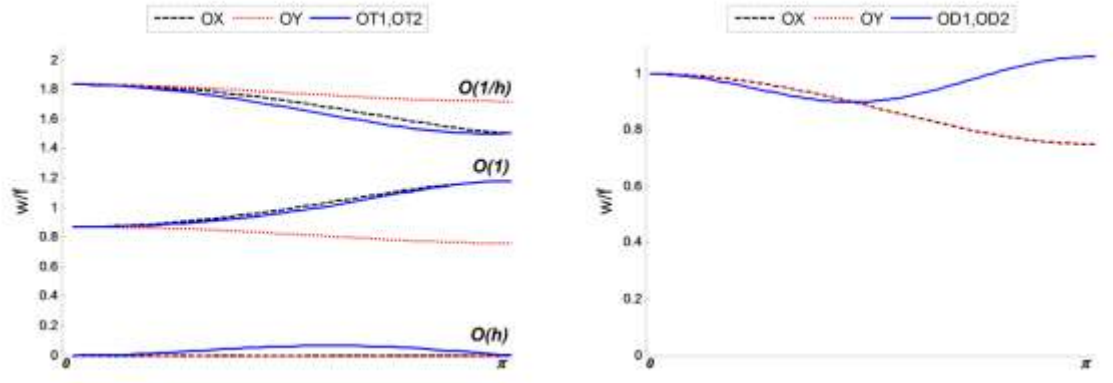

(c) (d)

Fig. 4.6 - Dispersion relation results of non-dimensional frequency ω/f with $\lambda/h = 3/8$ for triangular C-grid with vertex angle of (a) $\alpha = 5\pi/24$, (b) $\alpha = \pi/6$, (c) $\alpha = \pi/8$ and (d) structured rectangular C-grid.

4.7. Fully-discrete Schemes

A Fourier analysis is now conducted to analyse the performance of the fully discretized finite volume triangular C-grid in combination with various time stepping techniques. Here, we employ three well-known second order temporal schemes, namely Improved Euler, Leap-Frog and Adams-Bashforth methods. To this end, first, by using various temporal schemes in combination with the C-grid spatial scheme, the governing equations (4.1) and (4.2) are discretized. Then, by submitting the periodic solution of the form $U = \tilde{U}e^{i(kx_j+ly_j+\omega t)}$ and $\eta = \tilde{\eta}e^{i(kx_j+ly_j+\omega t)}$ into the discretized form and vanishing the matrix, we can obtain the corresponding dispersion relation.

4.7.1. Improved Euler Scheme

Improved Euler method is an explicit predictor-corrector technique which tries to combine the advantages of the simplicity of Euler explicit method with the improved stability and accuracy of implicit methods. For the ordinary differential equation $\frac{d\boldsymbol{C}}{dt} = \emptyset(\boldsymbol{C}, t)$, it reads:

$$\boldsymbol{C}_1^{n+1} = \boldsymbol{C}^n + \Delta t\emptyset \quad (\boldsymbol{C^n}, \mathrm{t_n})$$

$$\boldsymbol{C}_2^{n+1} = \boldsymbol{C}^n + \Delta t\emptyset \quad \left(\boldsymbol{C_1^{n+1}}, \mathrm{t_n}\right)$$

$$\boldsymbol{C}^{n+1} = \frac{\boldsymbol{C}_1^{n+1} + \boldsymbol{C}_2^{n+1}}{2} \tag{4.26}$$

where $\boldsymbol{C}^n$ stands for the computed solution at time $t_n = n\Delta t$. Note that this predictor-corrector procedure has no effect on the continuity equation since the term at the right hand side (RHS) is not a function of water elevation (pressure) term available . Therefore the time discretization of the continuity equation leads to the simple Euler scheme. This method, indeed, affect the momentum equation, where the Coriolis term at the RHS is a function of velocity. Therefore, this method tries to improve the time discretization of the Coriolis term. The matrix form of the fully discrete scheme can be obtained after long mathematical manipulation and it is too long to be written.

4.7.2. Leap-Frog Scheme

The temporal terms can be discretized as follows using the Leap-Frog temporal scheme:

$$\boldsymbol{C}^{n+2} = \boldsymbol{C}^n + 2\Delta t \emptyset \ \ (\boldsymbol{C}^{\boldsymbol{n+1}}, t_{n+1}) \tag{4.27}$$

Note that in the Leap-Frog method, the spatial terms are estimated at the time t_{n+1}. We obtain the following matrix form for fully-discrete equations:

$$\begin{pmatrix} (E^2-1)I_2 & 2\beta HAE \\ 2\beta gBE & (E^2-1)I_3 \end{pmatrix} \begin{pmatrix} \vec{\tilde{U}} \\ \tilde{\vec{\eta}} \end{pmatrix} = \begin{pmatrix} 0 \\ 0 \end{pmatrix} \tag{4.28}$$

Where $E = e^{i\omega\Delta t}$ is the propagation factor, $\beta = \frac{\Delta t}{h}$. The dispersion relationship for propagation factor E is obtained by vanishing the left-hand side coefficient matrix of (28). However, the explicit form of the dispersion relation is too long to be written, and will be shown graphically and discussed in the following section.

4.7.3. Adams-Bashforth second order Scheme

Adams-Bashforth temporal scheme reads:

$$\boldsymbol{C}^{n+2} = \boldsymbol{C}^{n+1} + \Delta t \left[\frac{3}{2} \emptyset \ \ (\boldsymbol{C}^{\boldsymbol{n+1}}, t_{n+1}) - \frac{1}{2} \emptyset \ \ (\boldsymbol{C}^{\boldsymbol{n}}, t_n) \right] \tag{4.29}$$

This fully discrete scheme can be written in the following matrix form:

$$\begin{pmatrix} (E^2-E)I_2 & \beta HA(\frac{3E}{2}-\frac{1}{2}) \\ \beta gB(\frac{3E}{2}-\frac{1}{2}) & (E^2-E)I_3 \end{pmatrix}\begin{pmatrix} \vec{\tilde{U}} \\ \vec{\tilde{\eta}} \end{pmatrix} = \begin{pmatrix} 0 \\ 0 \end{pmatrix} \quad (4.30)$$

Similarly, the dispersion relation for this scheme is obtained by cancelling the determinant of the left-hand side of the matrix, but it is too long to be written, and will be shown graphically and discussed in the following section.

4.8. Analysis of fully-discrete method

Using the obtained dispersion relations for the various fully discretized methods, we can achieve the phase speed ratio. We define the phase speed as $C_{PH} = \frac{\omega}{\sqrt{k^2+l^2}}$ and then, the ratio of the computational phase speed which corresponds to the numerical method over the analytical solution which corresponds to the continuous case is defined as the phase speed ratio:

$$r_{PH} = \frac{C_{PH}^{CP}}{C_{PH}^{AN}} \quad (4.31)$$

From (4.24), one can rewrite equation (4.31) as follows:

$$r_{PH} = \frac{\omega_{CP}}{\sqrt{1+\left(\frac{\lambda}{h}\right)^2[(kh)^2+(lh)^2]}} \quad (4.32)$$

whereω_{CP}corresponds to $O(1)$ which is the computational inertia-gravity mode.

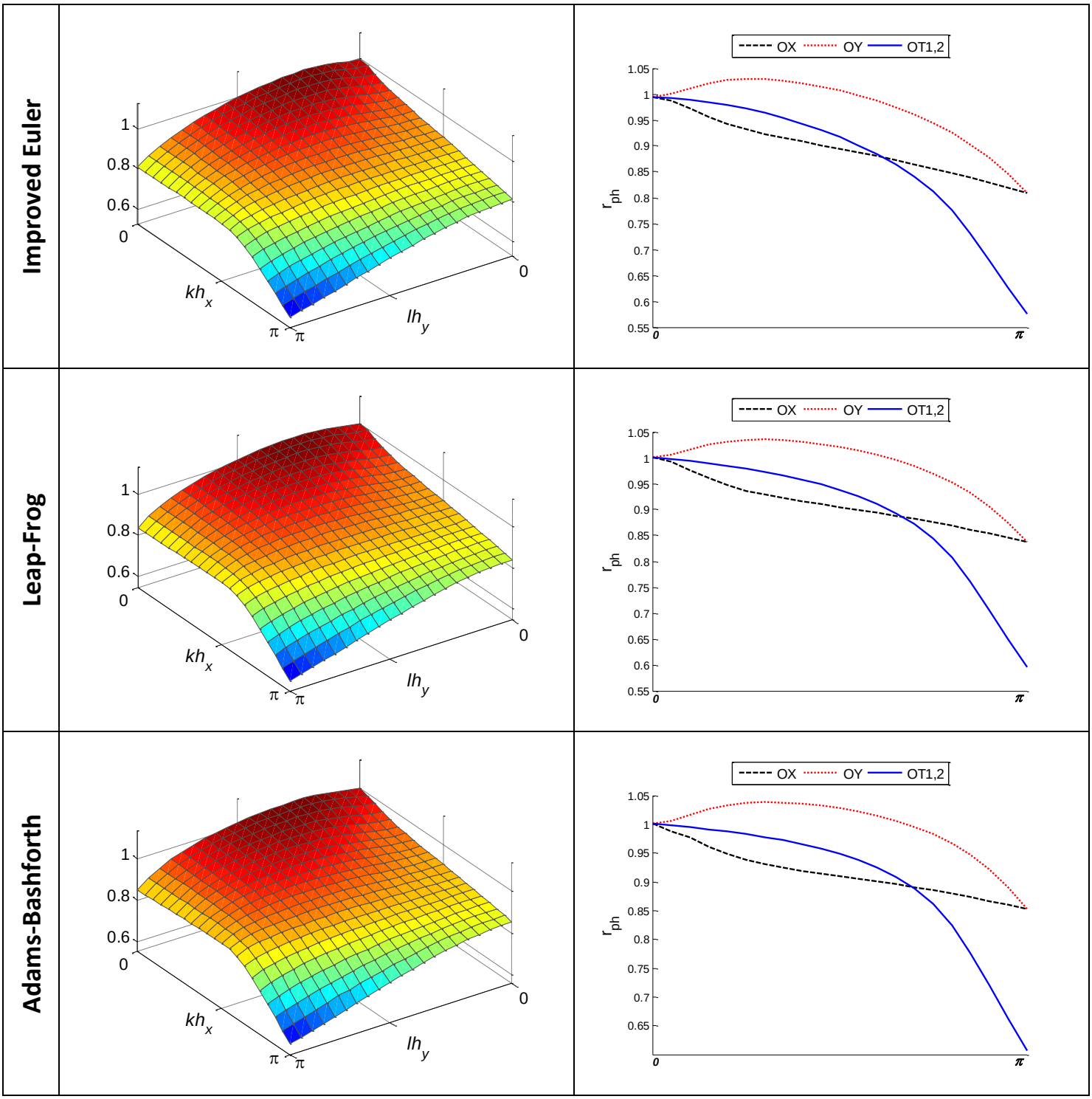

Fig. 4.7 - Phase Speed Ration r_{PH} of various temporal schemes for $CFL = 0.1$

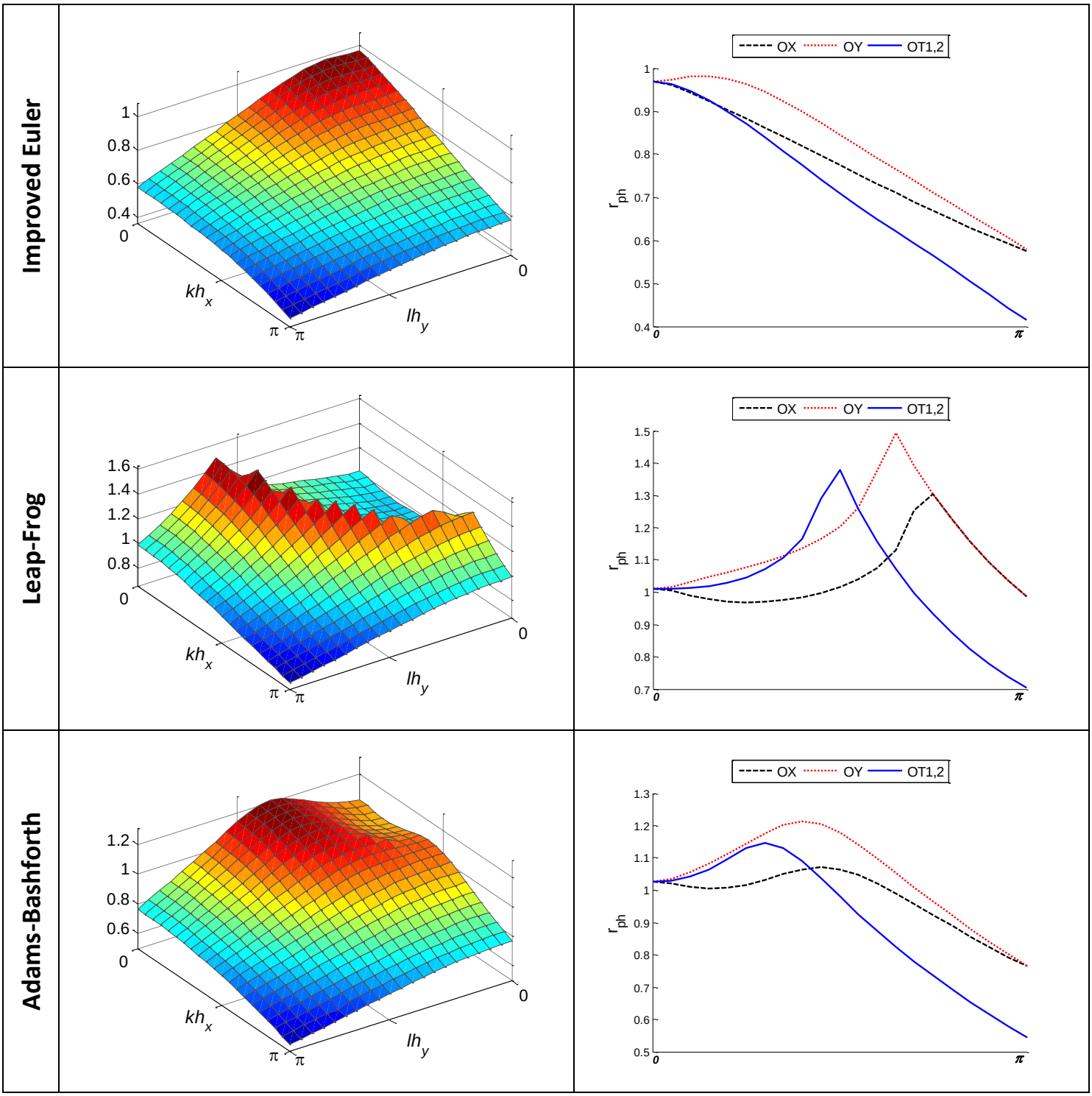

Fig. 4.8 - As of Fig. 4.7 but for $CFL = 0.5$

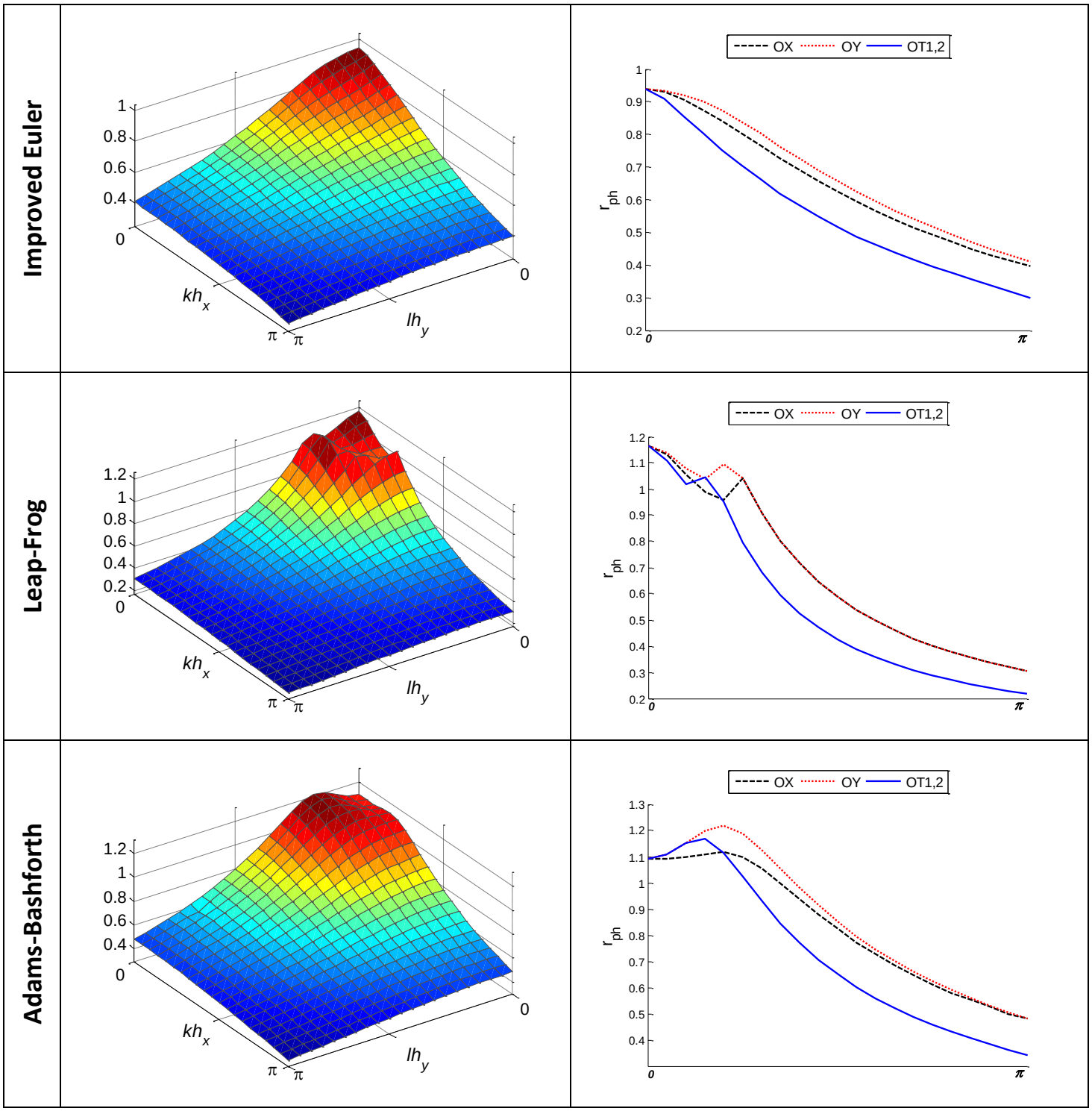

Fig. 4.9 - As of Fig. 4.7 but for$CFL = 0.9$

In order to analyse the effect of different time stepping techniques, we define $CFL = \frac{\sqrt{GH}}{h^*}\Delta t$ and consider the equilateral triangle case ($\alpha = \pi/6$) with resolution of $\lambda/h = 2$. The phase speed ratio of different methods for a wide range of CFL numbers are plotted in Fig. 4.7 to Fig. 4.9. The figures show the three dimensional views of the phase speed ratio (left column) as well as the variation along the selected axes OX, OY and $OT1{,}2$ (right column). For the low CFL number of 0.1, as it is expected, the results of various techniques are close together and reflect the semi-discrete behaviour since the effect of the time stepping technique is low. Indeed, the phase speeds are close to the continuous case for low and medium wave numbers while the longer waves propagate slower. However, Adams-Bashforth methods holds higher ratios along the $OT1{,}2$ axis for the longer waves.

For the $CFL = 0.5$, as can be seen in Fig. 4.8, the Improved Euler methods leads to the ratios close to one only for small wave numbers (short waves) while decelerates the wave with medium and large wave numbers. The phase speed ratio for Adams-Bashforth is close or higher than one for both short and medium waves while it drops lower than one for slow long waves, especially in $OT1{,}2$ direction. The Leap-Frog scheme dramatically improves the phase speed behaviour of semi-discrete method and leads to ratios close or higher than one for all wave numbers along the OX and OY directions. In addition, it holds higher values along the $OT1{,}2$ compared to the other schemes.

For the $CFL = 0.9$, one can see that the waves in Improved Euler method are propagating slower than the continues ones even for the medium wave numbers and the ratio drops faster by increasing the wave number. The behaviour of Leap-Frog and Adams-Bashforth methods are almost similar and they decelerate the waves with high wave numbers.

Further to the phase speed behaviour, we investigate the damping error $|E|$ associated to the Rossby mode. We found that there is no damping error for the Adams-Bashforth and Leap-Frog methods even for the higher CFL numbers (not shown). However, the damping error of Rossby wave for the Improved Euler method is plotted in Fig. 4.10 for various CFL numbers. One can see that the damping error for the low CFL number of 0.1 is negligible but it increases for the higher CFL numbers.

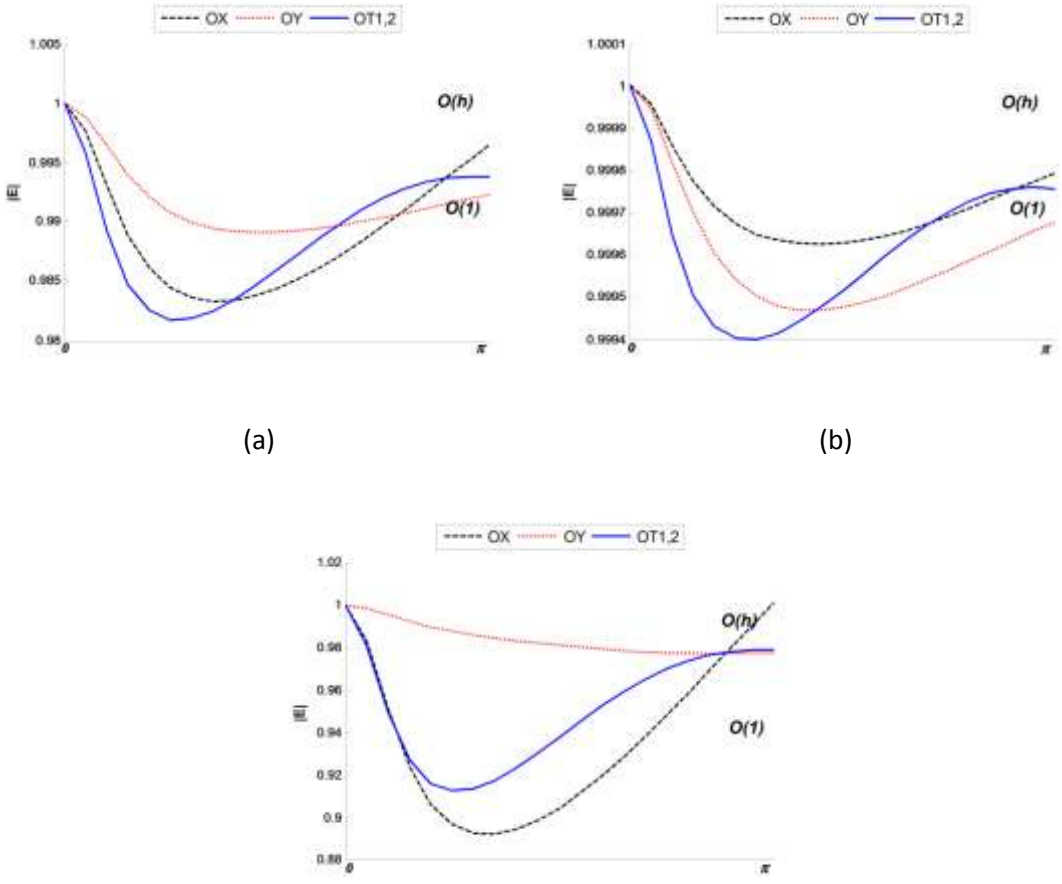

Fig. 4.10 - Damping Error $|E|$ associated to the Rossby mode for Improved Euler scheme with (a) $CFL = 0.1$, (b) $CFL = 0.5$ and (c) $CFL = 0.9$.

4.9. Numerical Tests

In this section, we verify the theoretical analysis and show the ability of the proposed finite volume unstructured C-grid scheme. The first example verifies the theoretical analysis of semi and fully discrete methods. In all other numerical examples, we examine the proposed combination of finite volume triangular C-grid (with equilateral triangles) with the Leap-Frog time-stepping technique. There are some important terms, such as Coriolis, wind

stress, bed friction, and bottom topographical changes which have an essential role in the derivation of oceanic waves which are considered in the following numerical tests.

4.9.1. geostrophic balance

This test was proposed in [Ref11] and later has been used in the literature [Ref]. In this test, we verify the theoretical analysis of dispersion relation for triangular C-grid with various vertex angles. We consider a rectangular domain with a source point of $0.1\,m$ at the middle of the domain and the water is initially at rest. We set the triangular grid resolution to $200\,m$ and keep $CFL = 0.1$ for all cases. The Leap-Frog and Adams-Bashforth time stepping techniques are used and they lead to almost the same results. The Coriolis is set to $f = 10^{-4}s^{-1}$ and with $\sqrt{GH} = 40, 7.5$ and $2.5\,ms^{-1}$ we have $\lambda/h = 2, 3/8$ and $1/8$, respectively. The results of the free surface elevation η for various triangles with different vertex angle are presented in Fig. 4.11. As one can see, for the $\lambda = 1/8$ the negative elevations appear in the domain around the source point which can be related to the non-monotonic behaviour of the non-dimensional frequency ω/f, as is shown in Fig. 4.5. For $\lambda/h = 3/8$, however, there is no negative free surface elevation around the source point for the equilateral triangle ($\alpha = \pi/6$) case which is in agreement with the theoretical analysis presented in Fig. 4.5, where the non-dimensional frequency is monotonic along all the directions. For triangles with $\alpha = 5\pi/24$and $\alpha = \pi/8$, one can see the appearance of very small negative values which are mostly along the directions which the behaviour of ω/f is non-monotonic. For the high resolution case $\lambda = 2$, all the cases show expected performance since the ω/f is monotonic in all directions.

4.9.2. Circular gravity wave propagation

In this example we test the behaviour of the proposed combination of the triangular C-grid scheme with the Leap-Frog time-stepping technique for modelling fast surface gravity waves in a circular basin. The fast gravity modes are important in surface waves; however, they are less essential in large-scale rotating flows. Nonetheless, an ideal numerical scheme should be capable of simulating a typical gravity wave.

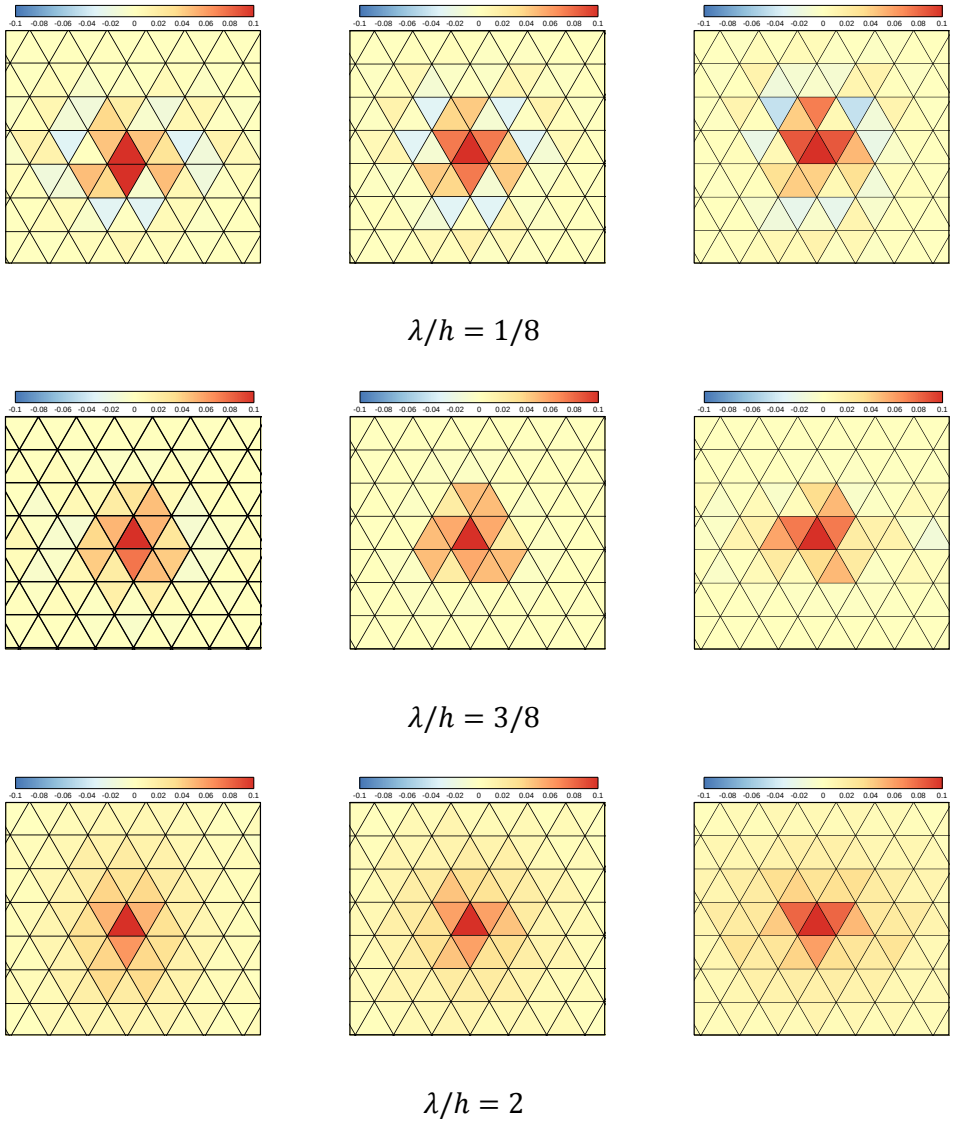

Fig. 4.11 - Water surface elevation around the source point for various grid resolution with vertex angle of $\alpha = 5\pi/24$ (left), $\alpha = \pi/6$ (midle) and $\alpha = \pi/8$ (right).

In a closed circular basin, an initial Gaussian water surface in the form $\eta(r,t) = ae^{-\frac{x^2+y^2}{b}}$ and zero initial velocity in the domain are considered. The exact solution of this problem can be found in the polar coordinates system, as follows (Le Roux 2005):

$$\eta(r,t) = \sum_1^\infty \mu_n J_0\left(r\sqrt{\lambda_n}\right)\cos\left(c\sqrt{\lambda_n}t\right), \quad (4.33)$$

where $\mu_n = \frac{\int_0^R \eta(r,0) J_0\left(r\sqrt{\lambda_n}\right) rdr}{\int_0^R {J_0}^2\left(r\sqrt{\lambda_n}\right) rdr}$, R is the radius of the domain, $r = \sqrt{x^2 + y^2}$, J is the Bessel function of first kind, and λ_n are estimated from the roots of $J_1\left(r\sqrt{\lambda_n}\right) = 0$.

In this numerical test, a circular domain with $R = 1000\ km$ and a triangular mesh grids with the triangle length of the $h = 25\ km$ is assumed. We consider a flat bottom and a mean depth $H = 2000$ which leads to $c = 100\sqrt{2}$. We set $CFL = 0.1$, and for the initial Gaussian water profile we assume $a = 100$ and $b = 6.4 \times 10^{-11}$. Fig. 4.12 shows the time sequences of the water surface at different stages obtained from the analytical solution (left column) and the numerical method (right column). At stage (a) the wave is in its initial form, and then moves toward the boundary of the circular basin in stage (b). Stage (c) shows the wave immediately after being reflected by the basin boundary. Stages (d) and (e) show the wave when it moves back to its initial place for first and second time, respectively. Comparing the panels in the right and left columns, one can see that the numerical results are in good agreement with the analytical ones. This confirms that the proposed triangular C-grid scheme is able to keep the solution symmetric, free of numerical oscillations, and accurate. To compare the results quantitatively, the absolute peak values for all stages are compared and presented in Table 4.1. As is shown, the relative true error is less than 1%, which confirms a good agreement of the numerical results with the analytical ones.

Table 4.1 - Comparison of numerical solution of absolute peak (maximum/minimum) values of water surface elevation for gravity wave with analytical solution.

Time (s)	0	3000	7000	9000	13660	28600
Analytical	99.54	16.05	23.15	15.10	80.76	95.57
Proposed Scheme	99.39	16.00	23.11	15.04	80.19	94.77
True relative error(%)	**0.2**	**0.3**	**0.2**	**0.4**	**0.7**	**0.8**

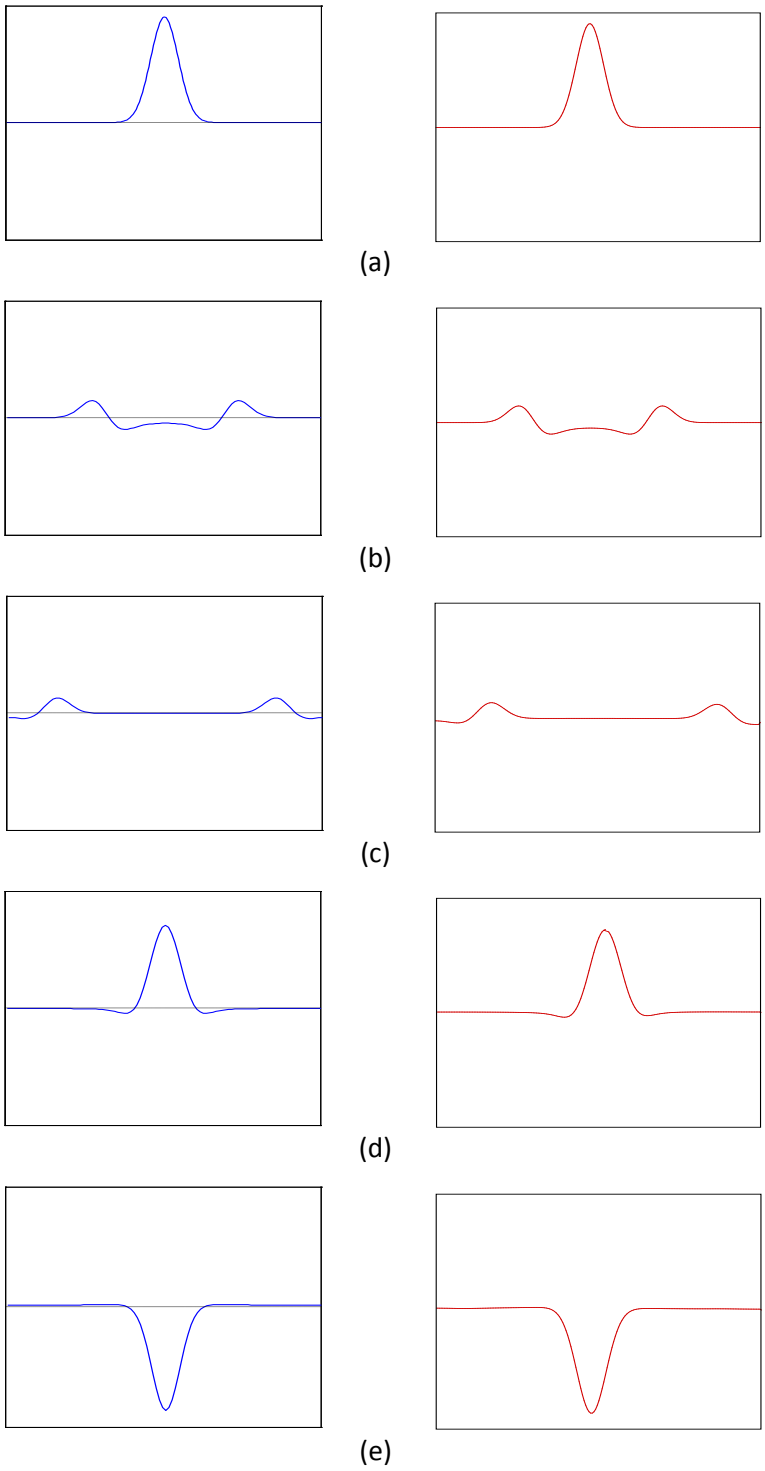

Fig. 4.12 - Vertical cross sections (1D slices along $y = 0$) of the water elevation for surface gravity wave η: Results obtained by analytical solution (right) and using proposed numerical scheme (left). Water surface elevation when the wave is (a) at its initial condition of Gaussian distribution, (b)

moving toward the basin wall (c) moving back to the center after hitting the wall, (d) returned to the starting point for first and (e) second time.

4.9.3. Equatorial Rossby waves

In the previous test we examined the numerical method with a fast gravity wave, and now we test the ability of the model to resolve slow waves. In this section we examine the proposed triangular C-grid scheme with large-scale equatorial waves. Indeed, we consider the exact solution of the linear β-plane equatorial shallow water equations, which is called symmetric equatorial Rossby waves of Index 1. As these waves are long and slow, they have an essential role in transferring energy in the ocean.

When we assume the exact solution of an equatorial Rossby wave, a numerical method should be able to preserve the solution. However, many of the available schemes fail to do so (Beljadid et al. 2013).

Linear case

First we write the analytical solution of linear shallow water equations (4.1) and (4.2) for symmetric equatorial Rossby waves of Index 1. We assume a Rossby wave with a wavelength of $W_L = 11{,}000\,km$ which propagates in a $2W_L \times W_L$ domain. We set the mean depth $H = 300m$and gravity$g = 0.03ms^{-2}$, and we use equation (4.5) to estimate the characteristic length, time, and velocity. The non-dimensional domain $2L \times L$ is obtained by $L = 16$. The dispersion relation for this wave is as follows:

$$\omega^2 - k^2 - \frac{k}{\omega} = 3 \tag{4.34}$$

where$k = 2\pi/L$ is the wave number. The analytical solution of an equatorial Rossby wave with an amplitude of A_w is given by:

$$r^+ = -A_w \frac{2y^2 - 1}{k - \omega_R} sin(kx - \omega_R t) e^{-\frac{y^2}{2}}$$

$$r^- = -A_w \frac{-1}{k+\omega_R} sin(kx - \omega_R t) e^{-\frac{y^2}{2}} \tag{4.35}$$

$$\eta = \frac{r^- - r^+}{2}$$

$$u = \frac{r^- - r^+}{2}$$

where$r^{\pm}$ are the Riemann invariants and ω_R is the smallest root in the dispersion relation (4.34). The water surface elevation for a Rossby wave with $A_w = 1$ obtained from analytical solution (4.26) is shown in Fig. 4.13 (right) at time $T = 250$, which is equivalent to 5 wave periods.

Now, in order to examine the proposed C-grid scheme, the analytical solution (4.35) is used as an initial condition for simulating a large-scale equatorial Rossby wave. To this end, a mesh grid with cell area approximately equal to 1500 $km^2$is employed, and we set $CFL = 0.1$. The contour plot of the water surface elevation for Rossby waves obtained from the proposed scheme at $T = 250$ is shown in Fig. 4.13 (left). Compared to the results of the upwind κ schemes reported in (Beljadid et al. 2013),as an example of well-known finite volume methods, the obtained results are promising. Fig. 4.13 shows that the proposed C-grid triangular method preserves the symmetric form of the solution well. It also gives an accurate results compared with the analytical one, without any significant damping.

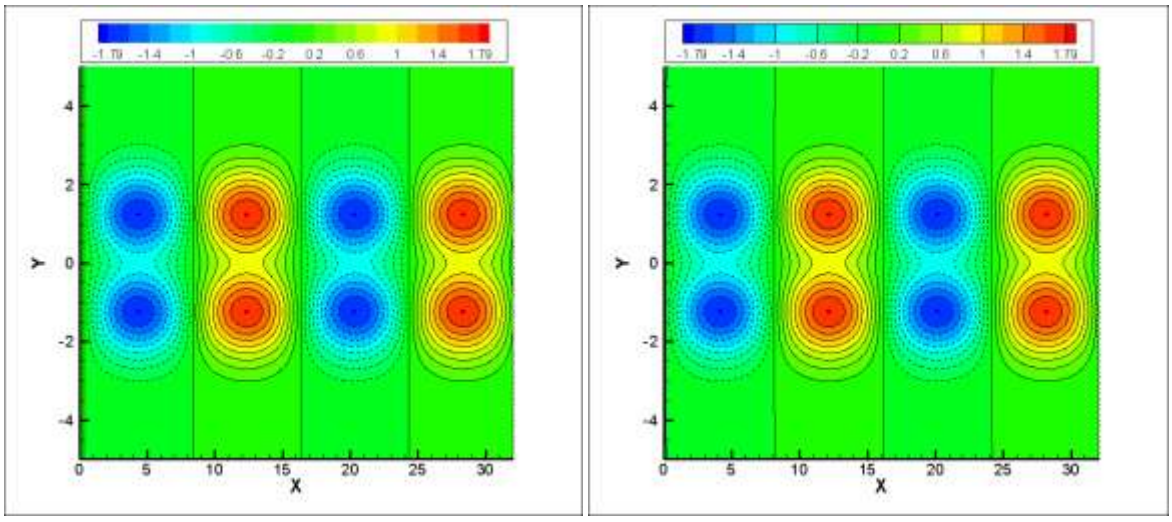

Fig. 4.13 - Water surface elevation for Rossby waves at $t = 250$: Using proposed scheme with CFL=0.1 (left) and analytical solution (right)

A 1-D slice of the computed water surface elevation is also shown and compared to the analytical one in Fig. 4.14. As one can see, neither significant damping nor any substantial phase error is observed in the solution, and they are in good agreement.

By decreasing the mesh grid resolution, we also examine the accuracy of the method in terms of predicting the maximum value of the water surface elevation. As presented in Table 4.2, we compare the maximum value of the water surface for Rossby waves computed using various cell sizes. As can be seen, the damping is negligible for a range of grid resolutions. Table 4.2 also shows the relative true errors for different cases, which confirms that the damping is less than 1%.

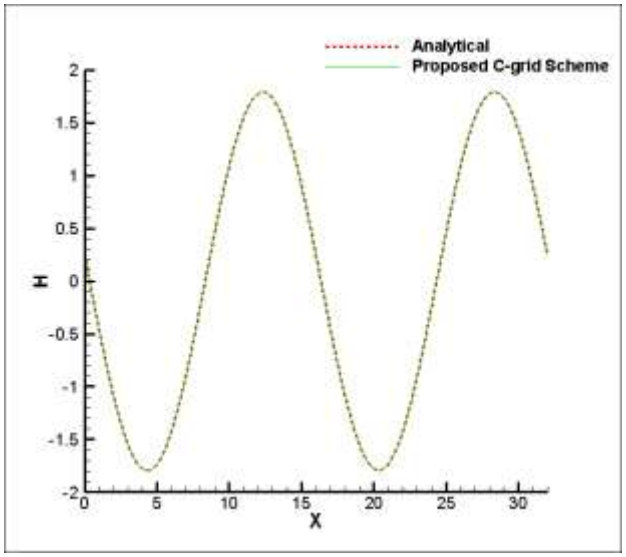

Fig. 4.14 - Comparison of numerical and analytical solution of water surface elevation for Rossby wave after 5 periods ($t = 250$)

Using this numerical test with an analytical solution, the spatial order of accuracy for the proposed triangular C-grid scheme is also obtained. In order to numerically determine the rate of accuracy for spatial convergence, the CFL number is set to a small value in order to vanish the error due to the temporal discretization. We use different mesh grids with various resolutions and obtain the results for water surface elevation for a Rossby wave at $t = 250$. Equippedwith the corresponding analytical solution, we obtain the L^2error for

each case. The evolution of theL^2 error versus the length of the computational triangle cells (Δx) is plotted in a $log - log$ scale in Fig. 4.15. It shows that the spatial order of accuracy for the proposed scheme is 1.95, which is close to the official order of spatial accuracy of 2 for the C-grid. The results show the capability of the proposed method in the simulation of large-scale slow and long oceanic waves.

Table 4.2 - Maximum values of the analytical and computed water surface elevation for Rossby wave for various grid sizes

Cell Area (km^2)	**952.6**	**1488.5**	**2325.8**	**3810.5**	**5953.9**	**15242.0**	**60968.2**
Analytical	1.793	1.791	1.788	1.788	1.784	1.745	1.675
Proposed Scheme	1.793	1.791	1.787	1.788	1.782	1.742	1.670
True relative error (%)	**0**	**0**	**0.1**	**0.0**	**0.1**	**0.2**	**0.3**

Nonlinear case

Finally, we modify the equatorial Rossby wave test by considering the non-linear shallow water equations (4.8) and (4.15). We use a coarser mesh grids with cell area of $2325\ km^2$ and keep other conditions and parameters similar to the linear experiment. The water surface elevation for Rossby wave is shown in Fig. 4.16. As one can see, there is no numerical noise in the results and proposed scheme preserved the symmetric shape of the wave without any significant damping. This demonstrates that the model is able to account properly the non-linear terms.

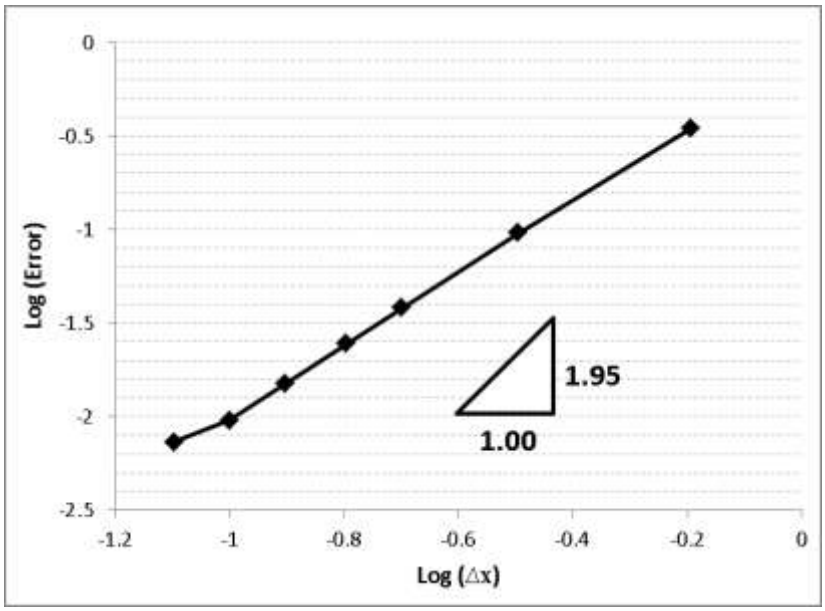

Fig. 4.15 - Evolution of L^2 error for Rossby wave after 5 periods ($t = 250$) in Log-Log scale

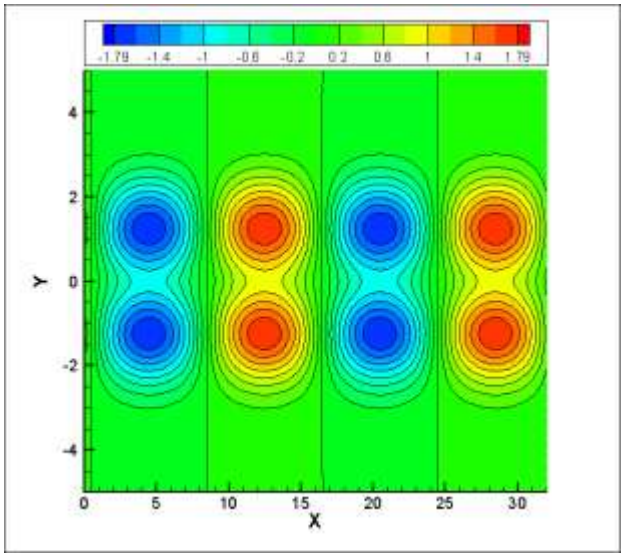

Fig. 4.16 - Computed water surface elevation for Rossby waves at $t = 250$ using non-linear shallow water equations.

4.9.4. The Stommel problem

This numerical example is a wind-driven large-scale circulation test originally proposed by Stommel (1948) and widely used in the literature (Adcroftet al. 1999l;Hanert et al. 2004;

Le Roux 2005). Wind, as one of the main factors in generating the surface waves in the oceans, is considered in this example. In addition to the surface wind, we consider linearized bottom friction as well as Coriolis force in a square basin with a flat bottom. Since we employ the β −plane approximation $f = f_0 + \beta y$, the solution is expected to be a concentrated crowding of streamlines toward the boundary due to changes in Coriolis force through the basin.

The linear shallow water equations, considering the effect of surface wind and bottom friction, can be written as follows:

$$\frac{\partial \eta}{\partial t} + \frac{H}{A_i}\sum_{j=1}^{3} U_j d_j = 0 \tag{4.36}$$

$$\frac{\partial U}{\partial t} + fvn_x - fun_y + g\frac{\partial \eta}{\partial n} = \boldsymbol{\tau} - \xi u n_x - \xi v n_y \tag{4.37}$$

where$\boldsymbol{\tau}$is the surface wind stress vector and ξ is the bottom drag coefficient.

We consider a square domain of $4000\,km \times 4000\,km$ and set a non-flow boundary condition all around the basin. The mean depth of the water is assumed to be $H = 400\,m$ and the reduced gravity acceleration is $g' = 0.01\,ms^{-2}$. For the β − plane approximation of $= f_0 + \beta y$, we set $f_0 = 10^{-4}s^{-1}$ and $\beta = 10^{-11}m^{-1}s^{-1}$, which leads to the radius of deformation $R_d = \frac{\sqrt{g'H}}{f_0} = 20\,km$.

A zonal wind is considered, which results in a surface stress of $\boldsymbol{\tau} = (\tau_x, \tau_y)$ with:

$$\begin{cases} \tau_x = \tau_0 \sin\left(\frac{\pi y}{L}\right) \\ \tau_y = 0 \end{cases} \tag{4.38}$$

where$-\frac{L}{2} < y < L/2$ and $\tau_0 = 2 \times 10^{-7}\,ms^{-2}$, spinning up a single anticyclonic gyre. We set the bottom drag coefficient$\xi = 10^{-6}s^{-1}$, leading to a Stommel layer width of $\delta = \frac{\xi}{\beta} = 100\,km$. Two cases, of low- and high-resolution mesh grids, are considered in this numerical experiment. We set the computational triangular cells at size $h =$

$20\ km$ and $h = 200\ km$ for the low-and high-resolution grids respectively, and we take $CFL = 0.1$.

The main objective of this test is to examine the proposed triangular C-grid shallow water model with simulation of the evolution of the velocity divergence field. In a general circulation model, an accurate estimation of velocity divergence is essential for good resolution of the vertical velocity field. Note that in this test, we consider the effect of wind in combination with Coriolis force and bed shear stress as important factors affecting the surface oceanic waves. The structured rectangular C-grid scheme has already been examined with this test by (Adcroft 1999; Le Roux 2005) and the results reported for both the low- and high-resolution grids.

The obtained divergence of the velocity field using an triangular C-grid scheme after 100 days of simulation is shown in Fig. 4.17 for both the low- and high-resolution grids. In the high-resolution case, one can see a good agreement with the obtained results of the triangular C-grid scheme and those reported for a structured C-grid scheme in (Adcroft 1999; Le Roux 2005). More precisely, one can see the appearance of the eddy at the bottom right corner of the basin. Moreover, a zoom of the bottom left corner of the basin (Fig. 4.17b) is presented in Fig. 4.19a, which shows that the results are free of numerical oscillations even very close to the basin wall. With respect to the results obtained using low-resolution grids (Fig. 4.17a),one can see a great improvement compared to the results for the structured C-grid reported in (Adcroft 1999) which confirms the dispersion relation analysis results, as explained in Section (4) of this paper.

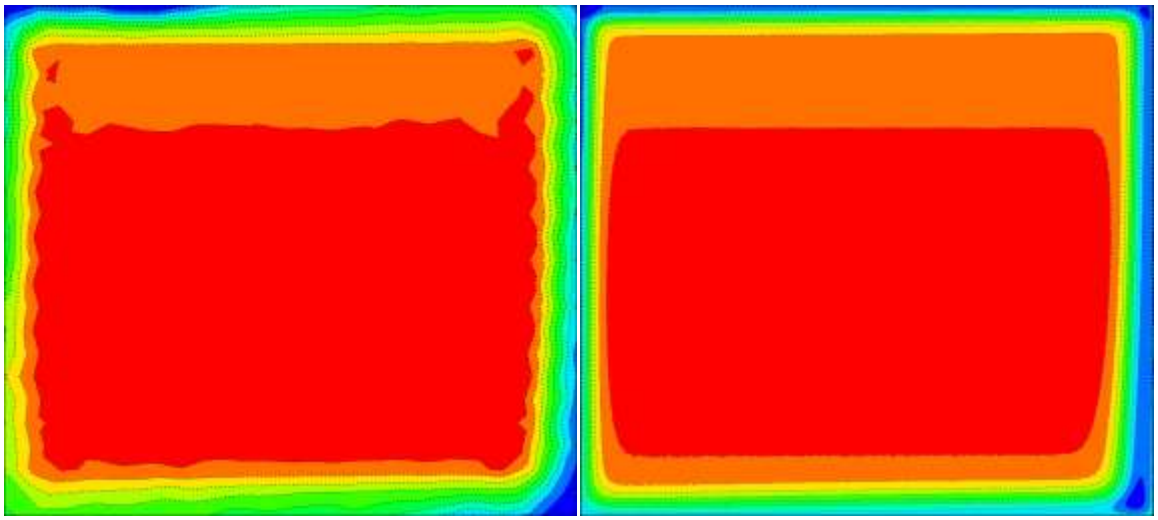

(a) (b)

Fig. 4.17 - Contour plots of the divergence field computed by unstructured C-grid scheme after 100 $days$ using (a) low resolution and (b) high resolution mesh grids.

The obtained divergence of the velocity field after 500 days of simulation is also shown in Fig. 4.18 for both low- and high-resolution grids. It can be seen that the evolution of the divergence field is resolved well by the triangular C-grid scheme. Again, the eddy appears and is developed accurately at the bottom right corner of the basin. For the high-resolution grid. One can see a zoom of the bottom left corner of the basin in Fig. 4.19b, which shows that the results are free of numerical noises close to the boundary. In the low-resolution case (Fig. 4.18a), the results are in agreement with the high-resolution one, and one can see the appearance of the eddy at the bottom left corner of the basin. One can also compare the results with those reported for low-resolution grids computed by a CD-grid in (Adcroft 1999; Le Roux 2005).

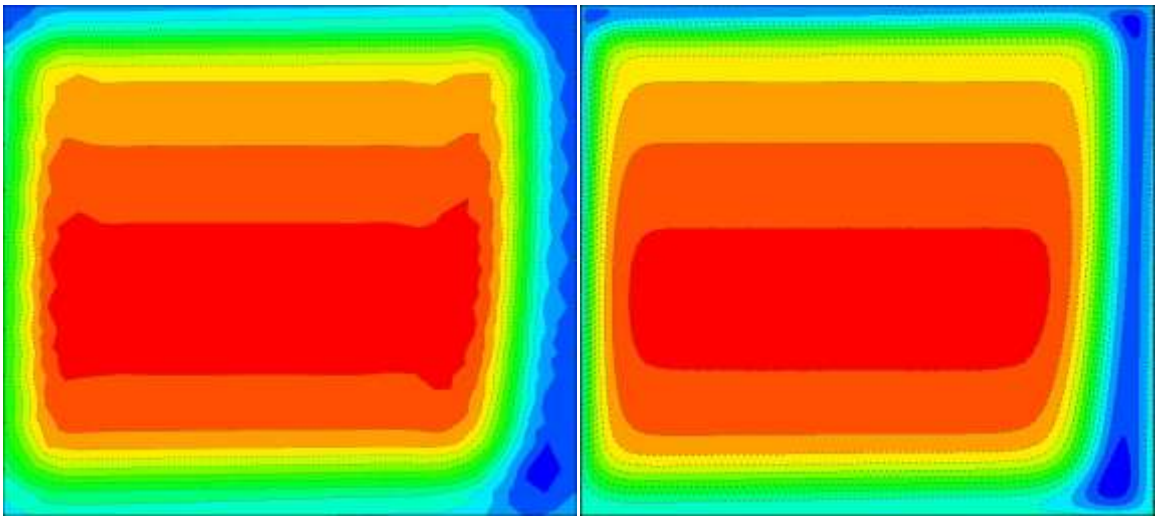

(a) (b)

Fig. 4.18 - As of Fig. 4.10 but after 500 $days$.

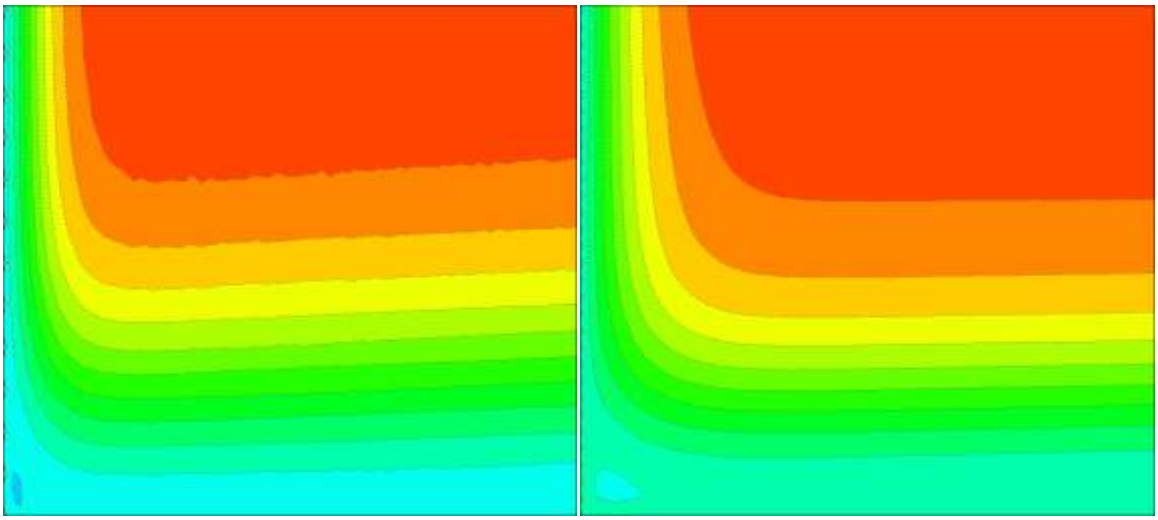

(a) (b)

Fig. 4.19 - Zoom of the bottom left corner of the basin for divergence of velocity field after (a) 100 $days$ and (b) 500 $days$. T

Altogether, the results of the Stommel test show that the proposed triangular C-grid method performs well and is accurate even when using low-resolution mesh grids.

4.9.5. Non-linear wind induced circulation in a circular basin of uneven topography

This numerical test was originally proposed by (Kranenburg 1992) and then broadly has been used in the literature (Bukatov and Zav'yalov 2004; Skoula et al. 2006; Rogers et al. 2001). In this test case, simulation of the topographic gyres is considered due to a uniform wind field. In addition to the surface wind stress term in the momentum equation, the non-uniform topographical changes of the bottom as well as bottom friction are considered. We modify this test by taking into account the non-linear velocity advection term in the momentum equation. In this case, the non-linear shallow water equations read:

$$\frac{\partial \eta}{\partial t} + \frac{h_t}{A_i}\sum_{j=1}^{3} U_j d_j = 0 \tag{4.39}$$

$$\frac{\partial (h_t U)}{\partial t} + h_t(\boldsymbol{n}\cdot\boldsymbol{u}\nabla\boldsymbol{u}) + h_t f v n_x - h_t f u n_y + g h_t \frac{\partial(\eta)}{\partial n} = \frac{1}{\rho}(\boldsymbol{\tau} - \tau_{bx} n_x - \tau_{by} n_y) \tag{4.40}$$

where$h_t = h_s + \eta$ is the total depth, h_s is the still water depth at the basin, τ_{bx} and τ_{by} are bed friction stresses, $\boldsymbol{\tau} = (\tau_x, \tau_y)$is the surface wind stress vector, and ρ is water density. Following the work of Kranenburg (1992), we use the axially-symmetric expression for the still water depth as follows:

$$h_s = \frac{1}{1.3}\left(0.5 + \sqrt{0.5 - \frac{0.5r}{R}}\right) \tag{4.41}$$

where$r$ is the radial distance from the center of the circular basin and R is the radius of the basin.

The bed friction terms are given by $\tau_{bx} = \rho C_f u\sqrt{u^2 + v^2}$ and $\tau_{by} = \rho C_f v\sqrt{u^2 + v^2}$where C_f is an empirical coefficient based on bed roughness. We use the following equation based on the Chezy friction law:

$$C_f = \frac{g}{C^2}$$

where C is the Chezy friction coefficient. In order to take into account the bottom topographical changes, we estimate the gradient term in (4.40) as follows (Skoula 2006):

$$gh_t \frac{\partial(\eta)}{\partial n} = g\eta \frac{\partial(h_s\ )}{\partial n} + \frac{1}{2} g \frac{\partial(\eta^2 + 2\eta h_s)}{\partial n} \tag{4.42}$$

We also use equations (4.10)-(4.13) to estimate the non-linear advection term in momentum equation(4.40). It should be noted that wherever the total depth value is required at the cell face j, we use a linear interpolation of the total depths at the center of cells $i = 1,2$ which share the face j:

$$(h_t)_j = \frac{1}{D_j}(d_{1j}^* h_{t_1} + d_{2j}^* h_{t_2}) \tag{4.43}$$

We assume a circular basin with $R = 192\ m$. The triangular grids with approximate cell area of $29\ m^2$ is used and CFL is set to $CFL = 0.2$. The uneven bathymetry contour lines and the unstructured triangular mesh grid is shown in Fig. 4.20. No-flow boundary with free-slip condition is applied at the basin wall. Mean depth is set to $H = 0.769\ m$ and other parameters are taken as $\tau_x = 0.02\ N/m^2$, $C = 33.11\ m^{\frac{1}{2}}/s$ and$f = 0$.

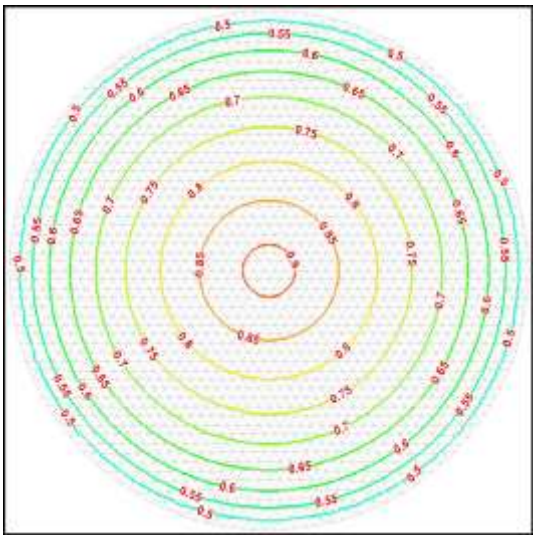

Fig. 4.20 - Unstructured triangular mesh grids of the circular basin along with the still water depth contour lines.

The results obtained from the triangular C-grid scheme at steady state condition at $t = 5000\ s$ are presented in the following. Fig. 4.21 shows the water surface elevation.

One can see that the proposed scheme resolved the flow pattern well and they are in agreement with those reported in (Skoula 2006). The steady state velocity field can be also seen in Fig. 4.22. The results obtained using the triangular C-grid scheme is in agreement with those reported by (Skoula 2006). As can be seen, the results are free of spurious modes and demonstrate the ability of the proposed scheme in simulation of wind-driven surface waves with an uneven bathymetry.

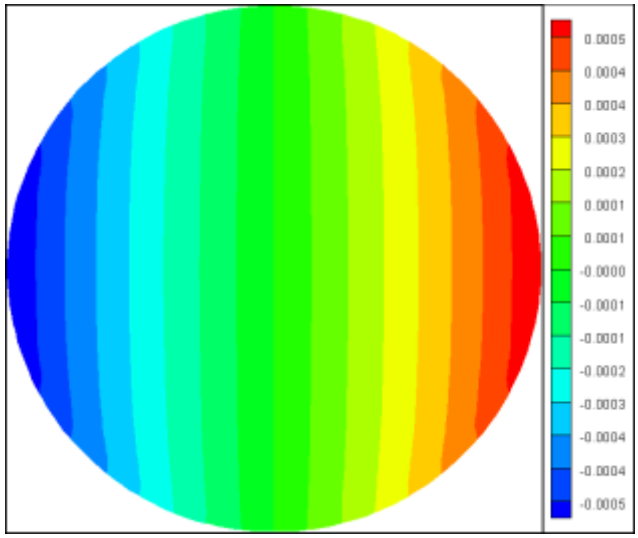

Fig. 4.21 - Water surface elevation at $t = 5000\ s$.

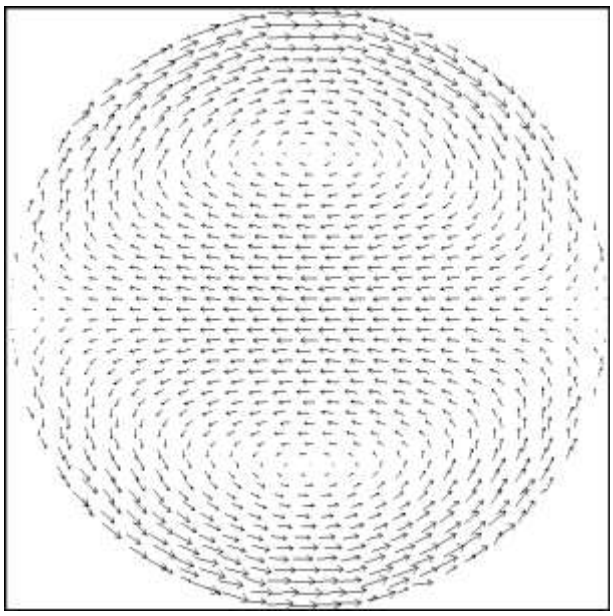

Fig. 4.22 - Velocity field component of the solution at $t = 5000\ s$.

4.9.6. Nonlinear Rossby soliton waves

In this numerical test, we examine the behaviour of the proposed C-grid scheme with a non-linear equatorial Rossby wave as a slowly propagating wave. This wave, also called an equatorial Rossby soliton, is driven by gravity and rotational Coriolis force. This test was originally proposed by Boyd 1980) and since then has been widely used in the literature (Iskandarani et al. 1995; Le Roux 2000;Hanert et al. 2005).These waves are observed about the equator, and in the absence of dissipation they preserve their shape while propagating at a constant phase speed.

We consider the non-linear shallow water equations (4.8) and (4.14), and we use the dimensionless characteristic parameters (4.4) for using a dimensionless version of non-linear shallow water equations on an equatorial $\beta-$ plane. In this test, we consider a non-dimensional domain of 32×6 with a non-flux boundary condition along the basin walls. We take the mean depth $H = 100\, m$ and reduced gravity $g' = 0.04$. We consider a mesh grid with a cell area of 0.01, and we set $CFL = 0.2$. Setting $t' = 0$, the initial velocity and water surface elevation is obtained from the previous works of Boyd (1980), as described in (Hanert et al. 2005):

$$u = A_s B_s^2 \frac{6y'^2 - 9}{4} \operatorname{sech}^2\big(B_s(x' - C_s t')\big) \exp\left(-\frac{y'^2}{2}\right)$$

$$v = -4A_s B_s^3 y\, tanh\big(B_s(x' - C_s t')\big) \operatorname{sech}^2\big(B_s(x' - C_s t')\big) \exp\left(-\tfrac{y'^2}{2}\right) \qquad (4.44)$$

$$\eta = A_s B_s^2 \frac{6y'^2 + 3}{4} \operatorname{sech}^2\big(B_s(x' - C_s t')\big) \exp\left(-\frac{y'^2}{2}\right)$$

where $A_s = 0.771$, $B_s = 0.395$, and $C_s = -1/3 - 0.395 B_s^2$. The contour plot of the initial condition for water surface elevation along with its maximum value is shown in Fig. 4.23a. Using the initial condition, at the very beginning of the simulation, the Rossby soliton wave loses 5% of its initial amplitude, which propagates as a Kelvin wave to the eastward of the domain, opposite to the Rossby soliton wave propagation. This is due to the fact that the initial condition is not exactly a solitary wave. The contour plot of the

water surface elevation and its maximum value computed by the proposed scheme is shown in Fig. 4.23b. As can be seen, the wave structure is well resolved by the numerical scheme. In addition, the proposed scheme preserved the symmetric form of the solution, while damping is negligible. If we consider the aforementioned 5% loss of amplitude for the Rossby soliton, which can be observed at the top boundary of the basin in Fig. 4.23b, then the computed maximum value of the water surface is in good agreement with the analytical solution. In addition, the asymptotic solution of the Rossby soliton by Boyd (1980)predicts the phase speed of the wave as equal to $0.79\,ms^{-1}$. The phase speed computed by the numerical method is $0.80\,ms^{-1}$, which is in good agreement with the asymptotic solution. Fig. 4.24 also shows a 3-D view of the computed water surface elevation. The results show the ability of the model to preserve the wave shape and phase speed for slow Rossby waves.

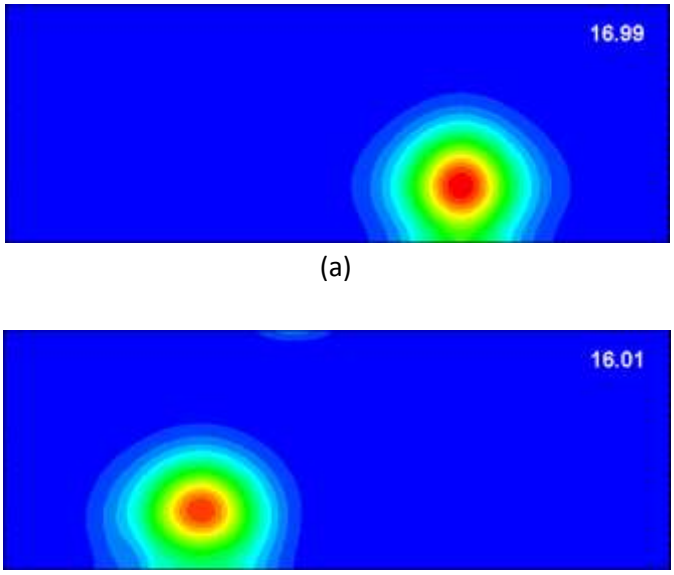

Fig. 4.23 - Contour plots of water surface elevation for Rossby soliton wave: (a) the initial condition (b) computed by proposed scheme at dimensionless time $t^{'} = 32$ (Equivalant to $55\ days$).

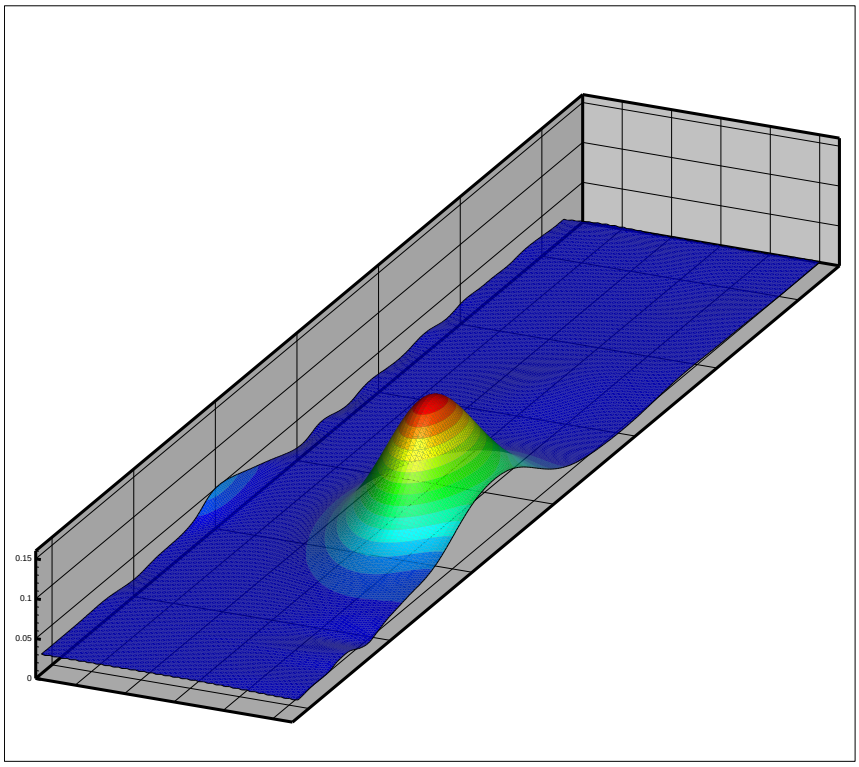

Fig. 4.24 - 3D view of the Rossby soliton computed by proposed scheme at dimensionless time of $t' = 32$.

4.10. Summary and Conclusion

Dispersion relation analysis was implemented in this paper in order to investigate the performance of a finite volume triangular C-grid scheme in shallow water equations. Indeed, the proposed C-grid approach was analyzed in the presence of the Coriolis term, which plays an essential role in inertia-gravity waves. We considered triangular grids made up of isosceles triangles with various vertex angles with the linear shallow water equations. The results of the dispersion relation analysis were compared with those of the analytical one, which belongs to the continuous case. We also reproduced the results of structured rectangular C-grid scheme (finite difference) in order to compare them with the triangular C-grid. Different cases of low and high resolution grids were considered for dispersion relation analysis. Analysis showed that the same Rossby mode $\omega = 0$ as continuous case exists for $\alpha = \pi/6$, while it does not for the triangles with $\alpha \neq \pi/6$. The mode in $O(1)$ coincide with the continuous case for $\alpha = \pi/6$ while it is not the case for other vertex angles. In addition we found the spurious mode $O(1/h)$ for all cases. We also noticed that

for the triangles with $\alpha \neq \pi/6$, there is a mode in $O(h)$. However, we found it remains bounded and very close to zero for both low and high resolution cases. In addition, results showed that for the $\lambda/h \geq 3/8$ the non-dimensional frequency has a monotonic behaviour along the all directions as the continuous case for $\alpha = \pi/6$. It is also valid for the $\alpha \neq \pi/6$ but for some directions. In the relatively low resolution case of $\lambda = 3/8$, an improvement was shown for the triangular C-grid scheme compared to the structured rectangular one. We also examined three time stepping methods, namely, Adams-Bashforth, Leap-Frog and Improved Euler in combination with finite volume triangular C-grid. The phase speed ratio for a wide range of CFL numbers were studied and results showed advantageous of the Leap-Frog and Adams-Bashforth techniques over the Improved Euler. More precisely, the Leap-Frog scheme better improved the phase speed ratio behaviour of the semi discrete case at $CFL = 0.5$.

Through a number of numerical tests, we verified the theoretical analysis of dispersion relation and examined the performance of proposed combination of the finite volume triangular C-grid (equilateral case) with the Leap-Frog method. We considered the Coriolis force, wind stress, bottom friction and bottom topographical changes, and examined the proposed fully discrete scheme with various oceanic waves, such as fast gravity waves, as well as with long and slow inertia-gravity waves.

The results of gravity wave propagation in a circular basin were compared to the analytical ones. The results showed that the model is capable of modelling the fast waves while preserving the symmetric shape of the solution without significant damping. Then, the model was examined with a long slow equatorial Rossby wave. The results obtained after 5 periods were compared to the analytical solution, and they were in good agreement. The symmetrical shape of the wave was preserved by the model, while the maximum water surface elevation was well predicted. The maximum values of the water surface elevation were compared to the analytical ones for various grid resolutions. The results confirmed that even using a relative coarse mesh, there is no considerable damping associated with the solution. Moreover, the spatial order of accuracy for the triangular C-grid scheme were sought by investigating the evolution of the L^2 error of water surface elevation. The

obtained rate was very close to the official spatial order of accuracy for the C-grid. Furthermore, the non-linear shallow water equations are also examined with the equatorial Rossby wave. The results was is good agreement with the analytical one and confirmed that the model can correctly take into account the non-linear terms.

In order to further examination, we applied the proposed model to the Stommel problem for two low- and high-resolution grids. The results demonstrated the ability of the model in predicting the divergence of the velocity field. In this test, we examined the proposed triangular C-grid for low and high resolution cases. The results of high resolution case was satisfactory. With regard to the low-resolution scenario, a great improvement was obtained in comparison to the structured C-grid schemes which confirmed the theoretical dispersion analysis. The model was also examined with uneven bottom topography and wind-induced circulation in a circular basin. Using an unstructured grid, the water surface elevation and velocity field were computed by the proposed scheme. The results confirmed the ability of the model to correctly account for the surface wind stress as well as for variable bottom topography. In addition, the non-linear shallow water equations were considered through the Rossby soliton wave. The results were in good agreement with those obtained by the asymptotic solution. In sum, the model showed good performance in the simulation of various ocean waves ranging from fast gravity waves to long and slow Rossby waves.

To summarize, in line with the main objective of this paper, the following points could be emphasized on to highlight the novelty and contribution of the current study: (i) The dispersion relation of the finite volume triangular C-grid scheme was analyzed for shallow water equations in presence of Coriolis term, (ii) in order to have a perception of triangular C-grid behaviour on fully unstructured grid, we considered isosceles triangles with various vertex angles, (iii) analysis showed the mode in $O(1)$does not coincide with the continuous case when $\alpha \neq \pi/6$ (iv) there is spurious mode $O(1/h)$ in all triangular cases and no same Rossby mode $\omega = 0$ exists for $\alpha \neq \pi/6$ (v) various second-order time stepping techniques were investigated and Leap-Frog was shown to have a better performance,(vi) the performance of triangular C-grid was shown to be improved compared to the structured C-grid, especially for lower resolution, (vii) the order of accuracy of the semi-discrete finite volume triangular C-grid was sought and it was very close to the formal order of accuracy

of the scheme, (viii) the proposed C-grid method showed satisfactory performance for many numerical examples including short-fast and long-slow waves, (vi) various source terms such as bottom topography, wind stress and bottom friction which are of essential importance in practical applications were considered and the proposed method performed well for both linear and non-linear numerical examples.

Chapter 5

A well-balanced positivity-preserving central-upwind scheme for shallow water equations on unstructured quadrilateral grids[4]

Abstract

We introduce a new second-order central-upwind scheme for shallow water equations on the unstructured quadrilateral grids. We propose a new technique for bottom topography approximation over quadrilateral cells as well as an efficient water surface correction procedure which guarantee the positivity of the computed fluid depth. We also design a new quadrature for the discretization of the source term, using which the new scheme exactly preserves "lake at rest" steady states. We demonstrate these features of the new scheme as well as its high resolution and robustness and its potential advantages over the triangular central-upwind scheme in a number of numerical examples.

Keywords*: Shallow water equations, central-upwind scheme, unstructured quadrilateral grids*

5.1. Introduction

In this paper we consider the two-dimensional (2D) shallow water equations (SWEs):

$$\begin{cases} h_t + (hu)_x + (hv)_y = 0, \\ (hu)_t + \left(hu^2 + \frac{1}{2}gh^2\right)_x + (huv)_y = -ghB_x, \\ (hv)_t + (huv)_x + \left(hv^2 + \frac{1}{2}gh^2\right)_y = -ghB_y. \end{cases} \tag{5.1}$$

Here, $h(x,y,t)$ is the water depth, $u(x,y,t)$and $y(x,y,t)$ are the $x-$ and$y-$ velocities, respectively, $B(x,y)$ is bottom topography and g is the gravitational constant. 2D SWEs

[4] **H. Shirkhani**, A. Mohammadian, O. Seidou, H. Qiblawey, "A well-balanced positivity-preserving central-upwind scheme for shallow water equations on unstructured quadrilateral grids", *Computer and Fluids*, 2016, 126: 25–40. doi:10.1016/j.compfluid.2015.11.017.

are commonly used to simulate a wide range of problems in water resources engineering, modelling oceans, rivers and coastal areas, etc.

The system (5.1) admits several steady-state solutions. One of the practically most important steady states is a so-called "lake at rest" state satisfying,

$$u \equiv v \equiv 0, h + B = const. \quad (5.2)$$

A good numerical method for the SWEs (5.1) should be well-balanced, that is, it should be capable to exactly preserve the "lake at rest" steady states (5.2). It should also preserve positivity of the water depth h.

Many numerical methods for SWEs were developed in past decades. We refer the reader, for example, to finite difference (Casulli 1990; Xing and Shu 2005; Casulli and Walters 2000), finite element (Hanert et al. 2005; White et al. 2008; Triki 2014) and finite volume (Casulli and Walters 2000; Bonaventura et al. 2006; Mohamed 2014) methods. There are also high order schemes developed for hyperbolic systems (Liu et al. 1994; Bassi andRebay 1997; Giraldo et al. 2002; Xing et al. 2010) but they are comparatively computationally expensive. In this paper we focus on the finite volume method which are based on the integral form of (5.1) and thus are naturally designed to conserve the mass.

One of the finite volume methods that are both well-balanced and positivity preserving are the central upwind schemes. Central-upwind schemes are Riemann-problem-solver- free Godunov-type methods that were originally introduced in (Kurganov andTadmor 2000) for general multidimensional systems of hyperbolic conservation law and further developed in (Kurganov et al. 2001; Kurganov andTadmor 2002; Kurganov and Lin 2007; Kurganov andPetrova 2005). In (Kurganov and Levy 2002; Kurganov andPetrova 2007), the central-upwind scheme for the SWEs were developed in the 1D and 2D cases using Cartesian grids. In (Bryson et al. 2011), the central-upwind schemes were extended to unstructured triangular meshes, and in (Beljadid et al. 2014), they were also generalized for polygon cell-vertex meshes.

The main goal of this paper is to develop a second-order well-balanced positivity preserving central-upwind scheme for (5.1) on unstructured quadrilateral grids. Such grids

have been widely used in finite volume methods for various applications such as solving incompressible Navier–Stokes, Diffusion Equations, Semilinear Elliptic and Elliptic systems, see, e.g., (Chou et al. 2003; Sheng and Yuan 2008; Feng et al. 2012; Xie andXiao 2014) and references therein. In particular, quadrilateral grids have been used to develop finite volume methods for the 2D SWEs, see, e.g., (Kuiryaet al. 2012; Wu et al. 2011; Chou et al. 1999; Suli1992; Kernkampet al. 2011; Begnudelli and Sanders 2007). Unstructured quadrilateral grids are popular since they allow one to relatively easily implement local and adaptive mesh refinement techniques (Liang et al. 2008; Greaves 2004), increase the formal order of spatial accuracy of the scheme, as well as discretize second- and higher-order terms (Wu et al. 2011; Alcrudo and Garcia-Navarro 1993). Comparing to the triangular grids, one of the main advantages of the quadrilateral ones is that quadrilateral cells have more neighbouring cells and thus the quadrilateral time evolution procedure is typically more accurate.

The proposed quadrilateral central-upwind scheme is an extension of the triangular central -upwind scheme from (Bryson et al. 2011). However, some of the ingredients of the triangular scheme cannot be directly carried to the quadrilateral case. For example, one cannot obtain a continuous piecewise linear approximation of the bottom topography. Instead, we introduce a new bottom topography approximation: In each quadrilateral cell the bottom topography function B is replaced with four continuous linear pieces, each of which connects the values of B at two of the neighbouring cell vertices with the approximation value of B at the geometric center of the cell. Another novelty of our quadrilateral scheme is a new water surface reconstruction correction technique, required to guarantee the positivity of the water depth at the reconstruction step of the central-upwind scheme. To this end, we first perform a piecewise linear reconstruction of the water surface and then, in the cells where some values of the reconstructions fall below the corresponding values of the bottom topography, we replace the linear piece with four continuously matched linear pieces whose shape is similar to the bottom topography approximant in this cell. As we prove in Theorem 1, this will guarantee positivity of water depth h. To ensure the well-balanced property of the proposed scheme, we design a special

quadrature for the cell average of the geometric source term, which leads to a perfect balance of the source and fluxes for the "lake at rest " state.

To the best of our knowledge, the designed central-upwind scheme is among the first well-balanced positivity preserving scheme on unstructured quadrilateral grids.

The paper is organized as follows. The proposed central-upwind scheme is described in Section 2 and its well- balanced and positivity preserving properties are proved in Sections 3 and 4. In Section 5, the new scheme is tested on a number of numerical experiments which demonstrate high accuracy robustness of the proposed scheme and also emphasize its potential advantages over its triangular counterpart. Finally, we finish the paper with concluding remarks in Section 6.

5.2. Central-Upwind Scheme on Unstructured Quadrilateral Grids

First, we introduce the water surface variable $w = h + B$ and rewrite the system (5.1) in the following equivalent form:

$$U_t + F(U,B)_x + G(U,B)_y = S(U,B) \quad , \tag{5.3}$$

where

$$U = (w, hu, hv)^T, \tag{5.4}$$

$$F(U,B) = \left(hu, \frac{(hu)^2}{w-B} + \frac{g}{2}(w-B)^2, \frac{(hu)(hv)}{w-B}\right)^T , \tag{5.5}$$

$$G(U,B) \quad = \left(uh, \frac{(hu)(hv)}{w-B}, \frac{(hu)^2}{w-B} + \frac{g}{2}(w-B)^2\right)^T , \tag{5.6}$$

$$S(U,B) = \quad \left(0, -g(w-B)B_x , -g(w-B)B_y\right)^T . \tag{5.7}$$

Let the computational domain discretization $\Omega = \bigcup_{j=1}^{N} E_j$ be covered by a quadrilateral grids with the cellsE_j of size $|E_j|$. A typical cell E_j together with its neighbours $E_{jk}, k = 1,2,3,4$are outlined in Fig. 5.1.

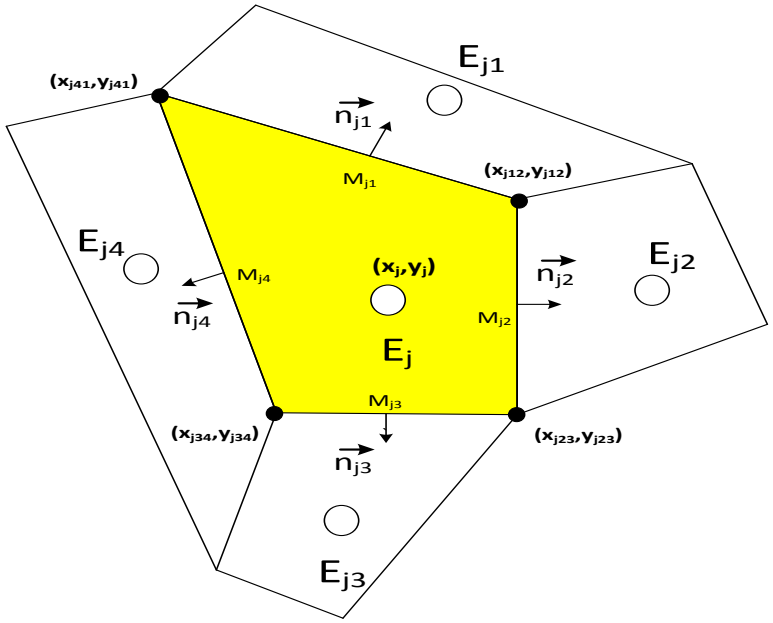

Fig. 5.1- An unstructured quadrilateral cell with its four neighbouring cells

We denote by $\vec{n}_{jk} := \left(\cos(\theta_{jk}), \sin(\theta_{jk})\right)$ the outer unit normals of the corresponding sides of E_j of length $l_{jk}, k = 1,2,3,4$. The coordinates of the geometric center (center of mass) of the $E_j$are denoted by (x_j, y_j) and $M_{jk} := (x_{jk}, y_{jk})$ is the midpoint of the $k-$th side of the quadrilateral $E_j, k = 1,2,3,4$.

In the semi discrete central-upwind scheme, the cell average of the computed solutions, $\bar{U}_j^{(t)} \approx \frac{1}{E_j}\int_{E_j} U(x,y,t)dxdy$, are evolved in time by solving the following system of ODEs:

$$\frac{d\bar{U}_j}{dt} = -\frac{1}{|E_j|}\sum_{k=1}^{4}\frac{l_{jk}\cos(\theta_{jk})}{a_{jk}^{in}+a_{jk}^{out}}\left[a_{jk}^{in}F\left(U_{jk}(M_{jk}),B(M_{jk})\right)+a_{jk}^{out}F\left(U_j(M_{jk}),B(M_{jk})\right)\right]$$

$$-\frac{1}{|E_j|}\sum_{k=1}^{4}\frac{l_{jk}\sin(\theta_{jk})}{a_{jk}^{in}+a_{jk}^{out}}\left[a_{jk}^{in}G\left(U_{jk}(M_{jk}),B(M_{jk})\right)+a_{jk}^{out}G\left(U_j(M_{jk}),B(M_{jk})\right)\right]$$

$$+\frac{1}{|E_j|}\sum_{k=1}^{4} l_{jk}\frac{a_{jk}^{in}a_{jk}^{out}}{a_{jk}^{in}+a_{jk}^{out}}\left[U_{jk}\left(M_{jk}\right)-U_j\left(M_{jk}\right)\right]+\bar{S}_j\,, \tag{5.8}$$

which can be derived similarly to the derivation procedure proposed for a triangular grids in (Kurganov andPetrova 2005; Bryson et al. 2011). Notice that all the indexed quantities in (5.8) are functions of t, but from now on we omit this dependence for the sake of brevity.

The values $U_j\left(M_{jk}\right)$ and $U_{jk}\left(M_{jk}\right)$ are the values at M_{jk} of the two polynomial pieces reconstructed in cells E_j and E_{jk}, respectively. The corresponding piecewise linear reconstruction is:

$$\widetilde{U}_j(x,y)=\bar{U}_j+(U_x)_j\left(x-x_j\right)+(U_y)_j(y-y_j). \tag{5.9}$$

To minimize the oscillations, the slopes $(U_x)_j$ and $(U_y)_j$ are to be computed using a nonlinear limiter. We propose the following minmod-type limiter which will be applied in a component wise manner. Consider the ith component of U we first construct four linear interpolations $L_j^{12}, L_j^{23}, L_j^{34}$ and L_j^{41}, each of which is obtained by considering the three points at the geometric center of E_j and corresponding two neighbouring cells. For example, L_j^{12} is obtained by passing the plane through $\left(x_j, y_j, \bar{U}_j^{(i)}\right)$, $\left(x_{j1}, y_{j1}, \bar{U}_{j1}^{(i)}\right)$ and $\left(x_{j2}, y_{j2}, \bar{U}_{j2}^{(i)}\right)$. Notice that all four of the obtained interpolants are conservative in the cell E_j by construction. We then select the linear piece with the smallest magnitude of the gradient, say L_j^{km}, and we set:

$$\left((U_x)_j^{(i)}, \left(U_y\right)_j^{(i)}\right)=\nabla L_j^{km}. \tag{5.10}$$

In order to further minimize the reconstruction oscillations, the reconstructed values calculated at the points $M_{jk}, k=1,2,3,4$ are checked. If the reconstructed value of $U_j^{(i)}\ \left(M_{jk}\right)$ is not between the cell averages $\bar{U}_j^{(i)}$and $\bar{U}_{jk}^{(i)}$, we set

$$\left((U_x)_j^{(i)}, \left(U_y\right)_j^{(i)}\right)=0. \tag{5.11}$$

The quantity $\bar{S}_j$ which is used in (5.8) is a discretization of the cell averages of the source term:

$$\bar{S}_j(t) \approx \frac{1}{|E_j|}\int_{E_j} S\big(U(x,y,t), B(x,y)\big)\, dxdy. \tag{5.12}$$

The well-balanced discretization form of the source term $\bar{S}_j$ will be discussed in Section 3.

Finally $a_{jk}^{in}$and a_{jk}^{out} in (5.8) are directional local speeds of propagation at the kth interface of the cell E_j, which are defined as the smallest and largest eigenvalues of the Jacobian

$$V_{jk} = \cos\big(\theta_{jk}\big)\frac{\partial F}{\partial U} + sin(\theta_{jk})\frac{\partial G}{\partial U} \tag{5.13}$$

with

$$a_{jk}^{in} = -min\left\{\lambda_1\left[V_{jk}\left(U_j\big(M_{jk}\big)\right)\right], \lambda_1\left[V_{jk}\left(U_{jk}\big(M_{jk}\big)\right)\right], 0\right\},$$

$$a_{jk}^{out} = max\left\{\lambda_3\left[V_{jk}\left(U_j\big(M_{jk}\big)\right)\right], \lambda_3\left[V_{jk}\left(U_{jk}\big(M_{jk}\big)\right)\right], 0\right\}, \tag{5.14}$$

where$\lambda_1[V_{jk}] \le \lambda_2[V_{jk}] \le \lambda_3[V_{jk}]$are the eigenvalues of V_{jk}.

It should be noted that if the $a_{jk}^{in}$and a_{jk}^{out} are zero or very close to zero, the semi discrete scheme (5.8) will reduce to:

$$\frac{d\bar{U}_j}{dt} = -\frac{1}{|E_j|}\sum_{k=1}^{4}\frac{l_{jk}\cos(\theta_{jk})}{2}\left[a_{jk}^{in}F\left(U_{jk}\big(M_{jk}\big), B\big(M_{jk}\big)\right) + a_{jk}^{out}F\left(U_j\big(M_{jk}\big), B\big(M_{jk}\big)\right)\right] -$$

$$\frac{1}{|E_j|}\sum_{k=1}^{4}\frac{l_{jk}\sin(\theta_{jk})}{2}\left[a_{jk}^{in}G\left(U_{jk}\big(M_{jk}\big), B\big(M_{jk}\big)\right) + a_{jk}^{out}G\left(U_j\big(M_{jk}\big), B\big(M_{jk}\big)\right)\right] + \bar{S}_j. \tag{5.15}$$

In all the numerical experiments reported in this paper, we have used (5.15) instead of (5.8) whenever $a_{jk}^{in} + a_{jk}^{out} < 10^{-8}$.

The semi-discretization (5.8) is a system of ODEs, which has to be integrated in time using a sufficiently accurate and stable ODE solver. In all of the numerical experiments, we have used the third-order strong stability preserving (SSP) Runge-Kutta method (Gottlieb et al. 2001; Gottlieb et al. 2011).

5.3. Piecewise linear approximation of the bottom

In this section, we describe how the bottom topography function $B(x,y)$is replaced by its continuous piecewise linear approximation $\tilde{B}(x,y)$. To this end, we first define values of the bottom topographyB_{j_κ} , $\kappa = 12{,}23{,}34{,}41$, at the vertices of the cell E_j. If the function $B(x,y)$ is continuous at the vertices we simply take $B_{j_\kappa} = B\left(x_{j_\kappa}, x_{j_\kappa}\right)$, otherwise we use the following formula:

$B_{j_\kappa} = \frac{1}{2}\left(\max_{\zeta^2+\eta^2=1} \lim_{h,l\to 0} B\left(\tilde{x}_{jk} + h\zeta, \tilde{y}_{jk} + l\eta\right) + \min_{\zeta^2+\eta^2=1} \lim_{h,l\to 0} B\left(\tilde{x}_{jk} + h\zeta, yjk + l\eta\right.\right.$.

By B_{jk} we denote the value of the bottom topography at the center of kth side of the cell E_j, which equals to the average of the values of the bottom topography at the two vertices of the corresponding side, for example, $B_{j1} = \frac{B_{j_{12}} + B_{j_{41}}}{2}$. Then, we approximate the value of the bottom topography at the geometric center of cell E_j as follows:

$$\int_{E_j} B(x,y)\, dxdy \approx \sum_{k=1}^{4} \mu_k B_{jk} =: B_j, \qquad (5.16)$$

where$\mu_k = |A_{jk}|/|E_j|$ and $|A_{jk}|$ is the area of the triangle whose first vertex is (x_j, y_j) and two other vertices are the vertices of the kth side of the cell E_j, see Fig. 5.2.

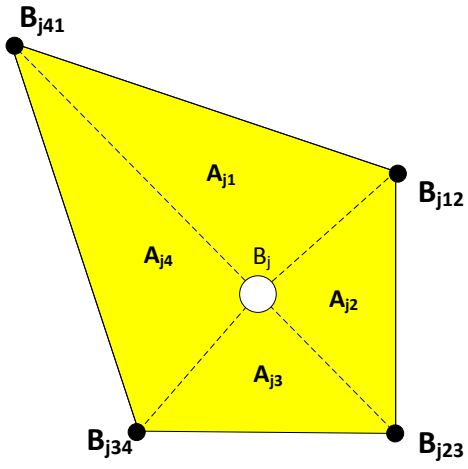

Fig. 5.2 - Subdividing cell $E_j$into four triangles $A_{j1}, A_{j2}, A_{j3}$and A_{j4}

This way, the bottom approximation in each cell will consist of four linear pieces that continuously match along the segments $[B_j, B_{j_\kappa}], \kappa = 12,23,34,41.$

Finally, we obtain the continuous piecewise linear approximation of the bottom topography $\tilde{B}(x,y) \approx B(x,y)$.

5.4. Positivity Preserving Reconstruction for Water Surface Elevation

In this section, we propose a simple and efficient algorithm for the positivity preserving reconstruction of water surface level. Generally, the reconstruction of w is positivity preserving if it leads to nonnegative computed values of water depth $h_j(M_{jk}), k = 1,2,3,4,$ for all the cells E_j in the computational domain. First we compute $h_j(M_{jk})$ using the reconstructed values of $\widetilde{w}$and $\tilde{B}$as follows:

$$h_j(M_{jk}) = \widetilde{w}_j(M_{jk}) - B_{jk}\,, k = 1,2,3,4. \tag{5.17}$$

However, some of the obtained values of $h_j(M_{jk})$ may be negative even where$\overline{w}_j \geq \quad B_j$. Therefore, we may need to correct the original reconstruction for w to ensure $h_j(M_{jk}) \geq 0$ for all j,k. In the proposed correction procedure, the correction is required when we have $\widetilde{w}(x_{j_\kappa}, y_{j_\kappa}) < B_{j_\kappa}$ at any of the vertices of the cell E_j (note that since $\overline{w}_j \geq B_j$ it is impossible to have $\widetilde{w}(x_{j_\kappa}, y_{j_\kappa}) < B_{j_\kappa}$ at all four vertices of the cell E_j). In this case we replace the original reconstruction of w by four linear planes over the same four triangles, as used in Section 2.1 to obtain the bottom topography approximation. To this end, we need to specify the new (corrected) values at each of the vertices. we set $w_{j_\kappa}^{corr} = B_{j_\kappa}$ at the vertices at which $\widetilde{w}(x_{j_\kappa}, y_{j_\kappa}) < B_{j_\kappa}$ and for the rest of vertices we set $w_{j_\kappa}^{corr} = h^*{}_j + B_{j_\kappa}$ where,

$$h_j^* = \frac{\overline{w}_j - B_j}{\sum_1^4 \mu_k \alpha_k}\,, \alpha = \begin{cases} 1, & if\ \widetilde{w} \geq \tilde{B}\ at\ both\ ends\ of\ the\ k^{th}\ side\ of\ E_j, \\ \frac{1}{2}, & if\ \widetilde{w} \geq \tilde{B}\ at\ one\ of\ the\ ends\ of\ the\ k^{th}\ side\ of\ E_j, \\ 0, & if\ \widetilde{w} < \tilde{B}\ at\ both\ ends\ of\ the\ k^{th}\ side\ of\ E_j, \end{cases} \tag{5.18}$$

and, as before, $\mu_k = |A_{jk}|/|E_j|$. We also set $w_j^{corr} = \bar{w}_j$ to be the value of w at the geometric center of E_j. One can show that the corrected reconstruction of w, which consists of four linear pieces in the cell E_j, is conservative. Indeed,

$$\frac{1}{|E_j|}\int_{E_j}\left[\tilde{w}_j^{corr}(x,y) - B(x,y)\right]dxdy = \frac{1}{|E_j|}\sum_{k=1}^{4}\int_{A_{jk}}\left[\tilde{w}_j^{corr}(x,y) - B(x,y)\right]dxdy$$

$$= \sum_{k=1}^{4}\frac{(\bar{w}_j - B_j) + 2\alpha_{jk}h^*}{3}\mu_{jk} = \frac{\bar{w}_j - B_j}{3} + \frac{2}{3}h^*\sum_{k=1}^{4}\alpha_{jk}\mu_{jk} = \bar{w}_j - B_j,$$

which implies that

$$\frac{1}{|E_j|}\int_{E_j}\tilde{w}_j^{corr}(x,y)dxdy = \bar{w}_j. \qquad (5.19)$$

Also note that since the linear pieces of the corrected reconstruction of w are over the same triangles $A_{jk}, k = 1,2,3,4$ as the linear pieces of the $\tilde{B}$, all of the obtained values of h will be nonnegative.

Having the corrected reconstruction $\tilde{w}$, we continue with the computation of the velocities u and v, and the one-sided local speeds needed in (5.8). Since the computed values of water depth h may be very small (or even zero), we use the following desingularization procedure to calculate the velocities (Bryson et al. 2011):

$$u = \frac{\sqrt{2}h(hu)}{\sqrt{h^4 + \max(h^4, \varepsilon)}} \text{ and } v = \frac{\sqrt{2}h(hv)}{\sqrt{h^4 + \max(h^4, \varepsilon)}},$$

where ε is a prescribed positive tolerance. In all our numerical tests, we have used $\varepsilon = \max\{|Ej|^2\}$. After computing h, u, and v, we recompute the flux vectors F and G as

$$(hu) = h \cdot u,$$

$$(hv) = h \cdot v,$$

$$F(U,B) = \left(hu, hu \cdot u + \frac{g}{2}(w - B)^2, hu \cdot v\right)^T,$$

$$G(U,B) \quad = \left(hv, hv\cdot u, hv\cdot v + \frac{g}{2}(w-B)^2\right)^T, \tag{5.20}$$

at the corresponding points used in (5.8). Now, we are also able to compute the one-sided speeds of propagation:

$$a_{jk}^{in} = -min\left\{u_j^{\theta}(M_{jk}) - \sqrt{gh_j(M_{jk})}, u_{jk}^{\theta}(M_{jk}) - \sqrt{gh_{jk}(M_{jk})}, 0\right\},$$

$$a_{jk}^{out} = max\left\{u_j^{\theta}(M_{jk}) + \sqrt{gh_j(M_{jk})}, u_{jk}^{\theta}(M_{jk}) + \sqrt{gh_{jk}(M_{jk})}, 0\right\},$$

$$u_j^{\theta}(M_{jk}) = \cos(\theta_{jk})\,u_j\ (M_{jk}) + \sin(\theta_{jk})\,v_j\ (M_{jk})\,, u_{jk}^{\theta}(M_{jk}) = \cos(\theta_{jk})\,u_{jk}(M_{jk}) + \sin(\theta_{jk})\,v_{kj}(M_{jk}), \tag{5.21}$$

where$u_j^{\theta}(M_{jk})$ and $u_{jk}^{\theta}(M_{jk})$ are the normal velocities at the midpoint of the kth side M_{jk}.

5.5. Well-Balanced Discretization of the Source Term

Here, we propose a new well-balanced discretization of the source term for unstructured quadrilateral grids. Indeed, the proposed semi-discrete central-upwind scheme (5.8) includes the cell averages of the source term $\bar{S}_j$. Recall that a well- balanced scheme should exactly preserve steady-state solutions. For this aim, a specific quadrature must be designed in order to exactly preserve a "lake at rest" with $w \equiv C$, $u \equiv v \equiv 0$, where C is a constant. In this case, the two momentum equations in (5.8) will become:

$$-\frac{g}{2|E_j|}\sum_{k=1}^{4} l_{jk}\cos(\theta_{jk})(C - B_{jk})^2 + \bar{S}_j^{(2)} = 0,$$

$$-\frac{g}{2|E_j|}\sum_{k=1}^{4} l_{jk}\sin(\theta_{jk})(C - B_{jk})^2 + \bar{S}_j^{(3)} = 0, \tag{5.22}$$

We now design an appropriate quadrature in order to satisfy the well-balancing conditions (5.22). First, we use the divergence theorem,$\int_{E_j} div\ \vec{\varsigma} dxdy = \int_{\partial E_j} \vec{\varsigma}.\vec{n} ds$, to obtain

$$\bar{S}_j^{(2)} = -\frac{g}{|E_j|}\int_{E_j}\big(w(x,y)-B(x,y)\big)B_x dxdy$$

$$= -\frac{g}{|E_j|}\sum_{k=1}^{4}\int_{\partial E_{jk}}\frac{\big(w(x,y)-B(x,y)\big)^2}{2}\cos(\theta_{jk})\,ds - \frac{g}{|E_j|}\int_{E_j}\big(w(x,y)-B(x,y)\big)w_x dxdy \quad (5.23)$$

where ∂E_{jk} is the kth side of the quadrilateral $E_j, k = 1,2,3,4$. Due to the correction of water surface reconstruction, it may happen that we have four linear planes, instead of one, for each cell E_j, with different w_x. Thus, the second integral on the RHS of (5.23) should be subdivided into four integrals over $A_{jk}, k = 1,2,3,4$ (see Fig. 5.2):

$$-\frac{g}{|E_j|}\int_{E_j}\big(w(x,y)-B(x,y)\big)w_x dxdy = -\frac{g}{|E_j|}\sum_{k=1}^{4}\int_{A_{jk}}\big(w(x,y)-B(x,y)\big)w_x dxdy \quad (5.24)$$

Finally, applying the midpoint rule to the integrals on the RHS of (5.23) and (5.24) and replacing B with its piecewise linear approximant $\tilde{B}$, we arrive at the following quadrature for the cell average $\bar{S}_j^{(2)}$,:

$$\bar{S}_j^{(2)} = \frac{g}{|E_j|}\sum_{k=1}^{4}\left[\frac{\big(w(M_{jk})-B(M_{jk})\big)^2}{2}\cos(\theta_{jk})\,l_{jk} - \big(\bar{w}_j - B_j\big)(w_x)_{jk}\right]. \quad (5.25)$$

Similarly, we obtain the quadrature for the cell average $\bar{S}_j^{(3)}$,:

$$\bar{S}_j^{(3)} = \frac{g}{|E_j|}\sum_{k=1}^{4}\left[\frac{\big(w(M_{jk})-B(M_{jk})\big)^2}{2}\sin(\theta_{jk})\,l_{jk} - \mu_{jk}\big(\bar{w}_j - B_j\big)(w_y)_{jk}\right]. \quad (5.26)$$

It should be noted that for the lake at rest with $U \equiv (C,0,0)^T$, we have $w \equiv C$ and $w_y \equiv w_x \equiv 0$, and the designed quadratures (5.25) and (5.26) satisfy (5.22).

5.6. Positivity preserving property of the scheme

In this section, we prove the positivity preserving property of the proposed scheme. The prove is valid either for the forward Euler or any higher-order SSP Runge-Kutta method used for time discretization of the system of ODEs. For the sake of brevity, we formulate the result for the forward Euler method.

Theorem 1. *Consider the proposed central-upwind scheme (5.8), (5.9), (5.21) and (5.28) for the system (5.3)-(5.7). Assume that the forward Euler method is used for solving the system of ODEs (5.8) while* $w_j^n \geq B_j$ *for all* j *at time* $t = t^n$. *Then,* $w_j^{n+1} \geq B_j$ *for all* j *at* $t = t^{n+1}$, *provided that*

$$\Delta t \leq \frac{1}{2a} \min_{j,k}\{d_{jk}\}, \tag{5.27}$$

where $a = \max_{j,k}\{a_{jk}^{in}, a_{jk}^{out}\}$ *and* d_{jk} *is the distance between the center of mass of cell* E_j *and its* k*-th side.*

Proof. Using the forward Euler time stepping method for the first component of the system (5.8) we obtain

$$\begin{aligned}\bar{w}_j^{n+1} = \bar{w}_j^n &- \frac{\Delta t}{|E_j|}\sum_{k=1}^{4}\frac{l_{jk}\cos(\theta_{jk})}{a_{jk}^{in}+a_{jk}^{out}}\left[a_{jk}^{in}(hu)_{jk}(M_{jk}) + a_{jk}^{out}(hu)_j(M_{jk})\right] \\ &- \frac{\Delta t}{|E_j|}\sum_{k=1}^{4}\frac{l_{jk}\sin(\theta_{jk})}{a_{jk}^{in}+a_{jk}^{out}}\left[a_{jk}^{in}(hv)_{jk}(M_{jk}) + a_{jk}^{out}(hv)_j(M_{jk})\right] \\ &+ \frac{\Delta t}{|E_j|}\sum_{k=1}^{4}\frac{a_{jk}^{in}a_{jk}^{out}}{a_{jk}^{in}+a_{jk}^{out}}\left[w_{jk}(M_{jk}) - w_j(M_{jk})\right].\end{aligned} \tag{5.28}$$

Since the piecewise linear interpolant $\tilde{B}$ of the bottom topography is continuous, one has:

$$w_{jk}(M_{jk}) - w_j(M_{jk}) = h_{jk}(M_{jk}) - h_j(M_{jk}). \tag{5.29}$$

In addition, (5.16), (5.17) and $\bar{w}_j^n = \sum_{k=1}^{4}\mu_{jk}\, w_j(M_{jk})$ implythat $\bar{w}_j^n - B_j = \sum_{k=1}^{4}\mu_{jk}\, h_j(M_{jk})$.

(5.30)

From (5.28) and (5.29), replacing B_j from both sides of (5.30) and using the notation (5.21), we write,

$$\bar{h}_j^{n+1} = \frac{\Delta t}{|E_j|}\sum_{k=1}^{4} h_{jk}(M_{jk})\frac{l_{jk}a_{jk}^{in}}{a_{jk}^{in}+a_{jk}^{out}}\left[a_{jk}^{out} - u_{jk}^{\theta}(M_{jk})\right]$$

$$+\sum_{k=1}^{4} h_{jk}(M_{jk})\left(\mu_{jk} - \frac{\Delta t}{|E_j|}\frac{l_{jk}a_{jk}^{out}}{a_{jk}^{in}+a_{jk}^{out}}\left[a_{jk}^{in} + u_j^{\theta}(M_{jk})\right]\right). \quad (5.31)$$

From the definitions of the local speeds (5.21) we obtain that $a_{jk}^{out} \geq u_{jk}^{\theta}(M_{jk})$ and therefore, all terms in the first sum on the RHS of (5.31) are nonnegative since the corrected reconstruction for w guarantees that $h_{jk}(M_{jk}) \geq 0$ for all j and $k = 1, 2, 3, 4$.We also obtain that

$$\frac{\Delta t}{|E_j|}\frac{l_{jk}a_{jk}^{out}}{a_{jk}^{in}+a_{jk}^{out}}\left[a_{jk}^{in} + u_j^{\theta}(M_{jk})\right] \leq \frac{\Delta t}{|E_j|} l_{jk}a_{jk}^{out}. \quad (5.32)$$

Thus, the positivity of the second termon the RHS of (5.31) is guaranteed provided

$$\Delta t \leq \frac{\mu_{jk}|E_j|}{l_{jk}a_{jk}^{out}}. \quad (5.33)$$

Recall that $\mu_k = A_{jk}/|E_j|$and $A_{jk} = \frac{d_{jk}l_{jk}}{2}$, hence (5.35) becomes $\Delta t \leq \frac{1}{2a}\min_{j,k}\{d_{jk}\}$, and this completes the proof of the thoreme. □

Remark. In all our numerical tests, adaptive time step is implemented in all the numerical examples and it is selected to satisfy the condition (5.27).

5.7. Numerical Experiments

In this section, we apply our proposed central-upwind scheme on unstructured quadrilateral grids to several test problems. We perform the numerical experiments using the organized unstructured grids shown in Fig. 5.3. However, we would like to point out that the proposed method can be applied on any quadrilateral grids. In all examples below, the gravitational constant is $g = 1$.

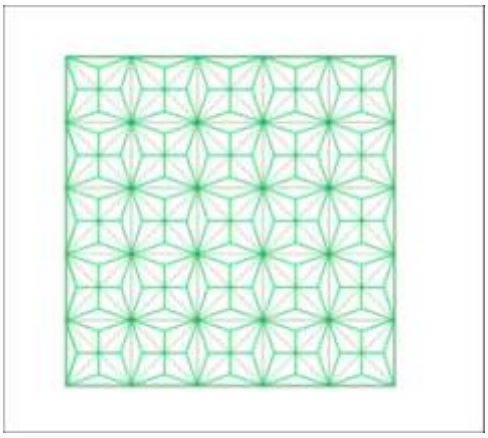

Fig. 5.3 - Organized unstructured quadrilateral mesh.

Example 1 – Accuracy test

In the first example, we experimentally test the order of accuracy of the proposed scheme. The scheme is applied to the following initial data and bottom topography:

$$w(x,y,0) = 1, u(x,y,0) = 0.3, B(x,y) = 0.5\exp(-25(x-1)^2 - 50(y-0.5)^2). \quad (5.36)$$

The computational domain is [0, 2] × [0, 1] and the transparency conditions are imposed at all its boundaries. We use a fine grid with $6 \times 400 \times 400$cells and consider the obtained results as a reference solution. The solution converges to the steady state by the time $t = 0.07$. The L^1- and L^∞-errors are presented in Table 5.1.

Table 5.1 - Example1: L^1- and L^∞-errors and numerical orders of accuracy.

Number of cells	L^1-error	order	L^∞-error	order
$\mathbf{6 \times 50 \times 50}$	$3.61\,e-04$	-	$7.45\,e-03$	-
$\mathbf{6 \times 100 \times 100}$	$1.48\,e-04$	1.29	$3.09\,e-03$	1.27
$\mathbf{6 \times 200 \times 200}$	$4.27\,e-05$	1.80	$9.38\,e-04$	1.72

Comparing the results with those reported in Bryson et al. (2011) shows that the obtained orders are higher. The water surface computed at $t = 0.07$ using the mesh with $6 \times 50 \times 50$ quadrilaterals is shown inFig. 5.4. Although a relatively coarse mesh has been used, the water surface is well resolved by the scheme.

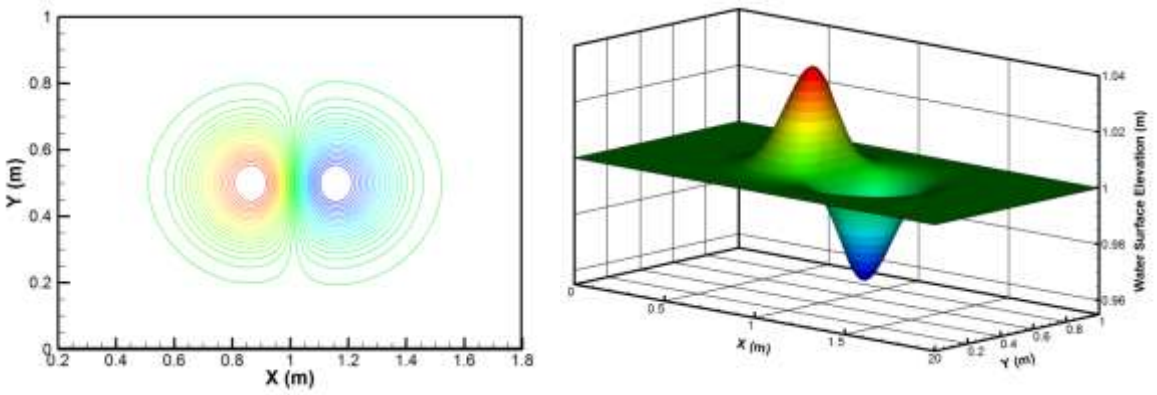

Fig. 5.4 - Example1: Contour plot (left) and 3D view (right) of w.

Example 2 - Small Perturbation over an Exponential Hump

In this numerical experiment, originally proposed in (LeVeque 1998) and then widely used in the literature (Xing et al. 2010; Xing and Shu 2005; Bryson et al. 2011), we investigate the capability of the proposed scheme to accurately capture the propagation of a small perturbation of the "lake at rest" steady state. The computational domain is [0, 2] × [0, 1] and the bottom consists of an elliptically shaped hump:

$$B(x,y) = 0.8\exp(-5(x-0.9)^2 - 50(y-0.5)^2). \quad (5.37)$$

The water initially is at rest and its surface is flat everywhere except for 0.05 < x < 0.15:

$$w(x,y,0) = \begin{cases} 1+\epsilon, & 0.05 < x < 0.15 \\ 1, & otherwise, \end{cases}, \quad u(x,y,0) \equiv v(x,y,0) \equiv 0, \quad (5.38)$$

whereε is the perturbation height. The transparency boundary conditions are implemented at vertical boundaries of the domain while the horizontal boundaries are periodic. First, in order to numerically verify the well-balanced property of the proposed scheme, a very small $\varepsilon = 10^{-12}$ is selected and the solution is computed using a coarse mesh with $6 \times 10 \times 10$cells. $Max\ (w-1)$as a function of t is plotted in Fig. 5.5 and it can be clearly seen that no instabilities are developed and the balance between the fluxes and the geometric source terms is exactly preserved numerically.

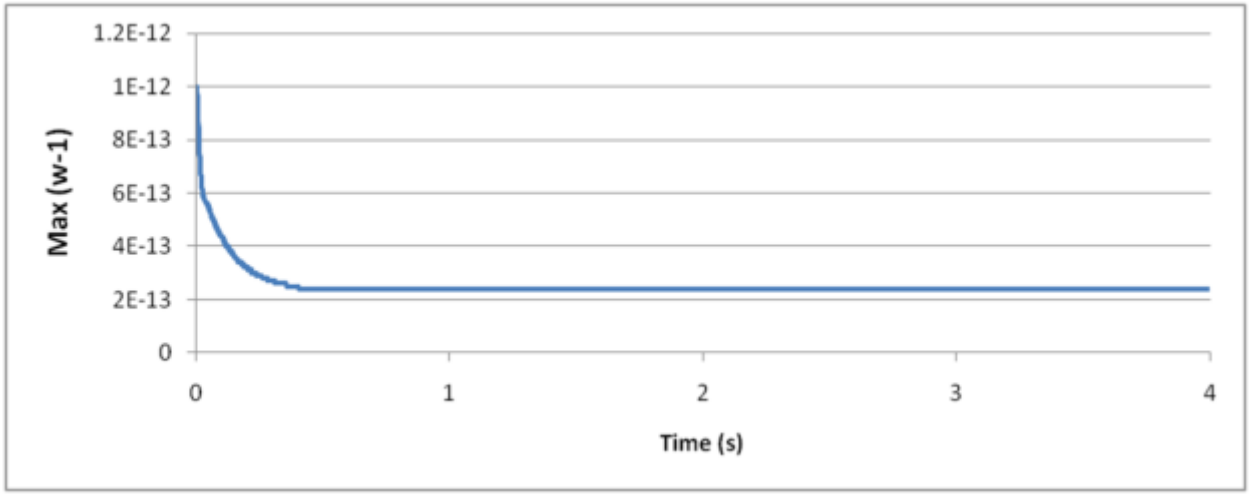

Fig. 5.5 - Example2: max$(w-1)$ as a function of $t$for $\varepsilon = 10^{-12}$.

Next, a larger perturbation height $\varepsilon = 10^{-4}$, is selected. The 3D view of water surface elevation computed using the mesh with $6 \times 100 \times 100$ cells at $t = 0.6, 0.9, 1.2, 1.5$ and 1.8 is shown in Fig. 5.6. It can be seen that the water surface is well resolved and it is free of noises and spurious waves.

In order to show the importance of well-balanced property of the scheme, we apply a non-well-balanced version of our scheme to the initial-boundary value problem with $\varepsilon = 10^{-4}$. To obtain the non-well-balanced scheme, the proposed well-balanced quadrature (5.28) is replaced with a straightforward midpoint rule discretization:

$$\bar{S}_j^{(2)} = -g\left(\overline{w_j} - B_j\right)B_x\,,\ \bar{S}_j^{(3)} = -g\left(\overline{w_j} - B_j\right)B_y. \tag{5.39}$$

The non-well-balanced solution (water surface) computed at times $t = 0.6, 0.9, 1.2, 1.5$ and 1.8 on the same grid is shown in Fig. 5.7 (right column) and compared with the results obtained from the proposed well-balanced scheme (left column).

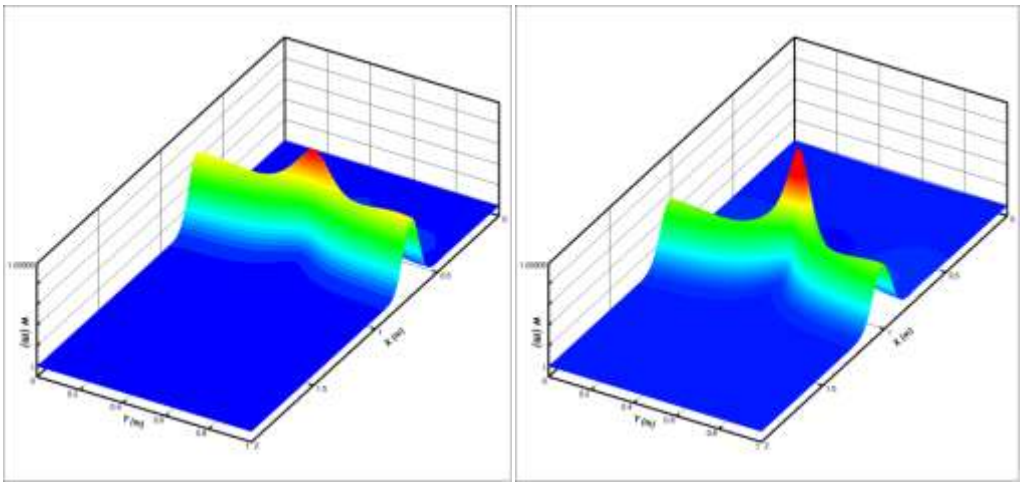

t=0.6 t=0.9

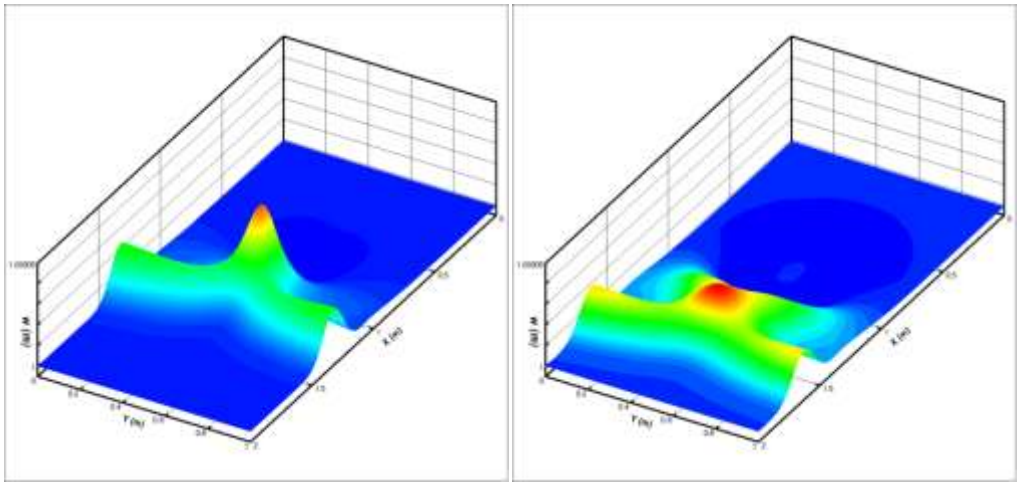

t=1.2 t=1.5

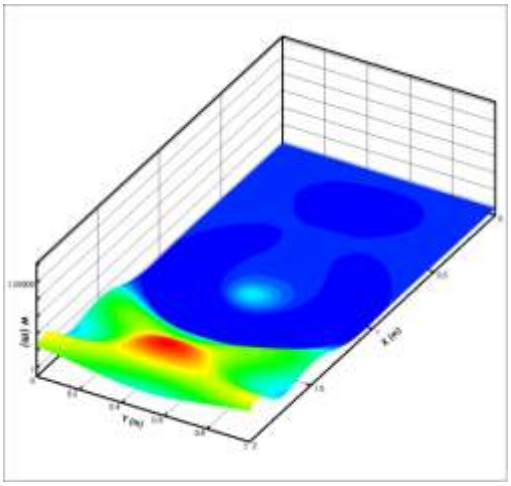

t=1.8

Fig. 5.6 - Example2: 3D view of w computed using the mesh with $6 \times 100 \times 100$ cells for $\varepsilon = 10^{-4}$.

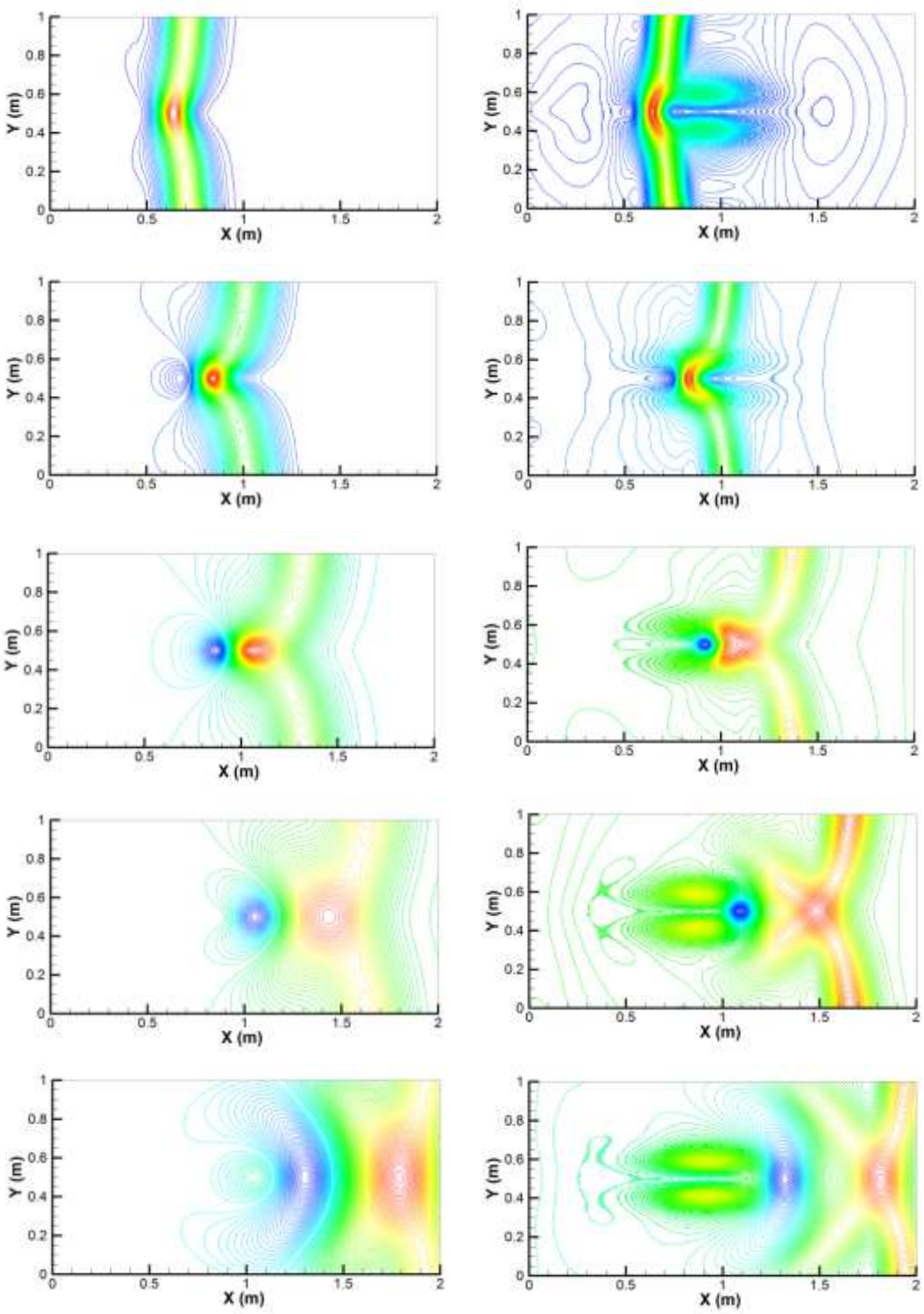

Fig. 5.7- Example2: w for $\varepsilon = 10^{-4}$ computed using the well-balanced (left column) and non-well-balanced (right column) schemes.

One can see that in this case, even with the larger value of ε, there are spurious waves propagating in the domain and their magnitudes are close to the magnitude of the perturbation. This can evidently prove the advantage of the well-balanced proposed quadrature (5.28) used for source term discretization.

Example 3 - Small Perturbation over Submerged Flat Plateau

In this numerical test, taken from Bryson et al. (2011), we study the case of a submerged flat plateau as schematically shown in Fig. 5.8. Notice that in this example, the plateau is very close to the water surface, and that the initial water depth over the plateau is close to the perturbation height $\varepsilon = 10^{-4}$. The computational domain is [0,1]×[0,1] and the bottom topography is given by

$$B(x,y) = \begin{cases} 1-2\epsilon, & r \le 0.1, \\ 10(1-2\epsilon)(0.2-r), & 0.1 \le r \le 0.2, \\ 0, & otherwise, \end{cases} \tag{5.40}$$

where $r = \sqrt{(x-0.5)^2 + (y-0.5)^2}$ and the initial data are:

$$w(x,y,0) = \begin{cases} 1+\epsilon, & 0.1 \le x \le 0.2 \\ 1, & otherwise, \end{cases}, u(x,y,0) \equiv v(x,y,0) = 0. \tag{5.41}$$

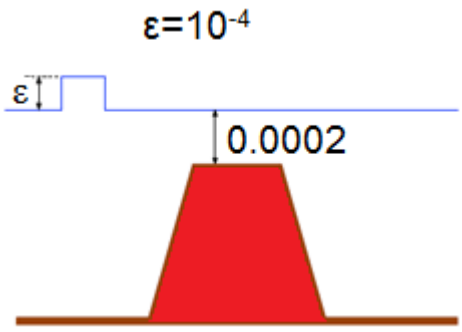

Fig. 5.8 - Example3: 1D slice of bottom topography (5.40). The plot is not to scale.

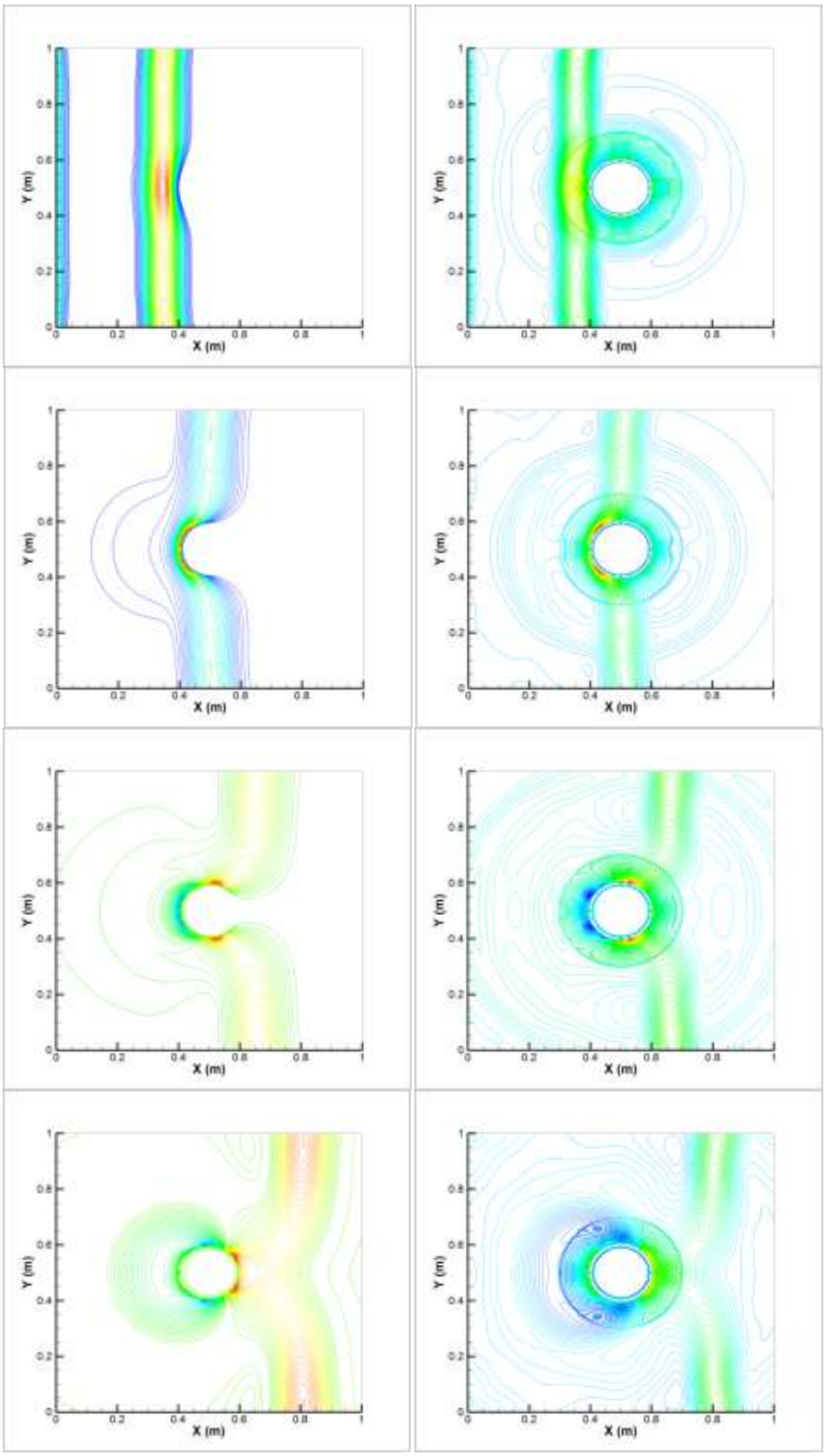

Fig. 5.9 - Example3: *w* computed by the proposed well-balanced (left) and non-well-balanced (right) schemes.

The transparency boundary conditions are implemented at vertical boundaries of the domain while the horizontal boundaries are periodic. The solution is computed by the proposed well-balanced central-upwind scheme using $6 \times 100 \times 100$ quadrilateral cells and the obtained water surface w is plotted in Fig. 5.9 (left column) at $t = 0.2, 0.35, 0.5\ and\ 0.65$. As one can observe, the general structure of the solution is well captured by the proposed method and there is no spurious wave propagating in the domain.

The water surface w computed using the non well-balanced scheme on the same grid with $6 \times 100 \times 100$ cells is shown in Fig. 5.9 (right column).

As Fig. 5.9 shows, the spurious waves generated around the plateau dominate the solution. Comparing the results to those computed by the proposed well-balanced scheme, instructively shows the advantage of the well-balanced scheme.

Example 4 - Small Perturbation Bending around a Round-Shape Island

In this example, we examine both well-balanced and positivity preserving properties of the new scheme by testing its ability to handle a situation with a small perturbation of a "lake at rest" propagating around an island.

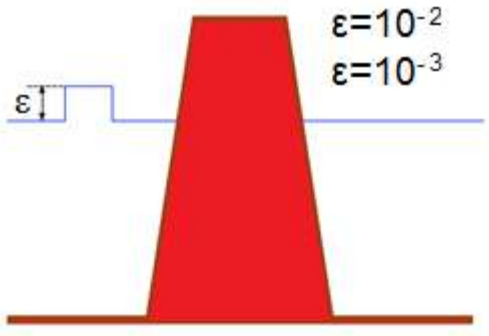

Fig. 5.10 - Example4: 1D slice of the bottom topography (5.42). The plot is not to scale.

The bottom hump is above the water surface so that there is a disk-shaped island at the origin,

$$B(r) = \begin{cases} 1.1, & r \le 0.1, \\ 11(0.2 - r), & 0.1 < r < 0.2 \\ 0, & otherwise, \end{cases},$$

(5.42)

seeFig. 5.10. The computational domain is [0,1] ×[0,1]and the initial conditions are given by

$$w(x,y,0) = \begin{cases} 1 + \epsilon, & 0.1 < x < 0.2 \\ \max\ \{1, B\left(\sqrt{x^2 + y^2}\right)\}, & otherwise, \end{cases}, u(x,y,0) \equiv v(x,y,0) = 0. \quad (5.43)$$

3D-view of the water surface w computed at times $t = 0.2, 0.35, 0.5$ and 0.65 using $6 \times 100 \times 100$ cells with $\varepsilon = 10^{-2}$is shown in Fig. 5.11 where the right-going disturbance bends around the island. Though there are dry and almost dry cells which are changing their wet/dry status repetitively, the solution obtained by the proposed central-upwind scheme is non-oscillatory and well resolved. In order to make the experiment more challenging, we set $\varepsilon = 10^{-3}$. The water surface w computed at times $t = 0.2, 0.35, 0.5$ and 0.65 using -$6 \times 100 \times 100$ cells is presented in Fig. 5.12 (left column). To test the numerical convergence of the proposed method, we refine the mesh and use $6 \times 200 \times 200$ cells. The obtained results, plotted in Fig. 5.12 (right column), demonstrate nice convergence property of the developed central-upwind scheme.

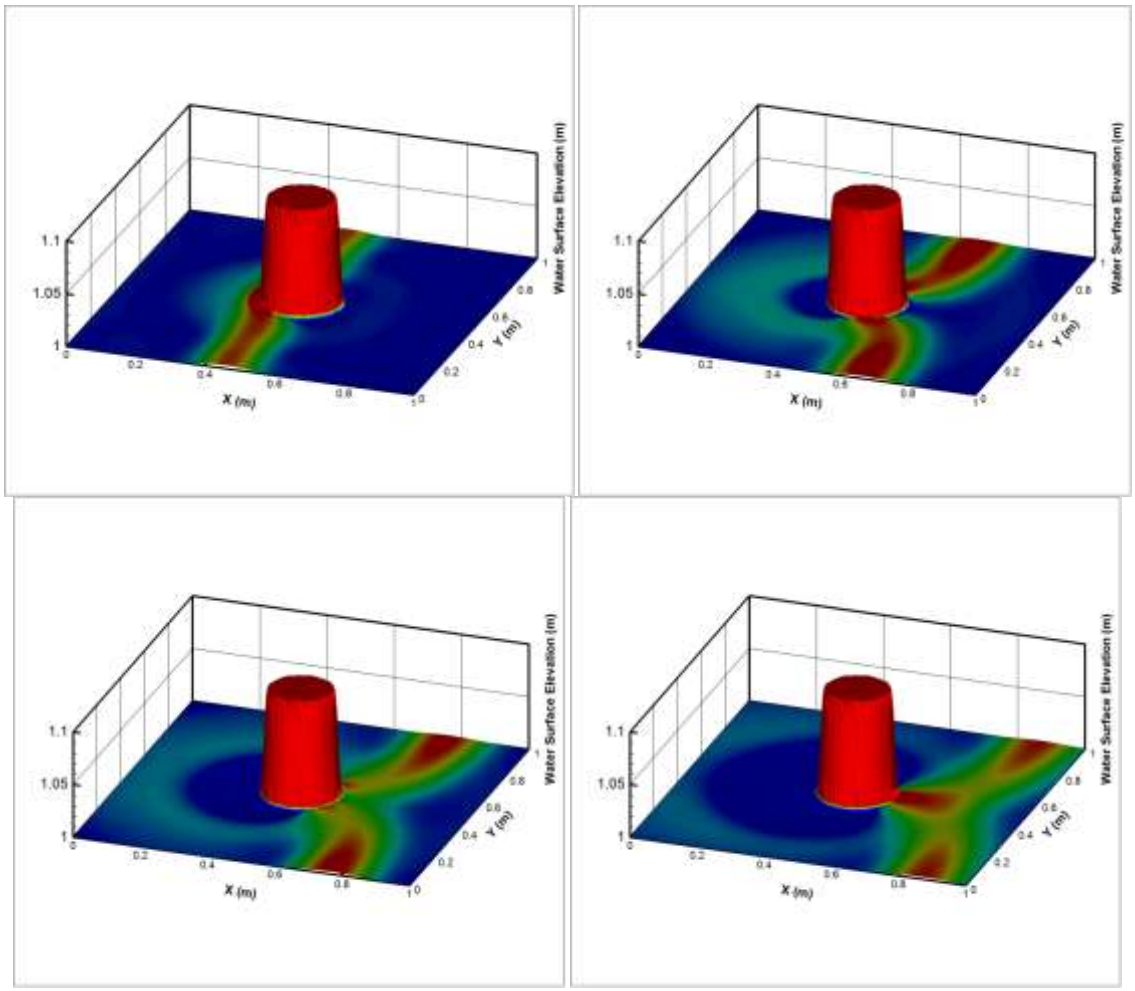

Fig. 5.11 - Example4: 3D view of w for $\varepsilon = 10^{-2}$ computed using $6 \times 100 \times 100$ quadrilaterals

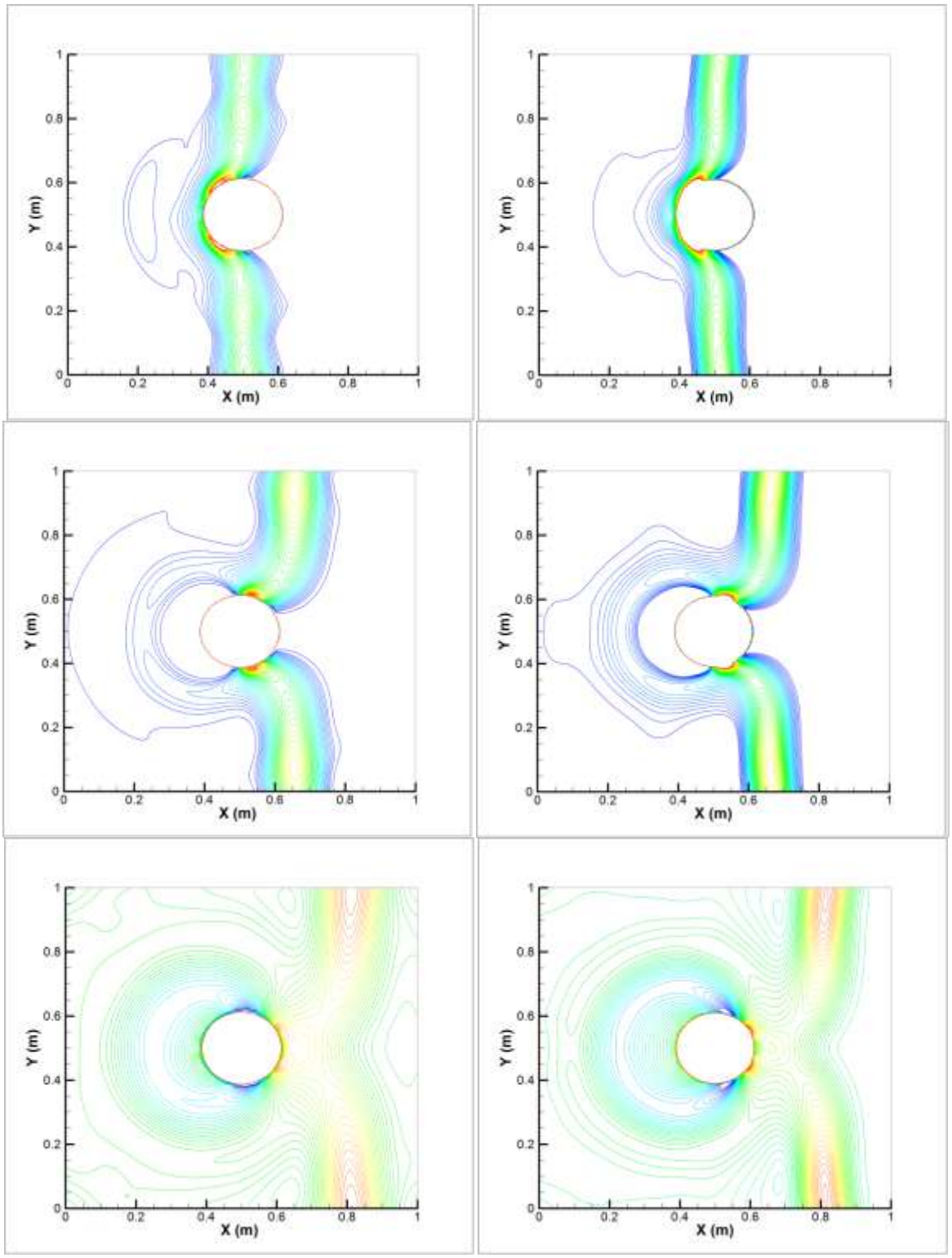

Fig. 5.12 - Example4: w with $\varepsilon = 10^{-3}$ computed using the grids with $6 \times 100 \times 100$ (left column) and $6 \times 200 \times 200$ (right columns) cells.

Example 5 - Dam Break over Discontinuous Bottom Topography

In the final example, we not only verify the ability and robustness of the proposed central-upwind scheme on the quadrilateral grid, but also demonstrate an advantage of the proposed scheme over the triangular central-upwind scheme from Bryson et al. (2011). The computational domain is $[-4,4] \times [-4,4]$ and a cylindrical dam is assumed to be placed on a dry island with the following bottom topography:

$$B(x,y) = \begin{cases} 1, & |x| + |y| \le 2, \\ 0, & otherwise. \end{cases} \tag{5.44}$$

The water is initially at rest ($u(x,y,0) \equiv v(x,y,0) \equiv 0$) and the water level is given by

$$w(x,y,0) = \begin{cases} 9, & x^2 + y^2 \le 1, \\ 1, & x^2 + y^2 > 1 \; and \; |x| + |y| \le 2, \\ 0, & otherwise. \end{cases} \tag{5.45}$$

The initial setting is shown in Fig. 5.13.

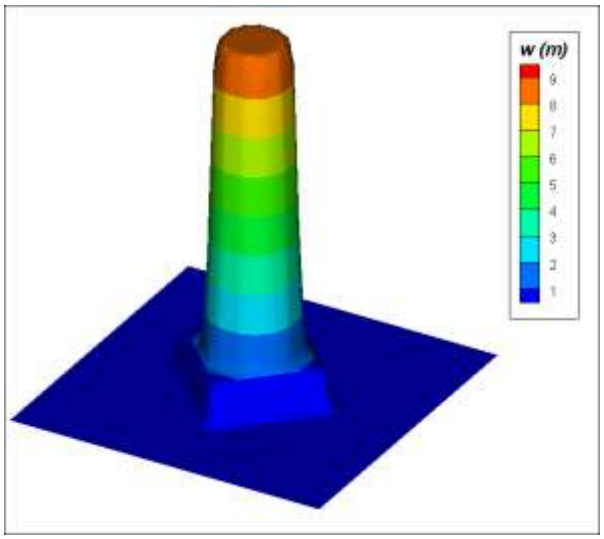

Fig. 5.13 - Example5: 3D view of the bottom topography (5.44) and initial water surface (5.45).

The dam is getting broken at time $t = 0$. The flow structure after the dam break is very complex. In order to make a proper comparison between the proposed scheme on the quadrilateral grid and the triangular central-upwind scheme, we keep the number of cells (cell areas) equal in both cases. In Fig. 5.14, we plot 1D cross sections of the computed solutions at $y = 0$. The water surface w component of the solution computed at $t = 0.6$ by the new scheme using $6 \times 50 \times 50$ quadrilateral cells and by the triangular central-upwind scheme using $4 \times 62 \times 62$ triangular cells are shown in Fig. 5.14 (left). One can clearly see that the water surface structure is resolved more accurately by the proposed quadrilateral central-upwind scheme. We then refine the mesh and use $6 \times 100 \times 100$ quadrilaterals versus $4 \times 124 \times 124$ triangular cells. The finer results are presented in Fig. 5.14 (right). Evidently, even with a finer mesh, the structure of solution is better resolved by the proposed scheme.

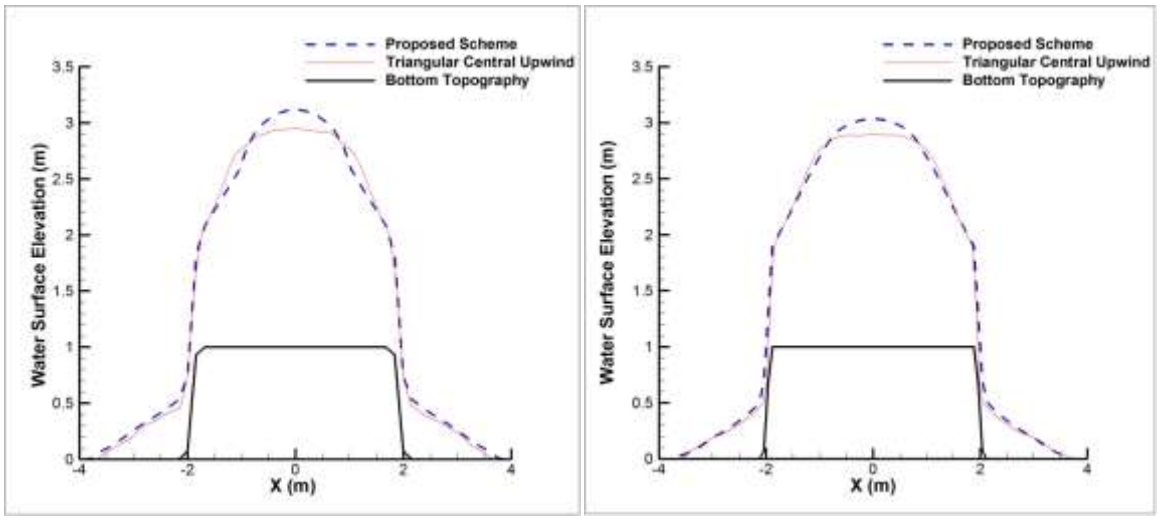

Fig.5.14 - Example5: 1D slices of w computed using the proposed quadrilateral and triangular central-upwind schemes using coarser (left) and finer (right) grids.

The contour lines of the water surface w computed at $t = 0.6$ using the finer grids are presented in Fig. 5.15. One can clearly observe that the proposed scheme on a quadrilateral grid has captured and resolved the complex flow patterns, both over and around the island,

with a significantly higher resolution. In addition, some fluctuations can be observed in the water surface computed by the triangular scheme, while the one obtained using quadrilateral grids is well resolved and free of fluctuations.

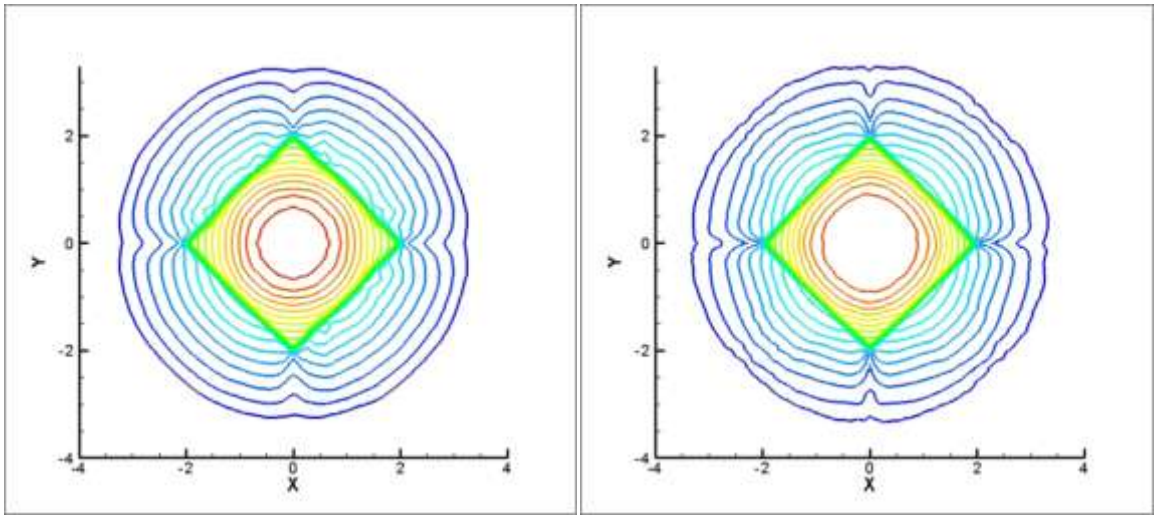

Fig. 5.15 - Example5: Contour plots of w at $t = 0.6$using the proposed quadrilateral (left) and triangular (right) central-upwind schemes.

The velocity ($u$and v) components of the solution computed at $t = 0.6$ using both the coarser and finer grids are also presented in Fig. 5.16. One can clearly observe that although u computed by both schemes are quite close, the velocity computed by the proposed method is smoother and the velocity spark over the island is much lower (Fig. 5.16a). However, by refining the mesh the results become closer (Fig. 5.16b). For the v component of the solution, one can see that the results obtained from the triangular grids is noisy, while those computed using the quadrilateral grids are completely smooth and free of oscillations and fluctuations (Fig. 5.16c). In addition, one can see that even by refining the mesh, the results of the triangular central-upwind scheme keep fluctuating (Fig. 5.16d).

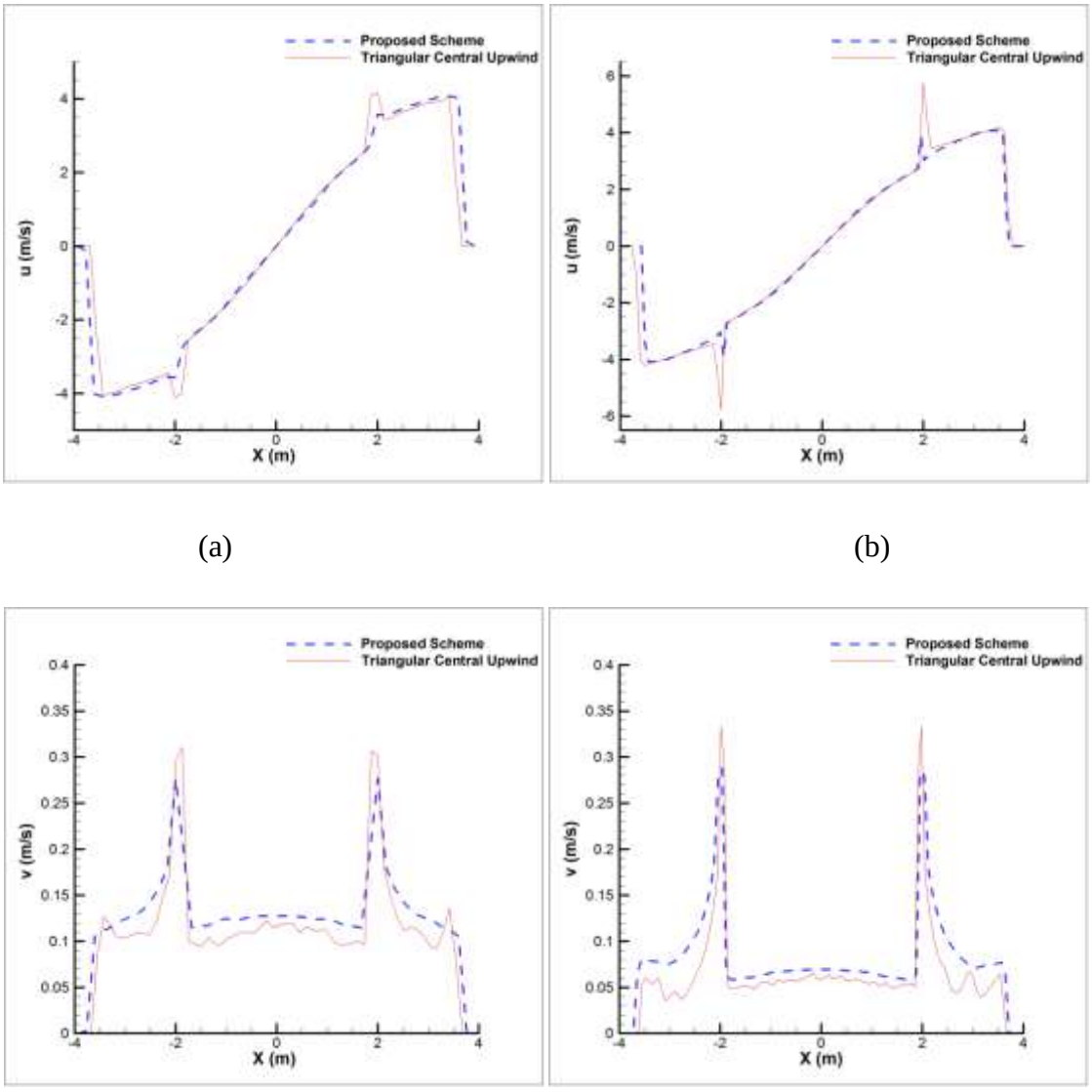

Fig. 5.16 - Example5: 1D slices of u computed using (a) the coarser grids with $6 \times 50 \times 50$ quadrilateral cells ($4 \times 62 \times 62$ triangular cells); (b) finer grids with $6 \times 100 \times 100$ quadrilateral cells ($4 \times 124 \times 124$ triangular cells) ; and v computed using (c) the coarser and (d) finer grids.

Finally, in Fig. 5.17, the time evolution of the v component of the solution computed on the finer grids is illustrated at $t = 0.2, 0.3, 0.4, 0.5$ for both schemes. It clearly shows that the proposed scheme has a better performance in predicting the velocity. The results of

time evolution of v component of the solution (not shown here) also confirm that the velocity field computed by the triangular central-upwind scheme is noisy, while the one computed by the developed scheme on the quadrilateral grid is quite smooth and oscillation-free.

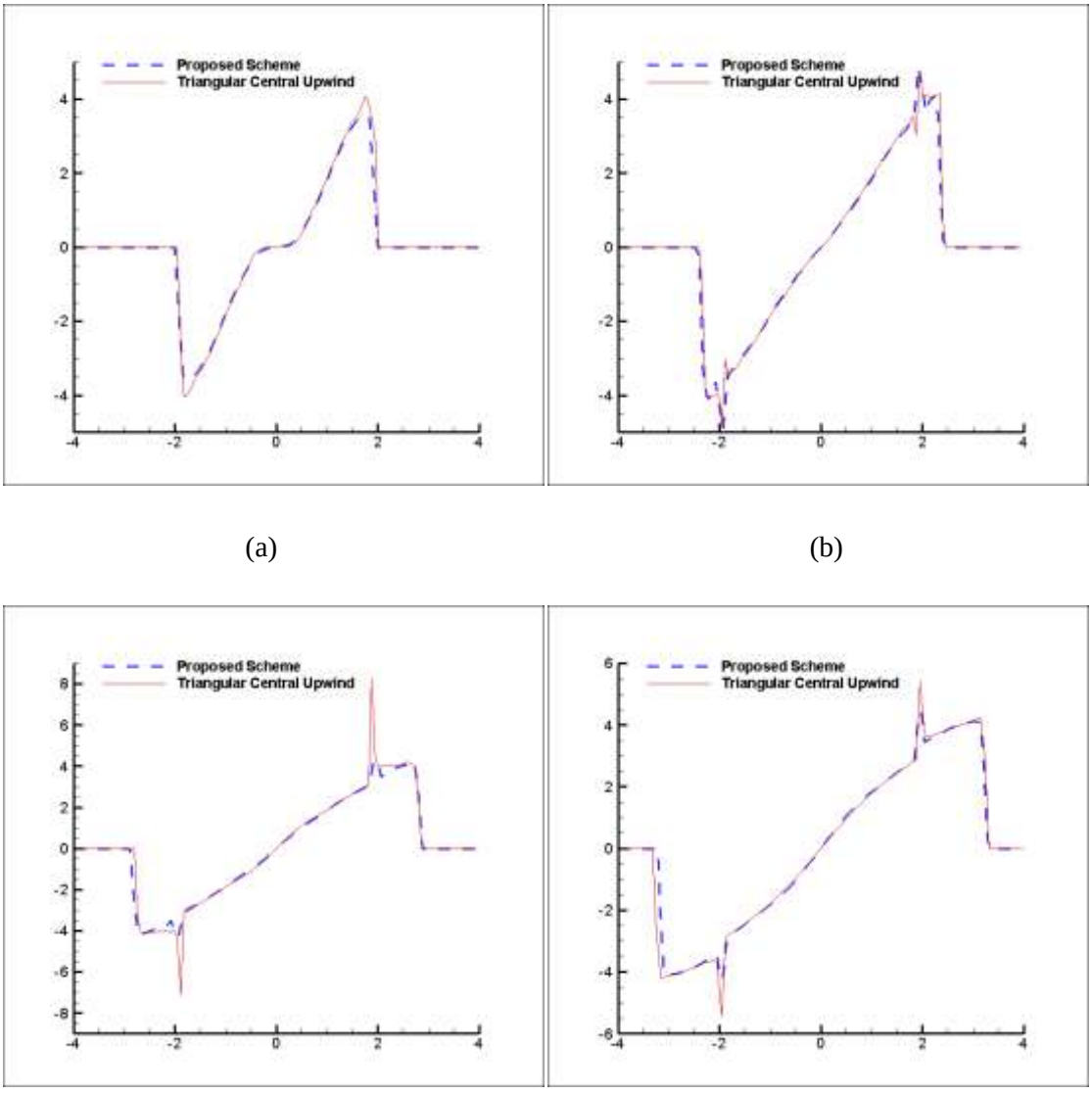

Fig. 5.17 - Example5: Comparison of u (1D slices along $y = 0$) computed using the finer grids at (a) $t = 0.2$, (b) $t = 0.3$, (c) $t = 0.4$ and (d) $t = 0.5$.

Example 6 - Steady flow over a bump

In order to show the performance of the proposed method in modelling the steady state flow, we consider simulation of steady flow over a bump which has been widely used in the literature (Xing and Shu 2005; Mohammadian and Le Roux 2006). We consider a flume with the following topography:

$$B(x,y) = \begin{cases} 0.2 - 0.05(x-10)^2, & 8 < x < 12, \\ 0, & otherwise. \end{cases}$$

In order to have a Transcritical flow with shock, boundary conditions for the water level $h = 0.33m$ and the discharge $uh = 0.18\frac{m^2}{s}$ are imposed at the downstream and upstream, respectively. The analytical solution of this problem is also given in Goutal andMaurel (1997). The water surface w and discharge uh components of the solution computed by the proposed scheme using $6 \times 8 \times 88$ quadrilateral cells are compared with the exact solutions in Fig. 5.18. The computed water surface and discharge are in good agreements with the analytical solutions. However, there is a very small level of numerical oscillations. It should be mentioned that such a level of numerical oscillations has also been reported in most existing available models in the literature (Xing and Shu 2005; Mohammadian and Le Roux 2006; Valianand Begnudelli 2006,Hou et al. 2013) and is considered as acceptable.

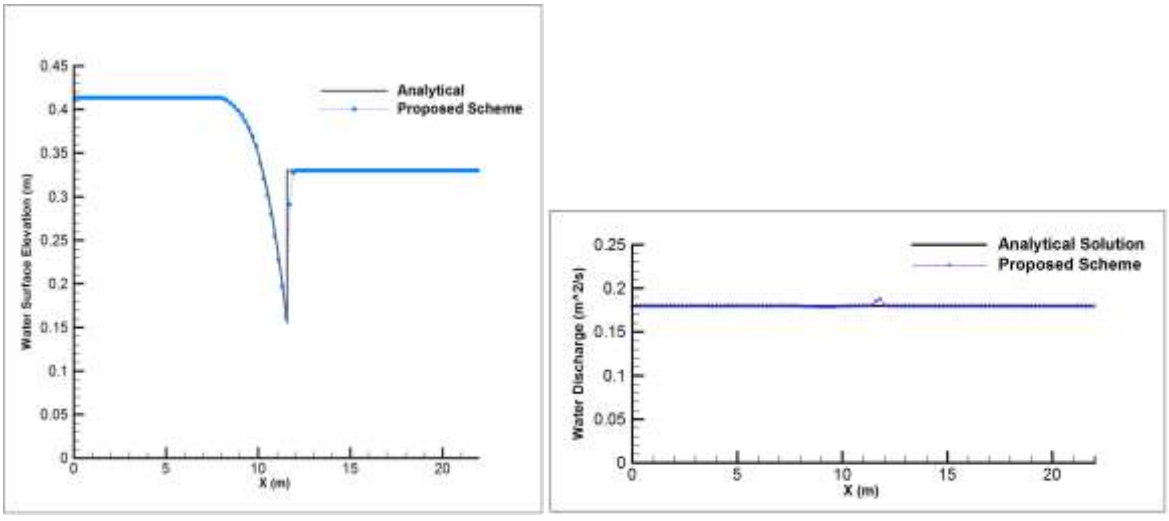

Fig. 5.18 - Example 6: Steady transcritical flow over a bump with a shock: (left) water surface elevation and (right) water discharge.

Example 7 - 2D dam break simulation

In this example, we examine the performance of the proposed model in simulation of a two dimensional dam-break with complex geometry. The laboratory measurements for this experiments were reported by Bellos et al. (1991). The dam break was carried out in a 21.2m long flume with slope of 0.01. The plan view of the flume can be seen in Fig. 5.19 where the fully unstructured quadrilateral grids are also shown. As can be seen, a converging - diverging formation creates two dimensional effects. The manning roughness coefficient of the flume is $n = 0.012$ and we estimate the bed friction in x and y direction using $gn^2\left(\frac{\sqrt{2}h}{\sqrt{h^4+\max(h^4,\varepsilon)}}\right)^{\frac{7}{3}}\sqrt{(hu)^2+(hv)^2}(hu)$ and $gn^2\left(\frac{\sqrt{2}h}{\sqrt{h^4+\max(h^4,\varepsilon)}}\right)^{\frac{7}{3}}\sqrt{(hu)^2+(hv)^2}(hv)$, respectively. Note that the water depth is estimated using the same desingularization procedure used for velocity estimation.

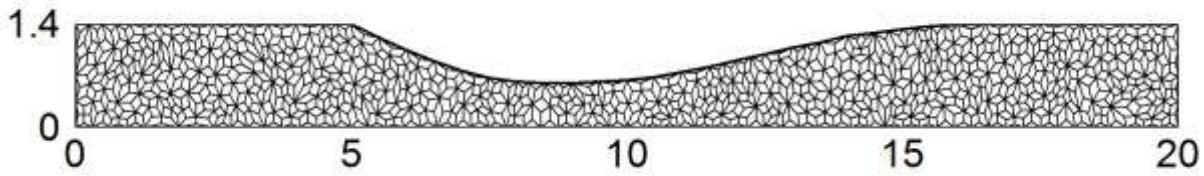

Fig. 5.19 - Example 7: Plan view of the flume for the 2D dam break test along with the unstructured quadrilateral grids.

With the water depth of 0.15 m at the dam, the water depth profiles at times $t = 2.0\ s$, $t = 6.0\ s$ and $t = 20.0\ s$ are compared to the measurements in Fig. 5.20.

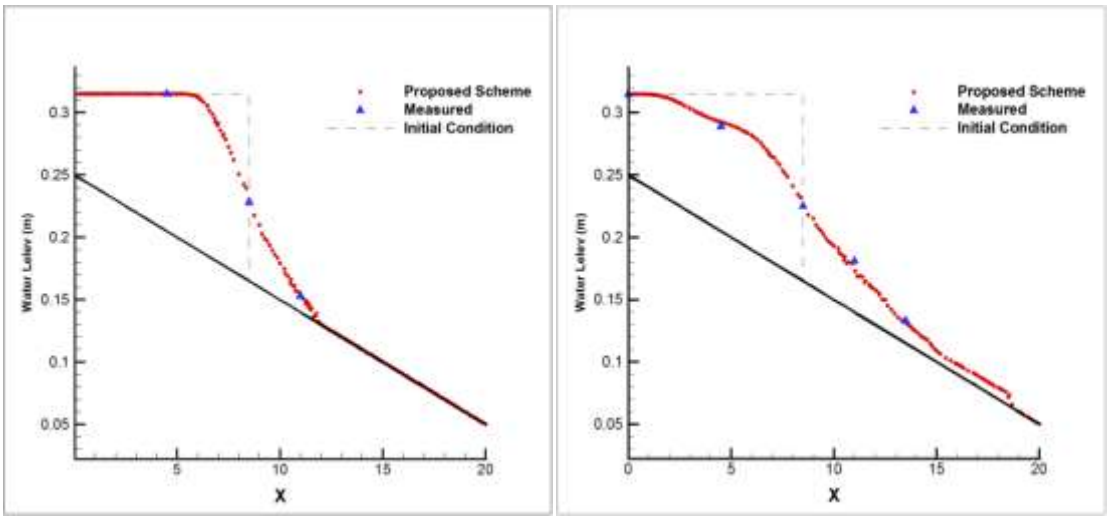

(a) (b)

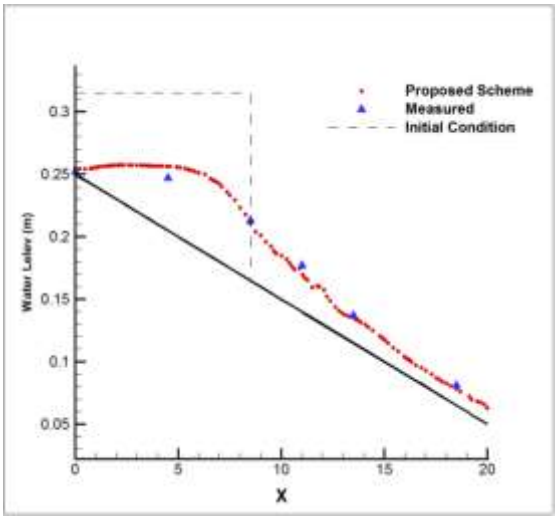

(c)

Fig. 5.20 - Example 7: Comparison between computed and measured water surface profiles at (a) $t = 2s$, (b) $t = 6s$ and (c) $t = 20s$

In this test, the water surface profile is strongly affected by the two-dimensional shape of theflume and the wave speed increases due to the sloping bed. As can be seen in Fig. 5.20, for an initiallydry bed, the proposed scheme performs well and the predicted water surface profile are considered to be satisfactory.

Example 8 - Dam break and advance over a triangular obstacle

In this test case, we examine the performance of the proposed scheme with a dam break wave over a triangular obstacle at the downstream of the dam. The reservoir, channel and triangular obstacle geometry along with the location of the measurement gauges are presented in Fig. 5.21. The reservoir with initial water depth of $0.75\ m$ is connected to a rectangular channel with a symmetric triangular obstacle situated downstream of the dam. The Manning roughness coefficient is 0.0125 for the bed. The boundaries are solid walls except for the free outlet at the end of the channel.

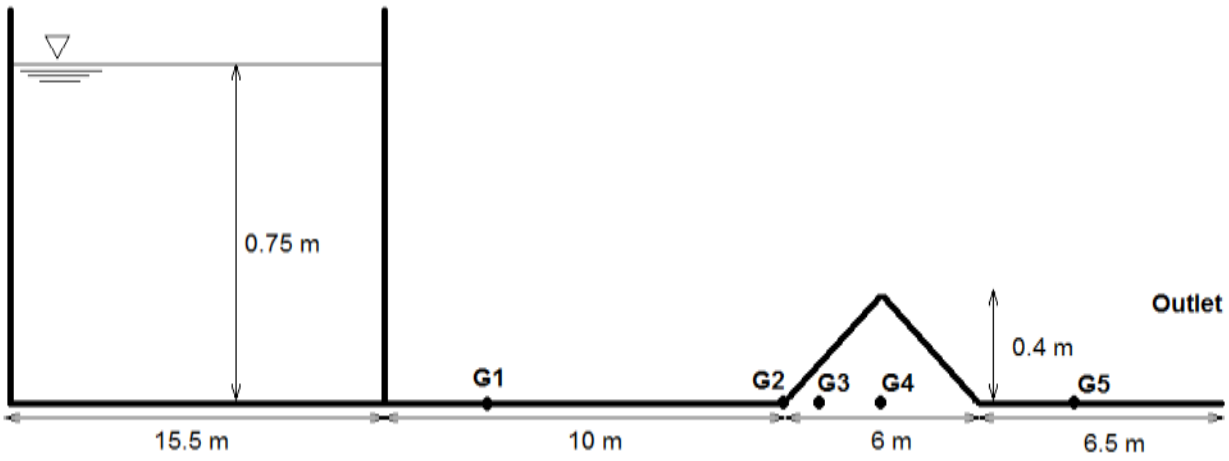

Fig. 5.21 - Example 8: Schematic side view of the experimental model and gauge points location in example 8

The experimental data are reported in Liang and Marche (2009) for gauging points G1, G2, G3, G4, and G5 which are located at 4m, 10 m, 11 m, 13m and 20m downstream of the reservoir.

The computed evolutions of water depths using a quadrilateral mesh grid with $6 \times 100 \times 8$ number of cells are compared with the measured values at the gauge points in Fig. 5.22. The results indicate a satisfactory agreement between the computed and measured values.

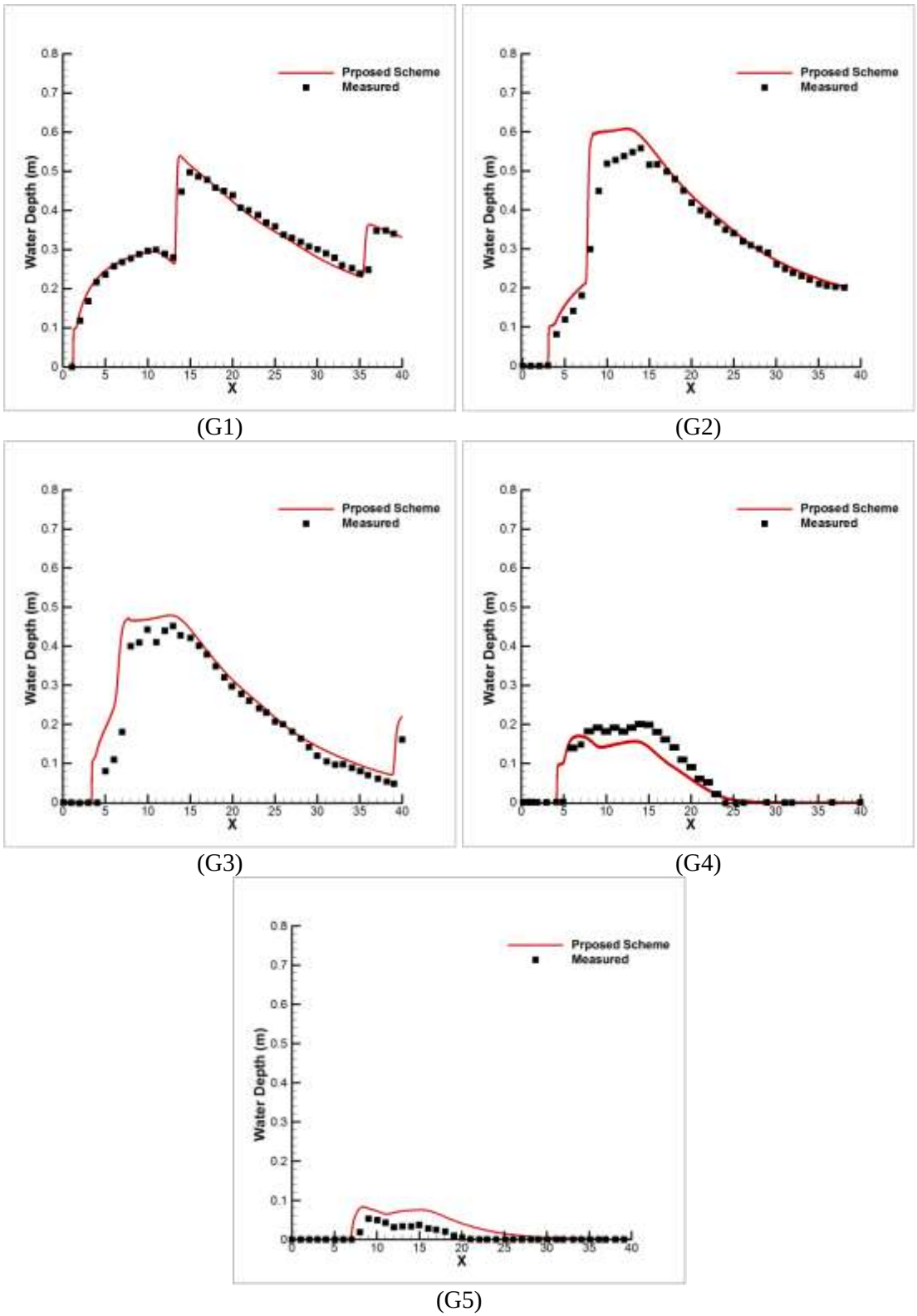

Fig. 5.22 - Example 8: Comparison of the computed evolutions of water depth during 40*s* with the measured values at the gauge points

For the Gauges G1, G2 and G3 which are located before the obstacle vertex the water depth and the arrival time of the wave are well predicted. In additio9n, for Gauge G4 with a crucial location at the obstacle vertex, the wet/dry conversion is correctly predicted. At the Gauge G5, however, a little disagreement is observed where the amount of water is not considerable. It may raise from vertical non-hydrostatic motions which are not considered in SW equations. The same feature is also reported in (Mohammadian and Le Roux 2006; Liang and Marche 2009; Brufau et al. 2002).

5.8. Conclusion

A new second-order central-upwind scheme for shallow water equations on the unstructured quadrilateral grids has been developed. To this end, we have proposed a new technique for bottom topography approximation over quadrilateral cells as well as an efficient water surface correction procedure. Moreover, we have designed a new quadrature for discretization of the source term. The proposed scheme guarantees the positivity of the computed fluid depth and exactly preserves “lake at rest” steady states. The proposed scheme on unstructured quadrilateral grids has several advantages over the triangular central-upwind scheme from (Bryson et al. 2011). For instance, such grid uses more information from the neighbouring cells in time evolution of the cell average values. We applied the proposed scheme to various numerical tests which exhibit complex flow patterns. The numerical tests include "lake at rest" steady state with very small perturbations as well as completely dry and almost dry areas. The obtained results confirm the capability of the scheme to preserve the positivity of h and demonstrate that no instabilities are developed at the (almost) dry states. In the other numerical test, the results computed by the new scheme have been compared with those computed by the triangular central-upwind scheme. When the new scheme was used, the water surface component of the solution was resolved with higher resolution and was free of fluctuations. The velocity fields computed by the new scheme were also smooth while those computed by the triangular scheme were noisy. We also have examined the proposed scheme with transcritical flow over a bump. The results of water surface elevation and discharge were compared to the analytical ones. The results showed that the model is capable of simulating

such flows. Moreover, the model was examined with a 2D dam break on a sloping flume with friction. The results of water surface computed using a fully unstructured grids were compared to the experimental measurements and showed the ability of the model to take into account the complex domain geometry as well as friction term. In the last numerical example, a dam break over a triangular obstacle was simulated and the results were compared to the experimental measurements. The results confirmed the ability of the model to correctly predict the wetting and drying features of the flow. In sum, the results confirmed robustness and high accuracy of the new scheme and also demonstrated its potential advantages over the triangular central-upwind scheme.

Chapter 6

Changes in Flow hydrodynamics over Persian Gulf Under a Changing Climate

Abstract

The main objective of this section is to model the flow hydrodynamics over the Persian Gulf for the next decades with consideration of the climate change. Indeed, this chapter serves as a proof of the concept for the methodology proposed in this thesis. The large scale triangular finite volume C-grid scheme was implemented in a large scale hydrodynamic model of the Persian Gulf. The large scale model is validated using the observed water levels at WAKRAH and UMMSAID. Then, by employing the developed positivity preserving well-balanced central-upwind scheme the flow over a local coastal area along the Qatar coast is simulated. The outputs of the large-scale model are used as the boundary conditions for the local hydrodynamic model. Downscaled wind speed under different RCP scenarios are also used as an input into the local flow model. The results of flow field under the climate change can be implemented for a wide range of practical applications, from mixing of industrial outfalls to designing and maintaining coastal structures.

6.1. Introduction

Prediction of flow hydrodynamics over gulfs and estuaries is of essential importance and has many practical implementations. Indeed, evaluation of the effect of climate change on the flow field through the short, medium and long term is a requirement for a wide range of practical applications. This section of this study proves the applicability of the developed models for evaluation of flow hydrodynamics under changing climate. To this end, we consider the Persian Gulf as an area of interest. As one of the most important climate variables which affects the flow field, we consider the wind speed to be projected within the future time spans. In line with this goal, we use the developed Quantile-Quantile downscaling method to predict the wind speed over the coastal areas of Qatar. We use the historical data at the Doha International Airport together with the various GCM outputs

under different RCP emission scenarios to develop the downscaling method. Later, we use the results of the projected wind speeds as an input to the flow models. In order to model the flow field in a large-scale, we employ the developed finite volume triangular C-grid in combination with the Leap-Frog time stepping technique. The historical water level data is used as the boundary condition and also for validating the flow model. The results of the large scale model (water level) will be used as boundary condition for the local model.

Finally, we use the developed quadrilateral central-upwind scheme to simulate the flow hydrodynamics along the coastal area of Qatar. Fig. 6.1 shows the area of interest for both large-scale and local model. The results of flow models can be implemented for many practical applications.

Fig. 6.1 - The study area over the Persian Gulf. Large and small rectangles represent the domains of large-scale and local flow models, respectively.[adopted from Google Map]

6.2. Climate change model: wind speed

In order to consider the impact of climate change on the flow hydrodynamics, we consider the changes of wind speed,as one of the most important variables in deriving the flows and waves on estuaries. To this end, the Quantile-Quantile downscaling method, described in Chapter 2, is used to project the wind speed over the Qatar coastal areas. A multi-model

multi-scenario approach has been employed to take into account the uncertainties associated with the GCM outputs. Since the area of the study is located along the Qatar coastal areas, we use the historical wind speed data at the Doha International Airport to project the wind speed. The results of the future wind speed can be directly implemented into the flow models as the wind stress in the shallow water equations. Since this part of the study intends to proof the applicability of the developed models, we use the results of the predicted daily wind speed under the RCP85 scenario of the ensemble average model.

6.3. Large-scale flow model

The focus of Sections 3 and 4 of this study was to develop an appropriate large scale numerical model for shallow water equations. Various dispersion relations and Fourier analyses were used to investigate the behaviour of the triangular finite volume C-grid in combination with different time-stepping methods. The various analyses were performed for both short fast gravity and slow long Rossby waves. Both of these flows are of essential importance and an appropriate numerical model should be capable of modelling them.

The C-grid scheme showed the ability to preserve the symmetric shape of different waves, and there is no significant damping associated with the results. The results demonstrated that the scheme is capable of simulating both short fast gravity waves as well as long slow waves. Various source terms such as Coriolis force, surface wind, bed shear stress and uneven bottom topography terms,which are very important in practical applications, were considered in the momentum equation through a number of numerical experiments, and the results were satisfactory. Both the linear and non-linear behaviour of the numerical scheme were also examined, and the scheme performed well in both cases (Shirkhani et al., 2015).

We consider the shallow water equations with the Coriolis force, wind stress, bottom friction and bottom topography terms in the momentum equation, see equations (4.36-4.37). The bed friction terms are estimated by $\tau_{bx} = \rho C_f u\sqrt{u^2 + v^2}$ and $\tau_{by} = \rho C_f v\sqrt{u^2 + v^2}$where C_f is an empirical coefficient based on bed roughness. We use the following equation based on the Chezy friction law:

$$C_f = \frac{g}{C^2}$$

where$C$ is the Chezy friction coefficient. In order to estimate the wind stress $\boldsymbol{\tau} = (\tau_x, \tau_y)$, we use the following equation:

$$\tau_x = \rho\gamma V^2 \cos\psi \quad (6.1)$$

$$\tau_y = \rho\gamma V^2 \sin\psi \quad (6.2)$$

where$V$ is the wind speed, γ is the wind stress coefficient and ψ is the wind direction.

As the final step, we employ the triangular finite volume C-grid scheme to simulate the flow over the Persian Gulf. Fig. 6.2 shows the unstructured triangular grids used for the large scale model. All the basin walls are closed boundaries except for the vertical boundary at the right side of the domain, which is an open boundary. We use the measured water level values at this boundary. The wind stress coefficient γ and Chezy friction coefficient$C$ as the calibration parameters were considered. Using the available observed data of water level at UMMSAID, we calibrate the large scale flow model.

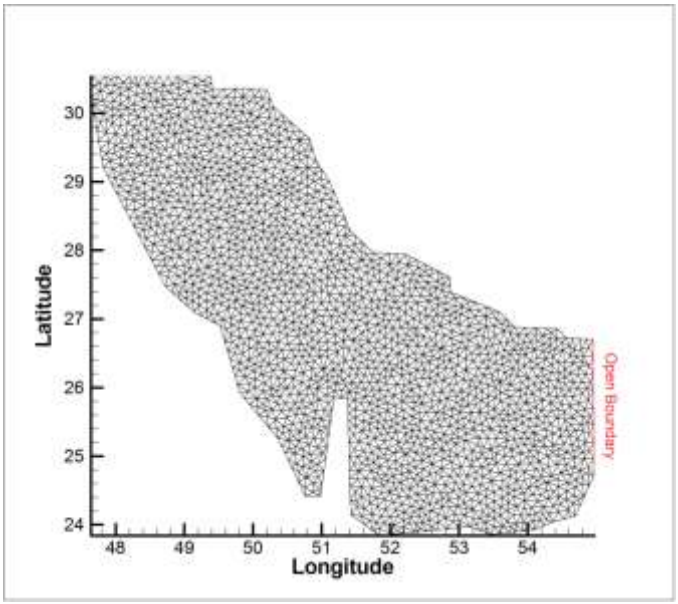

Fig. 6.2 - Unstructured triangular grids generated for the large-scale flow model. The vertical open boundary is shown at the right of the domain.

The calibrated parameters are found to be $\gamma = 5 \times 10^{-6}$and $C = 70$. In Fig. 6.3, the computed water level is compared to the observed values at UMMSAID for a 15-day period from 2010-05-14 to 2010-05-29. As it can be seen, there is a good agreement between the computed and observed data.

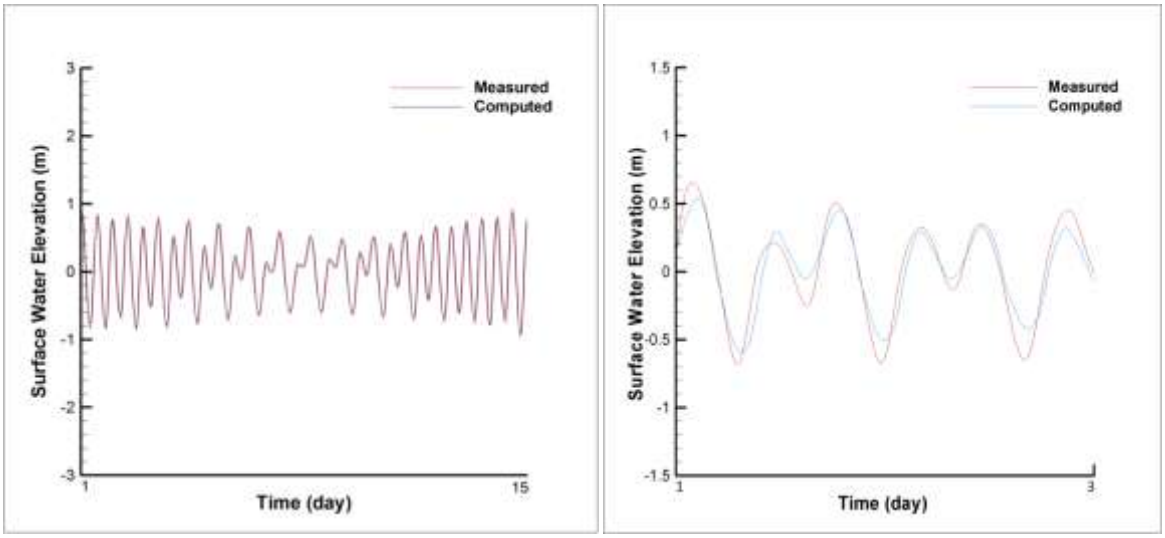

(a) (b)

Fig. 6.3 - Comparison of the computed and observed water levels at (a) UMMSAID for 15 days and (b) WAKRAH for 3 days.

Now, we implement the calibrated large-scale model to predict the flow hydrodynamics over the Persian Gulf for the year 2016. As for the boundary condition, since the information of water level is limited to the observed historical data, one needs to use appropriate projected water level values for year 2016. As a matter of fact, there are many possible ways to extrapolate the available historical data through the time. For instance, one can perform a trend analysis on the historical data of the water levels. However, since this is not in the scope of this study, we use the results of analysis performed by Sultan et al. (1995)on sea level over Persian Gulf. They reported the increase of 0.21 cm/yr for

mean sea level. Therefore, we shift the available water level data of year 2014 by 0.42 cm and use it as the boundary condition in the large scale flow model.

We also use the bathymetry data for the Persian Gulf and consider the topography term in the momentum equations. Fig. 6.4 shows a sample of results of the water elevation as well as velocity field over the Gulf. The water surface and velocity components of the solutions can be employed as the boundary condition of the local model.

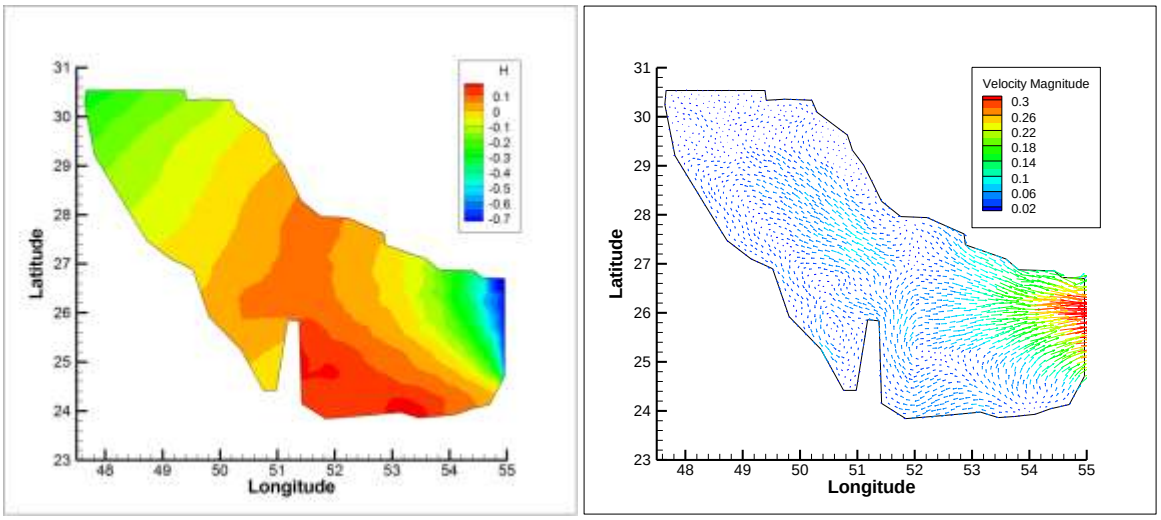

Fig. 6.4 - Results of the large-scale flow model within year 2016. Surface water elevation (m) (left) and velocity vectors (m/s) (right)

6.4. Local flow model

Finite volume schemes are useful tools for modelling shallow water equations. Finite volume upwind schemes denote a class of finite volume numerical discretization methods that take into account the direction of propagation of information in a flow field. The main advantage of the central upwind schemes is that they are Riemann solver free and no characteristic decomposition involved in the scheme. They are also high resolution, due to the smaller amount of the numerical dissipation. Moreover, they have an upwind nature, since they respect the directions of wave propagation. In chapter 5 of this study, we

developed a well-balanced positivity preserving central-upwind scheme for unstructured quadrilateral grids.

We now employ the developed model to locally simulate the flow over the Qatar coastal area. We generate a fully unstructured quadrilateral mesh grid for the selected domain which is shown in Fig. 6.5. As can be seen, all the basin boundaries are closed walls except for one horizontal and one vertical open boundary.

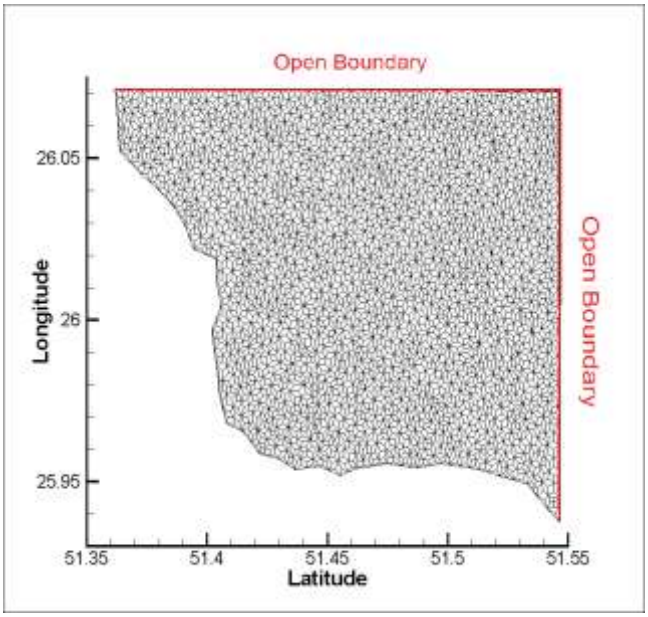

Fig. 6.5 - Unstructured quadrilateral grids generated for the local coastal model. Open boundaries are represented by the red lines at the top and left of the domain.

We apply the results of water level over year 2016 from the large-scale model as the boundary condition at the open boundaries. Beside the wind stress term, we also consider the uneven topography changes and bed friction terms. We use the same calibrated values, as the large scale model, for the bed friction and wind stress coefficients. A sample results of water depth and velocity field are presented in Fig. 6.6.

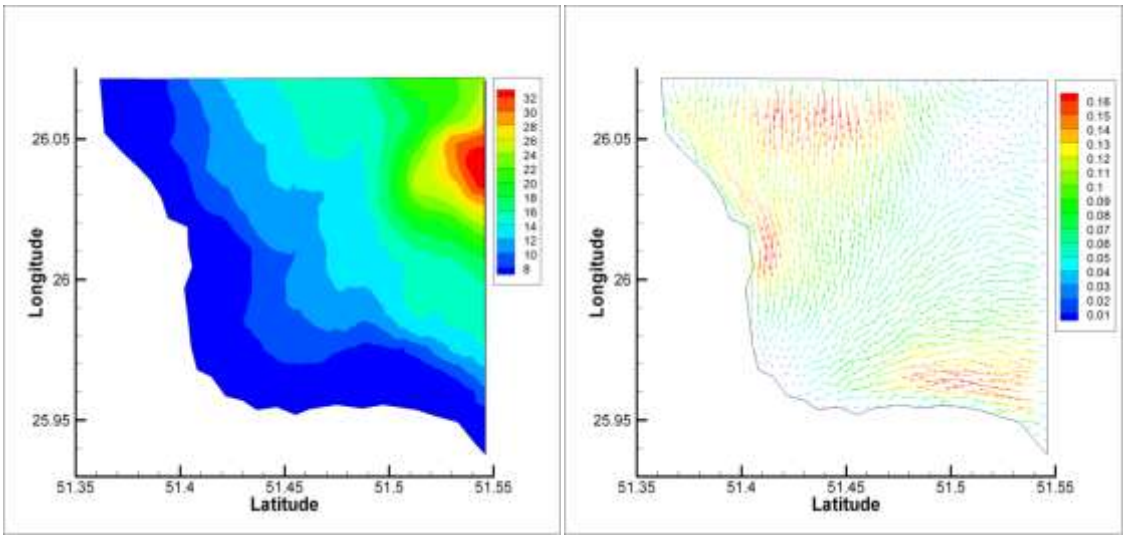

Fig. 6.6 - Results of the local flow model within year 2016. water depth (left) and velocity vectors (right)

By simulating the flow over the Persian Gulf under the changing climate, one can evaluate the changes on the flow hydrodynamics. We now consider the flow hydrodynamics over a 1-month period in year 2012 and evaluate the changes under the climate change for the same month in year 2016. For year 2012 the historical daily wind speeds are used while in year 2016 the projected daily wind speeds are employed. In order to have a range of possible changes in flow hydrodynamics, the results of wind downscaling under two different RCP scenarios (RCP26 and RCP85) are used. The results are presented in Fig. 6.7 and Fig. 6.8 for three different points through the local coastal domain. Fig. 6.7 compares the time series of water surface elevation at different points for January 2012 and 2016. Comparing the results of year 2012, which are computed using the historical wind speeds, to those of year 2016, which estimated by using projected wind speeds, one can evaluate the changes in the water surface elevation. The figure shows that the use of various RCP scenarios will result in a different water level time series. For instance, at the second point (Fig. 6.7-middle), RCP85 and RCP26 hold different results at most times. Indeed, RCP85 predicts higher water elevation than RCP26. Note that the effect of climate change will not be the same through all the domains. As can be seen in Fig. 6.7 (top), under both RCPs, the results of projected water level is almost the same as the historical one, while this is not the case in the other two points.

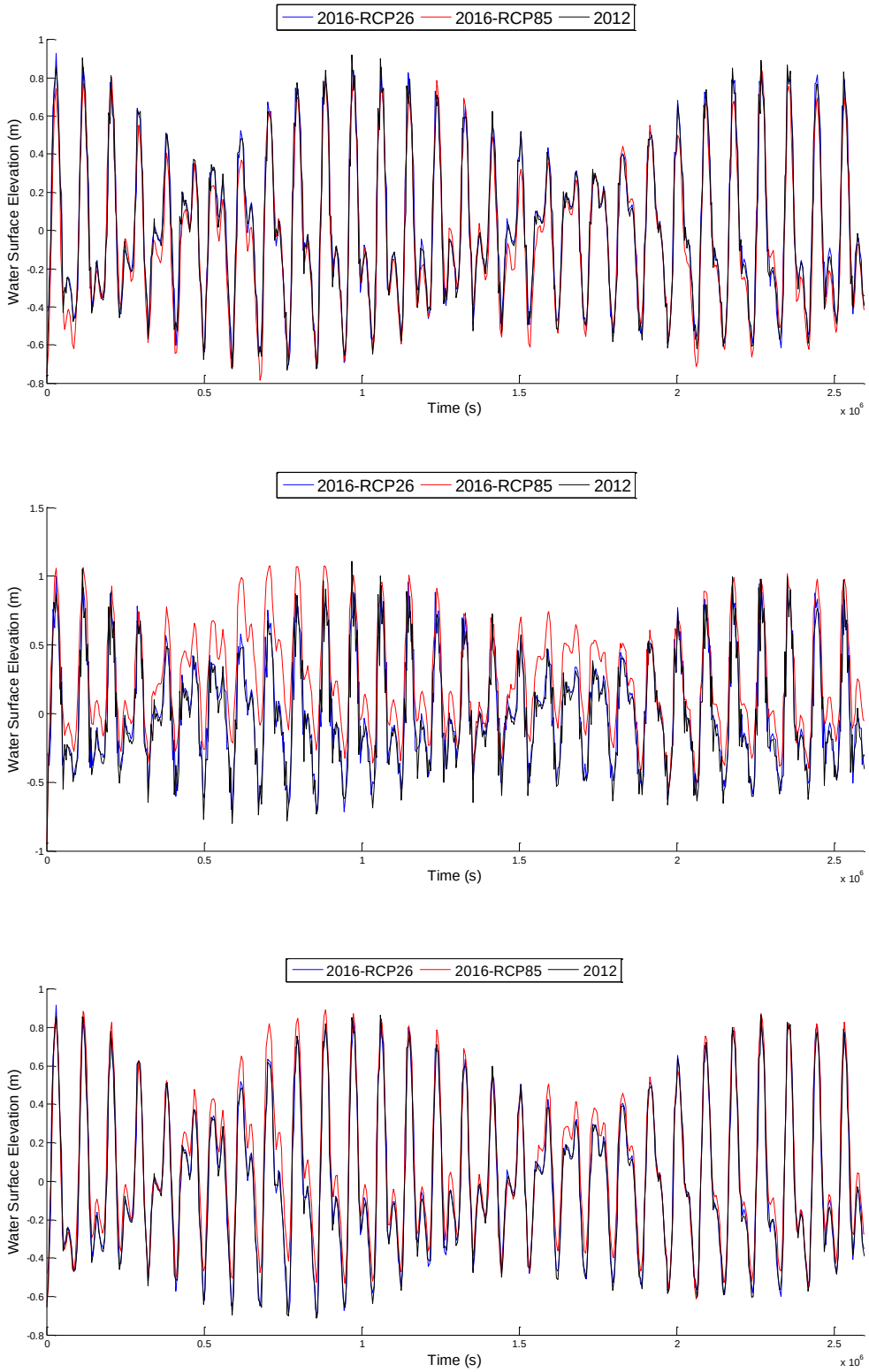

Fig. 6.7 - Comparison of computed time series of water level elevation at three different points through the local domain.

Fig 6.8 shows the monthly statistical distribution of the waves at three different points. Again, the results of wave height under climate change in year 2016 are compared with those of 2012. This graph shows that the wave climatology at first point does not significantly change in year 2016. However, in the two other points some changes are observed. It can be seen that at the second point, the wave height under RCP26 and RCP 85 decreases and increases respectively compared to the historical one. Based on the definition, one may also extract the significant wave height (as the wave height of the highest third of the waves) from this graphs. Generally, it can be concluded that under RCP26, the significant wave height does not change while it increases under RCP85. It should be noted that one may use the proposed methodology for a longer time span and evaluate the short, medium and long term effect of the climate change on the flow characteristic, which is beyond the scope of this study.

6.2. Conclusion

The objective of this section was to simulate the flow over the Persian Gulf under the changing climate. To this end, first, we have come up with the projected wind speed under the climate change. Second, we have developed different numerical schemes and examined them with various benchmark numerical tests.

In order to consider the climate change impacts on the flow condition over the coastal area of Persian Gulf, the wind speed as the main climate variable which affects the flow and wave fields has been considered. A multi-model multi-scenario approach was employed to project the wind speed over the Qatar coastal areas. Indeed, we have used three different models from CMIP5 experiments under various RCP scenarios. This allows us to take into account the high uncertainties associated with the general circulation models.

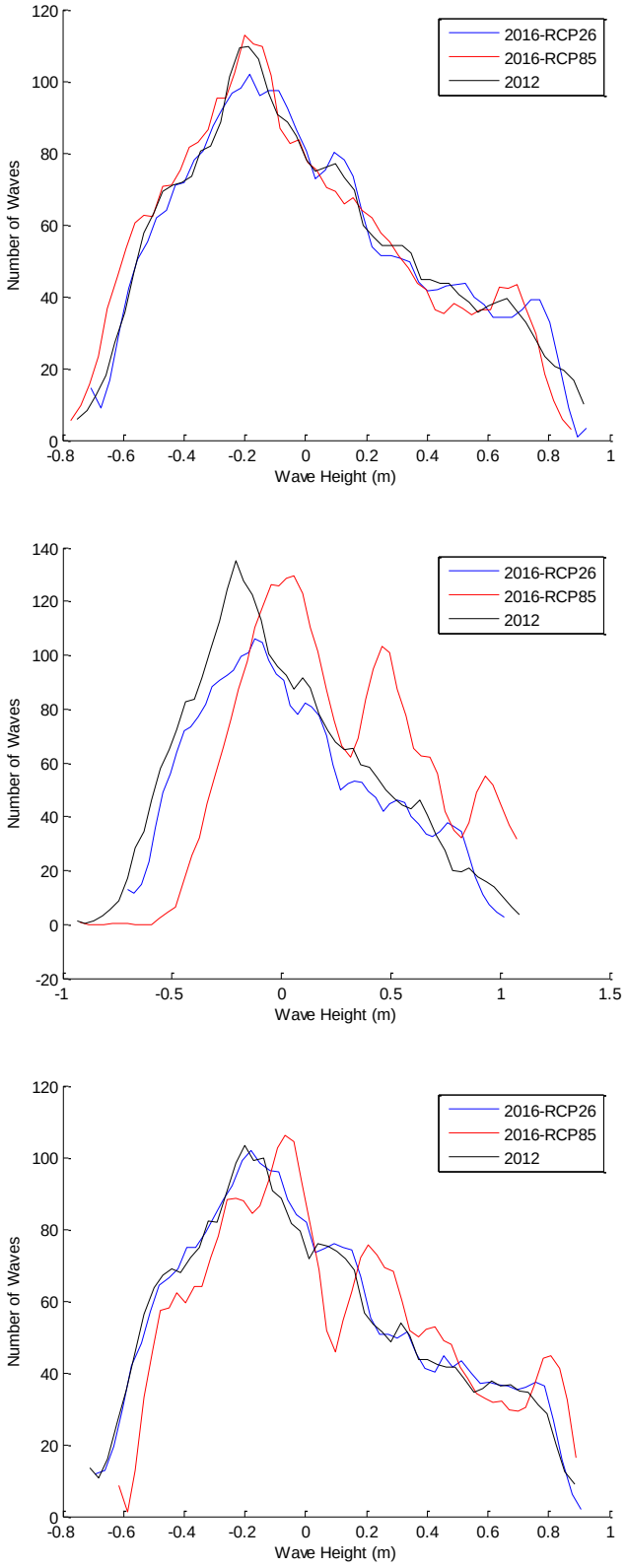

Fig. 6.8 - Monthly statistical wave distribution at three different points under various RCPs.

We employed two different statistical approaches, namely, the nearest neighbour search and the Quantile-Quantile schemes, in order to downscale the GCM outputs over the coastal areas. Equipped with the historical wind speed data, we projected the wind speed and verified the results. We concluded that the Quantile-Quantile method performs betterprediction, particularly for extreme events.

In regards with the numerical scheme for solving shallow water equations, we also analyzed the finite volume unstructured C-grid scheme using dispersion relation analysis. We examined the C-grid scheme in combination with improved Euler, second order Adams-Bashforth and Leap-Frog time stepping methods and concluded that the Adams-Bashforth leads to more accurate results while the Leap-Frog is more stable. The triangular C-grid scheme also showed ability to preserve the symmetric shape of different waves while there is no significant damping associated with the results. The results demonstrated that the scheme is capable of simulating fast gravity waves as well as long slow waves, which play an essential role in transferring the energy. Various source terms such as surface wind, bed shear stress and uneven topography terms were considered in the momentum equation trough the number of numerical experiment and the results were satisfactory. Both linear and non-linear behaviour of the scheme also examined and the scheme performed well in both cases.

In order to consider the climate change impact, we considered the projected wind speed as the surface wind stress term in the shallow water equations. We simulated the flow over the Persian Gulf under the changing climate. The water surface and velocity components of the solutions can be employed for many practical purposes.

Chapter 7

Summary, Concluding Remarks and future works

7.1. Summary and Concluding Remarks

The current study can be divided to the three major parts, namely, developing the climate change model, large-scale flow model and local coastal flow model.

In the first part of this study, the monthly distribution of wind speed was statistically downscaled to station-level scale using Quantile-Quantile transformation and nearest neighbor search methods. Observed daily wind speed data were used as predictand while climate variables including wind speed and maximum and minimum temperature from CMIP5 models under RCP emission scenarios were used as predictors. The empirical probability density functions derived from observations and downscaled GCM outputs were favorably compared using visual analysis and a two-sample Kolmogorov-Smirnoff test. In addition, the probability distribution of raw and downscaled GCM data were compared to the observations, which revealed that both models are capable of constructing the probability distribution of wind speed. It was, however, found that the nearest neighbor approach was not suitable for the estimation of future extreme wind speeds. As an example of practical application of wind speed projection, the significant wave height estimated using the downscaled wind speed. Results indicated that under RCP26/RCP45 scenarios, changes between 20 and 40% in the 100-year significant wave height might take place. The results also will be used in the flow model.

At the next stage, we considered the finite volume C-grid scheme for shallow water without Coriolis term. While the finite volume triangular classic C-grid scheme is employed in many numerical models and is very common, the second part of this study seems to be the one of the first dispersion relation analyses of this spatial scheme. In this section, first, the dispersion relation of a semi-discrete scheme was obtained for shallow water system and then analyzed. The results showed that the dispersion relation of the spatial scheme is purely real; i.e., there is no imaginary part. Therefore, all waves, including long and short waves, were not damped in the numerical solution. The phase

speed ratio was also close to one for the long and intermediate waves. However, the spatial scheme decelerates the shorter waves. Despite the fact that the short waves do not transfer much energy in the domain, since they are not effectively damped by the numerical scheme they may lead to oscillatory results.

In addition, the fully discrete schemes were analyzed. They were developed based on the proposed combination of three different temporal schemes: namely, the forward Euler, Leap-Frog and Adams-Bashforth methods, with the C-grid spatial discretization scheme. In fact, the implementation of various time-stepping methods can change the semi-discrete performance. For all numerical schemes, with a small CFL number (CFL=0.1) the phase speed ratio is very close to the semi-discrete one.

With regard to the amplification factor, for the forward Euler scheme we have $|E| > 1$, which means that the scheme is not stable unless there is a small CFL number. The dispersion relation analysis for the Leap-Frog method showed that the time-stepping scheme improves the phase speed behavior of the spatial discretization and makes it much closer to one for a wide range of wavelengths, including the shorter waves. In addition, the amplification factor is almost equal to 1, which shows that the numerical scheme does not damp the results. For higher CFL numbers (CFL=0.9), the Leap-Frog scheme accelerates the intermediate waves, while it is very close to one for long waves. The Adams-Bashforth scheme exhibits higher phase speed errors with higher CFL numbers (CFL>0.1) for a wider range of wave lengths, including the intermediate waves. However, the results show that it could also damp the results for shorter waves.

Three numerical tests were performed in order to first confirm the analytical results and, second, assess the convergence rate and accuracy of the proposed fully discrete methods. The first experiment was intended to confirm the results of analytical dispersion results by propagating a pure gravity wave in a channel. The results of the test showed that the wave front propagated at the same speed as the analytical results indicated. In addition, it showed the dispersion effects prior to the front, which confirms that numerical schemes decelerate the waves ($C_r \leq 1$). It also showed that by increasing the CFL number, the oscillation decreases for the Leap-Frog scheme, while it increases for the Adams-Bashforth scheme.

This clearly confirmed the analytical dispersion results. In the second test, a seiche in a rectangular closed basin was simulated as an example of shallow water waves. The results of the numerical methods were compared with the exact solution. The results were examined with different wave numbers, and showed that the phase speed error increases for the shorter waves, as the analytical analysis indicated. However, the results showed that the phase speed error for the shorter waves with higher CFL numbers is decreased using the Leap-Frog time-stepping technique. In the third numerical test, numerical schemes were implemented for simulation of a pure gravity wave with Gaussian initial distribution. The results of both Leap-Frog and Adams-Bashforth methods were compared to the analytical Bessel function solution and they were in good agreement. The spatial and temporal evolutions of the numerical solution were estimated based on the L^2error. The results showed that the proposed combination of spatial and temporal techniques converges, while the time step and spatial step decrease. In addition, the results showed that the error of the Adams-Bashforth scheme is lower and that the Leap-Frog scheme is stable for higher CFL numbers. The above analysis shows how the proposed method can help either in assessing the performance of the spatial discretization techniques or in the selection of the time-stepping technique in combination with it. In addition, the results of non linear tests confirm the ability of the C-grid approach, in the proposed combination with the Adams-Bashforth time stepping technique, to simulate the non-linear behavior of shallow water flows. The behaviour of the scheme was found to be satisfactory for the various numerical examples with consideration of various source terms which are of essential importance in practical applications.

Dispersion relation analysis was also implemented in order to investigate the performance of a finite volume triangular C-grid scheme in shallow water equations in presence of Coriolis term, which plays an essential role in inertia-gravity waves. We considered triangular grids made up of isosceles triangles with various vertex angles for the linear shallow water equations. The results of the dispersion relation analysis were compared with those of the analytical one, which belongs to the continuous case. We also reproduced the results of structured rectangular C-grid scheme (finite difference) in order to compare them with the finite volume triangular C-grid. Different cases of low and high resolution

grids were considered for dispersion relation analysis. Analyses showed that the same Rossby mode $\omega = 0$ as continuous case exists for $\alpha = \pi/6$, while it does not for the triangles with $\alpha \neq \pi/6$. The mode in $O(1)$ coincide with the continuous case for $\alpha = \pi/6$ while it is not the case for other vertex angles. In addition we found the spurious mode $O(1/h)$ for all cases. We also noticed that for the triangles with $\alpha \neq \pi/6$, there is a mode in $O(h)$. However, it was shown that it remains bounded and very close to zero for both low and high resolution cases. In addition, results showed that for the $\lambda/h \geq 3/8$, the non-dimensional frequency has a monotonic behaviour as the continuous case along the all directions for $\alpha = \pi/6$. It is also valid for the $\alpha \neq \pi/6$ but for some directions. In the relatively low resolution case of $\lambda = 3/8$, an improvement was shown for the finite volume triangular C-grid scheme compared to the structured rectangular one. We also examined three time stepping methods, namely, Adams-Bashforth, Leap-Frog and improved Euler in combination with finite volume triangular C-grid. The phase speed ratio for a wide range of CFL numbers were studied and results showed better performance of the Leap-Frog and Adams-Bashforth techniques compared to the Improved Euler. More precisely, the Leap-Frog scheme better improved the phase speed ratio behaviour of the semi discrete case at $CFL = 0.5$.

Through a number of numerical tests, we verified the theoretical analysis of dispersion relation and examined the performance of proposed combination of the finite volume triangular C-grid (equilateral case) with the Leap-Frog method. We considered the Coriolis force, wind stress, bottom friction and bottom topographical changes, and examined the proposed fully discrete scheme with various oceanic waves, such as fast gravity waves, as well as with long and slow inertia-gravity waves.

The model was examined with a long slow equatorial Rossby wave. The results obtained after 5 periods were compared to the analytical solution, and they were in good agreement. The symmetrical shape of the wave was preserved by the model, while the maximum water surface elevation was well predicted. The maximum values of the water surface elevation were compared to the analytical ones for various grid resolutions. The results confirmed that even using a relatively coarse mesh, there is no considerable damping associated with

the solution. Moreover, the spatial order of accuracy for the triangular C-grid scheme were sought by investigating the evolution of the L^2 error of water surface elevation. The obtained rate was very close to the formal spatial order of accuracy for the C-grid. Furthermore, the non-linear shallow water equations were also examined with the equatorial Rossby wave. The results were in good agreement with the analytical one and confirmed that the model can correctly take into account the non-linear terms.

In order to further examine the scheme, we applied the proposed model to the Stommel problem for two low- and high-resolution grids. The results demonstrated the ability of the model in predicting the divergence of the velocity field. In this test, we examined the proposed triangular C-grid for low and high resolution cases. The results of high resolution case was satisfactory. With regard to the low-resolution scenario, a great improvement was obtained in comparison to the structured C-grid schemes which confirmed the theoretical dispersion analysis. The model was also examined with uneven bottom topography and wind-induced circulation in a circular basin. Using an unstructured grid, the water surface elevation and velocity field were computed by the proposed scheme. The results confirmed the ability of the model to correctly account for the surface wind stress as well as for variable bottom topography. In addition, the non-linear shallow water equations were considered through the Rossby soliton wave. The results were in good agreement with those obtained by the asymptotic solution. In conclusion, the model showed good performance in the simulation of various ocean waves ranging from fast gravity waves to long and slow Rossby waves.

As for the local coastal flow model, a new second-order central-upwind scheme for shallow water equations on the unstructured quadrilateral grids has been developed. To this end, we have proposed a new technique for bottom topography approximation over quadrilateral cells as well as an efficient water surface correction procedure. Moreover, we have designed a new quadrature for discretization of the source term. The proposed scheme guarantees the positivity of the computed fluid depth and exactly preserves “lake at rest” steady states. The proposed scheme on unstructured quadrilateral grids has several advantages over the triangular central-upwind scheme. For instance, such grid uses more information from the neighbouring cells in time evolution of the cell average values. We

applied the proposed scheme to various numerical tests which exhibit complex flow patterns. The numerical tests include "lake at rest" steady state with very small perturbations as well as completely dry and almost dry areas. The obtained results confirm the capability of the scheme to preserve the positivity of h and demonstrate that no instabilities are developed at the (almost) dry states. In the other numerical test, the results computed by the new scheme have been compared with those computed by the triangular central-upwind scheme. When the new scheme was used, the water surface component of the solution was resolved with higher resolution and was free of fluctuations. The velocity fields computed by the new scheme were also smooth while those computed by the triangular scheme were noisy.

We also tested the proposed scheme on a problem with a transcritical flow over a bump. The computed water surface elevation and discharge were compared to the analytical ones. The results showed that the proposed central-upwind scheme is capable of quite accurately simulating such flows. In the next test, we have simulated a 2D dam break on a sloping flume with friction. The water surface values computed using a fully unstructured grids were compared to the experimental measurements and showed the ability of the developed scheme to take into account both complex domain geometry and a friction term. In the final numerical example, a dam break over a triangular obstacle was simulated and once again the obtained results were compared to the experimental measurements. This test helped us to confirm the ability of our quadrilateral central-upwind scheme to accurately predict the wetting and drying features of the flow. In summary, our numerical results confirmed robustness and high accuracy of the new scheme and also demonstrated its potential advantages over the triangular central-upwind scheme.

As the final step, we employed the proposed improved methodology for simulating the flow hydrodynamics under the changing climate over the Persian Gulf. In order to consider the climate change impact, we considered the projected wind speed as the surface wind stress term in the shallow water equations. In addition, we used the bathymetry data of the Persian Gulf and considered the uneven topography term in the momentum equations. Then, we simulated the flow over the Persian Gulf under the changing climate. The

proposed methodology for obtaining accurate water surface and velocity components of the solutions can be employed for many practical purposes.

This study showed that the proposed methodology is able to improve the evaluation of the flow hydrodynamics over the estuaries. The proposed methodology is efficient in terms of computational cost since it uses a large-scale model to simulate the flow over a large water body. Moreover, the large-scale model used in the proposed system was shown to perform better than the rectangular C-grid schemes which is normally used in most of the large-scale oceanic models. The developed methodology uses a well-balanced positivity preserving central-upwind method that was shown to be capable of resolving complex flow patterns. It, indeed, effectively simulates the wet/dry areas which can be the case in many local coastal regions. In addition, the unstructured quadrilateral grid helps to simulate the areas with more complex boundaries. The other feature of the proposed mythology is to consider the climate change impacts on the flow hydrodynamics. In the current study, the focus was on the wind speed as the climate variable that can affect the flow (wave) field. Taking into account the effect of climate change, one can evaluate the possible changes of the flow hydrodynamics under various climate change scenarios within next decades. The output of the proposed methodology can be used for many practical applications.

7.2. Future Work

There are number of other aspects that can be considered in order to improve the present study. As an example, one may perform other theoretical analysis on the other versions of C-grid schemes to investigate the feasibility of incorporating them in the methodology. Depending upon the availability of the historical data, by considering more downscaling points through the large-scale domain, the effect of climate change can be better considered in the large-scale model. This can be of particular importance at the domain boundaries. In addition, the climate change impact can be also considered for other important variables throughout the domain. Finally, while the Quantile-Quantile method showed a good performance, one may try other downscaling techniques as well.

References

Adcroft A, Hill C, Marshall J. A New Treatment of the Coriolis Terms in C-Grid Models at Both High and Low Resolutions. *Mon Wea Rev*. 1999;127(8):1928-1936. doi:10.1175/1520-0493(1999)127<1928:antotc>2.0.co;2.

Adcroft, Alistair, et al. Overview of the formulation and numerics of the MIT GCM. *Proceedings of the ECMWF seminar series on Numerical Methods, Recent developments in numerical methods for atmosphere and ocean modelling*. 2004.

Aiki H, Greatbatch R. A New Expression for the Form Stress Term in the Vertically Lagrangian Mean Framework for the Effect of Surface Waves on the Upper-Ocean Circulation. *J PhysOceanogr*. 2014;44(1):3-23. doi:10.1175/jpo-d-12-0228.1.

Alameddine, I., El-Fadel, M. Brine discharge from desalination plants: a modeling approach to an optimized outfall design. *Desalination*, 2007; *214*(1), 241-260.

Alcrudo F, Garcia-Navarro P. A high-resolution Godunov-type scheme in finite volumes for the 2D shallow-water equations. *International Journal for Numerical Methods in Fluids*. 1993;16(6):489-505. doi:10.1002/fld.1650160604.

Al-Mutaz, I. S., Al-Mojjly, A., &Abashar, M. E. Thermal and brine Dispersion from coastal MSF desalination plants. In *4th International conference on marine wastewater discharges and coastal environment (MWWP) Antalya Turkey*. 2006.

Andreas E, Wang S. Predicting significant wave height off the northeast coast of the United States. *Ocean Engineering*. 2007;34(8-9):1328-1335. doi:10.1016/j.oceaneng.2006.08.004.

Arakawa, Akio, and Vivian R. Lamb. "Computational design of the basic dynamical processes of the UCLA general circulation model." *Methods in computational physics* 17 (1977): 173-265.

Argüeso D, Evans J, Fita L. Precipitation bias correction of very high resolution regional climate models. *Hydrol Earth Syst Sci*. 2013;17(11):4379-4388. doi:10.5194/hess-17-4379-2013.

Bassi F, Rebay S. A High-Order Accurate Discontinuous Finite Element Method for the Numerical Solution of the Compressible Navierâ€“Stokes Equations. *Journal of Computational Physics*. 1997;131(2):267-279. doi:10.1006/jcph.1996.5572.

BATTEEN M, HAN Y. On the computational noise of finite-difference schemes used in ocean models. *TELLUSA*. 1981. doi:10.3402/tellusa.v33i4.10725.

Begnudelli L, Sanders B. Conservative Wetting and Drying Methodology for Quadrilateral Grid Finite-Volume Models. *Journal of Hydraulic Engineering*. 2007;133(3):312-322. doi:10.1061/(asce)0733-9429(2007)133:3(312).

Beljadid A, Mohammadian A, Kurganov A. Well-Balanced Positivity Preserving Cell-Vertex Central-Upwind Scheme for Shallow Water Flow, (2015) (Submitted).

Beljadid A, Mohammadian A, Qiblawey H. An unstructured finite volume method for large-scale shallow flows using the fourth-order Adams scheme. *Computers & Fluids*. 2013;88:579-589. doi:10.1016/j.compfluid.2013.10.018.

Bellos C, Soulis J, Sakkas J. Computation of two-dimensional dam-break-induced flows. *Advances in Water Resources*. 1991;14(1):31-41. doi:10.1016/0309-1708(91)90028-m.

Bernard P, Remacle J, Legat V. Modal analysis on unstructured meshes of the dispersion properties of the pair. *Ocean Modelling*. 2009;28(1-3):2-11. doi:10.1016/j.ocemod.2008.03.005.

Bleck R, Smith L. A wind-driven isopycnic coordinate model of the north and equatorial Atlantic Ocean: 1. Model development and supporting experiments. *J Geophys Res*. 1990;95(C3):3273. doi:10.1029/jc095ic03p03273.

BLUMBERG A, MELLOR G. *A Description Of A Three-Dimensional Coastal Ocean Circulation Model*.; 1987.

Bonaventura, L., E. Miglio, and F. Saleri. Finite Volume Solvers for the Shallow Water Equations Using Matrix Radial Basis Function Reconstruction. *Numerical Mathematics and Advanced Applications*. Springer Berlin Heidelberg, 2006. 207-214.

Boyd J. Equatorial Solitary Waves. Part I: Rossby Solitons. *J PhysOceanogr*. 1980;10(11):1699-1717. doi:10.1175/1520-0485(1980)010<1699:eswpir>2.0.co;2.

Brufau P, Vpazquez-Cendpon M, Garcpia-Navarro P. A numerical model for the flooding and drying of irregular domains. *International Journal for Numerical Methods in Fluids*. 2002;39(3):247-275. doi:10.1002/fld.285.

Bryson S, Epshteyn Y, Kurganov A, Petrova G. Well-balanced positivity preserving central-upwind scheme on triangular grids for the Saint-Venant system. *ESAIM: M2AN*. 2010;45(3):423-446. doi:10.1051/m2an/2010060.

Bukatov A, Zavâ€™yalov D. Wind-induced motion of water in shallow-water closed basins. *PhysOceanogr*. 2004;14(5):284-294. doi:10.1007/s11110-005-0009-2.

Carter, T. R., Parry, M. L., Harasawa, H., &Nishioka, SIPCC technical guidelines for assessing climate change impacts and adaptations with a summary for policy makers and a technical summary. . (1994).

Casulli V, Walters R. An unstructured grid, three-dimensional model based on the shallow water equations. *International Journal for Numerical Methods in Fluids*. 2000;32(3):331-348. doi:10.1002/(sici)1097-0363(20000215)32:3<331::aid-fld941>3.0.co;2-c.

Casulli V, Zanolli P. Semi-implicit numerical modeling of nonhydrostatic free-surface flows for environmental problems. *Mathematical and Computer Modelling*. 2002;36(9-10):1131-1149. doi:10.1016/s0895-7177(02)00264-9.

Casulli V. A semi-implicit finite difference method for non-hydrostatic, free-surface flows. *International Journal for Numerical Methods in Fluids*. 1999;30(4):425-440. doi:10.1002/(sici)1097-0363(19990630)30:4<425::aid-fld847>3.0.co;2-d.

Casulli V. Semi-implicit finite difference methods for the two-dimensional shallow water equations. *Journal of Computational Physics*. 1990;86(1):56-74. doi:10.1016/0021-9991(90)90091-e.

Chou S, Kwak D, Kim K. Mixed finite volume methods on nonstaggered quadrilateral grids for elliptic problems. *Mathematics of Computation*. 2002;72(242):525-540. doi:10.1090/s0025-5718-02-01426-6.

Chou S, Kwak D, Vassilevski P. Mixed UpwindingCovolume Methods on Rectangular Grids for Convection-Diffusion Problems. *SIAM J SciComput*. 1999;21(1):145-165. doi:10.1137/s1064827597321052.

deRooy W, Kok K. A Combined Physicalâ€“Statistical Approach for the Downscaling of Model Wind Speed. *Wea Forecasting*. 2004;19(3):485-495. doi:10.1175/1520-0434(2004)019<0485:acpaft>2.0.co;2.

Despotis G, Tsangaris S. A finite volume method for the solution of the extrudate swell problem on unstructured triangular meshes. *IntJnl of Num Meth for HFF*. 1996;6(6):65-83. doi:10.1108/09615539610131271.

Devis A, van Lipzig N, Demuzere M. A new statistical approach to downscale wind speed distributions at a site in northern Europe. *Journal of Geophysical Research: Atmospheres*. 2013;118(5):2272-2283. doi:10.1002/jgrd.50245.

Didier, S.S., 2003. Numerical modeling of tidal-modulated dispersion of brine discharges from a desalination plant in Singapore coastal waters", M.Sc. thesis, National University of Singapore.

Dobricic S. An Improved Calculation of Coriolis Terms on the C Grid. *Mon Wea Rev*. 2006;134(12):3764-3773. doi:10.1175/mwr3277.1.

Doescher E, de Campos Velho H, Ramos F. Criteria for mixed grids in computational fluid dynamics. *Mathematics and Computers in Simulation*. 2006;73(1-4):156-167. doi:10.1016/j.matcom.2006.06.019.

Dukowicz J. Mesh Effects for Rossby Waves. *Journal of Computational Physics*. 1995;119(1):188-194. doi:10.1006/jcph.1995.1126.

Feng X, Li R, He Y, Liu D. P 1-Nonconforming Quadrilateral Finite Volume Methods for the Semilinear Elliptic Equations. *J SciComput*. 2011;52(3):519-545. doi:10.1007/s10915-011-9557-4.

Fowler H, Blenkinsop S, Tebaldi C. Linking climate change modelling to impacts studies: recent advances in downscaling techniques for hydrological modelling. *International Journal of Climatology*. 2007;27(12):1547-1578. doi:10.1002/joc.1556.

Fringer O, Gerritsen M, Street R. An unstructured-grid, finite-volume, nonhydrostatic, parallel coastal ocean simulator. *Ocean Modelling*. 2006;14(3-4):139-173. doi:10.1016/j.ocemod.2006.03.006.

Giraldo F, Hesthaven J, Warburton T. Nodal High-Order Discontinuous Galerkin Methods for the Spherical Shallow Water Equations. *Journal of Computational Physics*. 2002;181(2):499-525. doi:10.1006/jcph.2002.7139.

Gossard, C. M., and R. L. Kolar. Phase behavior of a finite volume shallow water algorithm. *Proceedings of CMWR XIII Volume* 2 (2000): 921-928.

Gottlieb S, Ketcheson D, Shu C. *Strong Stability Preserving Runge-KuttaAnd Multistep Time Discretizations*. Hackensack, NJ: World Scientific; 2011.

Gottlieb S, Shu C, Tadmor E. Strong Stability-Preserving High-Order Time Discretization Methods. *SIAM Rev*. 2001;43(1):89-112. doi:10.1137/s003614450036757x.

Goutal, N., and F. Maurel. *Proceedings of the 2nd workshop on dam-break wave simulation*. Electricité de France. Direction des étudesetrecherches, 1997.

Gray W, Lynch D. Time-stepping schemes for finite element tidal model computations. *Advances in Water Resources*. 1977;1(2):83-95. doi:10.1016/0309-1708(77)90026-4.

Greaves D. A quadtree adaptive method for simulating fluid flows with moving interfaces. *Journal of Computational Physics*. 2004;194(1):35-56. doi:10.1016/j.jcp.2003.08.018.

Hanert E, Le Roux D, Legat V, Deleersnijder E. Advection schemes for unstructured grid ocean modelling. *Ocean Modelling*. 2004;7(1-2):39-58. doi:10.1016/s1463-5003(03)00029-5.

Hanert E, Roux D, Legat V, Deleersnijder E. An efficient Eulerian finite element method for the shallow water equations. *Ocean Modelling*. 2005;10(1-2):115-136. doi:10.1016/j.ocemod.2004.06.006.

Hashmi M, Shamseldin A, Melville B. Statistical downscaling of watershed precipitation using Gene Expression Programming (GEP). *Environmental Modelling & Software*. 2011;26(12):1639-1646. doi:10.1016/j.envsoft.2011.07.007.

Hemer M, Fan Y, Mori N, Semedo A, Wang X. Projected changes in wave climate from a multi-model ensemble. *Nature Climate Change*. 2013;3(5):471-476. doi:10.1038/nclimate1791.

Hewitson B, Crane R. Consensus between GCM climate change projections with empirical downscaling: precipitation downscaling over South Africa. *International Journal of Climatology*. 2006;26(10):1315-1337. doi:10.1002/joc.1314.

Horvath K, BajiÄ‡ A, Ivatek-Å ahdan S. Dynamical Downscaling of Wind Speed in Complex Terrain Prone To Bora-Type Flows. *J Appl Meteor Climatol*. 2011;50(8):1676-1691. doi:10.1175/2011jamc2638.1.

Hou J, Simons F, Mahgoub M, Hinkelmann R. A robust well-balanced model on unstructured grids for shallow water flows with wetting and drying over complex topography. *Computer Methods in Applied Mechanics and Engineering*. 2013;257:126-149. doi:10.1016/j.cma.2013.01.015.

IPCC (Intergovernmental Panel on Climate Change). (2007). "Towards new scenarios for analysis of emissions, climate change, impacts, and response strategies." Expert Meeting Rep., Noordwijkerhout, Netherlands.

Iskandarani M, Haidvogel D, Boyd J. A staggered spectral element model with application to the oceanic shallow water equations. *International Journal for Numerical Methods in Fluids*. 1995;20(5):393-414. doi:10.1002/fld.1650200504.

Iwasaki S, Isobe A, Kako S. Atmosphereâ€"Ocean Coupled Process along Coastal Areas of the Yellow and East China Seas in Winter. *Journal of Climate*. 2014;27(1):155-167. doi:10.1175/jcli-d-13-00117.1.

Jaber F, Mohtar R. Stability and accuracy of finite element schemes for the one-dimensional kinematic wave solution. *Advances in Water Resources*. 2002;25(4):427-438. doi:10.1016/s0309-1708(02)00005-2.

JakobThemeßl M, Gobiet A, Leuprecht A. Empirical-statistical downscaling and error correction of daily precipitation from regional climate models. *International Journal of Climatology*. 2010;31(10):1530-1544. doi:10.1002/joc.2168.

Jankowski J. Parallel implementation of a non-hydrostatic model for free surface flows with semi-Lagrangian advection treatment. *International Journal for Numerical Methods in Fluids*. 2009;59(10):1157-1179. doi:10.1002/fld.1859.

Jankowski, Jacek A. Further developments of UnTRIM: parallel implementation and its verification. *Proceedings of the IAHR Fifth International Symposium on Environmental Hydraulics,(ISEH V), Tempe, Arizona, USA*. 2007.

Jenkins, S. A., Wasyl, J. Oceanographic considerations for desalination plants in southern California coastal waters. *Scripps Institution of Oceanography*. 2005.

Jolley T, Wheater H. A Large-Scale Grid-Based Hydrological Model of the Severn and Thames Catchments. *Water and Environment Journal*. 1996;10(4):253-262. doi:10.1111/j.1747-6593.1996.tb00043.x.

Kernkamp H, Van Dam A, Stelling G, de Goede E. Efficient scheme for the shallow water equations on unstructured grids with application to the Continental Shelf. *Ocean Dynamics*. 2011;61(8):1175-1188. doi:10.1007/s10236-011-0423-6.

Kinnmark I, Gray W. The 2Î”x-test: A tool for analyzing spurious oscillations. *Advances in Water Resources*. 1985;8(3):129-135. doi:10.1016/0309-1708(85)90053-3.

Kranenburg C. Wind-driven chaotic advection in a shallow model lake. *Journal of Hydraulic Research*. 1992;30(1):29-46. doi:10.1080/00221689209498945.

Kuiry S, Sen D, Ding Y. A high-resolution shallow water model using unstructured quadrilateral grids. *Computers & Fluids*. 2012;68:16-28. doi:10.1016/j.compfluid.2012.07.018.

Kurganov A, Levy D. Central-Upwind Schemes for the Saint-Venant System. *ESAIM: M2AN*. 2002;36(3):397-425. doi:10.1051/m2an:2002019.

Kurganov A, Noelle S, Petrova G. Semidiscrete Central-Upwind Schemes for Hyperbolic Conservation Laws and Hamilton--Jacobi Equations. *SIAM J SciComput*. 2001;23(3):707-740. doi:10.1137/s1064827500373413.

Kurganov A, Petrova G. A Second-Order Well-Balanced Positivity Preserving Central-Upwind Scheme for the Saint-Venant System. *Communications in Mathematical Sciences*. 2007;5(1):133-160. doi:10.4310/cms.2007.v5.n1.a6.

Kurganov A, Petrova G. Central-upwind schemes on triangular grids for hyperbolic systems of conservation laws. *Numer Methods Partial Differential Eq*. 2005;21(3):536-552. doi:10.1002/num.20049.

Kurganov A, Tadmor E. New High-Resolution Central Schemes for Nonlinear Conservation Laws and Convectionâ€“Diffusion Equations. *Journal of Computational Physics*. 2000;160(1):241-282. doi:10.1006/jcph.2000.6459.

Kurganov A, Tadmor E. Solution of two-dimensional Riemann problems for gas dynamics without Riemann problem solvers. *Numer Methods Partial Differential Eq*. 2002;18(5):584-608. doi:10.1002/num.10025.

Kurganov, Alexander, and Chi-Tien Lin. On the reduction of numerical dissipation in central-upwind schemes. *Commun. Comput. Phys* 2.1 (2007): 141-163.

Langtangen H, Mardal K, Winther R. Numerical methods for incompressible viscous flow. *Advances in Water Resources*. 2002;25(8-12):1125-1146. doi:10.1016/s0309-

1708(02)00052-0.

Lazure P, Dumas F. An externalâ€“internal mode coupling for a 3D hydrodynamical model for applications at regional scale (MARS). *Advances in Water Resources*. 2008;31(2):233-250. doi:10.1016/j.advwatres.2007.06.010.

Le Roux D, Lin C, Staniforth A. A Semi-implicit Semi-Lagrangian Finite-Element Shallow-Water Ocean Model. *Mon Wea Rev*. 2000;128(5):1384-1401. doi:10.1175/1520-0493(2000)128<1384:asislf>2.0.co;2.

Le Roux D, Pouliot B. Analysis of Numerically Induced Oscillations in Two-Dimensional Finite-Element Shallow-Water Models Part II: Free Planetary Waves. *SIAM J SciComput*. 2008;30(4):1971-1991. doi:10.1137/070697872.

Le Roux D, Rostand V, Pouliot B. Analysis of numerically induced oscillations in 2d finite-element shallow-water models part I: inertia-gravity waves. *SIAM J SciComput*. 2007;29(1):331-360. doi:10.1137/060650106.

Le Roux D. A New Triangular Finite-Element with Optimum Constraint Ratio for Compressible Fluids. *SIAM J SciComput*. 2001;23(1):66-80. doi:10.1137/s1064827500367403.

Le Roux D. Dispersion Relation Analysis of the $P^NC_1 - P^_1$ Finite-Element Pair in Shallow-Water Models. *SIAM J SciComput*. 2005;27(2):394-414. doi:10.1137/030602435.

Legates, D. R. Limitations of climate models as predictors of climate change. Brief analysis, (2002): 396.

LeVeque R. Balancing Source Terms and Flux Gradients in High-Resolution Godunov Methods: The Quasi-Steady Wave-Propagation Algorithm. *Journal of Computational Physics*. 1998;146(1):346-365. doi:10.1006/jcph.1998.6058.

Liang Q, Borthwick A, Taylor P. Wind-induced chaotic advection in shallow flow geometries. Part II: Non-circular basins. *Journal of Hydraulic Research*. 2006;44(2):180-188. doi:10.1080/00221686.2006.9521674.

Liang Q, Du G, Hall J, Borthwick A. Flood Inundation Modeling with an Adaptive Quadtree Grid Shallow Water Equation Solver. *Journal of Hydraulic Engineering*. 2008;134(11):1603-1610. doi:10.1061/(asce)0733-9429(2008)134:11(1603).

Liang Q, Marche F. Numerical resolution of well-balanced shallow water equations with complex source terms. *Advances in Water Resources*. 2009;32(6):873-884. doi:10.1016/j.advwatres.2009.02.010.

Liu X, Osher S, Chan T. Weighted Essentially Non-oscillatory Schemes. *Journal of Computational Physics*. 1994;115(1):200-212. doi:10.1006/jcph.1994.1187.

Malcangio D, Petrillo A. Modeling of brine outfall at the planning stage of desalination plants. Desalination. 2010;254(1-3):114-125. doi:10.1016/j.desal.2009.12.005.

Manual, S. P. (1984). Coastal Engineering Research Center. Department of the Army, Waterways Experiment Station, 1.

Maraun D, Wetterhall F, IresonA et al. Precipitation downscaling under climate change: Recent developments to bridge the gap between dynamical models and the end user. *Rev Geophys*. 2010;48(3). doi:10.1029/2009rg000314.

Marshall J, Adcroft A, Hill C, Perelman L, Heisey C. A finite-volume, incompressible Navier Stokes model for studies of the ocean on parallel computers. *J Geophys Res*. 1997;102(C3):5753. doi:10.1029/96jc02775.

Mellor G. *User's Guide For A Three-Dimensional, Primitive Equation, Numerical Ocean Model*. Princeton, N.J.: Atmospheric and Oceanic Sciences Program, Princeton University; 1993.

Mesinger, Fedor, and Akio Arakawa. Numerical methods used in atmospheric models, volume 1. *Global Atmospheric Research Program World Meteorological Organization, Geneva (Switzerland).*. Vol. 1. 1976.

Mohamed K. A finite volume method for numerical simulation of shallow water models with porosity. *Computers & Fluids*. 2014;104:9-19. doi:10.1016/j.compfluid.2014.07.020.

Mohammadian A, Le Roux D. Fourier analysis of a class of upwind schemes in shallow water systems for gravity and Rossby waves. *International Journal for Numerical Methods in Fluids*. 2008;57(4):389-416. doi:10.1002/fld.1617.

Mohammadian A, Le Roux D. Simulation of shallow flows over variable topographies using unstructured grids. *International Journal for Numerical Methods in Fluids*. 2006;52(5):473-498. doi:10.1002/fld.1167.

Mohammadian A. Numerical approximation of viscous terms in finite volume models for shallow waters. *International Journal for Numerical Methods in Fluids*. 2009:n/a-n/a. doi:10.1002/fld.2097.

Monahan A. Can We See the Wind? Statistical Downscaling of Historical Sea Surface Winds in the Subarctic Northeast Pacific. *Journal of Climate*. 2012;25(5):1511-1528. doi:10.1175/2011jcli4089.1.

Moss, Richard H., et al. Towards new scenarios for analysis of emissions, climate change, impacts, and response strategies. No. PNNL-SA-63186. Pacific Northwest National Laboratory (PNNL), Richland, WA (US), 2008.

NCDC (National Climatic Data Center). (2015). "NOAA (National oceanic and atmospheric administration)." ⟨http://www.ncdc.noaa.gov/⟩.

Okely, P., Yeates, P. S., Antenucci, J. P., Imberger, J., &Hipsey, M. R. Modelling of the impact of the Perth Seawater Desalination Plant discharge on dissolved oxygen in Cockburn Sound. *Centre for Water Research, University of Western Australia*. 2006.

Pattantyús-Ábrahám, M., Tél, T., Krámer, T., &Józsa, J. Mixing properties of a shallow basin due to wind-induced chaotic flow. *Advances in Water Resources*. 2008;31(3):525-534. doi:10.1016/j.advwatres.2007.11.001.

Perot B. Conservation Properties of Unstructured Staggered Mesh Schemes. *Journal of Computational Physics*. 2000;159(1):58-89. doi:10.1006/jcph.2000.6424.

Pietrzak J, Jakobson J, Burchard H, Jacob Vested H, Petersen O. A three-dimensional hydrostatic model for coastal and ocean modelling using a generalised topography following co-ordinate system. *Ocean Modelling*. 2002;4(2):173-205. doi:10.1016/s1463-5003(01)00016-6.

Popinet S, Rickard G. A tree-based solver for adaptive ocean modelling. *Ocean Modelling*. 2007;16(3-4):224-249. doi:10.1016/j.ocemod.2006.10.002.

Pryor S, Barthelmie R, Schoof J. The Impact of Non-Stationarities in the Climate System on the Definition of" A Normal Wind Year": A Case Study from the Baltic. *International Journal of Climatology*. 2005a;25(6):735-752. doi:10.1002/joc.1151.

Pryor S. Empirical downscaling of wind speed probability distributions. *J Geophys Res*. 200;110(D19). doi:10.1029/2005jd005899.

Räisänen, J., Hansson, U., Ullerstig, A., Döscher, R., Graham, L. P., Jones, C., ...&Willén, U. European climate in the late twenty-first century: regional simulations with two driving global models and two forcing scenarios. *Climate Dynamics*. 2004;22(1):13-31. doi:10.1007/s00382-003-0365-x.

Randall D. Geostrophic Adjustment and the Finite-Difference Shallow-Water Equations. *Mon Wea Rev*. 1994;122(6):1371-1377.doi:10.1175/1520-0493(1994)122<1371:gaatfd>2.0.co;2.

Ringler T, Thuburn J, Klemp J, Skamarock W. A unified approach to energy conservation and potential vorticity dynamics for arbitrarily-structured C-grids. *Journal of Computational Physics*. 2010;229(9):3065-3090. doi:10.1016/j.jcp.2009.12.007.

Rogers B, Fujihara M, Borthwick A. Adaptive Q-tree Godunov-type scheme for shallow water equations. *International Journal for Numerical Methods in Fluids*. 2001;35(3):247-280. doi:10.1002/1097-0363(20010215)35:3<247::aid-fld89>3.0.co;2-e.

RoldÃ¡n M, Valenzuela L, Zarza E. Thermal analysis of solar receiver pipes with superheated steam. *Applied Energy*. 2013;103:73-84. doi:10.1016/j.apenergy.2012.10.021.

Rowell D. A scenario of European climate change for the late twenty-first century: seasonal means and interannual variability. *ClimDyn*. 2005;25(7-8):837-849. doi:10.1007/s00382-005-0068-6.

Sankaranarayanan S, Spaulding M. Dispersion and stability analyses of the linearized two-dimensional shallow water equations in boundary-fitted co-ordinates. *International Journal for Numerical Methods in Fluids*. 2003;42(7):741-763. doi:10.1002/fld.552.

Schwab D, Beletsky D. Propagation of Kelvin waves along irregular coastlines in finite-difference models. *Advances in Water Resources*. 1998;22(3):239-245. doi:10.1016/s0309-1708(98)00015-3.

Shchepetkin A, McWilliams J. The regional oceanic modeling system (ROMS): a split-explicit, free-surface, topography-following-coordinate oceanic model. *Ocean Modelling*. 2005;9(4):347-404. doi:10.1016/j.ocemod.2004.08.002.

Shchepetkin A. A method for computing horizontal pressure-gradient force in an oceanic model with a nonaligned vertical coordinate. *J Geophys Res*. 2003;108(C3). doi:10.1029/2001jc001047.

Sheng Z, Yuan G. A Finite Volume Scheme for Diffusion Equations on Distorted Quadrilateral Meshes. *Transport Theory and Statistical Physics*. 2008;37(2-4):171-207. doi:10.1080/00411450802526533.

Shirkhani H, Mohammadian A, Seidou O, Kurganove A. A well-balanced positivity-preserving central-upwind scheme for shallow water equations on unstructured quadrilateral grids", *Computer and Fluids*, 2015, (Accepted pending revision-Revision Submitted)

Shirkhani H, Mohammadian A, Seidou O, Qiblawey H. Analysis of Finite Volume Triangular C-grid for Shallow Water Equations with Coriolis. *Advances in Water Resources*. 2015 (under review)

Shirkhani H, Mohammadian A, Seidou O, Qiblawey H. Analysis of triangular C-grid finite volume scheme for shallow water flows. *Advances in Water Resources*. 2015;82:176-195. doi:10.1016/j.advwatres.2015.04.011.

Shirkhani H, Seidou O, Mohammadian A, Qiblawey H. Projection of Significant Wave Height in a Coastal Area under RCPs Climate Change Scenarios. *Natural Hazards Review*. 2015:04015016. doi:10.1061/(asce)nh.1527-6996.0000192.

Shirkhani, H., Seidou, O., & Mohammadian, A. Downscaling Method for Wind Data: Case Study of Agadez in Niger. 3rd Specialty Conf. on Disaster Prevention and Mitigation, Canadian Society for Civil Engineering (CSCE), 2013. Montreal, Canada.

Skoula Z, Borthwick A, Moutzouris C. Godunov-type solution of the shallow water equations on adaptive unstructured triangular grids. *International Journal of Computational Fluid Dynamics*. 2006;20(9):621-636. doi:10.1080/10618560601088327.

Stommel H. The westward intensification of wind-driven ocean currents. *Trans AGU*. 1948;29(2):202. doi:10.1029/tr029i002p00202.

Stuhne G, Peltier W. An unstructured C-grid based method for 3-D global ocean dynamics: Free-surface formulations and tidal test cases. *Ocean Modelling*. 2009;28(1-3):97-105. doi:10.1016/j.ocemod.2008.11.005.

Suli E. The Accuracy of Cell Vertex Finite Volume Methods on Quadrilateral Meshes. *Mathematics of Computation*. 1992;59(200):359. doi:10.2307/2153062.

Sultan S, Ahmad F, Elghribi N, Al-Subhi A. An analysis of Arabian Gulf monthly mean sea level. *Continental Shelf Research*. 1995;15(11-12):1471-1482. doi:10.1016/0278-4343(94)00081-w.

Szpilka C, Kolar R. Numerical analogs to Fourier and dispersion analysis: development, verification, and application to the shallow water equations. *Advances in Water Resources*. 2003;26(6):649-662. doi:10.1016/s0309-1708(03)00028-9.

Taylor K, Stouffer R, Meehl G. An Overview of CMIP5 and the Experiment Design. *Bull Amer Meteor Soc*. 2012;93(4):485-498. doi:10.1175/bams-d-11-00094.1.

Thacker W. Some exact solutions to the nonlinear shallow-water wave equations. *J Fluid Mech*. 1981;107(-1):499. doi:10.1017/s0022112081001882.

Thuburn J, Ringler T, Skamarock W, Klemp J. Numerical representation of geostrophic modes on arbitrarily structured C-grids. *Journal of Computational Physics*. 2009;228(22):8321-8335. doi:10.1016/j.jcp.2009.08.006.

Thuburn J. Rossby wave dispersion on the C-grid. *AtmosSciLett*. 2007;8(2):37-42. doi:10.1002/asl.148.

Triki A. Multiple-grid finite element solution of the shallow water equations: Water hammer phenomenon. *Computers & Fluids*. 2014;90:65-71. doi:10.1016/j.compfluid.2013.11.007.

Valiani A, Begnudelli L. Divergence Form for Bed Slope Source Term in Shallow Water Equations. *Journal of Hydraulic Engineering*. 2006;132(7):652-665. doi:10.1061/(asce)0733-9429(2006)132:7(652).

Vaselali A, Vaselali M. Modelling of Brine Waste Discharges Spreading Under Tidal Currents.*Journal of Applied Sciences*. 2009;9(19):3454-3468. doi:10.3923/jas.2009.3454.3468.

Vasiliades L, Loukas A, Patsonas G. Evaluation of a statistical downscaling procedure for the estimation of climate change impacts on droughts. *Nat Hazards Earth Syst Sci*. 2009;9(3):879-894. doi:10.5194/nhess-9-879-2009.

Viles H. Interannual, decadal and multidecadal scale climatic variability and geomorphology. *Earth-Science Reviews*. 2003;61(1-2):105-131. doi:10.1016/s0012-8252(02)00113-7.

Walters R, Carey G. Numerical noise in ocean and estuarine models. *Advances in Water Resources*. 1984;7(1):15-20. doi:10.1016/0309-1708(84)90025-3.

Walters R, Carey G. Numerical noise in ocean and estuarine models. *Advances in Water Resources*. 1984;7(1):15-20. doi:10.1016/0309-1708(84)90025-3.

Walters R, Hanert E, Pietrzak J, Le Roux D. Comparison of unstructured, staggered grid methods for the shallow water equations. *Ocean Modelling*. 2009;28(1-3):106-117. doi:10.1016/j.ocemod.2008.12.004.

Walters, R. A., and Vincenzo Casulli. A robust, finite element model for hydrostatic surface water flows. Communications in Numerical Methods in Engineering 14.10 (1998): 931-940.

Wang Y, Hutter K, Bäuerle E. Three-dimensional wind-induced baroclinic circulation in rectangular basins. *Advances in Water Resources*. 2000;24(1):11-27. doi:10.1016/s0309-1708(00)00034-8.

White L, Deleersnijder E, Legat V. A three-dimensional unstructured mesh finite element shallow-water model, with application to the flows around an island and in a wind-driven, elongated basin. *Ocean Modelling*. 2008;22(1-2):26-47. doi:10.1016/j.ocemod.2008.01.001.

Wilby R, Tomlinson O, Dawson C. Multi-site simulation of precipitation by conditional resampling. *Climate Research*. 2003;23:183-194. doi:10.3354/cr023183.

Wilby R, Wigley T. Downscaling general circulation model output: a review of methods and limitations. *Progress in Physical Geography*. 1997;21(4):530-548. doi:10.1177/030913339702100403.

Wilby, R. L., Charles, S. P., Zorita, E., Timbal, B., Whetton, P., & Mearns, L. O. Guidelines for use of climate scenarios developed from statistical downscaling methods. (2004):1-27.

Wolfram P, Fringer O. Mitigating horizontal divergence â€œchecker-boardâ€• oscillations on unstructured triangular C-grids for nonlinear hydrostatic and nonhydrostatic flows. *Ocean Modelling*. 2013;69:64-78. doi:10.1016/j.ocemod.2013.05.007.

Wu W, Sánchez A, Zhang M. An Implicit 2-D Shallow Water Flow Model on Unstructured Quadtree Rectangular Mesh. *Journal of Coastal Research*. 2011;59:15-26. doi:10.2112/si59-003.1.

Xie B, Xiao F. Two and three dimensional multi-moment finite volume solver for incompressible Navierâ€“Stokes equations on unstructured grids with arbitrary quadrilateral and hexahedral elements. *Computers & Fluids*. 2014;104:40-54. doi:10.1016/j.compfluid.2014.08.002.

Xing Y, Shu C. High order finite difference WENO schemes with the exact conservation property for the shallow water equations. *Journal of Computational Physics*. 2005;208(1):206-227. doi:10.1016/j.jcp.2005.02.006.

Xing Y, Zhang X, Shu C. Positivity-preserving high order well-balanced discontinuous Galerkin methods for the shallow water equations. *Advances in Water Resources*. 2010;33(12):1476-1493. doi:10.1016/j.advwatres.2010.08.005.

Xu C. From GCMs to river flow: a review of downscaling methods and hydrologic modelling approaches. *Progress in Physical Geography*. 1999;23(2):229-249. doi:10.1177/030913339902300204.